OCEAN THERMAL ENERGY CONVERSION PLANTS: EXPERIMENTAL AND ANALYTICAL STUDY OF MIXING AND RECIRCULATION

by

Gerhard H. Jirka
David J. Fry

R. Peter Johnson
Donald R.F. Harleman

Energy Laboratory
Report No. MIT-EL 77-011

September 1977

OCEAN THERMAL ENERGY CONVERSION PLANTS: EXPERIMENTAL AND ANALYTICAL STUDY OF MIXING AND RECIRCULATION

by

Gerhard H. Jirka

R. Peter Johnson

David J. Fry

Donald R.F. Harleman

ENERGY LABORATORY

in association with

RALPH M. PARSONS LABORATORY FOR
WATER RESOURCES AND HYDRODYNAMICS
DEPARTMENT OF CIVIL ENGINEERING

MASSACHUSETTS INSTITUTE OF TECHNOLOGY

Energy Laboratory Report No. MIT-EL 77-011

September 1977

Prepared under the support of
Division of Solar Energy
U.S. Energy Research and Development Administration
Washington, D.C.

Contract No. EY-76-S-02-2909.M001

ABSTRACT

Ocean thermal energy conversion (OTEC) is a method of generating power using the vertical temperature gradient of the tropical ocean as an energy source. Experimental and analytical studies have been carried out to determine the characteristics of the temperature and velocity fields induced in the surrounding ocean by the operation of an OTEC plant. The condition of recirculation, i.e. the re-entering of mixed discharge water back into the plant intake, was of particular interest because of its adverse effect on plant efficiency. The studies were directed at the mixed discharge concept, in which the evaporator and condenser water flows are exhausted jointly at the approximate level of the ambient ocean thermocline. The OTEC plant was of the symmetric spar-buoy type with radial or separate discharge configurations. A distinctly stratified ocean with uniform, ambient current velocity was assumed.

The following conclusions are obtained:

The recirculation potential of an OTEC plant in a stagnant ocean is determined by the interaction of the jet discharge zone and a double sink return flow (one sink being the evaporator intake, the other the jet entrainment). This process occurs in the near-field of an OTEC plant up to a distance of about three times the ocean mixed layer depth. The stratified internal flow beyond this zone has little effect on recirculation, as have small ocean current velocities (up to 0.10 m/s prototype). Conditions which are conducive to recirculation are characterized by high discharge velocities and large plant flow rates. A design formula is proposed which determines whether recirculation would occur or not as a function of plant design and ocean conditions. On the basis of these results, it can be concluded that a 100 MW OTEC plant with the mixed discharge mode can operate at a typical candidate ocean site without incurring any discharge recirculation.

ACKNOWLEDGEMENTS

This study was sponsored by the Division of Solar Energy, U.S. Energy Research and Development Administration, under contract No. E(11-1)-2909 with the M.I.T. Energy Laboratory and the R.M. Parsons Laboratory and was administered by the M.I.T. Office of Sponsored Programs, Account No. 83746. The ERDA program officers were Dr. Robert Cohen during the initial stage and Dr. Lloyd Lewis for the remainder of the project. Program support was also provided by Dr. Jack Ditmars and his staff at the Argonne National Laboratory. The cooperation and assistance of these individuals is gratefully acknowledged.

The experimental work was conducted at the R.M. Parsons Laboratory. The assistance of Messrs. Edward F. McCaffrey, Electronics Engineer, Roy G. Milley, Arthur Rudolph, Machinists, and Jeffrey Freudberg, Undergraduate Student, was invaluable for completion of the project. Computer work was performed at the M.I.T. Information Processing Center. The report was aptly typed by Ms. Carole Bowman and Ms. Anne Clee.

The experimental and numerical studies were conducted by Mr. R. Peter Johnson and Mr. David J. Fry, Graduate Research Assistants. Research guidance and supervision was given by Dr. Gerhard H. Jirka, Research Engineer in the M.I.T. Energy Laboratory, and Dr. Donald R. F. Harleman, Ford Professor of Engineering and Director of the R.M. Parsons Laboratory.

TABLE OF CONTENTS

CHAPTER I

INTRODUCTION

1.1 Principles of OTEC Operation

Ocean thermal energy conversion (OTEC) is a method of generating power using the vertical temperature gradient of the tropical ocean as an energy source. The upper layer of the ocean collects energy by changing solar radiation to heat. The underlying water is colder due to the return flow from polar regions which occurs within the global circulation of the world ocean.

Ocean thermal energy conversion to produce economically usable forms of power is based on the same thermodynamic principles employed in conventional methods of power production. The thermal difference between the warm upper water and the cold lower water is used to vaporize and condense, respectively, a working fluid which, in turn, drives turbines. An OTEC plant differs from conventional power plants in that is has a very low thermodynamic efficiency.

Efficiency, e, based on the second law of thermodynamics, may be defined as:

$$e = \frac{T_w - T_c}{T_{av}} \tag{1.1}$$

T_w, T_c, T_{av} = warm, cold and average temperatures on an absolute scale

Figure 1.1 shows typical vertical temperature profiles for the tropical ocean. Using values of T_w = 300°K(27°C) and T_c = 281°K(8°C),

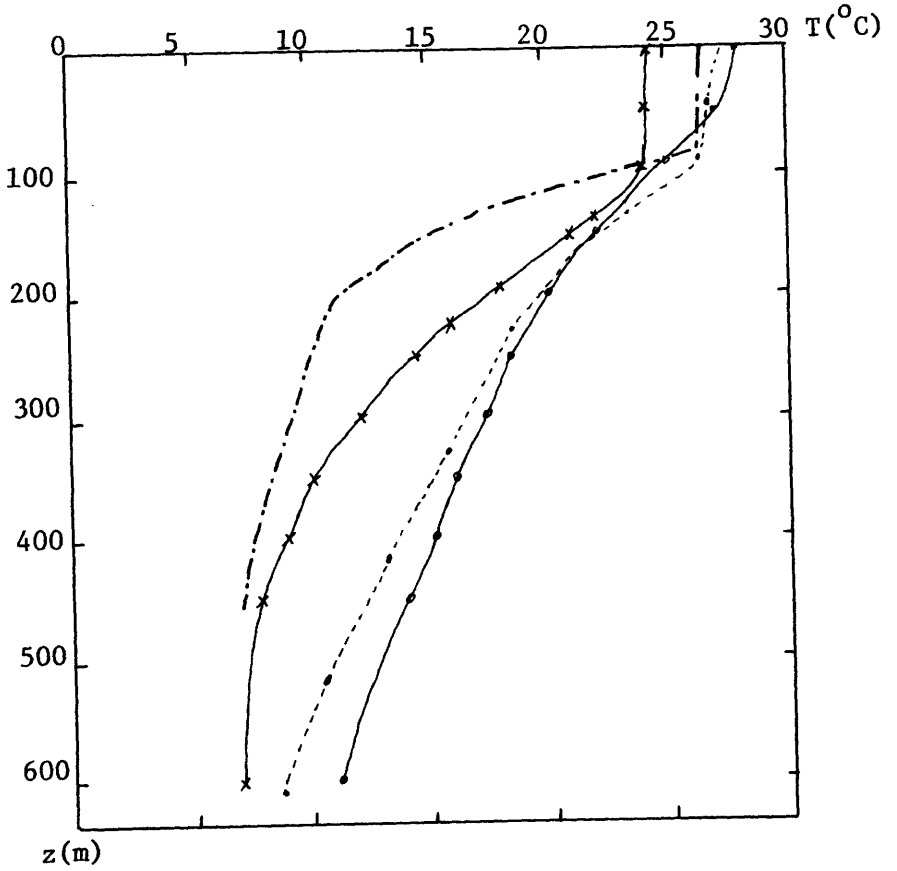

Figure 1.1 Examples of Vertical Temperature Profiles for the Tropical Ocean.

a theoretical maximum efficiency for an OTEC plant of the order of 0.07 may be calculated. Due to energy losses in the production process, such as from pumping, friction and imperfect transfer across the heat exchangers, the actual efficiency of a plant is expected to be of the order 0.02 to 0.03. This efficiency is very low compared to conventional steam-electric power cycles which have efficiencies on the order of 0.30 to 0.40. In order to produce power in quantities comparable to conventional plants, an OTEC plant must use very large quantities of water to exploit its low grade energy resource. For example, to produce 100 MWe, assuming a 2°C change in temperature across the heat exchangers and a plant efficiency of 0.02, a total flow rate of approximately 1200 m^3/sec (42000 cfs) is required.

1.2 Current Prototype Designs and the Need for this Investigation

All of the prototype designs currently (1977) being considered (see Chapter 2) are for free floating plants in the deep tropical ocean. Discharges and intakes, i.e. sources and sinks, may be approximated as occurring along a single column separated only by some vertical distance. The very large flow rates involved in plant operation should be expected to alter the ambient flow and temperature field. Since the intakes and discharge operate in the same region, it is possible that the discharged water, which has lost some of the initial temperature difference, may recirculate directly to the intakes. Should this happen the temperature difference across the plant would decrease, which would further reduce the thermodynamic efficiency. It is necessary to know if an OTEC plant, based on the prototype designs,

will be able to operate without destroying the resource it draws upon.

1.3 Purpose of this Study

The general purpose of this study is to examine the characteristics of the flow and temperature field in which an OTEC power plant would exist to determine constraints on the size and operation of the plant. In particular, this study is directed at experimental and analytical investigations to describe the flow and temperature fields formed by a schematic OTEC power plant discharging at the interface of a distinctly stratified ocean with and without ambient currents. Two discharge geometries are considered, namely a radial discharge around the plant circumference and four separate discharges at 90° to each other. The results are expected to serve as a first indication as to what will occur in a more complex design. The engineering sensitivities and limitations on plant design and ocean baseline parameters, including maximum and minimum flow rates and discharge velocities, maximum or minimum temperature differences and depth to the thermocline, can be examined in this schematic framework.

CHAPTER II

PROTOTYPE SCHEMATIZATION AND SCALE MODELING PARAMETERS

2.1 Physical Characteristics of the Prototype

Several different designs have been proposed for a prototype OTEC power plant. The designs considered in this paper are limited to those that can be modeled as symmetric vertical columns. Other designs, not considered here, rely upon the ambient ocean currents to provide a continuous stream of warm surface water to the upper intakes. This highly asymmetric type of plant must be designed for site-specific conditions. The column, or spar-buoy, design does not rely upon the ambient ocean currents. This is the design for which plant operating parameters and ocean baseline conditions are given in Table 2.1. The design conditions are taken from studies by Lockheed (1975), TRW (1975) and Carnegie-Mellon University (1975). In addition the Lockheed design has been reduced in power output to 100 MW, equal to the other designs. The range of these design parameters serves as a base from which a "standard" condition for the scale model can be drawn.

2.2 Schematization

Designs of this type, and the stratified ocean, can be simulated by a schematization as shown in Figure 2.1. This simplifies the scale model and the experimental procedure while retaining the most important aspects of the external flow and temperature fields.

Table 2.1

OCEAN BASELINE AND PLAN DESIGN PARAMETERS FOR VARIOUS PROPOSED PROTOTYPES

Oceanography	Lockheed	Lockheed (reduced output)	TRW	Carnegie-Mellon University
Thermocline Depth	60 m (200 ft)	60 m (200 ft)	X	X
ΔT Across Plant	18.3°C (33°F)	18.3°C (33°F)	22°C (40°F)	20°C (38°F)
Ambient Current(max)	2.75 m/sec (5.5 kts)	2.75 m/sec (5.5 kts)	1.0 m/sec (2 kts)	X
Plant Design				
Power Output	160 MW	100 MW	100 MW	100 MW
Intake Diameter	X	X	15.4 m (50 ft)	15.4 m (50 ft)
Plant Diameter at Level of Discharge Ports	143 m (470 ft)	143 m (470 ft)	60 m (200 ft)	X
Flowrate:				
Cold	1360 m^3/sec (48000 cfs)	850 m^3/sec (30000 cfs)	456 m^3/sec (16100 cfs)	368 m^3/sec (13000 cfs)
Warm	1800 m^3/sec (64000 cfs)	1133 m^3/sec (40000 cfs)	456 m^3/sec (16100 cfs)	637 m^3/sec (22500 cfs)
Discharge Velocity	1.5-2.4 m/sec (5-8 ft/sec)	1.5-2.4 m/sec (5-8 ft/sec)	2.4 m/sec (8 ft/sec)	2.13-3.35 m/sec (7-11 ft)
Discharge Depth:				
Cold	88 m (290 ft)	88 m (290 ft)	52 m (170 ft)	Thermocline
Warm	46 m (150 ft)	46 m (150 ft)	52 m (170 ft)	Thermocline

X: Unspecified or Not Known

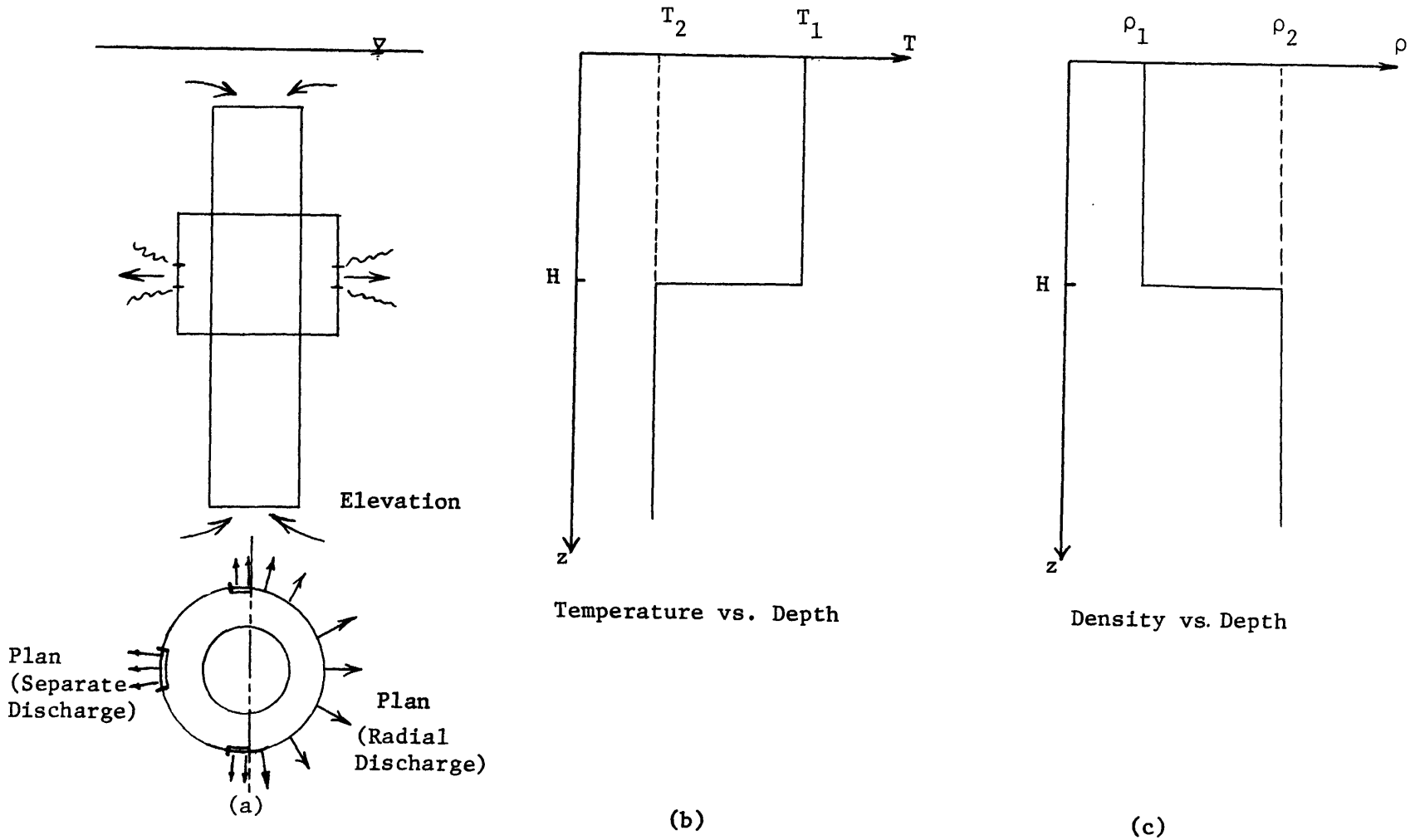

Figure 2.1 Schematization of OTEC Plant and Ambient Stratification Conditions

2.2.1 Schematization of the Ocean

Figures 2.1 (b,c) indicate that the ocean is approximated by two stagnant layers of water of distinctly different densities and temperatures. The stratification is stable. Both layers are assumed to be isothermal and are separated by an abrupt thermocline.

The adopted schematization is representative of actual ocean conditions. Figure 1.1 compares well, in form, with Figure 2.1 (b), particularly in the upper layer. Figure 2.2 shows a typical density profile of the tropical ocean. This corresponds to the schematic situation shown in Figure 2.1(c). The change in density from layer to layer is pronounced. Water density in the ocean is a function of salinity as well as temperature. Figure 2.3 serves to point out that salinity changes at the sites of interest are small and, hence, contribute little to the change in density over the depth.

The distinction between temperature and density is important in modeling an OTEC power plant. A plant generates power by operating on the thermal difference between layers. The external fluid dynamics, however, is controlled by the difference in densities (buoyancy). Buoyancy in the experiments is regulated solely by temperature.

2.2.2 Schematization of the Plant

Figure 2.1(a) shows that the OTEC plant is schematized to be a long, narrow, floating cylinder (spar-buoy). There is one intake port at the top of the cylinder for the warm water and one at the bottom for the cold water. The evaporator and condenser flows are assumed to be mixed together within the plant prior to the discharge so that the dis-

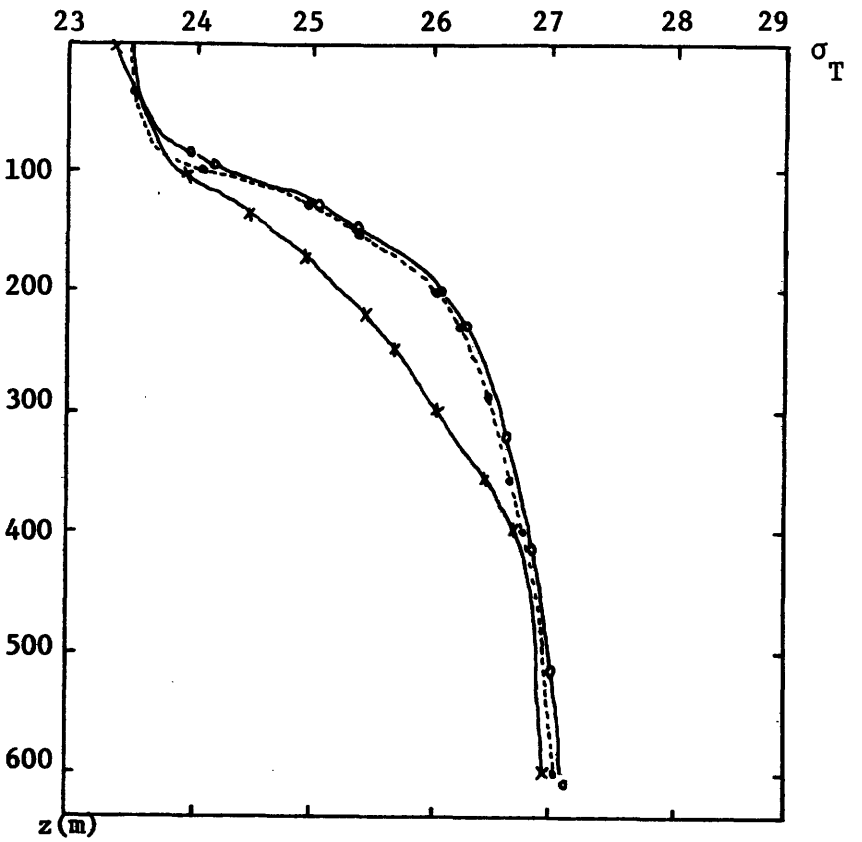

$\sigma_T = (\rho-1)1000$

---•--- Carribean (Fuglister, 1960)

—o— Florida Straits

—×— Hawaii (Bathen, 1975)

Figure 2.2 Examples of Vertical Density Profiles for the Tropical Ocean.

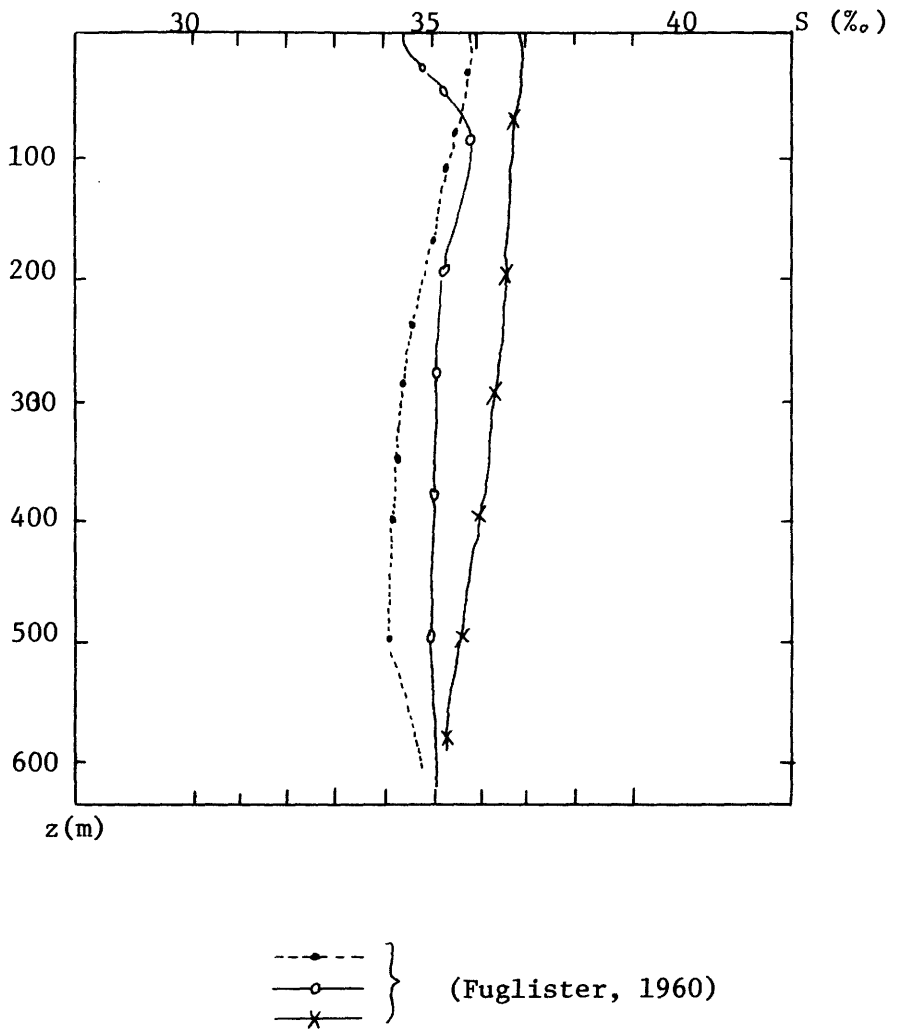

Figure 2.3 Examples of Vertical Salinity Profiles for the Tropical Ocean.

charge volume is the sum of the intake flows and the discharge temperature is the weighted average. The discharge is assumed to be exactly at the thermocline so that the jet trajectory will follow the thermocline, neither rising nor falling.

These assumptions of completely mixed flow released exactly at the thermocline are not strictly accurate. The actual OTEC designs being simulated in this study do not mix the warm and cold water within the plant, nor is the discharged water released in a neutrally buoyant position. In some designs (TRW, 1975), however, the separate discharge streams are arranged close to each other so that mixing immediately outside the plant can be assumed. Also, the distance which the discharge jets would rise or fall is expected to be small compared to the distance from the intakes. The qualitative differences of mixed and non-mixed discharge designs are further addressed in Chapter 9.

Two types of generic discharge configurations are evaluated in this study:

a) Radial discharge: The discharge geometry is assumed as a slot which completely encircles the plant circumference. Although none of the present designs exhibit this geometry, it is a useful basis for evaluation. It has an obvious advantage for analytical (cylindrically two-dimensional) and experimental modeling and it preserves the characteristics of the more complicated three-dimensional separate discharge design. This is possible so long as the radial discharge design retains equality of mass, momentum and heat fluxes.

b) Separate discharge: Four separate jets with rectangular cross-sections are arranged around the plant circumference at an angle of 90°

to each other. This closely approaches probable (round port) design conditions with the mixed discharge concept.

Table 2.2 lists the ocean baseline and plant design parameters with the two generic discharge configurations for a 100 MW "standard" OTEC plant.

2.2.3 Further Simplification for Experimental Purposes

Even though the schematic prototype greatly simplifies the description of the external velocity and temperature fields a further modification has been made in order to facilitate the experiments. Because of its relative shallowness, the upper layer is of primary interest because of the potential for recirculation. As a first approximation, the discharge jet geometry can be taken as symmetric with respect to the ambient abrupt thermocline. This restricts the model to the upper layer only with a half-jet discharge of different density, see Figure 2.4(a). This schematization reduces the total depth of water required for a physical model and eliminates the need to provide a carefully stratified ambient environment.

Finally, the model of the upper layer is inverted relative to the prototype, see Figure 2.4(b). This measure eliminates the wall friction that would occur if the discharge jet were at the floor of the model basin. On the other hand, the frictional effects on the inverted "surface" are considered to be negligible due to the small velocities of the intake flow. By inverting the model the effective direction of gravity has been reversed. In order to maintain the proper sense of

A. Ocean Baseline

Thermocline depth	H	50-100 m (average = 70 m)	(210 ft)
Ocean Current	u_a	0-2.8 m/sec	(0-4 kts)

B. Plant Design

Plant Radius	r_o	23 m	(75 ft)
Intake Flow	Q_i	500 m^3/sec	(17000 cfs)
Intake Radius	r_i	15 m	(50 ft)
Intake Depth from Surface	h_i	≃H	
Temperature Difference between Discharge and Upper Layer	ΔT_o	11°C	(20°F)
Density Difference between Discharge and Upper Layer	$\Delta\rho_o$	0.003 gm/cm^3	(.19 lb/ft^3)

(i) Radial Discharge Configuration

Discharge velocity	u_o	1.5-3.0 m/sec	(5-10 ft/sec)
Port half height	h_o	.62-1.25 m	(2-4 ft)
Port half area per quarter section	A_o	45.6 m^2	(490 ft^2)

(ii) Separate Discharge Configuration (Four Parts):

Discharge Velocity	u_o	1.5-3.0 m/sec	(5-10 ft/sec)
Port half height	h_o	3.8 m	(12.5 ft)
Port width	b_o	5.9-11.8 m	(19-39 ft)
Port half area	A_o	22-45 m^2	(72-148 ft^2)

Table 2.2: Prototype Ocean Baseline and Plant Design Parameters for 100 MW OTEC with Two Generic Mixed Discharge Configurations.

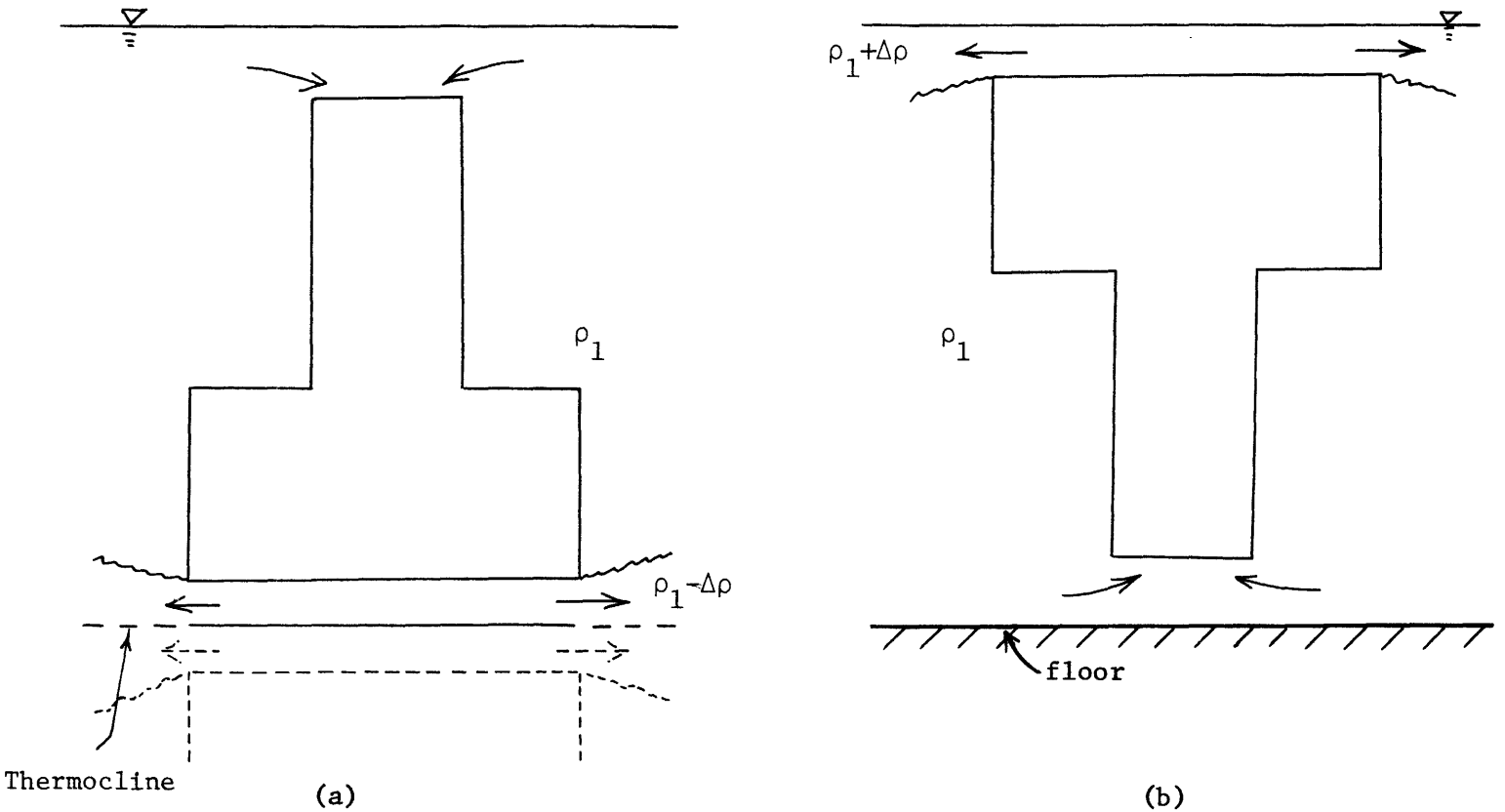

Figure 2.4 Schematization of the Upper Ocean Layer (a) and the Inverted Laboratory Model (b)

buoyancy the sign of the temperature difference is also inverted. The model discharge water is warmer, rather than colder, than the ambient upper layer water.

2.3 Model Scaling Parameters

To retain dynamic similitude between the prototype and a scale model it is necessary to know which effects will dominate the flow and temperature fields in both. An accurate scale model will reproduce those characteristics which are most important in the prototype situation. In order to determine what the controlling features are in both the model and prototype, it is necessary to consider the ocean background and engineering parameters. Table 2.3 lists the relevant physical variables that determine the external flow and temperature field generated by a schematized plant. The 20* listed variables involve five basic dimensions: mass, M; length, L; time, T; heat, J; and temperature, θ . According to the Buckingham π -theorem, 15 independent dimensionless groups can be formed from these variables. Table 2.4 lists one set of dimensionless groups that may be useful in this study.**

---

*19 for the radial discharge configuration.

**An alternative form of a densimetric Froude number uses the square-root of the discharge area, A_o (see Table 2.2). This "modified discharge Froude number"

$$\mathbb{F}_o^* = \frac{u_o}{\left(g \frac{\Delta\rho}{\rho} A_o^{1/2}\right)^{1/2}}$$

where $A_o = h_o b_o$ for separate jets

$= \frac{\pi}{2} r_o h_o$ for radial jets (choice of quarter section to compare with four separate jets)

eliminates the geometry effect of the discharge port and is useful for the comparison of discharge designs (Stolzenbach, et al., 1972; Jirka, et al., 1975; but with slight differences in the definition of discharge area).

Ocean

u_a = ambient current velocity [L/T]

H = upper layer depth [L]

ρ = ambient upper layer density [M/L^3]

β = thermal expansion coefficient [$M/L^3\theta$]

Discharge

u_o = discharge velocity [L/T]

h_o = discharge slot half-height [L]

b_o = separate discharge port width [L]

r_o = plant radius [L]

$\Delta\rho_o$ = discharge density difference [M/L^3] (= $f(\Delta T)$)

ΔT_o = discharge temperature difference [θ]

Intake

Q_i = corresponding full model intake volume flux [L^3/T]

h_i = intake distance to thermocline [L]

r_i = intake radius [L]

Medium

g = acceleration due to gravity [L/T^2]

ν = kinematic molecular viscosity [L^2/T]

ε = eddy viscosity [L^2/T]

σ = surface tension [M/T^2]

κ = eddy thermal diffusivity [L^2/T]

K = surface heat flux coefficient [$J/L^2T\theta$]

c_p = heat capacity [$J/M\theta$]

KEY: DIMENSIONS

L = length

T = time

M = mass

θ = temperature

J = heat

Table 2.3 List of Physical Parameters for Schematized OTEC Conditions

1.	Discharge Densimetric Froude Number ($\mathbb{F}r_o$ for radial jet) ($\mathbb{F}_o$ for separate jet)	$\dfrac{u_o}{\left(g \dfrac{\Delta\rho_o}{\rho} h_o\right)^{1/2}}$
2.	Intake Densimetric Froude Number ($\mathbb{F}_i$)	$\dfrac{Q_i}{\left(g \dfrac{\Delta\rho_o}{\rho} H^5\right)^{1/2}}$
3.	Discharge Reynolds Number ($\mathbb{R}_e$)	$\dfrac{4u_o h_o}{\nu}$
4.	Discharge Weber Number ($\mathbb{W}$)	$u_o\left(\dfrac{H\rho}{\sigma}\right)^{1/2}$
5.	Heat Loss Parameter	$\dfrac{K}{u_o \rho c_p}$
6.	Turbulent Prandtl Number ($\mathbb{P}_r$)	ε/κ
7.	Viscosity Ratio	ε/ν
8.	Density Difference Ratio	$\Delta\rho_o/\rho$
9.	Thermal Expansion Ratio	$\beta\Delta T_o/\rho$
10.	Ambient Current Flux Ratio	$\dfrac{u_a H^2}{Q_i}$
11.	Discharge Geometric Ratios	h_o/H
12.		h_o/r_o
13.		h_o/b_o (separate jets)
14.	Intake Geometric Ratios	h_i/H
15.		r_i/h_i

Table 2.4 List of Non-Dimensional Parameters for Schematized OTEC Conditions

Given that the same medium is used in the prototype and the model it is not possible to retain equality for each of the dimensionless parameters. The model has been scaled to preserve geometric similarity and densimetric Froude numbers. The model is undistorted and at a scale of 1:200 to the schematic prototype (Table 2.6). Densimetric Froude similarity preserves the buoyant mixing process, which is the most important characteristic in determining the external flow and temperature fields (Jirka, et al., 1975). The approximate scale of 1:200 was determined by the depth of the laboratory basin (35 cm) in relation to the characteristic upper layer depth of the schematic prototype (70 m).

This choice of modeling criteria satisfies similitude for non-dimensional parameters 1, 2 and 11 through 15 listed in Table 2.4. Parameters 8 and 9, the density difference ratios, are identical in a system stratified only by temperature. This ratio is made similar by proper choice of the discharge temperature.

The model scale must be large enough so that the other dimensionless parameters are nearly satisfied or describe effects which are negligible in both the prototype and the model. Table 2.5 lists the values of the non-dimensional parameters based on the design values given in Table 2.2 for the schematic prototype and for the experimental model.

The prototype is operating in the high discharge Reynolds number range. The model Reynolds number cannot be made the same since

		Prototype	Model (1:200)
1.	$\mathbb{F}r_o$ (radial)	13.5	7-120
	$\mathbb{F}_o$ (separate)	7.8	3.8-70
	$\mathbb{F}_o^*$	6.0	3.0-43.
2.	$\mathbb{F}_i$	0.012	0.012-0.034
3.	$\mathbb{R}e$	1.76×10^7	3100-12400
4.	W	Not Applicable	4.5-290
5.	Heat Loss	Not Applicable	$\sim 3 \times 10^{-5}$
8.	$\Delta\rho_o/\rho$	.003	0.0015-0.003
10.	Ambient Current Flux Ratio	0-27.4	0-1.4
11.	h_o/H (radial)	0.018	0.009-.018
	(separate)	.054	0.054
12.	h_o/r_o (radial)	0.054	0.027-.054
	(separate)	0.167	0.167
13.	h_o/b_o (separate)	.32	.32-.64
14.	h_i/H	0.86	0.86 (not varied)
15.	r_i/h_i	0.22	0.22 (not varied)

Table 2.5 Values and Ranges of Dimensionless Parameters for OTEC Prototype (see Table 2.2) and Model (at a scale of 1:200)

the modeling criteria and receiving medium are chosen. It has been shown that for

$$\mathbb{R}_e \geq 1500 \qquad (2.1)$$

fully turbulent flow of the discharge jet can be assumed (Jirka, et al., 1975). Under these conditions the characteristics of the jet mixing zone can be taken as Reynolds number independent and thus similar. Furthermore, if a sufficient turbulence level is maintained in the jet mixing zone, it can be assumed that the Prandtl number (6) and viscosity ratio (7) are also similar for model and prototype. The region outside the jet mixing zone is characterized by considerably less turbulence and possibly laminar conditions. However, the dynamic similarity of heat and momentum transfer in this region is of lesser importance due to differences in time scale.

The Weber number is not applicable in the prototype since surface tension plays no role in the discharge flow field. The model Weber number (Table 2.5), based on a value of σ = 71 dynes/cm, is sufficiently large, $\mathbb{W}$ = 18, to indicate that surface tension has little influence on the model flow field.

Another parameter, the heat loss ratio, is also not applicable to the prototype situation. For the model, the ratio, using a value of $K = 6.8 \times 10^{-4}$ cal/cm^2-sec-°C, is sufficiently small, $K/u_o\rho c_p = 3 \times 10^{-5}$, to indicate that most of the heat discharged from the model remains in the water and little escapes to the atmosphere within the scale of the experiment.

The model values for the dimensionless parameters listed in Table 2.5 show the variability with respect to the "standard" conditions given for the choice of the schematic prototype. In general, the model was operated over a certain range of the parameters to encompass various design and operating conditions. Different discharge and intake densimetric Froude numbers were generated by varying the choice of volumetric flow rate and discharge geometry (as indicated by the variability of the discharge design parameters, Table 2.6). The intake design parameters were maintained the same because the intake geometry can be expected to have only secondary effects on the type of intake sink flow generated. The equivalent prototype dimensions for the "standard" 100 MW OTEC plant (scaled at the ratio 1:200) which formed the base case for the experimental program is illustrated in Figure 2.5 for the two generic discharge geometries.

It was not possible to examine the entire range for the ambient current flux ratio in the model because the experimental current generation system was limited in its pumping capacity.

	Model: 1:200
Ocean Baseline	
H	0.35 m (not varied)
u_a	0-.01 m/sec
Plant Design	
u_o	0.10-.80 m/sec
h_o(radial)	.00317-.00635 m
(separate)	.0191 m (not varied)
b_o(separate)	.0296-.0592 m
r_o	0.114 m (not varied)
Q_i	4.4×10^{-4}-17.7×10^{-4} m^3/sec
r_i	0.076 m (not varied)
h_i	0.030 m (not varied)
ΔT_o	5.5-11^{o}C
$\Delta \rho_o$	0.0015-.003 g/cm^3

Table 2.6 Range of Model Ambient and Plant Design Parameters

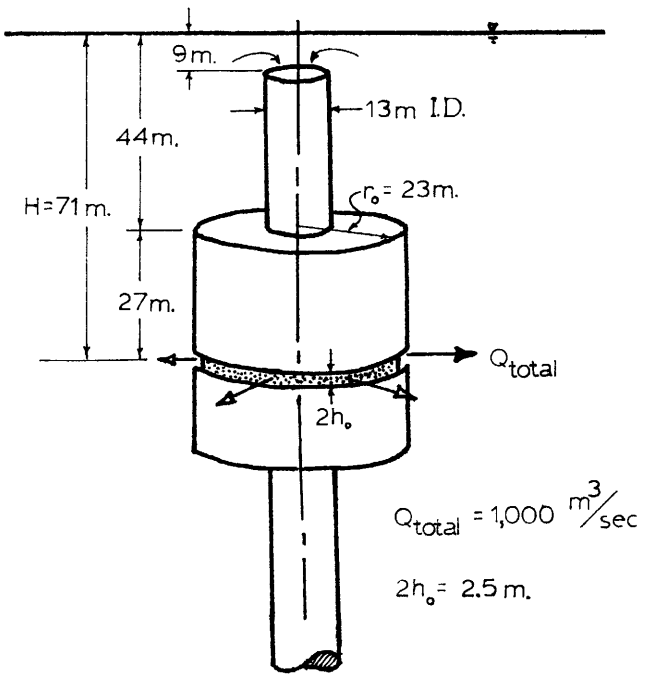

a) Radial Jet Discharge

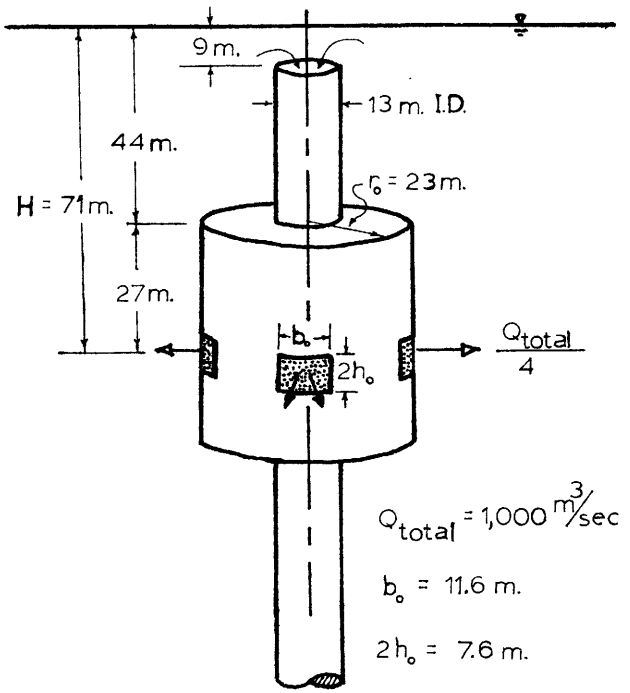

b) Separate Jet Discharge

Figure 2.5 Baseline Geometry and Flow Parameters for Mixed Discharge Conditions Assumed in Experimental Program ($\Delta T = 22^{o}C$) at an Assumed Scale Ratio of 1/200

CHAPTER III

EXPERIMENTAL LAYOUT AND OPERATION

3.1 The Basin

The physical experiments were conducted in a 12.2m x 18.3m x 0.35m (40' x 60' x 14") basin located on the first floor of the Ralph M. Parsons Laboratory for Water Resources and Hydrodynamics at M.I.T. The basin is equipped with a cross-flow generating capacity of velocities up to 1 cm/sec for the depth at which the experiments were conducted.

A 4.57 m (15 ft) long plexiglass window was installed in a wall of the basin for this experimental program. This allows visual observation and photography of the velocity field close to the wall.

3.2 The OTEC Model

Figure 3.1 is a cross-sectional view of the cylindrical plexiglass model used to simulate the upper portion of an OTEC power plant. Figure 3.2 is a photograph. Warm water enters through hoses at the top of the plexiglass model into bays separated by thin walls. Each hose discharges into a separate bay. The water passes through a thick plate with small holes drilled in it. This is to dissipate excess energy in the flow and break up jets that may form inside the model which would disrupt the uniform discharge distribution. Passing through the holes in the energy dissipator plate, the water impacts on the lower lip of the upper chamber. The water flows around the lip,

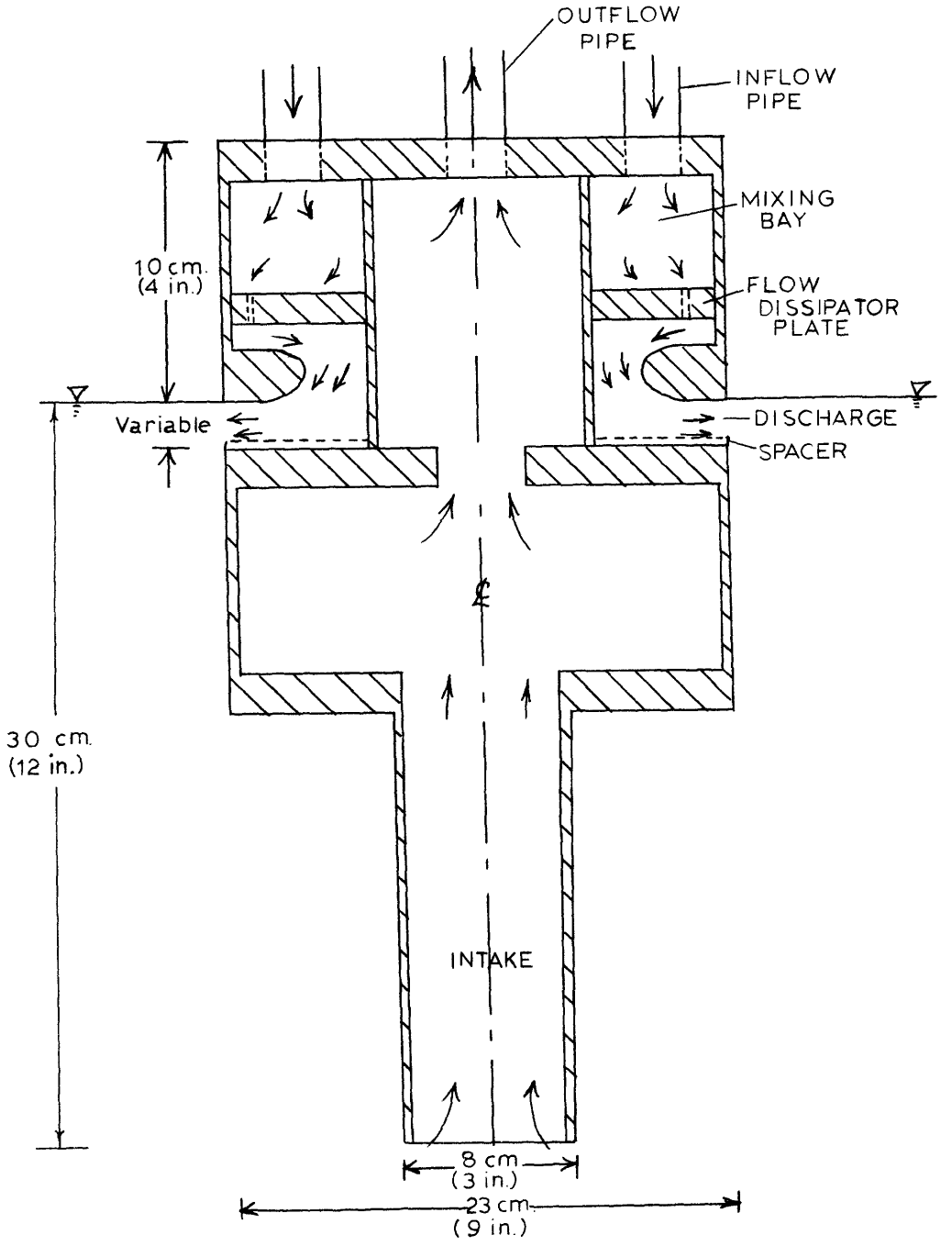

Figure 3.1 Schematic Diagram of the Plexiglass Model.

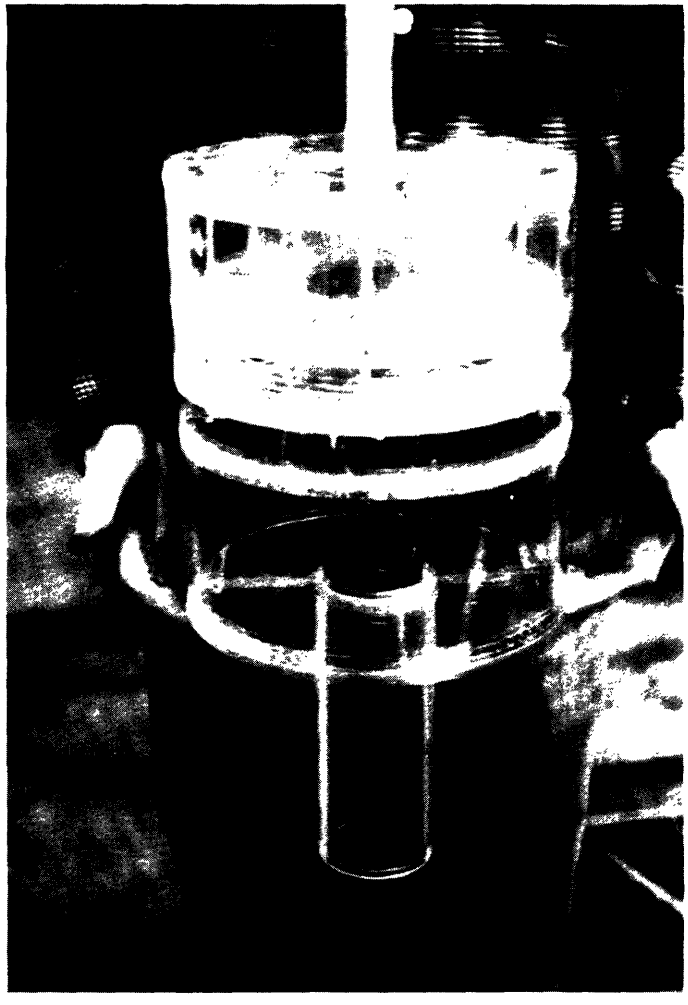

Figure 3.2 Photograph of the Plexiglass Model.

through the discharge slot and then into the basin. The discharge slot is designed to contract as the water flows away from the center of the model in such a way as to maintain a constant velocity while the water is inside the model. This measure helps to maintain uniformity of the discharge flow.

The model has the facility to vary the discharge slot configuration by inserting spacers into the model. Spacer "rings" of different thicknesses allow for discrete changes in the radial discharge slot height. The discharge can also be changed to separate ports by blocking portions of the circumferential slot. In this way rectangular ports can be represented. These two basically different configurations are referred to as "radial: and "separate" jet discharges.

The intake is at the bottom of the plexiglass model. Flow enters through the bottom into the lower chamber. From the lower chamber the water passes to the upper chamber inside a sleeve surrounded by the warm water bays. From the inner portion of the upper chamber the water is withdrawn through a suction hose.

The plexiglass model consists of two symmetric halves so that it can be attached flat to the plexiglass window for the wall set-up or bolted together and placed in the center of the model basin. Runs with both configurations were performed. Experiments with the half-model attached to the window make the basin effectively twice as big as those conducted with the full-model in the center. For the half-model runs the wall is taken to be a plane of symmetry. The full

model tests were conducted primarily to insure that wall friction is not important in the half-model experiments.

3.3 The Discharge and Intake Water Circuits

Figure 3.3 is a schematic diagram of the water flow circuits and cross-flow generating system.

Constant temperature must be maintained in the discharge flow to simulate an OTEC plant at steady state. This is accomplished by mixing cold tap water with hot water that has passed through a steam heat exchanger. A mixing valve adjusts the relative flows of hot and cold water to achieve the desired density.

From the mixing valve the hot water flows to a 0.21 m^3 (55 gal.), 3.0 m (10 ft) high constant head tank. This helps to provide a constant pressure in the delivery to the model, but more importantly damps out potential short period temperature fluctuations in the hot water system.

The hot water is pumped from the constant head tank through a flow meter and control valve to a manifold. The manifold has eight valves with connecting hoses to each separate bay in the upper chamber of the plexiglass model. The flow rate can be regulated by the valves on the manifold to make the flow from the plexiglass model uniformly distributed. The discharge temperature is monitored at the model.

The intake circuit draws water from the basin through the center of the plexiglass model. The water is withdrawn by a pump, measured by a flow meter and controlled by a valve. The intake temperature is monitored at the model.

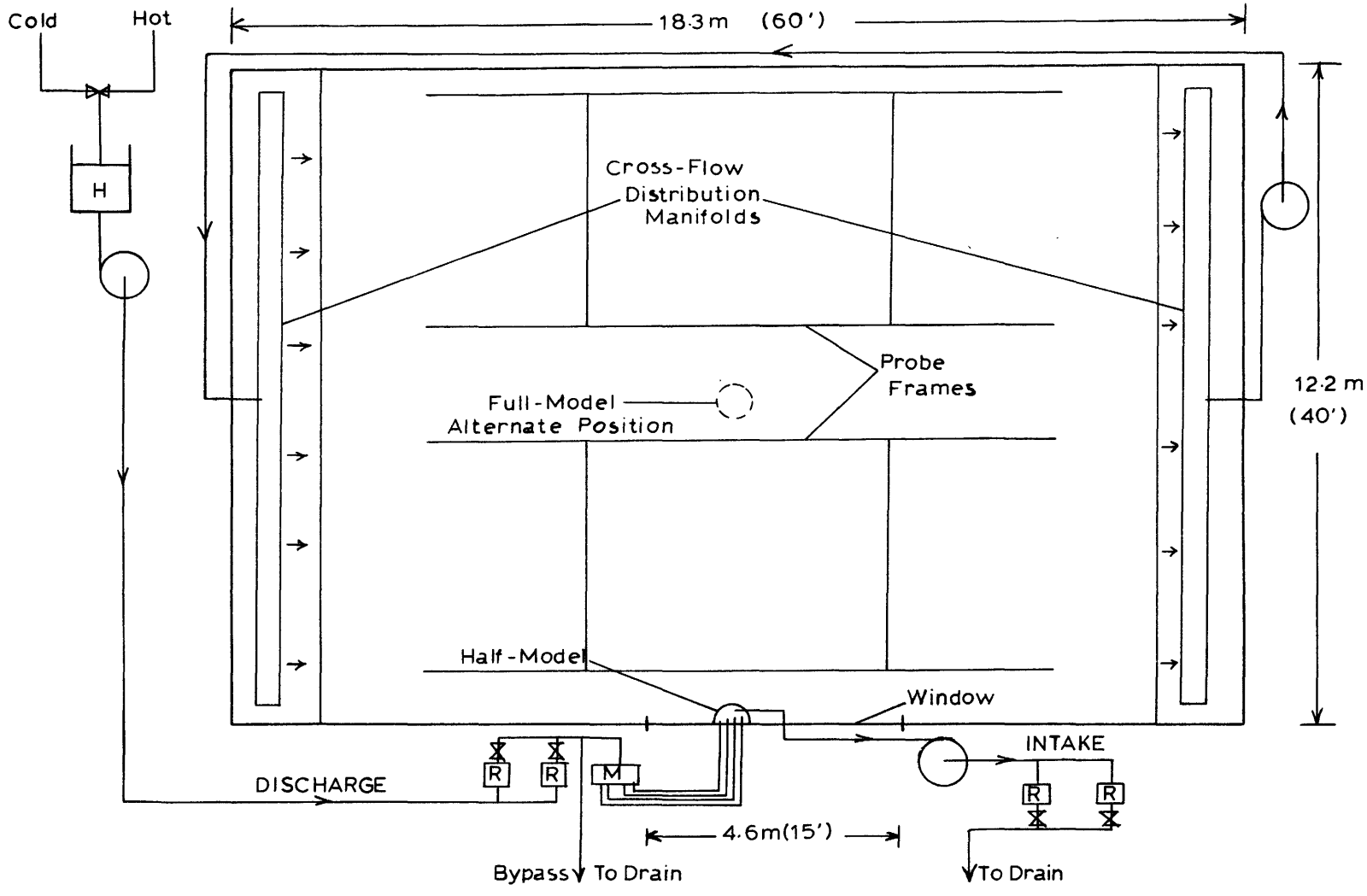

Figure 3.3 Schematic Diagram of the Experimental Setup.

3.4 Temperature Data Acquisition, Processing and Presentation

The bulk of the information collected from the physical experiments is temperatures at various places in the external flow field. 100 thermistor temperature probes with a time constant of 1.0 seconds were used. Two probes were placed in the hoses feeding the discharge. Three or four probes were used to monitor the intake temperature. The remaining 95 or 94 were mostly fixed to a vertically traversable frame to monitor the temperatures found in the external flow field. Figure 3.4 shows the five probe arrangements used in the experiments.

In the stagnant experiments the probes were set up as to capture the important parts of an anticipated temperature field. Radial experiments had probes arranged along rays extending out from the model. Each probe had a counterpart at the same radius on other rays. Separate jet experiments were set up to measure centerline temperature along with a few temperature cross-sections (for jet width determination).

Experiments with an ambient current had probe arrangements meant simply to cover the entire basin. As with the stagnant experiments, probe densities were higher near the model where the major temperature variations occurred.

A digital electronic volt meter with the capability to scan 100 thermistor temperature probes records the information on a paper printout and on punched paper tape. A typical experiment will record 5000 to 6000 temperature readings.

Computer facilities were used to calibrate, present, and store this large amount of data. Computer programs were developed to do each of these tasks.

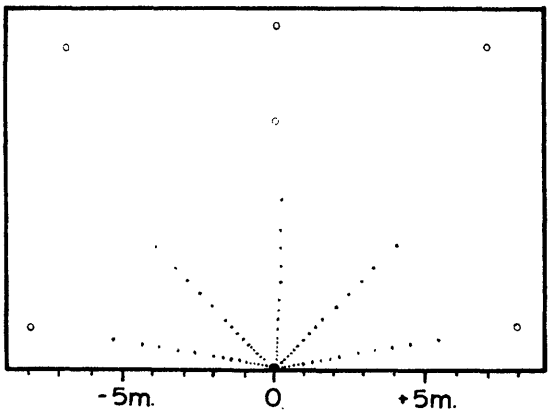

I; A
Exp. #1-8

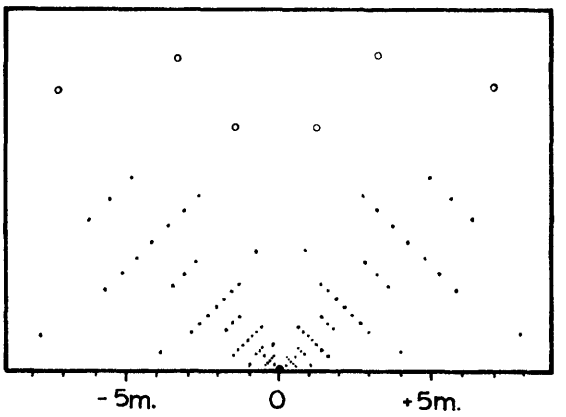

I; B
Exp. #9-15

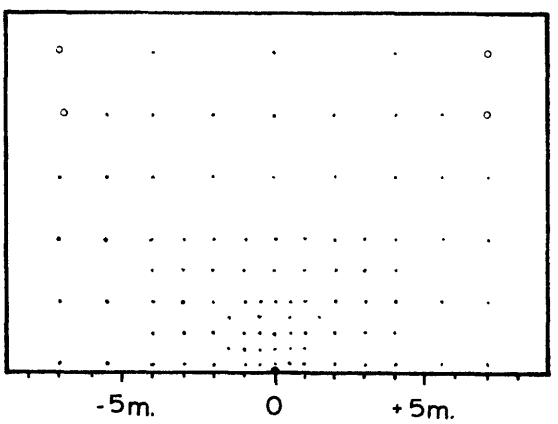

I; C,D
Exp. #16-24

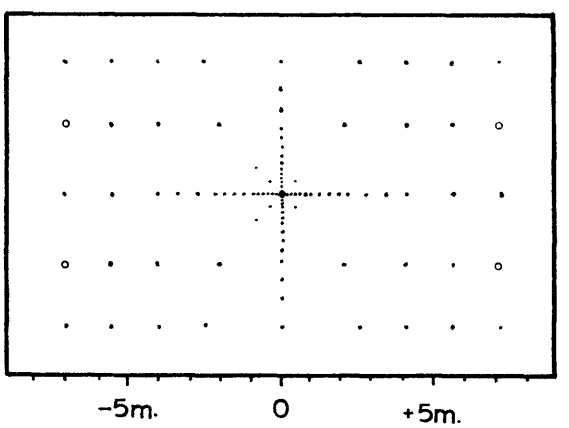

II; A,B,C,D
Exp. #25-42

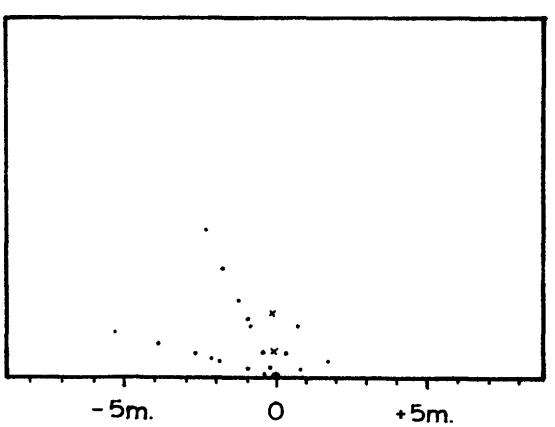

I; A
Exp. #49-61

I: Half Model Experiments

II: Full Model Experiments

A: Radial Jet, Stagnant Exp.

B: Separate Jet, Stagnant Exp.

C: Radial Jet, Current Exp.

D: Separate Jet, Current Exp.

TEMPERATURE PROBE KEY

· Vertically Traversing Probe

° Fixed Position Probe

+ Fast Response Probe

Figure 3.4 Probe Location Maps

A calibration of all probes was done before each of the five experimental setups (Figure 3.4). A constant temperature bath capable of an accuracy of ~±0.02°C was used to provide calibrations at 3 different temperatures over the expected experimental range. An additional calibration was done before each experiment by using the nearly isothermal initial condition existing in the stagnant basin water. A computer program linearly interpolated between calibrations to produce a corrected data set.

A versatile plotting program ("PLOT" written in PL1) was developed for presenting the data. Each of the thousands of temperatures recorded during an experiment is characterized by 4 coordinates: 3 spatial ones (cylindrical or Cartesian system) and time. "PLOT" can produce 2-dimensional temperature maps with any two of the spatial coordinates as axes and the third one set to a desired value. This defines a plane in the experimental temperature field. Any measurement taken on that plane over a specified time range is printed on the map at its appropriate location. Isotherms were easily drawn from these printouts. PLOT can also produce graphs of temperature versus any one of the 4 coordinates, including time (the remaining 3 being set to a desired value).

Reduction of the data set by time or spatial averaging is an option of the program, PLOT. Measurements taken at the same location during an experiment can be time averaged and outputed as a single temperature. Spatial averaging was possible over one of the horizontal coordinates. This was very convenient in radial experiments. Measurements at the same radius and depth could be averaged and plotted as one temperature neglecting angular locations.

Some data manipulations were easier using the recorded temperatures directly. A computer program (ANALYSIS in PL1) was developed to orderly print the numbers necessary for plotting a vertical temperature profile at each of the horizontal probe locations. Using the output of this program any vertical profile can easily be drawn by hand. Time and spatial averaging of the data is possible within this program as well.

The data set, supporting calibrations, and probe locations for each experiment were stored on magnetic tape.

3.5 Steady State Determination

The value of any data taken rests heavily on how nearly it approaches the steady state condition that would exist in an experimental basin without boundaries. Experiments were conducted specifically to determine what time window was available to take good measurements.

A stationary vertical column of ten temperature probes (at different elevations) was used to measure a vertical temperature profile. The probes could be scanned in about 5 seconds and thus provided a nearly "instantaneous" vertical temperature profile.

An experiment consisted of the measurements of four columns of 10 probes each. They were scanned at least twice a minute. In this way a detailed time history of the vertical temperature profile was obtained at four locations.

3.6 Direct Recirculation Measurements with Fluorescent Tracer

The short-circuiting of warm discharge water into the model intake is termed recirculation. It can be quantified by the volume fraction of discharge water in the intake flow. Temperature measurements of the intake water can indicate if any of the hot discharge water is recirculating. However practically, this method is of no value if the temperature rise is 0.05°C or less. Temperature non-uniformities in the ambient water can overshadow temperature rises of this magnitude. Thus the minimum recirculation reliably measureable from temperature data is $0.05/\ \Delta T_o = 0.0045$ ($\Delta T_o = 11°C$) or 1/2 %.

A more accurate measurement was attainable through the release of a fluorescent dye in the discharge water. A fluorometer (Turner Model III) allows concentration measurements down to 1 part per billion (ppb). Experiments could be run with discharge concentrations of as much as 50,000 ppb and basin background concentrations of less than 30 ppb. A dye concentration of 10 ppb above the background concentration was distinguishable. Thus recirculation measurements down to 10 ppb/ 50,000 ppb = 0.0002 or 0.02% were possible.

3.7 Fast Response Temperature Measurements

A vertically traversable temperature probe with a time constant of 0.07 seconds was also used in some experiments. This probe could provide a continuous plot of the vertical temperature profile by slowly traversing through the water depth and recording the temperature variation on a plotter connected to a volt meter.

Temperature fluctuations with time at a fixed point could

also be recorded with the same equipment. In this way a measure of turbulent temperature fluctuations could be obtained.

3.8 Velocity Measurements

Besides detailed information on the temperature field, it is desirable to determine the velocity distribution outside of the model. Velocity measurements are needed before complete understanding of the fluid mechanics external to an OTEC plant is possible.

In order to be able to observe the vertical velocity structure of the flow field a 4.57 m (15 ft) long plexiglass window was installed in one of the walls of the model basin (Figure 3.3). For the experiments conducted with the half-model, the model was attached directly to the window. Velocity measurements were made by taking a sequence of photographs of dye injected into the flow field. A running clock in the corner of each picture makes the calculation of the time of travel straightforward.

Three different methods of introducing the dye into the flow were developed, each providing different types of information. Dye was injected into the warm water feeder hoses. A visual check of the dye distribution in plan view would immediately show if the discharge was properly distributed. Photographs of the dye front through the window provided an average time of travel velocity for the discharge jet and the vertical extent to which the jet had penetrated.

A second method of flow visualization was to coat threads with dye crystals. A weight would be attached to one end of the thread.

When lowered into the water this would provide a continuous vertical line source of dye. By photographing the dye front it was possible to reconstruct the vertical velocity structure of that point.

The third method of visualization was to drop dye crystals directly into the water. Falling through the water the crystals leave a trail of dissolved dye which moves in the flow field. This would closely simulate a vertical line source. A single, well-defined line of dye would be produced which would be more exact than the front from a continuous source. The major problem with dropping dye crystals was that they did not always start to dissolve until they had fallen some distance through the water. This carried them completely through the discharge jet, providing no information in that region.

3.9 Experimental Procedure

A standard procedure for performing the experiments was established. The same procedure was followed for every run.

The model basin was filled with water and stirred the day before the experiment was to be conducted. This was to ensure that the water would be isothermal and stagnant. Before the experiment would be started, the warm water was turned on and run through a by-pass to a drain. This allowed the discharge temperature to stabilize before using it in the experiment. During this time the temperature probes were scanned to establish the ambient temperature and obtain a probe calibration. When the warm water had reached the desired temperature the model intake was turned on. If the basin water level

was correct, the discharge was started and dye was injected into the warm water feeder line to determine if the discharge distribution was uniform. After the dye front in the basin passed the last probe temperature scans were started to define the existing temperature field.

The data taking procedure for temperature is tailored to the flow situation. Close to the surface the discharge jet introduces significant turbulent temperature fluctuations. Therefore, close to the surface several scans at each level are taken so the temperature readings can be averaged. After one level has been scanned the frame supporting the probes is moved to a new depth. Thirty seconds are given for the probes to come to the new equilibrium and then the scans are repeated. Approximately twenty minutes were required to scan the entire basin depth.

During the experiment, photographs of dye strings, crystals and injections into the model are taken to provide information on the velocity structure. Readings with fast probes are also taken.

Three days or less were generally required to calibrate, plot, and store the results of an experiment. Procedures and results were continuously evaluated as the experimental program progressed.

CHAPTER IV

EXPERIMENTAL RESULTS: RADIAL DISCHARGE AND STAGNANT OCEAN

4.1 Run Conditions

A series of laboratory experiments was conducted to investigate the external flow and temperature fields induced in a stagnant ocean by a schematic radial OTEC plant characterized by the parameters varied over the ranges presented in Chapter II.

The dimensional parameters and a description of each experiment appear in Table 4.1. Table 4.2 contains the dimensionless governing parameters (as discussed in Section 2.3). Starting with the "standard" base case (100 MW) the experiments were designed to evaluate sensitivities by increasing the flow rate and discharge velocity and decreasing ΔT_o and slot height, h_o. There were four series of experiments with a radial discharge into a stagnant basin. The first series (Experiments 1-6 and 8) covered the desired range of parameters. The other three series were to support and detail the results of the first series.

The second series consisted of Experiments 26, 30, 31, and 33. They were done with the full model in the basin center. The main purpose was to determine if the wall in the half model experiments had a significant effect on the flow field.

Table 4.1

DIMENSIONAL PARAMETERS AND EXPERIMENT DESCRIPTIONS
STAGNANT RADIAL JET EXPERIMENTS

Run	Type Model		Q_i	u_o	A_o	h_o	T_D^*	T_A^{**}	$\Delta\rho \times 10^3$	Types of Measurements
	Half	Full	[cm^3/sec]	[cm/sec]	[cm^2]	[cm]	[°C]	[°C]	[gm/cm^3]	
1	X		884.	19.4	11.4	.64	34.6	23.6	3.23	A
2	X		442.	9.65	11.4	.64	34.6	23.0	3.37	A
3	X		884.	19.4	11.4	.64	27.9	22.2	1.45	A
4	X		1770.	38.8	11.4	.64	33.4	22.4	3.11	A
5	X		884.	38.8	5.7	.32	33.5	22.7	3.05	A
6	X		1770.	77.5	5.7	.32	33.1	22.2	3.04	A
7	X		1770.	77.5	5.7	.32	33.1	22.7	2.92	A
8	X		1770.	77.5	5.7	.32	38.1	22.9	1.37	A
26		X	884.	19.4	11.4	.64	23.9	13.9	1.96	A
30		X	884.	19.4	11.4	.64	26.6	13.5	2.68	A
31		X	884.	19.4	11.4	.64	28.0	15.3	2.83	A
33		X	884.	38.8	5.7	.32	28.2	15.4	2.86	A
44		X	884.	19.4	11.4	.64	29.2	17.2	2.82	B
45	X		884.	19.4	11.4	.64	30.6	18.8	2.97	B
46	X		1770.	38.8	11.4	.64	30.8	19.1	2.96	B
47	X		884.	38.8	5.7	.32	30.8	18.9	2.99	B
48	X		1770.	77.5	5.7	.32	30.9	19.2	2.97	B
49	X		1770.	77.5	5.7	.32	32.6	21.6	3.01	A,E
50	X		1770.	77.5	5.7	.32	32.4	21.3	3.03	A
51	X		1770.	77.5	5.7	.32	32.4	21.3	3.05	A,C,D
54	X		1770.	77.5	5.7	.32	26.4	23.3	0.77	A,E
55	X		1770.	77.5	5.7	.32	22.9	23.1	0.051	A,E
56	X		1770.	77.5	5.7	.32	35.0	24.6	3.25	A,C,D
57	X		1770.	77.5	5.7	.32	33.9	24.7	2.70	A,D
58	X		1770.	77.5	5.7	.32	34.8	25.0	2.95	A,D
59	X		884.	19.4	11.4	.64	35.0	24.9	3.06	A
60	X		884.	19.4	11.4	.64	34.7	24.8	2.97	A,C,D
61	X		884.	19.4	11.4	.64	34.6	24.8	2.90	A,D,E

Description Key

A. Overall Temperature Field
B. Steady-State Determination
C. Velocity (Dye Photograph)
D. Fast Temperature Probe
E. Fluorescent Dye Recirculation

* Discharge Temperature: Average of ∿ 25 Individual Measurements Taken Periodically during the Experiment.

** Ambient Temperature: Spatial Average of Basin Temperature Measurements just before the Experiment

Table 4.2

DIMENSIONLESS GOVERNING PARAMETERS
STAGNANT RADIAL JET EXPERIMENTS

Run	Type Model Half	Full	$\mathbb{F}_o^*$	$\mathbb{F}_{r_o}$	$\mathbb{F}_i$	h_o/H	r_o/h_o
1	X		5.91	13.62	.069	.018	18.
2	X		2.88	6.64	.034	.018	18.
3	X		8.81	20.31	.102	.018	18.
4	X		12.06	27.81	.140	.018	18.
5	X		14.49	39.73	.071	.0091	36.
6	X		29.02	79.58	.141	.0091	36.
7	X		29.62	81.22	.144	.0091	36.
8	X		43.13	118.3	.211	.0091	36.
26		X	7.59	17.50	.088	.018	18.
30		X	6.49	14.97	.075	.018	18.
31		X	6.32	14.57	.073	.018	18.
33		X	14.94	40.97	.073	.0091	36.
44		X	6.35	14.64	.073	.018	18.
45	X		6.19	14.27	.071	.018	18.
46	X		12.40	28.59	.143	.018	18.
47	X		14.67	40.23	.071	.0091	36.
48	X		29.40	80.62	.143	.0091	36.
49	X		29.15	79.93	.142	.0091	36.
50	X		29.07	79.72	.142	.0091	36.
51	X		28.99	79.50	.141	.0091	36.
54	X		57.42	157.5	.281	.0091	36.
55	X		224.3	615.1	1.091	.0091	36.
56	X		28.08	77.00	.137	.0091	36.
57	X		30.77	84.38	.150	.0091	36.
58	X		29.44	80.73	.143	.0091	36.
59	X		6.09	14.04	.070	.018	18.
60	X		6.19	14.27	.071	.018	18.
61	X		6.24	14.39	.072	.018	18.

The third series (Experiments 44-48) was steady-state determination tests with profile measurements taken at radiuses of 2 and 3.5 meters. Only experiment 44 was with a full model. The other four experiments were for a half model at the wall. Experiments 49-61 were conducted at the wall. The temperature field measurements were reduced to provide time for other types of measurements. Fast response temperature probe measurements, dye photography, and dye recirculation sampling were all done in this series.

4.2 Discussion of Results

Observations made thorughcut the experimental series allowed a qualitative picture of the flow field to be formed. Three flow zones were easily recognizable (Fig. 4.1). The jet and intake flow zones are a consequence of the model's discharge and intake ports. The return flow zone supplies the volumes of ambient water necessary for jet entrainment and the intake flow. For experiments with deep, high entrainment jets, return flow velocities approached the magnitude of the jet zone velocities.

4.2.1 Temperature Field Measurements

Figure 4.2 is a typical example of data provided by a radial stagnant experiment. The temperatures represent the spatial average of all probes of equal radial distance from the center of the model. The temperatures at different depths are not taken simultaneously because the probe frame takes some time to traverse to a new level (at a speed of 30.5 cm/min). However all temperatures were

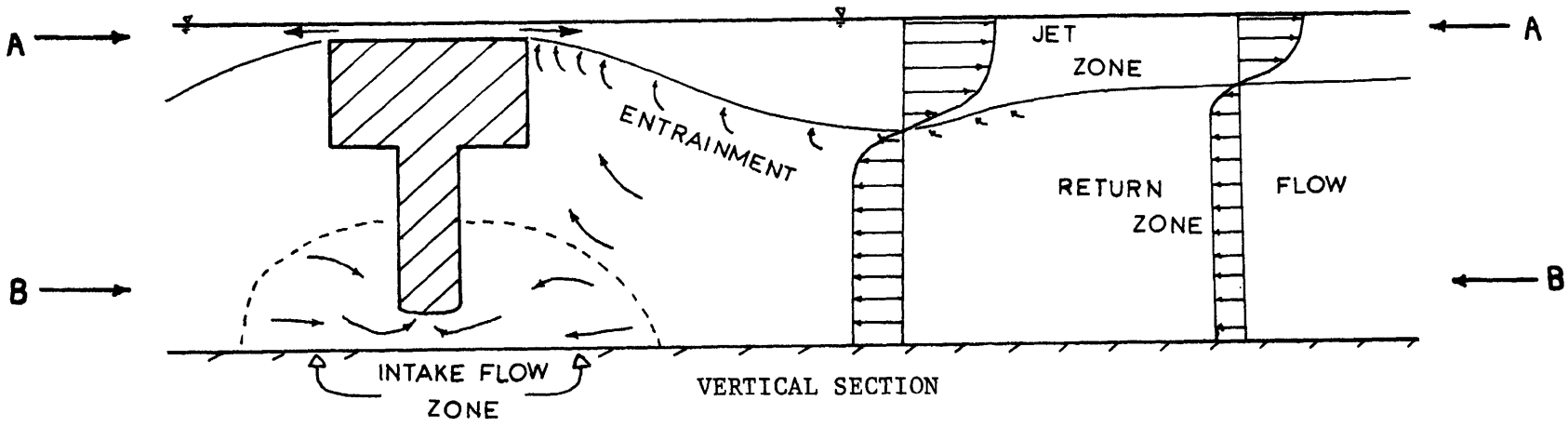

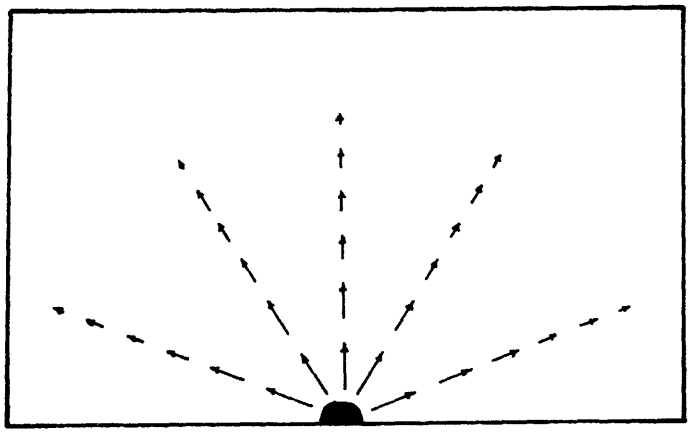

PLAN VIEW AT LEVEL A-A
"SOURCE FLOW"

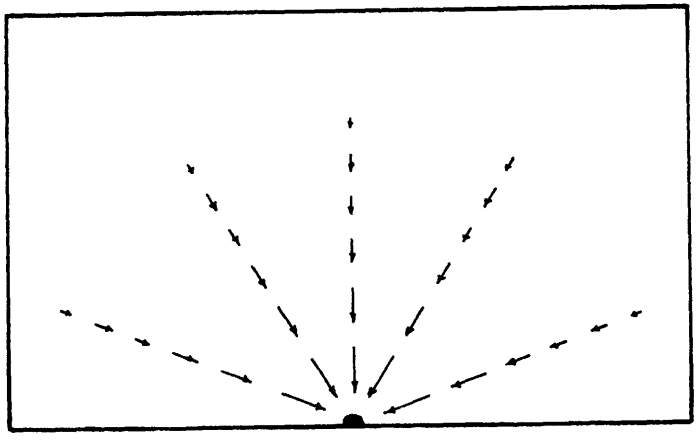

PLAN VIEW AT LEVEL B-B
"SINK FLOW"

Figure 4.1 Flow Field for Stagnant, Radial Jet Experiments

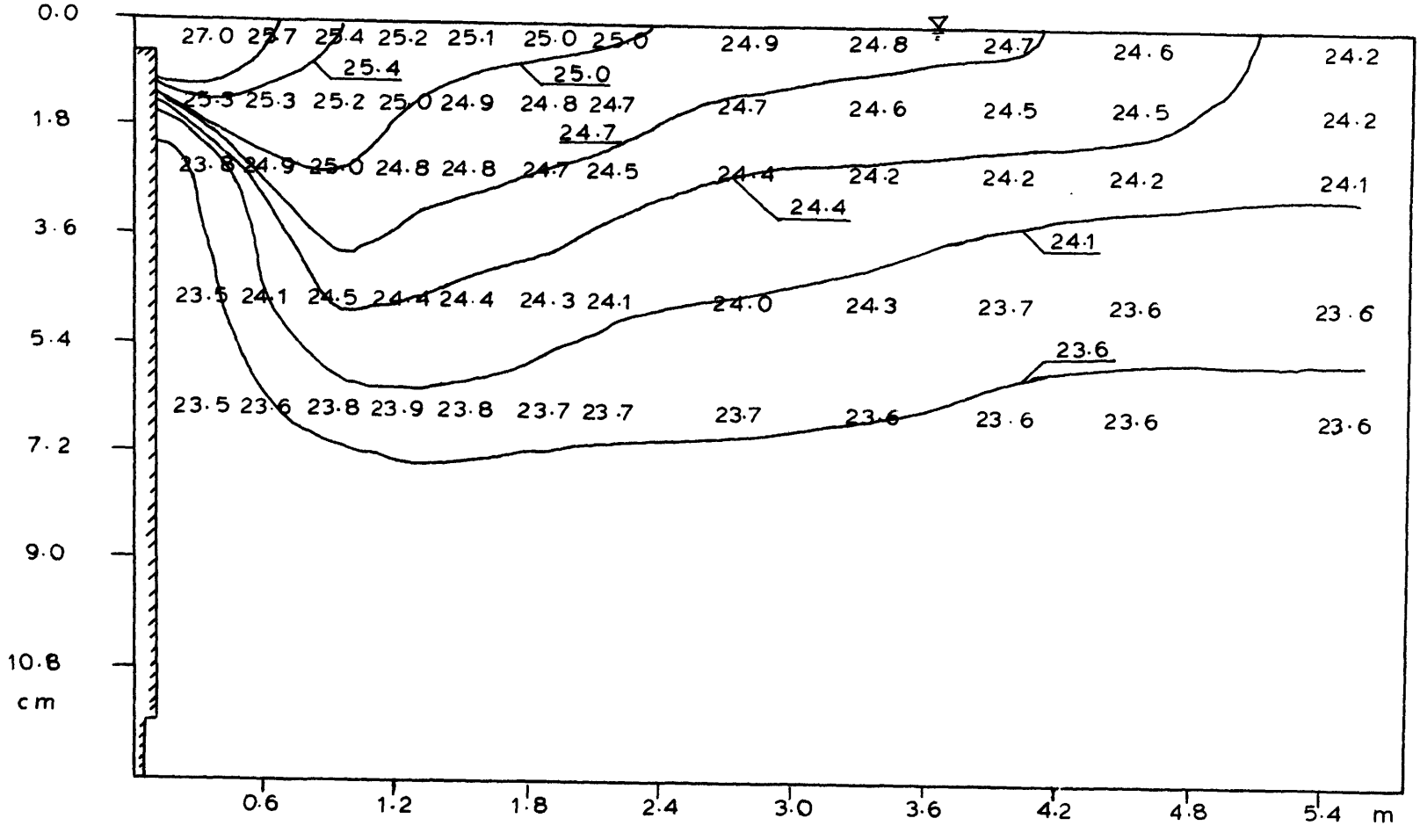

Figure 4.2 Typical Radially Averaged Transect for Stagnant Experiment with Radial Discharge (Exp. No. 1)

recorded within the time span in the experiment which approximates steady state. Multiple scans were taken at the levels closer to the surface to derive time-smoothed values that averaged out the local turbulent fluctuations. Due to time and spatial averaging, the values presented close to the surface represent a compilation of 20 data scans while the lower levels represent 5 data scans.

Figure 4.3 is a typical plan view of the isotherms for the level scanned closest to the surface (i.e. 0.5 cm below the surface). This figure shows that spatial averaging is, indeed, necessary because the discharge flow is not perfectly radial. This deviation from ideal radial flow can be caused by a non-uniform discharge distribution and by wall friction, in the case of the half-model experiments. Full model experiments 31 and 33 indicate that the radial nature of the flow field is reasonably well represented. Radial averaging of the data should minimize the error from not obtaining perfectly radial flow.

Appendix A.1 presents the radially averaged plots of the normalized isotherms, given in per cent, for each experiment.

4.2.2 Steady-State Determination Results

Typical results of these experiments are illustrated in Figure 4.4. Temperature scans were taken with high frequency to observe the jet front pass through the measurement location. Temperature readings then settled down to a steady state with only turbulent fluctuations. The end of the steady state was usually signaled by the uppermost probe that had been at ambient temperature. It would

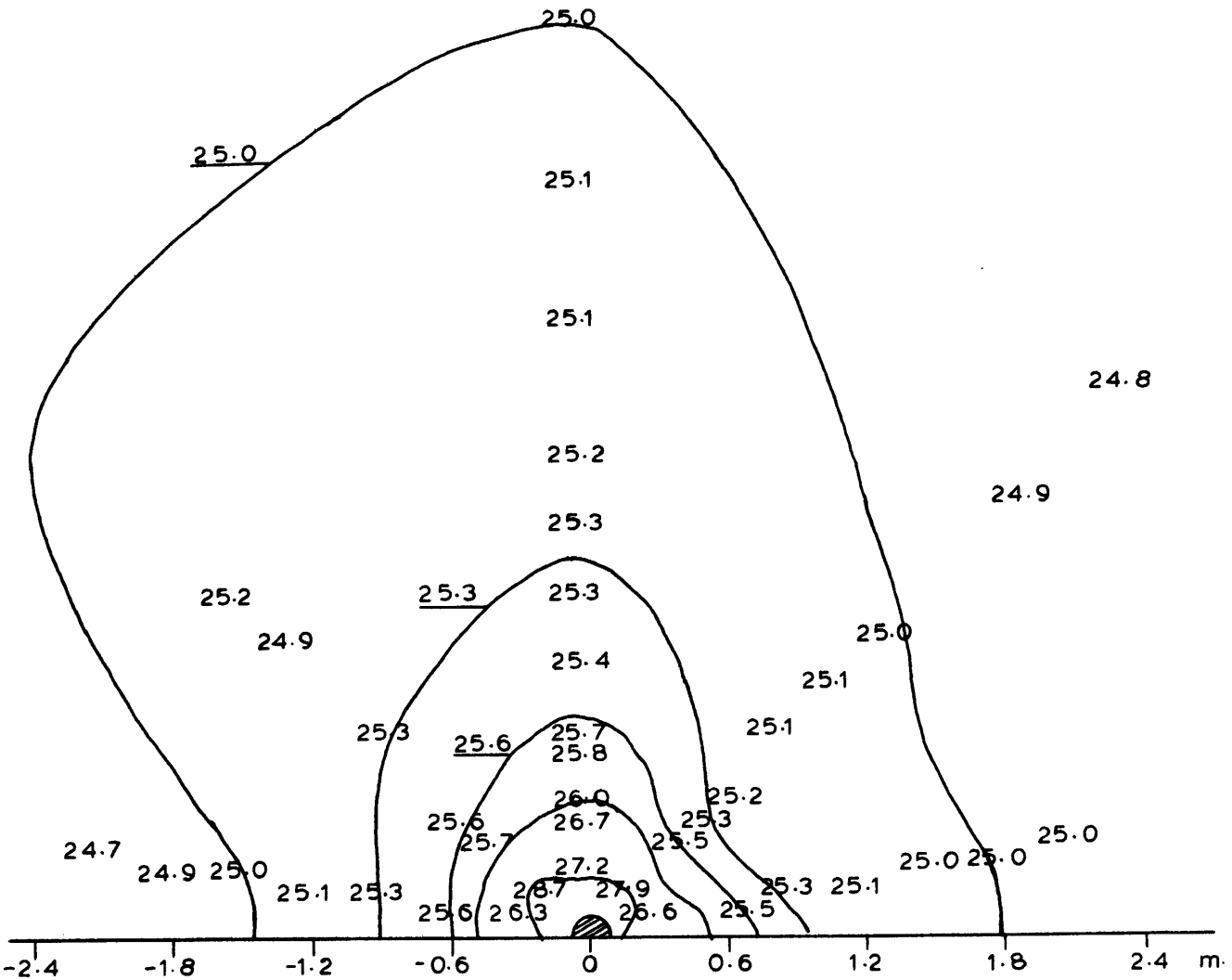

Figure 4.3 Typical Plan View of Surface Isotherms, Stagnant Experiment with Radial Discharge (Exp. No. 1)

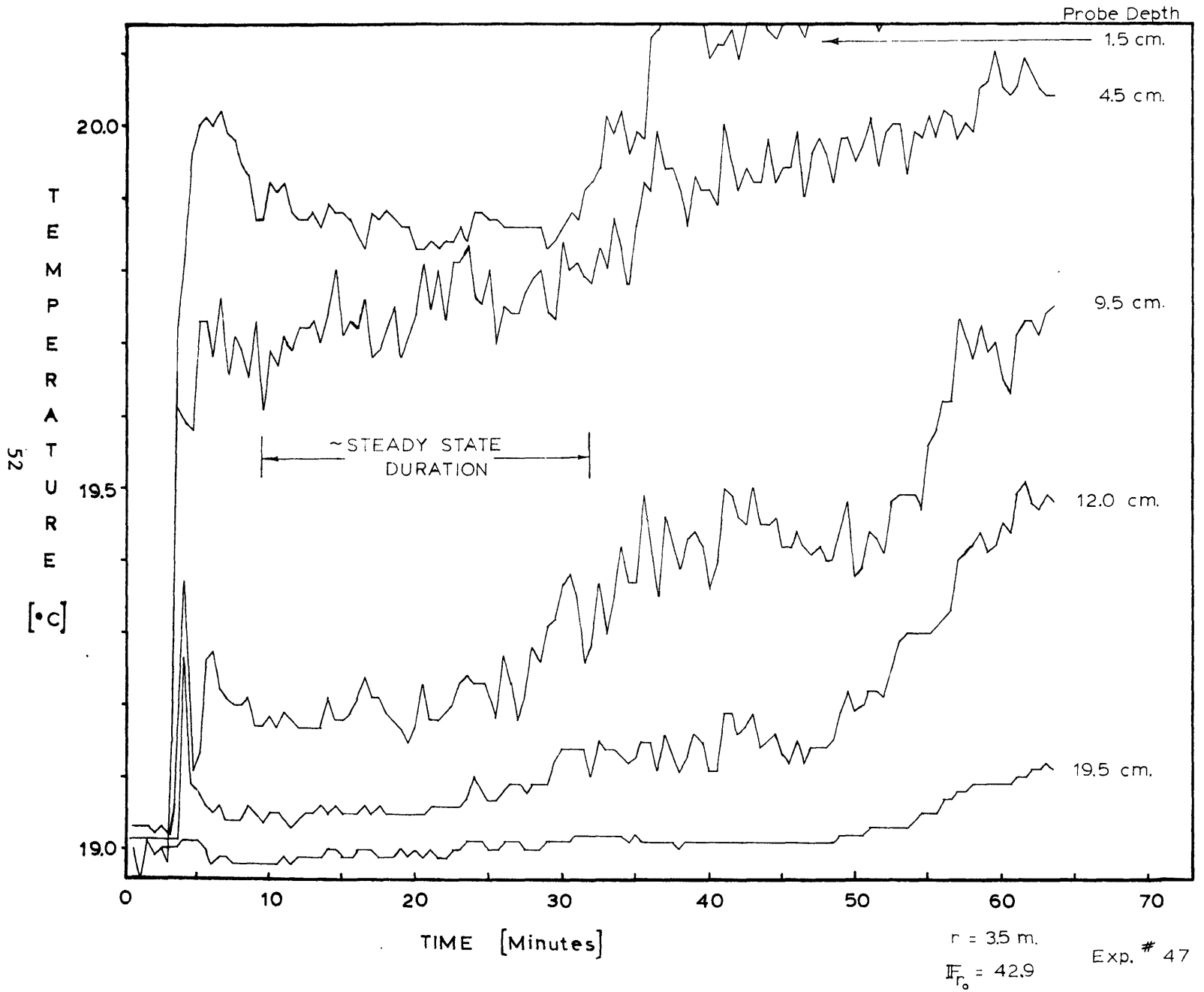

Figure 4.4 Temperature vs. Time at Various Depths

begin to show some heatup effect. The mean temperature of the probes in the jet would subsequently show a steady rise in temperature. It seems likely that the heated water building up at the edges of the basin forces an intermediate warm layer to flow back toward the model. This is supported by visual dye observations.

Table 4.3 is an attempt to determine the beginning of steady state and the onset of rising temperatures. The end of the steady state regime was not a perfectly abrupt phenomena. Some judgement had to be used in the construction of the table. In general, a mean temperature deviation of more than 0.1°C (at either the surface or in the middle of the jet) was considered the cutoff point for the steady state.

Exp.	F_o^*	Configuration	Model	Discharge Flow Rate (cm^3/sec)	Approximate Period of Steady State @ 3.5 m Start	End
43	15.30	Sep. Jet	Full	884.	9 min.	23 min.
44	6.35	Radial	Full	884.	11 min.	25 min.
45	6.18	Radial	Half	442.	10 min.	34 min.
46	12.39	Radial	Half	884.	8 min.	33 min.
47	14.66	Radial	Half	442.	9 min.	32 min.
48	29.42	Radial	Half	884.	7 min.	33 min.

Table 4.3 Experimental Steady State Durations

4.2.3 Velocity Measurements

Velocity measurements using the techniques described in Chapter III were taken at fixed points. Figure 4.5 is a photograph of a typical dye string used to construct a velocity profile. Velocity measurements obtained by these methods provide only local information. Since the flow field may have some non-uniformities, as it is linked to the non-uniform temperature field, it is difficult to generalize this local data to an average velocity distribution for the entire induced flow field. A typical velocity profile which shows the jet forward velocity in the surface layer and a lower, uniformly distributed return flow in the lower layer is shown in Figure 4.6. Other data on velocity measurements (taken in Experiments 51, 56, and 60) is summarized in Appendix B.

4.2.4 Fast Probe Measurements

Fast probe measurements were taken during 4 experiments (Experiments 51, 58, 60, and 61). The purpose was to examine the turbulent temperature fluctuations at two locations for conditions similar to experiments 1 and 6. Sets of measurements were taken at two different distances from the model (0.9 m and 2.1 m). A vertical profile and stationary measurements were taken at each location as described in Chapter 2.

The results and some preliminary analysis appear in Appendix C. A notable feature is the dominant slower temperature fluctuations near the bottom of the jet as compared to the higher frequency turbulent fluctuations in the upper portion of the jet.

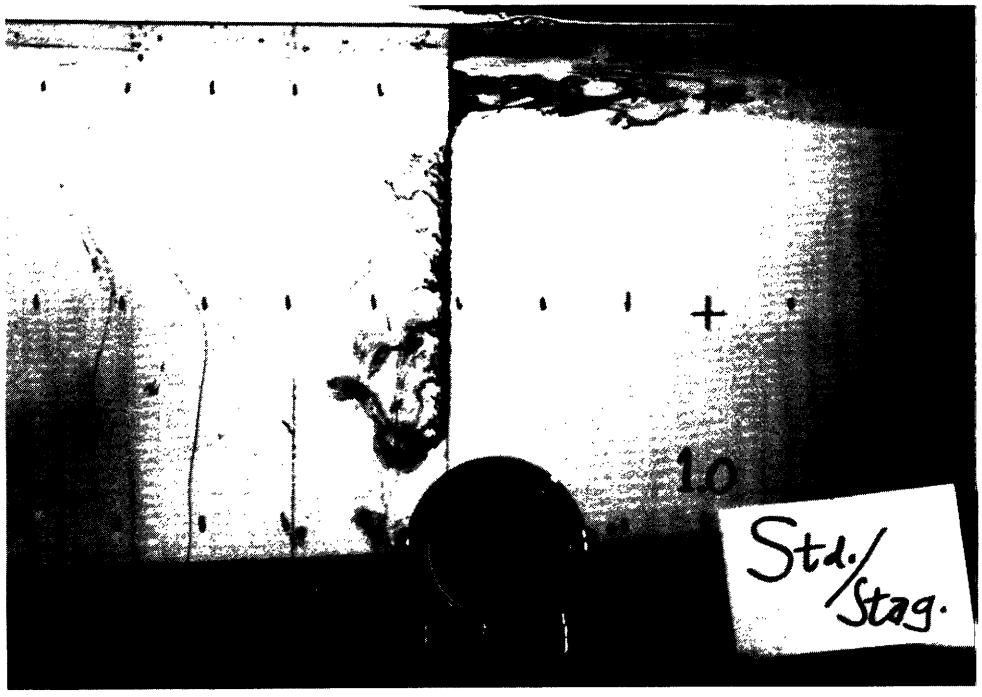

Figure 4.5 Photograph of Dye String Velocity Measurement.

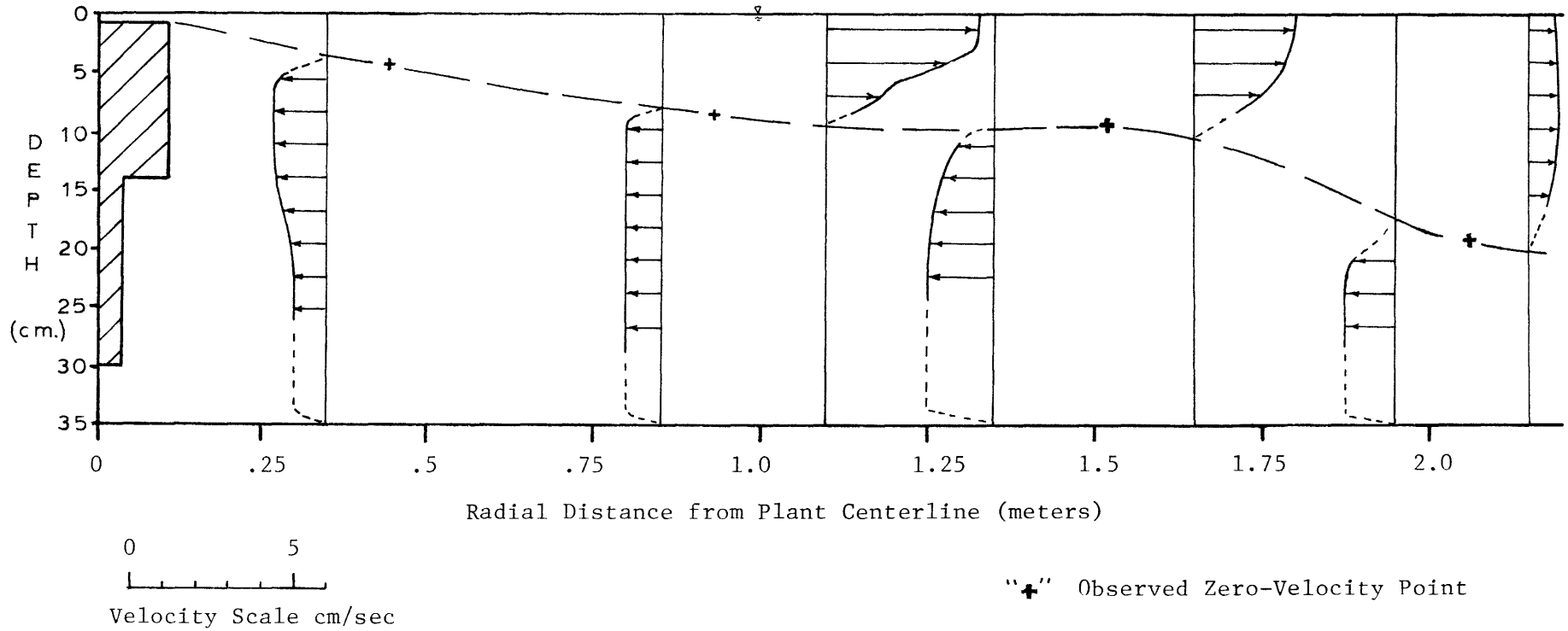

Figure 4.6 Mean Velocity Measurement Example [Exp #51]

4.2.5 Recirculation Measurements

All the low Froude number and low discharge experiments (1 to 5, without dye measurement; 61 with dye measurement) showed no indications of direct recirculation either in the temperature data, the visual dye observations, or the dye measurements within the time span for which the steady state condition persisted. In all these experiments, little vertical penetration of the surface layer was observed (less than 40% of the total depth) as shown in Appendix A.1. On the other hand, experiments with high Froude numbers and high discharges (6 and 8, without dye measurement; 44, 54, and 55 with dye measurement) indicated a tendency for recirculation based on the following observations:

1) Dyed discharge waters appeared to penetrate much deeper over the water column (more than 50% in Experiments 6 and 49; over the entire depth in Experiments 8, 54, and 55).
2) The intake temperature increased by a small amount (<.02°C for Experiment 8) within the first 30 minutes of simulation.
3) The dye concentration measurements showed small increases in concentration (However, no concentration rise was observed in Experiment 49, the repeat of Experiment 6). The recirculation measurement results are summarized in Table 4.4.

Exp.	F_o*	Recirculation % Values 10 min.	20 min.	30 min.	50 min.	Type Measurement
61	6.2	0.%(±.02%)*	0%(±.02%)	0%(±.02%)	-----	Fluorescent Dye
6	29.0	0.%(±2%)	0%(±2%)	0%(±2%)	-----	Intake Temperature
49	29.2	0.%(±4.%)	0%(±4.%)	0%(±4.%)	-----	Fluorescent Dye
8	43.1	.3%(±.3%)	.3%(±.3%)	.3%(±.3%)	-----	Intake Temperature
54	57.4	.5%**(±.08%)	.7%**(±.1%)	.16%(±.04%)	-----	Fluorescent Dye
55	224.***	12%(±2.%)	20%(±3.%)	18%(±3.%)	22%(±3.%)	Fluorescent Dye

* The estimated possible error of measurement is in parentheses

** Recirculation was increased by an intake flow rate 10% over the correct value

*** This discharge was negatively buoyant $\Delta T_o = -.2°C$

Table 4.4 Recirculation Measurements

In principle, recirculation could be caused by the intake flow directly entraining warm discharge water or by the model basin being too small to allow steady state to be achieved. It was shown in Table 4.3 that steady state jet behavior can at least be expected during a 15 minute period of the experiments. The fact that experiments 8, 54, and 55 measured recirculation during that period implies that the first kind of recirculation mechanism was observed.

The mechanism of recirculation was observable in Exp. 8 by introducing dye into the discharge water in short bursts. The patches of dyed discharge water could be observed through the basin window as they mixed. At a radius of approximately 0.75 m, the dyed water came in close proximity to the bottom. Occasionally, large eddies could be seen to mix locally all the way to the bottom, break off the jet, and become part of the return flow zone. Faintly dyed water was observed to enter the model intake occasionally.

The phenomena was very unsteady and appeared to occur randomly as far as time and angular location were concerned. The approximate radius of occurrence (about two water depths) though never changed. At larger distances from the model, a fairly well defined two layer flow was apparent from the temperature data. The layers were approximately of equal thickness.

4.3 Experimental Correlation of Discharge Behavior

Figure 4.7 is a graph of stable jet dilution as a function of the modified Froude number F_o^* (see footnote in Section 2.3)

$$F_o^* = \frac{u_o}{\left(\frac{\Delta\rho}{\rho} g \left[\frac{\pi}{2} r_o h_o\right]^{1/2}\right)^{1/2}} \qquad (4.1)$$

This governing parameter is chosen in order to more easily relate to the separate four-port discharge geometries. The stable jet dilution, S_s, is defined to be the total volumetric flow rate at a radius, where the temperature is changing slowly ("stable region"), divided by the

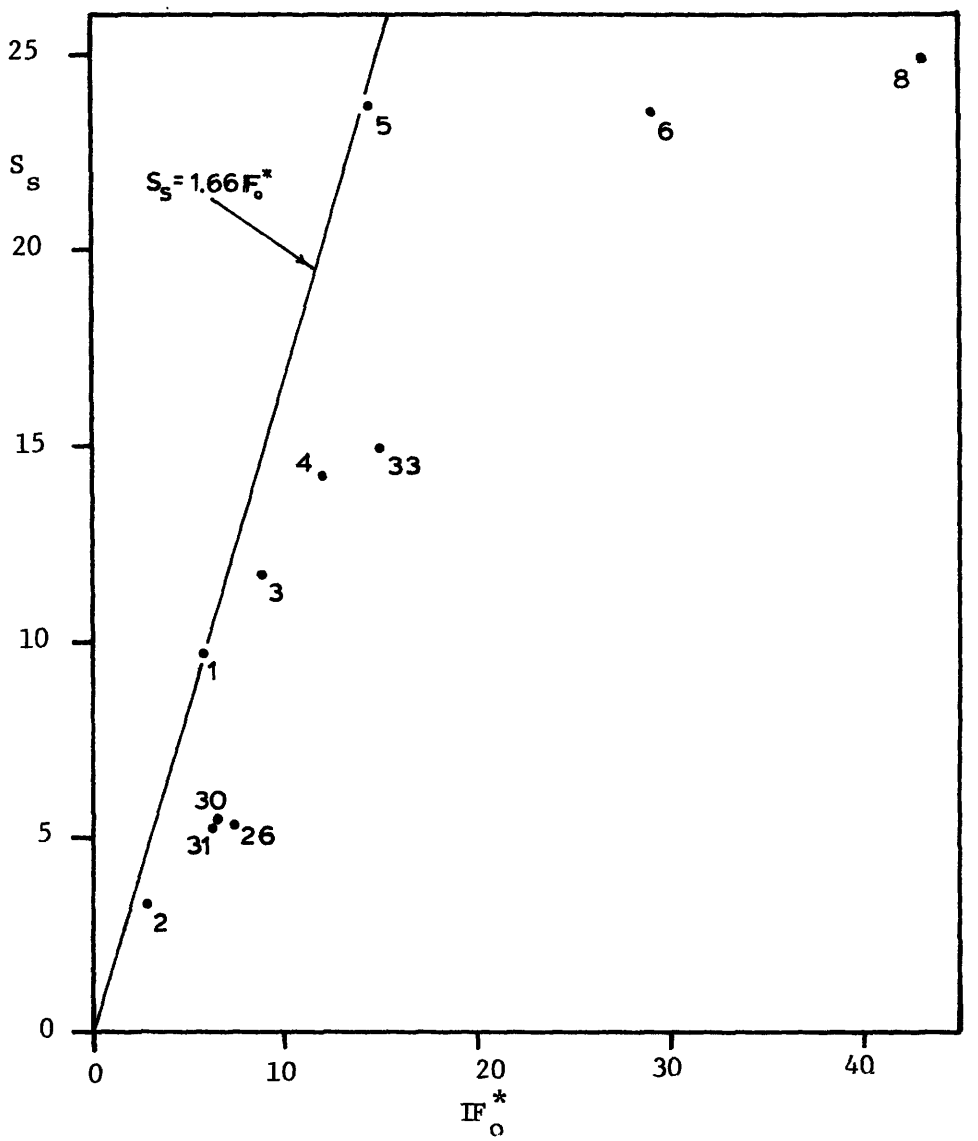

Figure 4.7 Stable Jet Dilution vs. Quarter Module "Port" Discharge Froude Number, Stagnant Experiments

discharge flow rate. Using the similarity assumptions presented in Chapter VII, it is possible to linearly relate the local jet dilution to the ratio of discharge temperature difference and the local jet surface temperature difference

$$S_s = \frac{\Delta T_o}{\Delta T_c} \frac{I_1}{IG} \tag{4.2}$$

where I_1 and IG are integration constants defined in Chapter VII.

Figure 4.7 shows that the majority of the experiments exhibit a linear relationship between S_s and $\mathbb{F}_o^*$. This is consistent with the theory of single port buoyant surface jets (Stolzenbach and Harleman*, 1971; Jirka, et. al.*, 1975) for which a correlation has been developed:

$$S_s = 1.66\ \mathbb{F}_o^* \tag{4.3}$$

The two highest Froude number points, corresponding to runs 6 and 8, do not agree with Equation (4.3), giving further indication that the mixing process is limited and recirculation may occur in these tests.

Figure 4.8 is a graph of the maximum jet half-temperature depth (i.e., the depth where the temperature difference above ambient is one-half the centerline value) normalized by the square-root of

*The result in these reports is given as $S_s = 1.4\ \mathbb{F}_o'$ where $\mathbb{F}_o' = 2^{\frac{1}{4}}\ \mathbb{F}_o^*$ due to differences in the port area definition.

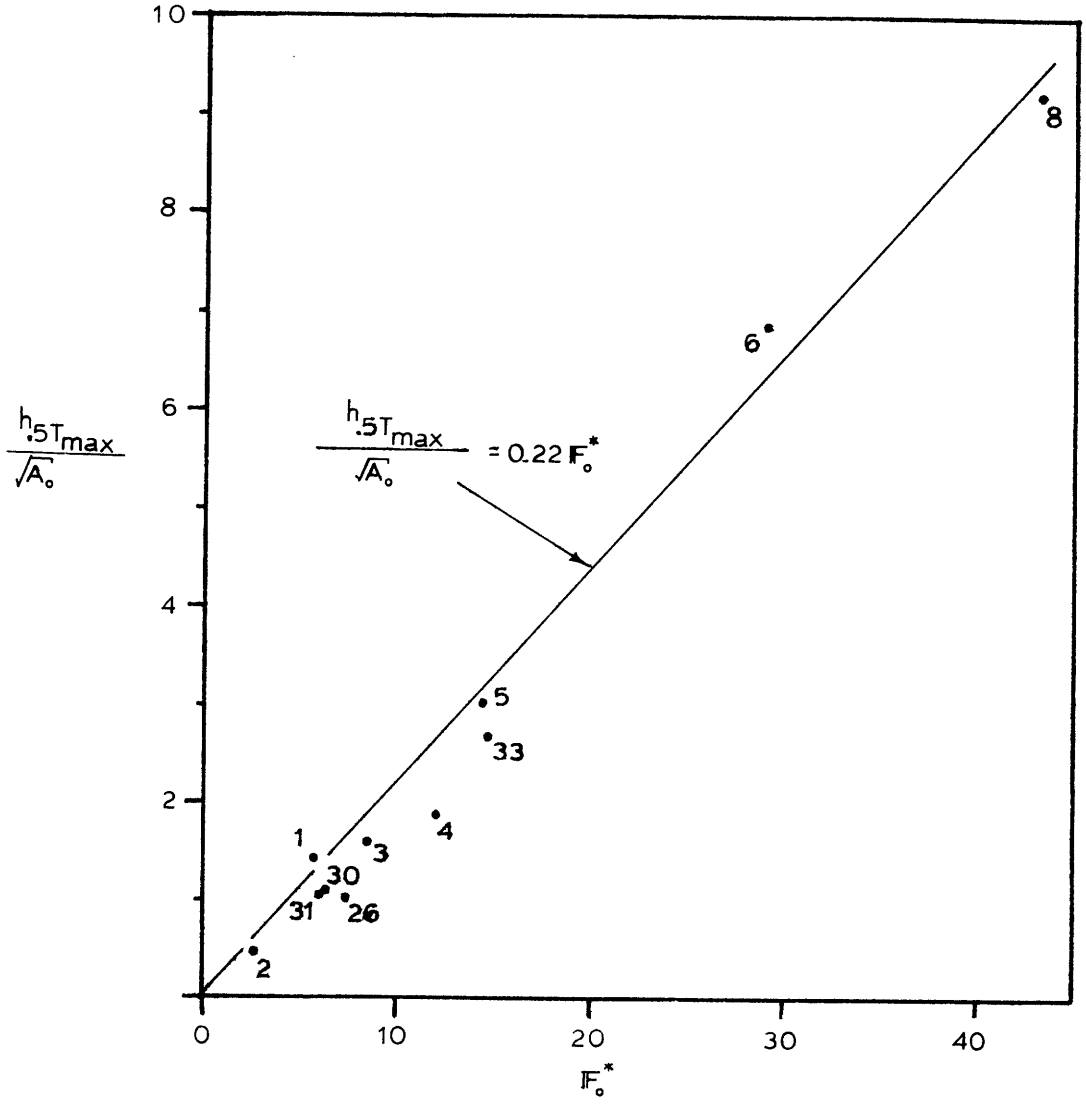

Figure 4.8 Normalized Maximum Half-Temperature Depth vs. Quarter Module "Port" Discharge Froude Number, Stagnant Experiments

the discharge area, $(\frac{\pi}{2} r_o h_o)^{\frac{1}{2}}$, as a function of F_o^*. The data point for run 8 is included even though the jet's temperature field appears to extend all the way to the basin floor. A linear trend in the data is appraent and the data correlation with the theory for single port buoyant jets is as good as that for S_s. Assuming a polynomial vertical temperature profile (Abramovich, 1963), the relationship between maximum half-temperature depth and F_o^* is (Jirka, et. al., 1975):

$$\frac{h_{.5T\ max}}{\sqrt{A}} = 0.22\ F_o^* \qquad (4.4)$$

It is significant that the data point for run 6 shows an upward deviation from the general trend set by the other experiments. This seems to indicate that the jet extends deeper due to the effects of depth limited mixing.

In summary, Figures 4.7 and 4.8 show that the greater the discharge Froude number, the more turbulent mixing (i.e., higher dilution) and the deeper the jet until some limiting value of the Froude number is realized where the effects of the confined layer limit entrainment and recirculation occurs.

4.4 Extreme Case Experiments

An important exterior flow phenomena of interest to OTEC operation is recirculation. But the experimental schematization of an OTEC plant in operation showed some tendency for, but no significantly high values of, this phenomenon over the chosen parameter ranges.

Therefore, experiments 8, 54, and 55 were conceived with lower discharge temperature differences and higher discharge Froude numbers. Higher values of recirculation were obtained, but because of the small temperature difference, the experiments lost some of their applicability to the mixed discharge configuration of an OTEC power plant (see Chapter 9).

Each of the three experiments showed some degree of measurable recirculation (Table 4.4). Only the most extreme experiment (Exp. 55 with $IF_o^* = 230$, $\Delta T_o = -.2^oC$) had a really sizable recirculation (which even appeared to show a transient rise). The dyed discharge waters were just reaching the basin boundaries when experiment No. 55 ended after fifty (50) minutes. Because of the decrease of buoyant spreading, this time of travel is approximately two to four times as long as in other experiments.

It must be kept in mind that the recirculation values of these experiments have no implications for OTEC operating with a mixed discharge configuration. However, the experiments show a definite possibility for recirculation in a non-mixed discharge scheme. In this case, smaller discharge temperature differences and higher discharge Froude numbers would realistically occur in the evaporator discharge jets. This aspect is further discussed in Chapter 9.

CHAPTER V

EXPERIMENTAL RESULTS: SEPARATE JET DISCHARGE AND STAGNANT OCEAN

5.1 Run Conditions

The separate jet discharge configuration of a schematic OTEC plant in a stagnant ocean was examined in a series of laboratory experiments. The induced external temperature and flow fields were investigated as discharge parameters were varied over the ranges presented in Chapter 2.

The dimensional parameters and a description of each experiment appear in Table 5.1. Table 5.2 contains the dimensionless governing parameters (as discussed in Section 2.3). Starting with the "standard" base case(100 MW), the experiments were designed to evaluate sensitivities by increasing the flow rate and discharge velocity and also decreasing ΔT_o and the port width, b_o. Half model experiments with the OTEC model attached to a wall consisted of two jets directed at 45^o from the wall and 90^o from each other. The full model in the basin center discharged four separate jets directed at 90^o from each other.

The experiments can be divided into three sets. The initial set of six half model experiments (Exp. 10-15) covered the desired range of parameters. The remaining two sets were for

Table 5.1

DIMENSIONAL PARAMETERS AND EXPERIMENT DESCRIPTIONS
STAGNANT SEPARATE JET EXPERIMENTS

Run	Type Model Half	Full	Q_i [cm^3/sec]	u_o [cm/sec]	A_o [cm^2]	h_o [cm]	b_o [cm]	T_o [°C]	T_A [°C]	$\Delta\rho \times 10^3$ [gm/cm^3]
10	X		884.	19.6	11.3	1.9	5.9	35.0	23.9	3.26
11	X		1770.	39.2	11.3	1.9	5.9	34.8	24.1	3.18
12	X		884.	19.6	11.3	1.9	5.9	27.4	21.8	1.40
13	X		884.	39.2	5.64	1.9	3.0	33.3	22.2	3.12
14	X		1770.	78.4	5.64	1.9	3.0	33.5	22.3	3.15
15	X		1770.	78.4	5.64	1.9	3.0	27.7	22.2	1.38
35		X	884.	19.6	11.3	1.9	5.9	30.6	18.9	2.97
37		X	884.	39.2	5.64	1.9	3.0	30.5	18.8	2.96
39		X	884.	19.6	11.3	1.9	5.9	28.9	16.4	2.92
41		X	884.	39.2	5.64	1.9	3.0	28.4	16.3	2.77
43*		X	884.	39.2	5.64	1.9	3.0	29.5	17.8	2.82

Table 5.2

DIMENSIONLESS GOVERNING PARAMETERS
STAGNANT SEPARATE JET EXPERIMENTS

Run	Type Model Half	Full	F_o^*	F_o	F_i	h_o/b_o	h_o/H	r_o/b_o
10	X		5.97	7.93	.068	.32	.054	1.93
11	X		12.10	16.06	.138	.32	.054	1.93
12	X		9.10	12.08	.104	.32	.054	1.93
13	X		14.50	16.19	.070	.64	.054	3.86
14	X		28.98	32.35	.139	.64	.054	3.86
15	X		43.56	48.64	.210	.64	.054	3.86
35		X	6.26	8.31	.071	.32	.054	1.93
37		X	14.90	16.64	.072	.64	.054	3.86
39		X	6.31	8.38	.072	.32	.054	1.93
41		X	15.40	17.19	.074	.64	.054	3.86
43		X	15.3	17.08	.073	.64	.054	3.86

verification purposes only. One set (Exp. 36, 38, 40 and 42) consisted of full model repeats of two half model experiments (Exp. 10 and 13). The last set was a single steady state determination test (as described in Chapter 3) for a full model (Exp. No. 43). The breakdown of steady state behavior appears to be caused by a build up of mixed water at the basin confines. The duration of steady state would then appear to depend on the overall mixing characteristics and be independent of the particular generic design. Experiment 43 showed that the separate jet discharges reached a quasi-steady state of similar duration found in radial experiments.

5.2 Discussion cf Results

The flow and temperature fields of these experiments are by nature 3-dimensional and more complex than the radial discharge case. Figure 5.1 illustrates the observed flow field in a typical experiment. The jet and intake flow zones have similar counterparts in the radial discharge case. However, the return flow has been divided into two separate zones: 1. lateral return flow; 2. bottom return flow.

The two return flow zones can be easily distinguished. The bottom return flow zone is made up of entirely ambient water. It mainly supplies the intake flow zone and entrainment flows to the underside of the jet. The lateral return flow zone, existing between the jets, has an associated temperature increase caused by eddies

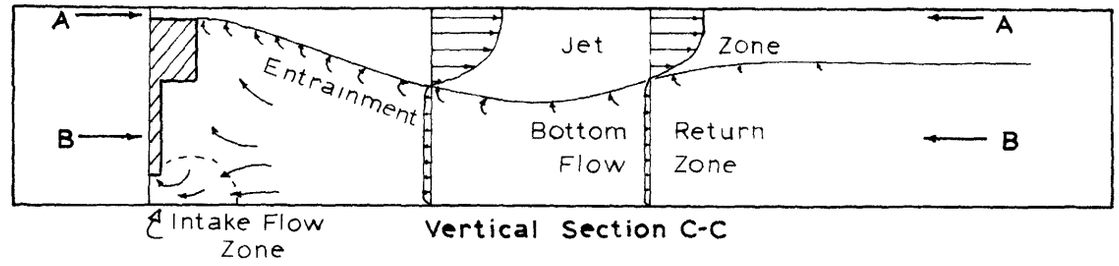

Fig. 5.1a

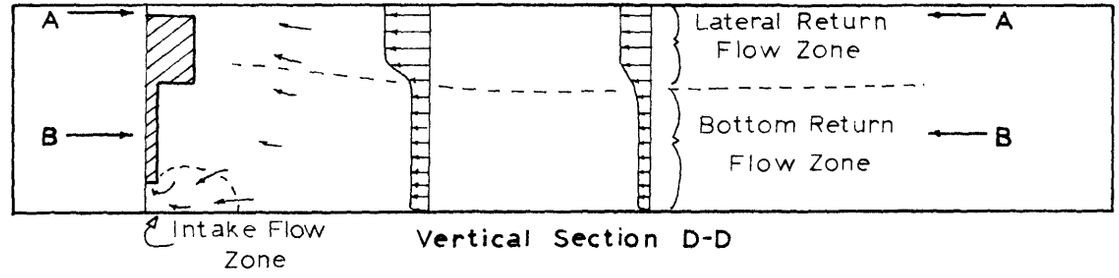

Fig. 5.1b

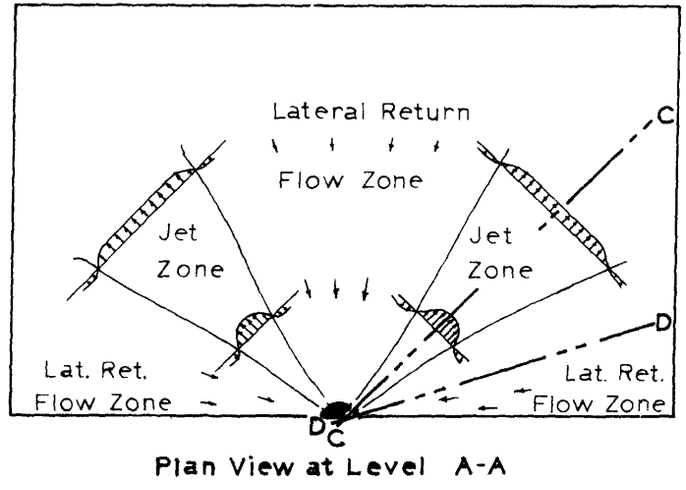

Fig. 5.1c

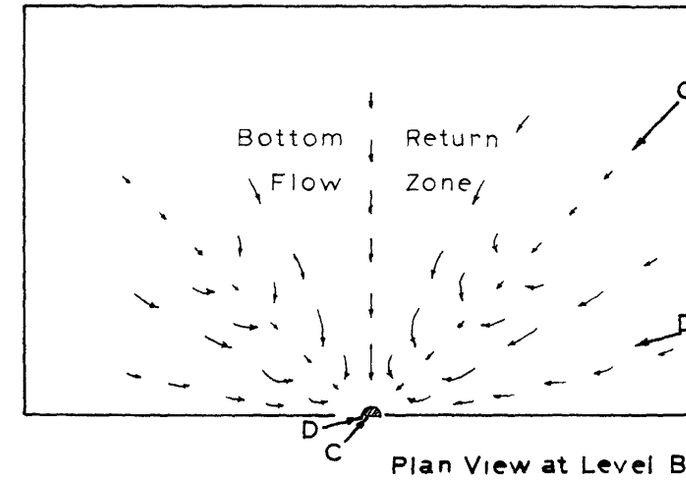

Fig. 5.1d

Figure 5.1 Flow Zones for Separate Jet Configuration

breaking off the jet and mixing into the return flow. This zone has a depth approaching the deepest penetration of the discharge jets. Thus, the entrainment flux at the lateral jet boundaries is made up of a mixture of ambient water and already mixed water which recirculates laterally. Particularly for cases with jet penetration approaching the total layer depth, the lateral return flow dominates the bottom return flow. In these cases, it makes up the major portion of the jet entrainment flow and, possibly, of the intake flow. This appears to be the probable mechanism for near field recirculation of this generic discharge design.

5.2.1 Temperature Field Measurements

Figures 5.2 - 5.4 are typical examples (Exp. No. 11) of the data provided by a separate jet stagnant experiment. Figures 5.2 and 5.3 are centerline sections of the two jets of a half-model experiment. Isotherm plots of this type appear in Appendix A.2 for the experiments in this series. The temperature (^{o}C) at depths above 10 centimeters represents the time averages of up to four actual measurements (all taken within two minutes of each other). The lower depth temperatures are single scans. This data collection procedure averaged out turbulent temperature fluctuations in the jet to obtain a better estimate of the mean temperature. As in the radial experiments, temperature measurements at different depths occurred at different times. But all the temperatures were taken within the time span in the experiment which approximates steady

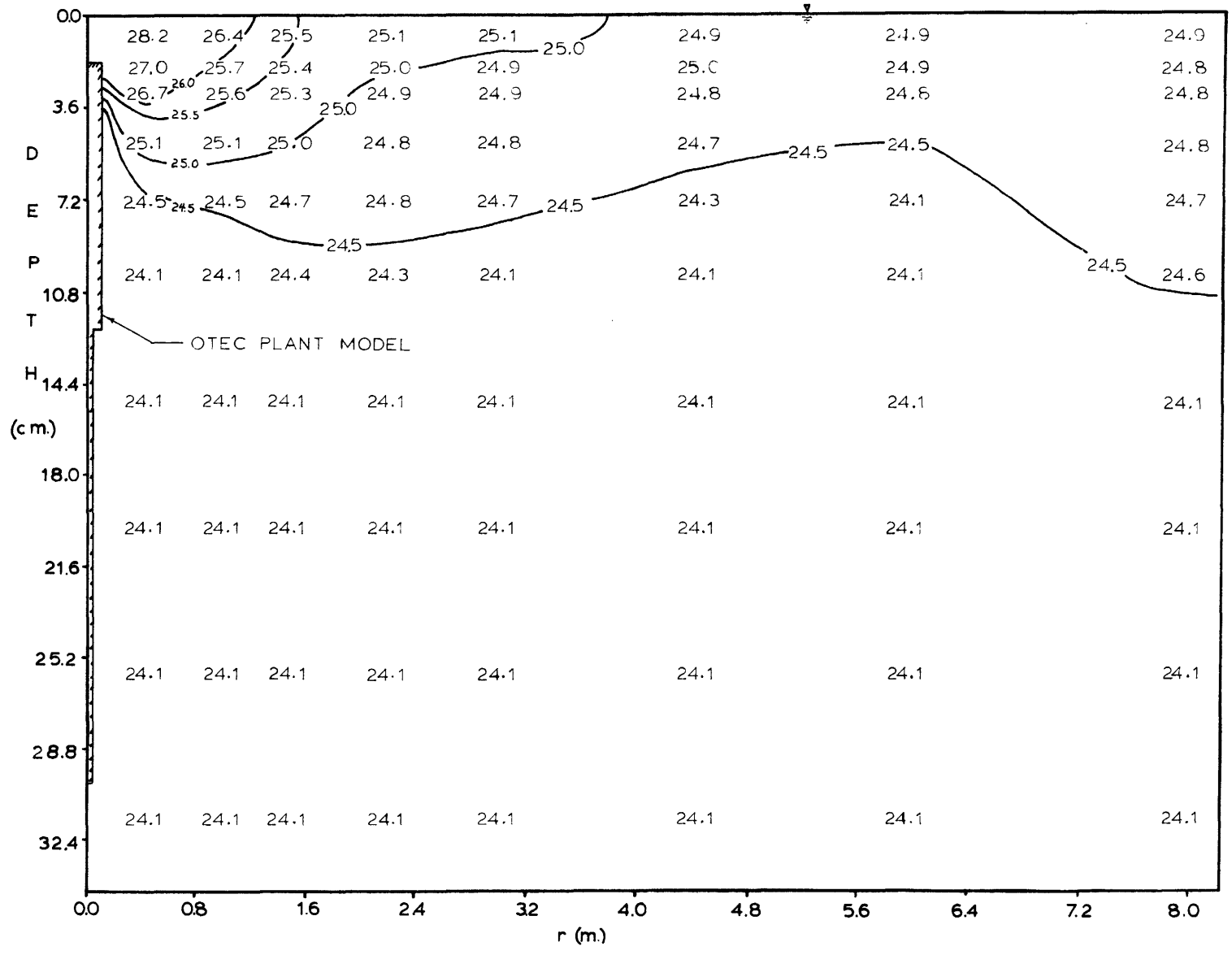

Figure 5.2 Centerline Temperature (°C) Transect Through the Right Jet, Experiment 11.

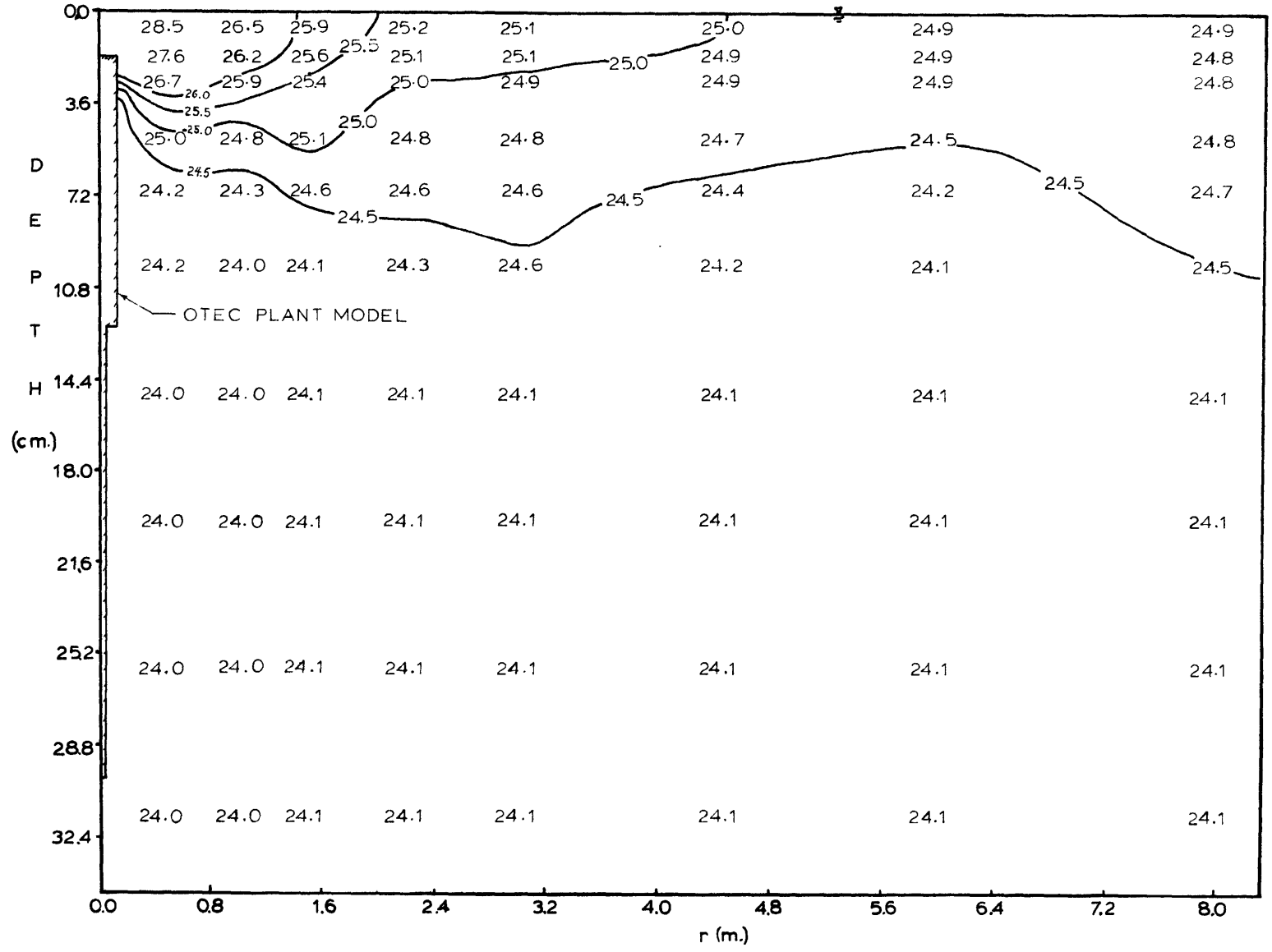

Figure 5.3 Centerline Temperature Transect Through the Left Jet, Experiment 11.

state.

Figure 5.4 is a typical plan view of the temperature field for the scan taken closest to the surface (in this case 1.0 cm below the surface). The two jets produce very similar and symmetric temperature fields. It is important to note that the temperature field gives no indication of the actual jet width. Even probes nearly halfway in between the jets, register a temperature rise above the ambient ($24.1^{o}C$). Observation of moving dye patches showed that these temperature probes were substantially outside of the jet velocity field. This jet structure is due to the lateral return flow mechanism as discussed earlier.

5.2.2 Steady-State Determination

The "steady state" time interval of these experiments can be approximated by the previous results for radial jets. The best approximation would be from a radial jet that dilutes to the same degree or that has the comparable discharge densimetric Froude number, F_o^*.

One steady state test though was done to examine the time varying behavior of the jet lateral return flow zone. Columns of probes (as described in Chapter 3) were placed at 2.0 and 3.5 meters from the model (full model experiment). There were two columns at each radius, one was located on a jet centerline and the other halfway between two jets. Figure 5.5 shows the time varying behavior

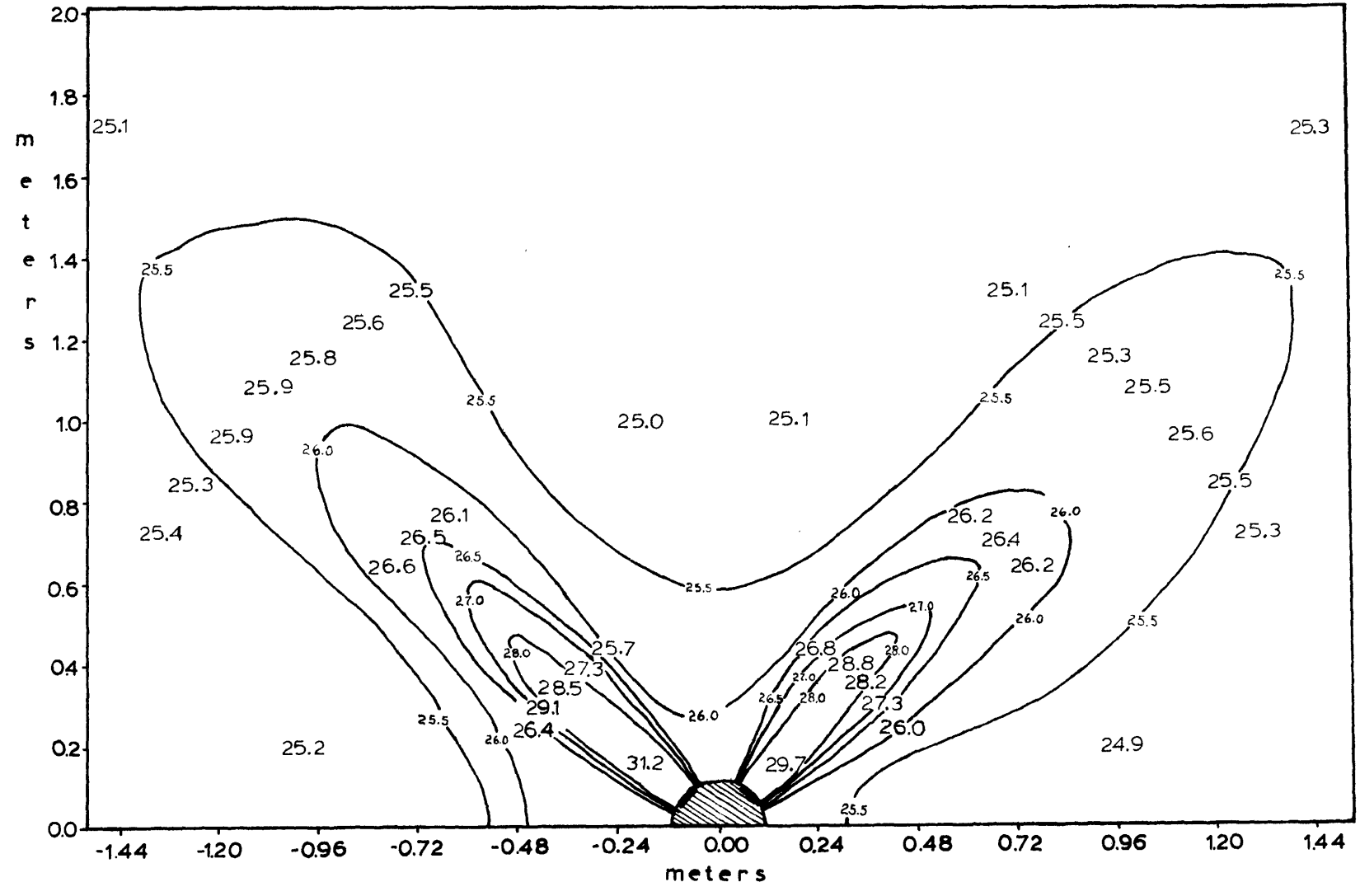

Figure 5.4 Typical Plan View of Surface Isotherms, Stagnant Experiment with Separate Jet Discharge (Exp. #11)

of temperature for a depth of 2 cm at each location.

The jet lateral return flow has a shorter steady state period than the jet flow. The period of 10-25 minutes is a reasonable approximation for this test. Half model experiments should have longer periods. It is important to note that the temperature rise in the lateral return flow zone occurs near the model first and progresses out from there. The chronology of Figure 5.5 clearly shows that the temperature rise in this zone is not caused by discharge jet waters reaching the basin boundaries, being turned, and flowing back toward the model (basin boundaries are $\sim$ 7 m. from the model).

5.2.3 Recirculation Indications

There were no direct fluorescent dye studies done for the separate jet design. Intake temperature records showed no definite indications of recirculation in any experiment. The two experiments with the highest Froude numbers and discharges (Exp. 14 and 15), however, indicated some tendency for recirculation based on the following observations.

1) Dyed discharge waters appeared to penetrate well over 50% of the water column. At least one of the jets in

*This lateral "shedding" of eddies is a characteristic feature of buoyant surface jets and has been documented in earlier investigations by Adams, Stolzenbach and Harleman (1975).

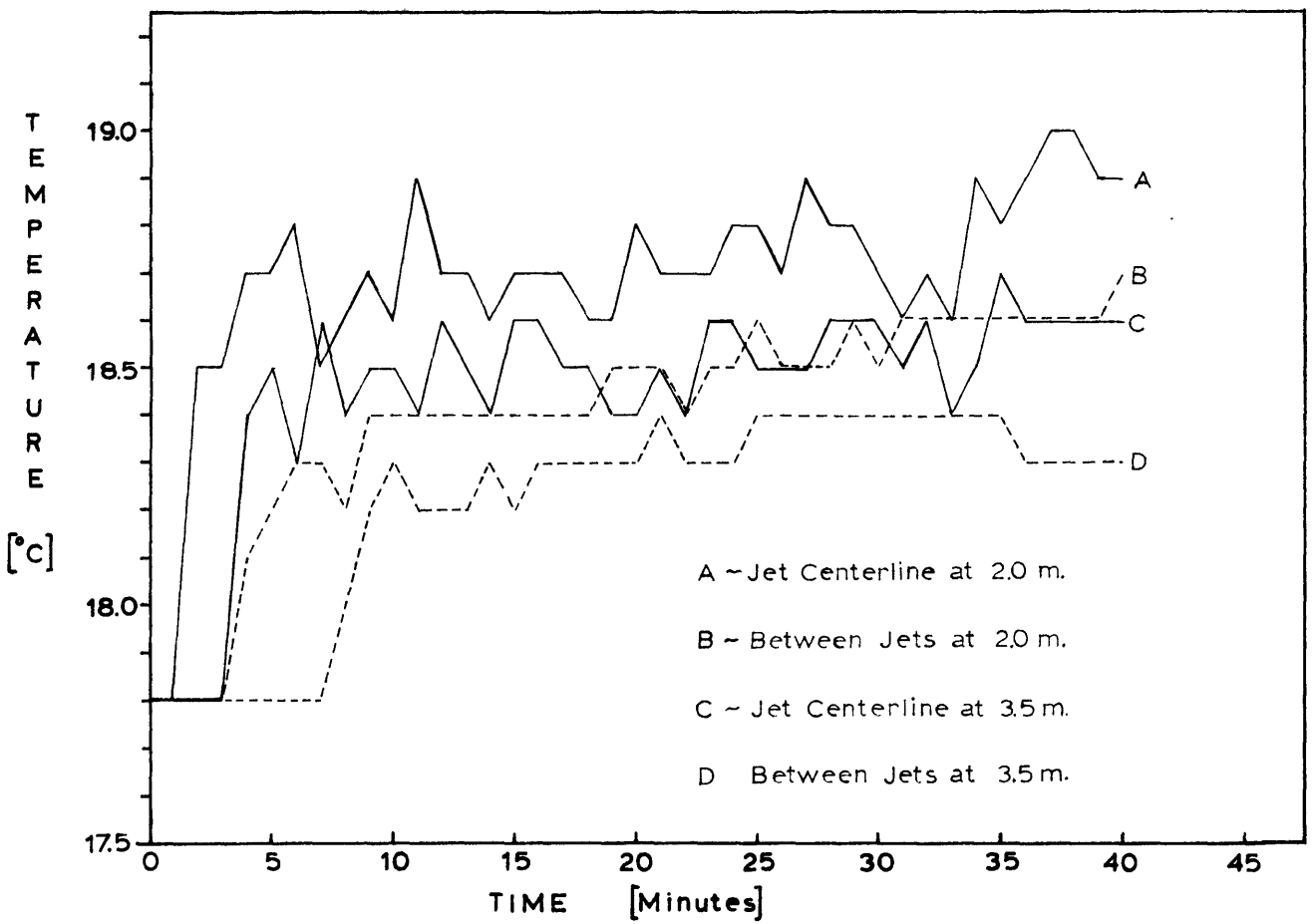

Figure 5.5 Steady-State Test for Stagnant Experiments with Separate Jet Discharge (Exp. #43)

Exp. 15 appeared to reach the basin floor.

2) Temperature profiles taken in the interaction return flow zone indicated a significantly deeper penetration of this zone. In Exp. 14, the penetration was over 50% of the water column. The zone in Exp. 15 appears to extend to 90% of the water column.

Experiment 15 may very well have experienced a small amount of recirculation. However, the intake temperature actually fell $0.03^{o}C$ due to temperature non-uniformities in the basin prior to the experiment.

5.3 Experimental Correlation of Discharge Behavior

5.3.1 Jet Behavior

Figure 5.6 is a graph of stable jet dilution as a function of the modified Froude number, F_o^* . The stable jet dilution, S_s, is defined to be the total volumetric flow rate at a distance where temperature is changing slowly ("stable region"), divided by the discharge flow rate. Using the similarity assumptions presented in Chapter VIII, it is possible to relate the local jet dilution to the ratio of discharge temperature difference and the local jet surface temperature difference:

$$S_s = 1.5\ \Delta T_o/\Delta T_c$$

Because surface heat loss can become important in the far

field region, it is best to measure the stable dilution (when temperature measurements are involved) at the beginning of the far-field zone. An estimate of the distance to the transition from near field to far field is given by Jirka et al. (1975).

$$x_t = 12.6\ \mathbb{F}_o^*\ \sqrt{h_o b_o} \tag{5.1}$$

The stable dilution was estimated from surface temperatures measured at approximately this distance from the discharge point. Measurements in each of the jets (2 for the half model and 4 for the full model) were averaged to obtain the experimental value.

Figure 5.6 shows that the majority of experiments exhibit a linear relationship between S_s and $\mathbb{F}_o^*$. Furthermore, it is consistent with the correlation developed by Stolzenbach and Harleman (1971) for single port buoyant surface jets.*

$$S_s = 1.66\ \mathbb{F}_o^* \tag{5.2}$$

The Stolzenbach-Harleman relation appears to slightly overestimate the dilutions (based on temperature measurements) for the lower Froude number experiments. This trend is explainable because the relationship was developed for a jet entraining ambient water, while the jets in the present experiments entrained some heated water from the lateral return flow zone. This would tend to decrease

*The numerical value of Eq. (5.2) differs due to changes in the Froude number definition.

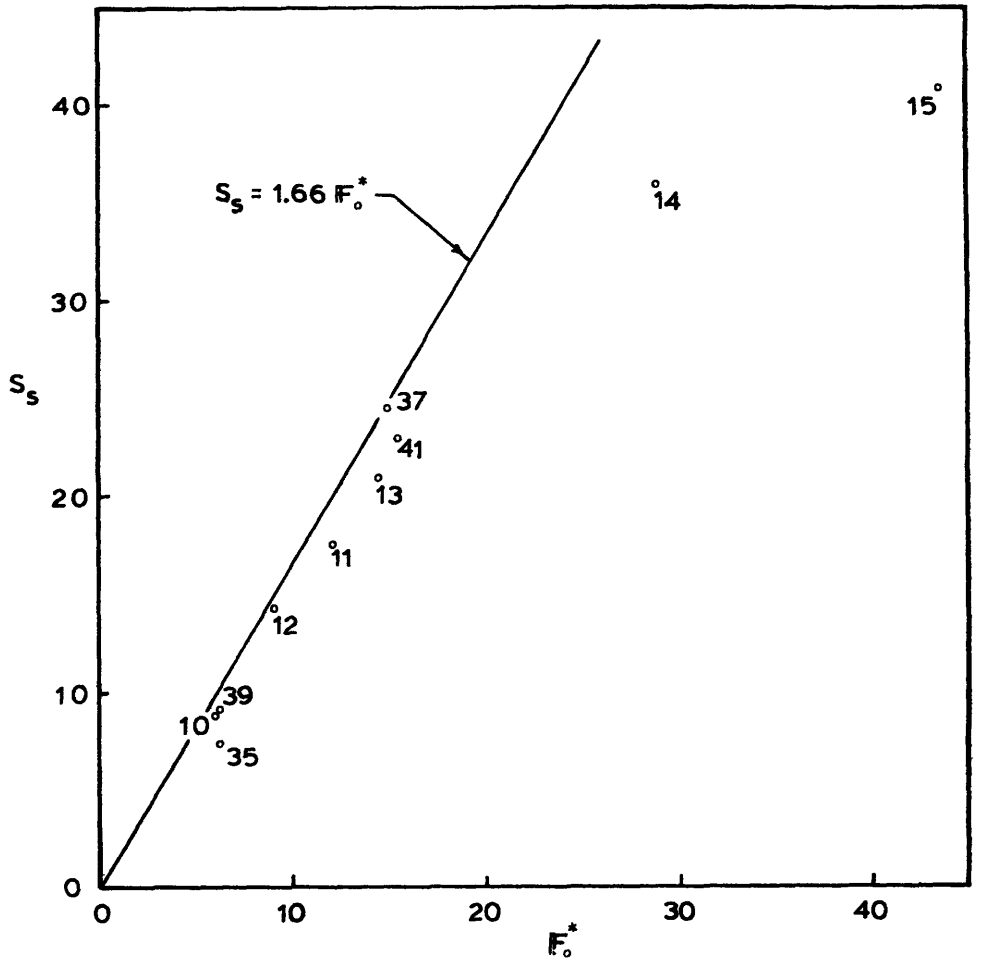

Figure 5.6 Stable Jet Dilution vs. Quarter Module "Port" Discharge Froude Number, Stagnant Experiments

the effective jet dilution.

The two highest Froude number experiments (Exp. 14 and 15) have dilutions considerably below the predicted values. Two explanations are possible. As was noted in Section 5.2.3, the jets in these two experiments penetrate deep into the water column. Possible interactions with the bottom probably limited dilution. Also, the calculated values of distance x_t to the far field were beyond the confines of the experimental basin (8.76 m. and 13.16 m.). This means that the jets possibly had not yet reached their stable dilutions at 8.0 meters where the temperature-dilution measurements were taken.

Figure 5.7 plots maximum experimental values of jet half-temperature depth (i.e., the depth where the temperature difference above ambient is one-half the centerline value) normalized by the square root of the discharge area, $(h_o b_o)^{\frac{1}{2}}$. These depths are plotted as a function $\mathbb{F}_o^*$. The linear trend in the data is apparent and extends to the large Froude number experiments as well. One cannot hope to extend the linear relationship much beyond Exp. 15 because (Section 5.2.3) the maximum jet depth in that experiment was clearly the experimental basin floor. Assuming a polynomial temperature profile (Abramovich, 1963), the relationship between half temperature depth and $\mathbb{F}_o^*$ is (Jirka, et. al., 1975)

$$\frac{h_{.5T\ max}}{\sqrt{b_o\ h_o}} = 0.18\ \mathbb{F}_o^* \qquad (5.3)$$

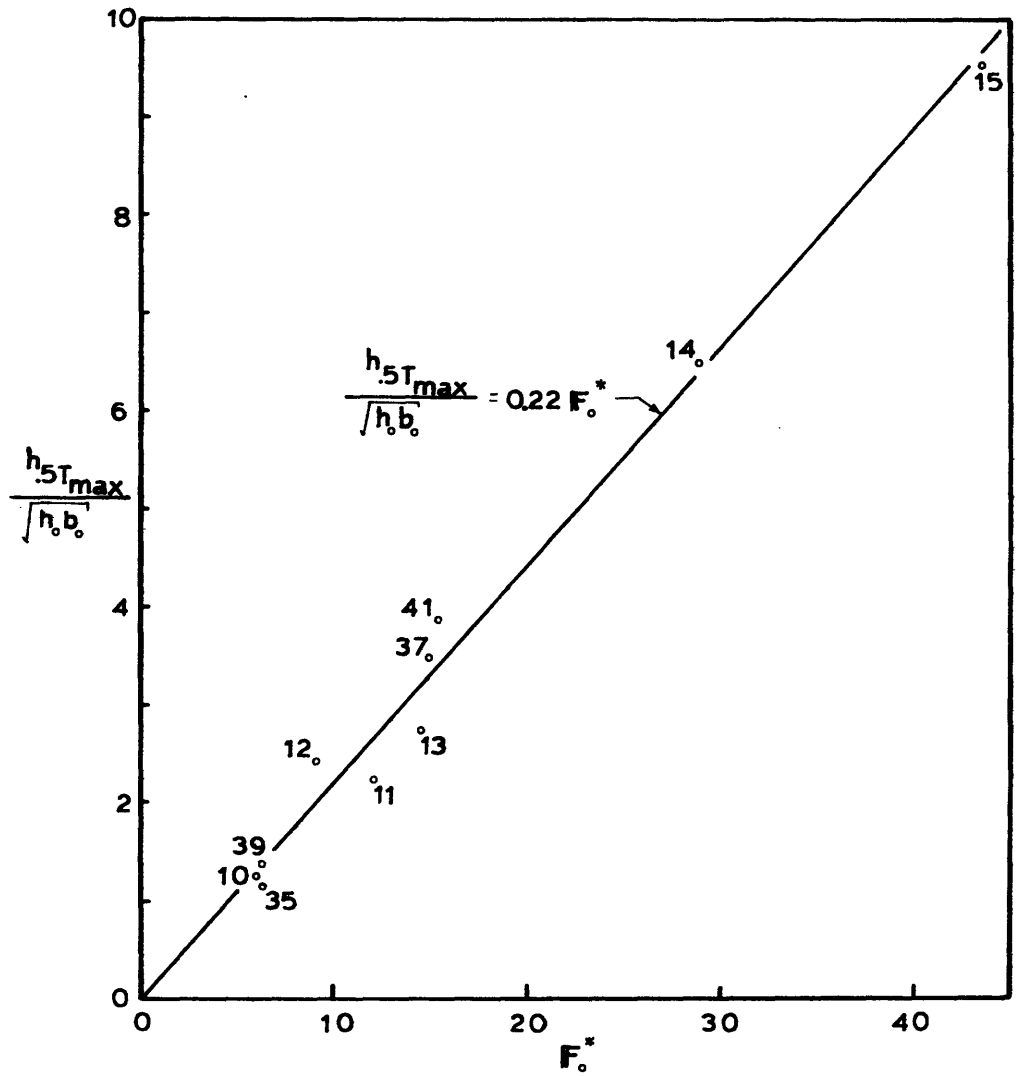

Figure 5.7 Normalized Maximum Half-Temperature Depth vs. Quarter-Module "Port" Discharge Froude Number; Stagnant Experiments

As seen in Figure 5.7, the data fits this relationship well.

5.3.2 Characteristics of the Lateral Return Flow

This section presents information derived from temperature profiles taken within the lateral return flow zone at distances of 1.0 m. and 4.0 m. from the OTEC model. The zone properties are averaged within an experiment (measurements were taken between different jets and between jets and the wall in half model experiments) and plotted as a function of F_o^*. The experimental range of the separation parameter, b_o/r_o, does not appear to affect the data trends.

Figures 5.8a and 5.9a are plots of surface temperature in the lateral return flow zone. Higher Froude number experiments achieve higher jet dilutions. Hence, the surface temperature in the return zone is less because the jets contributing the heated water are more diluted. The centerline jet temperatures at the same distance from the model are plotted for comparison. It is of note that (especially for low Froude number experiments), the return flow surface temperature is higher at 1 m. than the jet centerline temperature at 4 m. Apparently, some jet eddies are breaking off and entering the return flow between 1 m. and 4 m. from the model.

Figures 5.8b and 5.9b present an average half temperature depth in the zone for each experiment. It is notable in Figure 5.8b that the lateral return flow zone is much deeper than the jet zone for large Froude number experiments. Such conditions seem to indicate

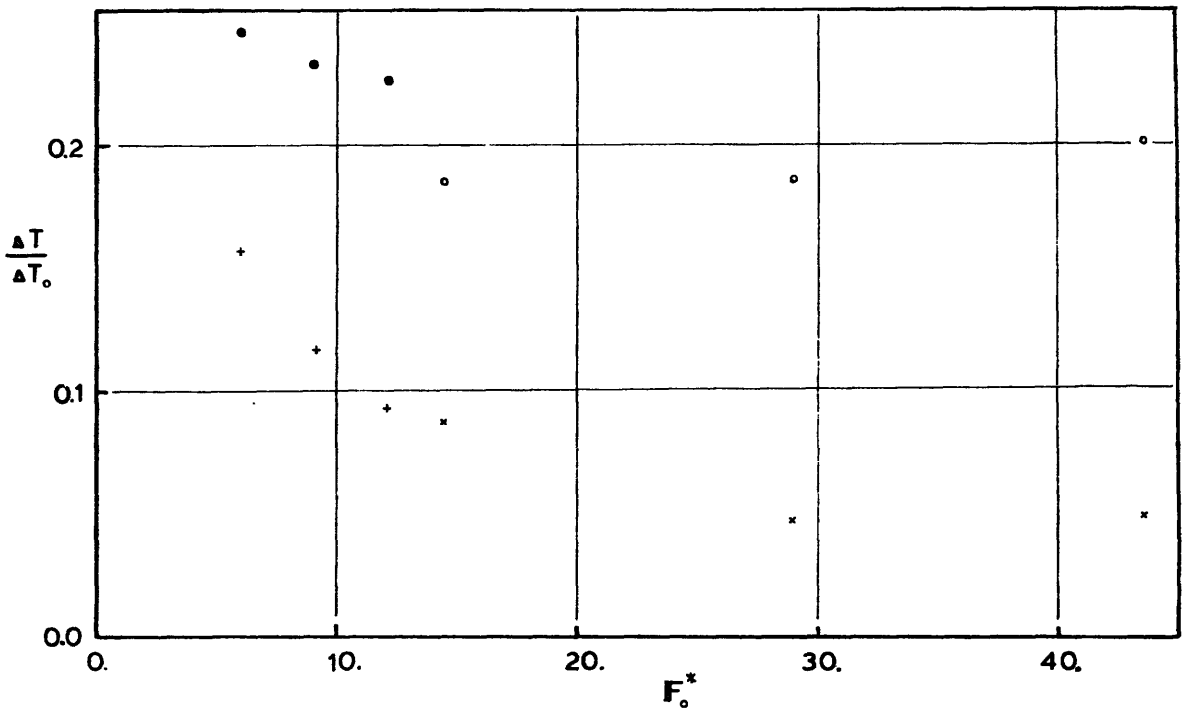

Figure 5.8a Comparison of Jet Centerline and Lateral Return Flow Surface Temperature Data at X = 1.0m.

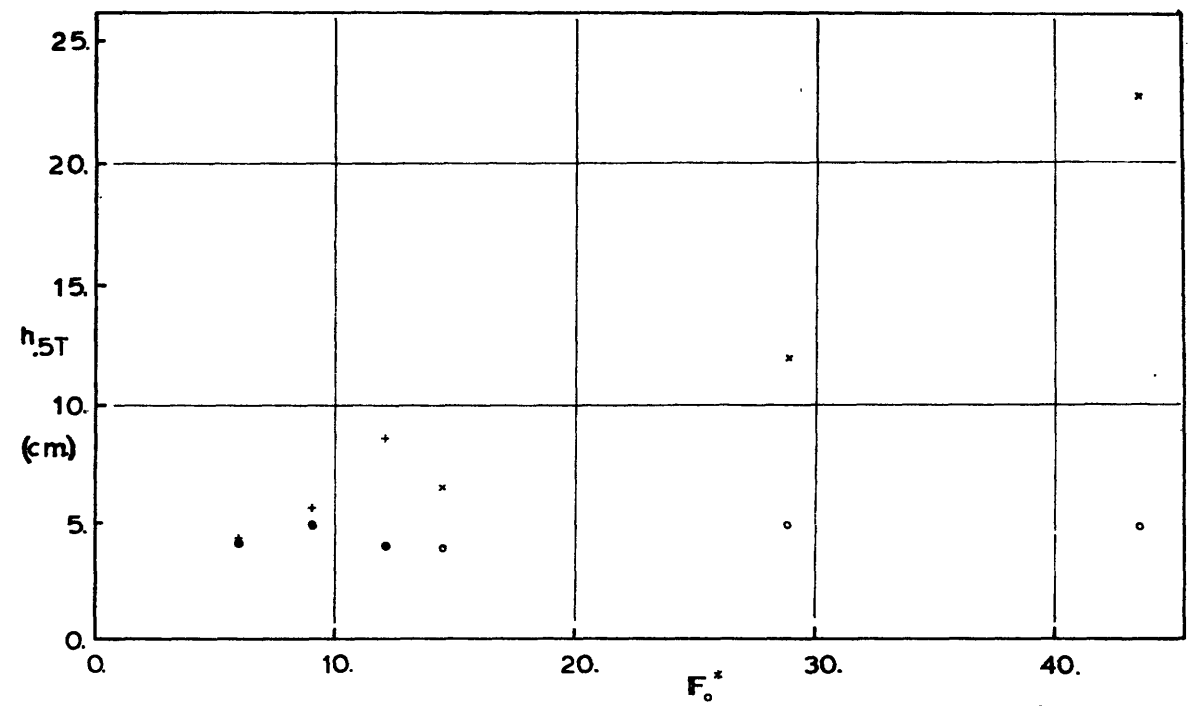

Figure 5.8b Comparison of Jet Centerline and Lateral Return Flow Half Temperature Depth Data at X = 1.0m.

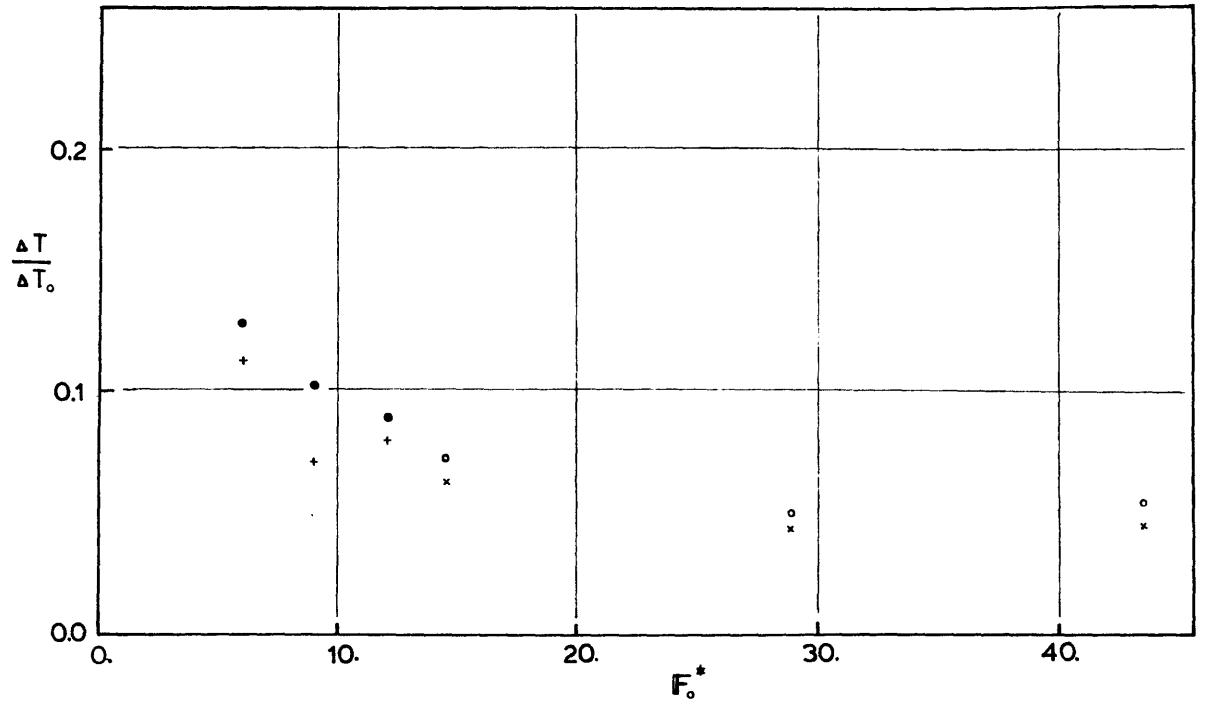

Figure 5.9a Comparison of Jet Centerline and Lateral Return Flow Surface Temperature Data at X = 4.0m.

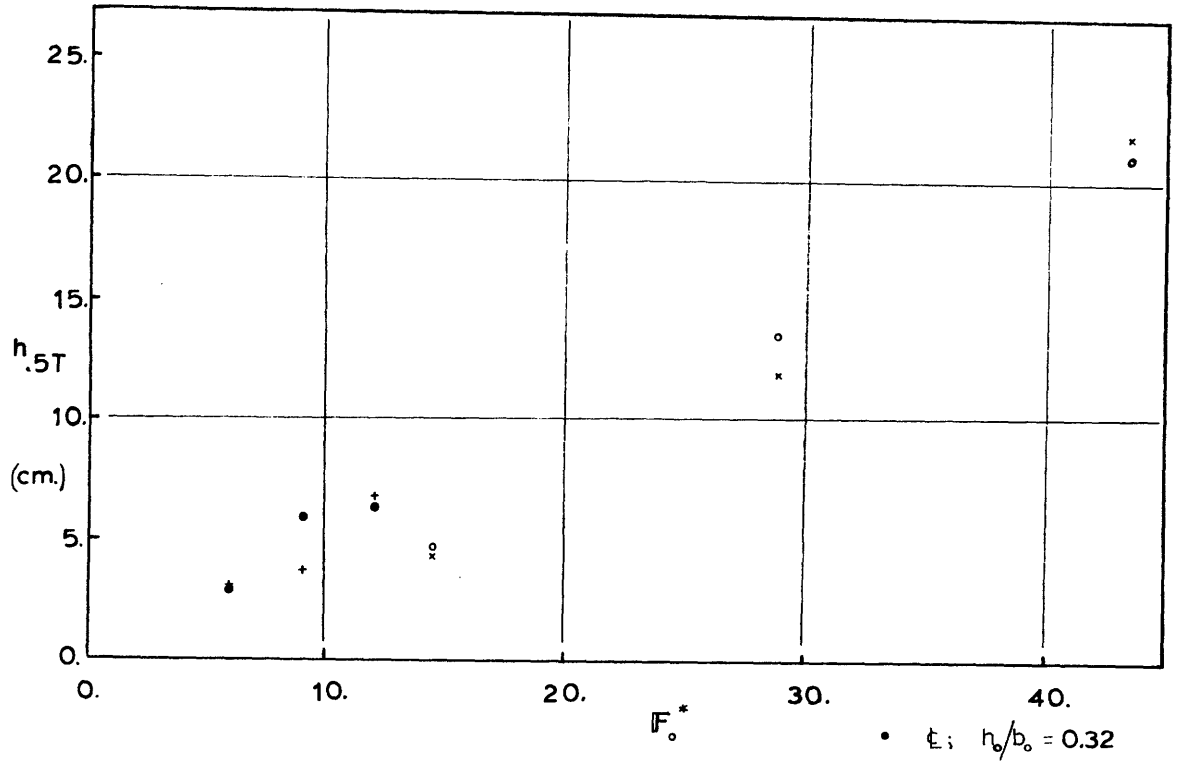

Figure 5.9b Comparison of Jet Centerline and Lateral Return Flow Half Temperature Depth Data at X = 4.0m.

that part of the entrainment flow through the bottom of the jet comes from the lateral return flow zone. Conceivably, for increasing densimetric Froude numbers, the intake flow would be supplied by this flow zone too. However, this possibility was not observed within the range of the experimental program.

CHAPTER VI

EXPERIMENTAL RESULTS: OCEAN CURRENT CONDITIONS

6.1 Run Conditions

Experiments with the model discharging into an ambient velocity field were conducted both with radial and separate jet geometry. The model ambient current flux ratio range presented in Table 2.5 is not as broad as the range to be found at a typical prototype site. The model current generation system was limited to average velocities of less than 1.0 cm/sec. for the water depth used in the experiments. At the approximate length scale of 1:200, this model velocity simulates only 0.25 knots in the prototype.

Another difficulty with the ambient current experiments was the non-uniformity of the vertical and lateral velocity distribution. Figure 6.1 is a typical ambient velocity profile in the vertical direction. Constant velocity from surface to bottom was not possible because of bottom friction and local non-uniformities in the flow. Lateral uniformity of the flow was also not guaranteed, partly because of the slow flows involved. Uniform withdrawal across the depth at the downstream end of the basin was difficult to achieve. In the thermally stratified system induced by the model preferential withdrawal from one particular layer could occur.

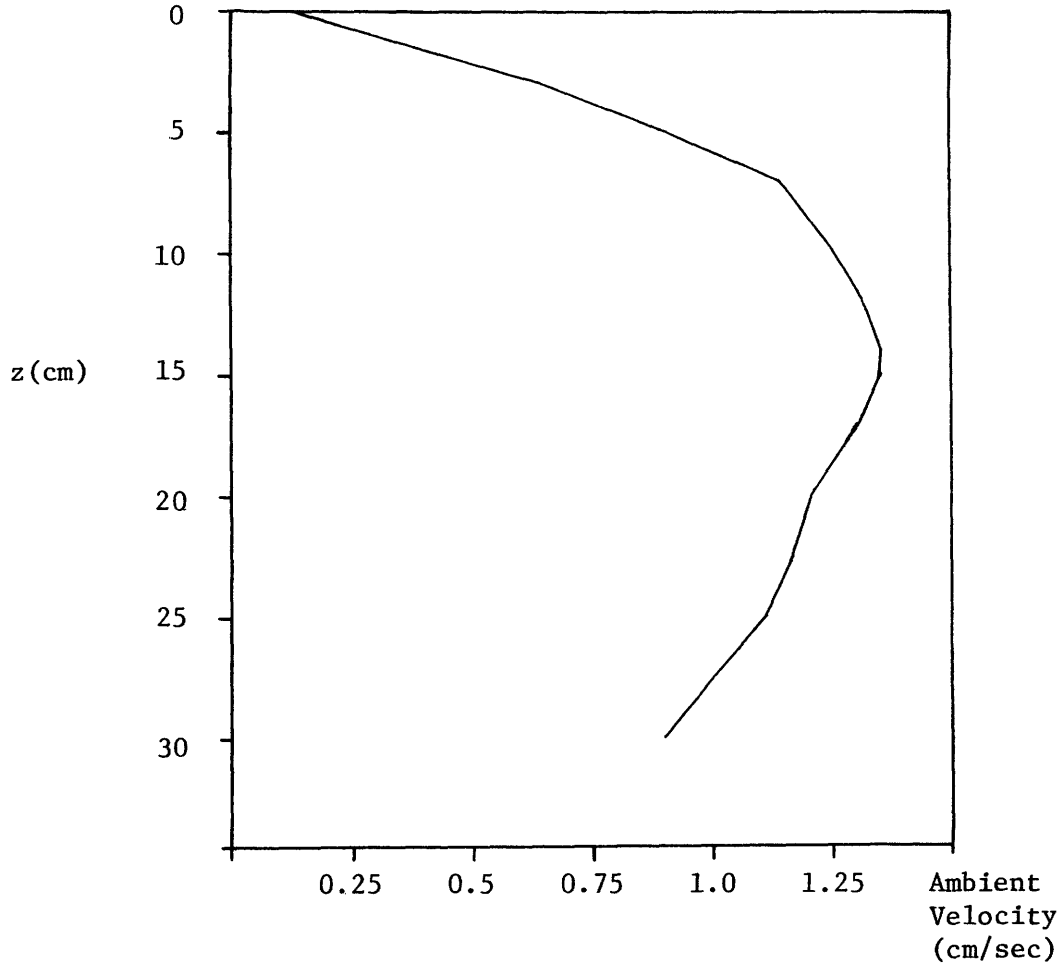

Figure 6.1 Typical Ambient Vertical Velocity Profile, Cross-Flow Experiment

Table 6.1 lists the dimensional operating and design parameters for the experiments. The dimensionless governing parameters appear in Table 6.2. Both radial and separate jet discharge configurations were tested with half and full model experiments. The half model tests for separate jets were limited to a single orientation due to symmetry considerations. The two jets had to be discharged 45^{o} and 135^{o} to the current direction. With the full model, any orientation of the separate jets was possible. In addition to the orientation used in the half model, tests were done with the orientation having jets directed upstream, downstream and 90^{o} to the current.

6.2 Experimental Results

A simple, unified description of the flow fields observed is not possible. Certain observations though are helpful in understanding the nature of the experiments.

Except for the deeply mixing case of Exp. 17, the model operation formed essentially a two layer flow system over most of the basin. The ambient current dipped down below the heated surface layer to form the lower layer. The upper layer was formed by the discharge and retained some of the mixing features of the stagnant experiments. The relative thickness of the layers depended on location. In general, the upper layer was thicker for strongly mixing, higher Froude number discharges.

Table 6.1a

DIMENSIONAL PARAMETERS AND EXPERIMENT DESCRIPTIONS
RADIAL DISCHARGE EXPERIMENTS WITH A CURRENT

Run	Type Model Half	Full	Q_i [cm^3/sec]	u_o [cm/sec]	A_o [cm^2]	T_o [°C]	T_A [°C]	$\Delta\rho$ x 10 [gm/cm^3]	u_a [cm/sec]
21	X		1770.	77.5	5.7	31.9	20.5	3.04	.75
22	X		884.	38.8	5.7	29.5	18.7	2.66	1.11
23	X		884.	38.8	5.7	29.1	18.2	2.65	1.27
24	X		884.	19.4	11.4	31.7	19.8	3.13	.97
32		X	884.	19.4	11.4	27.9	15.7	2.74	.94
34		X	884.	38.8	5.7	27.8	15.5	2.75	.94

Table 6.1b

SEPARATE JET EXPERIMENTS WITH A CURRENT

Run	Type Model Half	Full	Orientation 0°*	45°**	Q_i cm^3/sec	u_o cm/sec	A_o cm^2	T_o °C	T_A °C	$\Delta\rho$ x 10^3 gm/cm^3	u_a cm/sec
17	X			X	1770.	78.4	5.6	25.4	20.3	1.19	.41
18	X			X	1770.	78.4	5.6	30.5	20.2	2.68	.94
19	X			X	884.	39.2	5.6	30.7	20.3	2.71	.86
20	X			X	884.	19.6	11.3	33.5	23.0	3.01	.88
36		X	X		884.	19.6	11.3	30.3	19.4	2.78	.95
38		X	X		884.	39.2	5.6	30.0	18.6	2.82	.93
40		X		X	884.	19.6	11.3	28.6	16.5	2.81	.93
42		X		X	884.	39.2	5.6	28.7	16.5	2.82	.91

*Jets directed parallel and at 90° to current direction.

**Jets directed at 45° and 135° to current direction.

Table 6.2a

DIMENSIONLESS GOVERNING PARAMETERS
RADIAL DISCHARGE EXPERIMENTS WITH A CURRENT

Run	Type Model Half	Full	IF_o^*	IF_i	h_o/H	r_o/b_o	$u_a H^2/Q$
21	X		29.0	.141	.0091	36.	.52
22	X		15.5	.076	.0091	36.	1.54
23	X		15.5	.076	.0091	36.	1.76
24	X		6.0	.070	.018	18.	1.34
32		X	6.4	.074	.018	18.	1.30
34		X	15.2	.074	.0091	36.	1.30

Table 6.2b

SEPARATE JET EXPERIMENTS WITH A CURRENT

Run	Type Model Half	Full	Orientation 0^o	45^o	IF_o^*	IF_i	$A=h_o/b_o$	h_o/H	r_o/b_o	$u_a H^2/Q_i$
17	X			X	46.9	.226	.64	.054	3.86	.28
18	X			X	31.3	.151	.64	.054	3.86	.65
19	X			X	15.6	.075	.64	.054	3.86	1.19
20	X			X	6.2	.071	.32	.054	1.93	1.22
36		X	X		6.5	.074	.32	.054	1.93	1.32
38		X	X		15.3	.073	.64	.054	3.86	1.29
40		X	X		6.4	.074	.32	.054	1.93	1.29
42		X	X		15.3	.073	.64	.054	3.86	1.26

A persistent feature of the radial half model experiments with a current was that the portion of the flow discharged directly upstream separated from the wall, as can be seen in Fig. 6.2. Thus, the presence of the basin wall in the half model radial experiments could not be totally neglected. This separation was, of course, absent for the full model tests.

The temperature field near the surface for separate jets was essentially similar to the stagnant case (Figure 6.2). The jets were bent by the current until they were directed downstream. A lateral return flow zone of some form existed between each pair of jets (or a jet and the wall for half model experiments). The return zone between jets pointed 45^{o} to the upstream direction was mainly ambient water. But even in this zone, the surface temperature would rise near the model due to eddies breaking off the discharge jets.

None of the experimental currents were sufficiently strong to confine the model discharge widthwise within the basin. Heated water reached the far basin wall in each experiment. In some discharge configurations, heated water nearly reached the upstream basin wall as well.

6.2.1 Temperature Field Measurements

The data presentation is essentially the same for the current experiments as for the stagnant experiments. No spatial averaging is possible, however, because there is no intrinsic symmetry

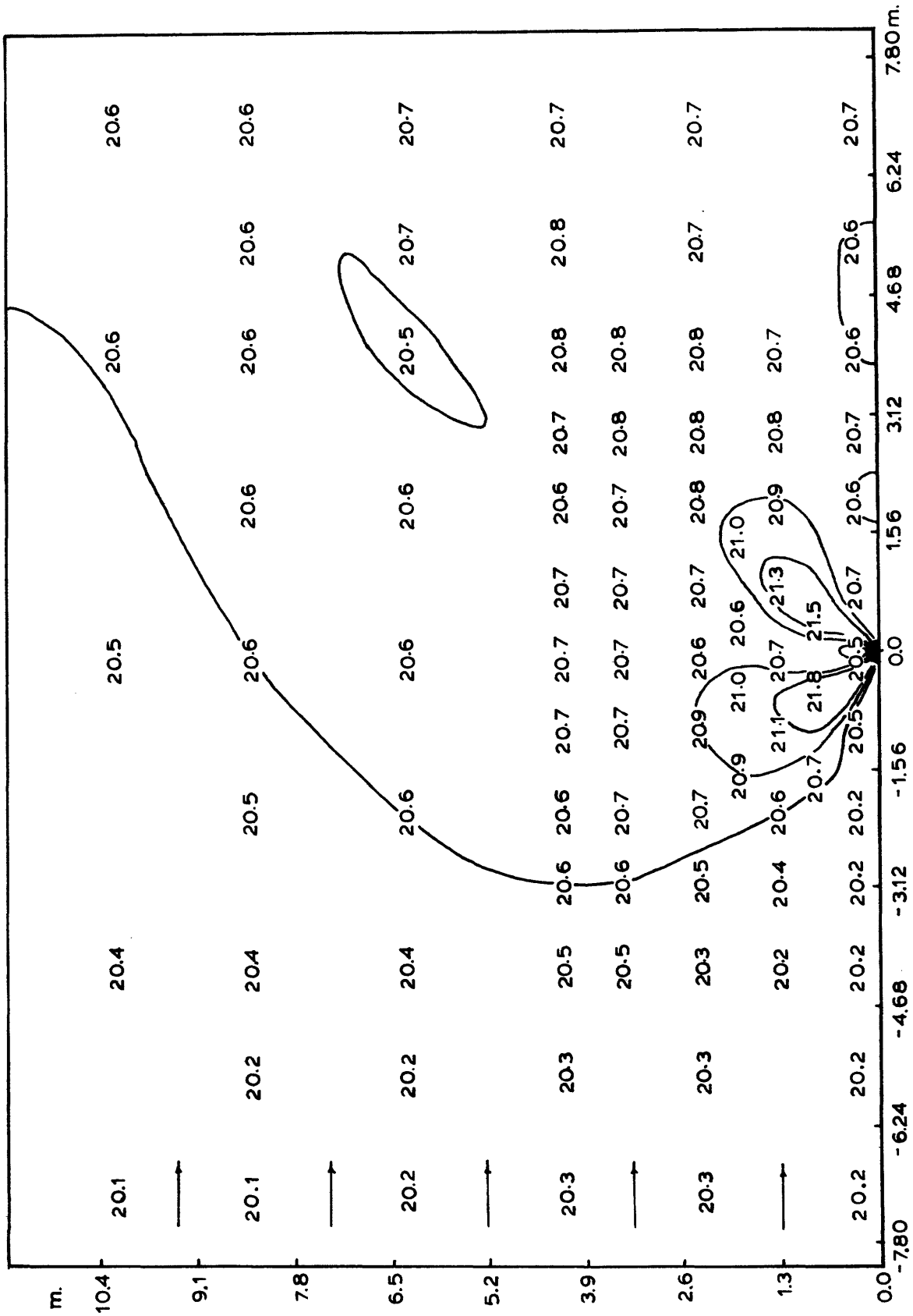

Figure 6.2 Typical Plan View of Surface Isotherms, Cross-Flow Experiment #18
Separate Jet Discharge, Half Model

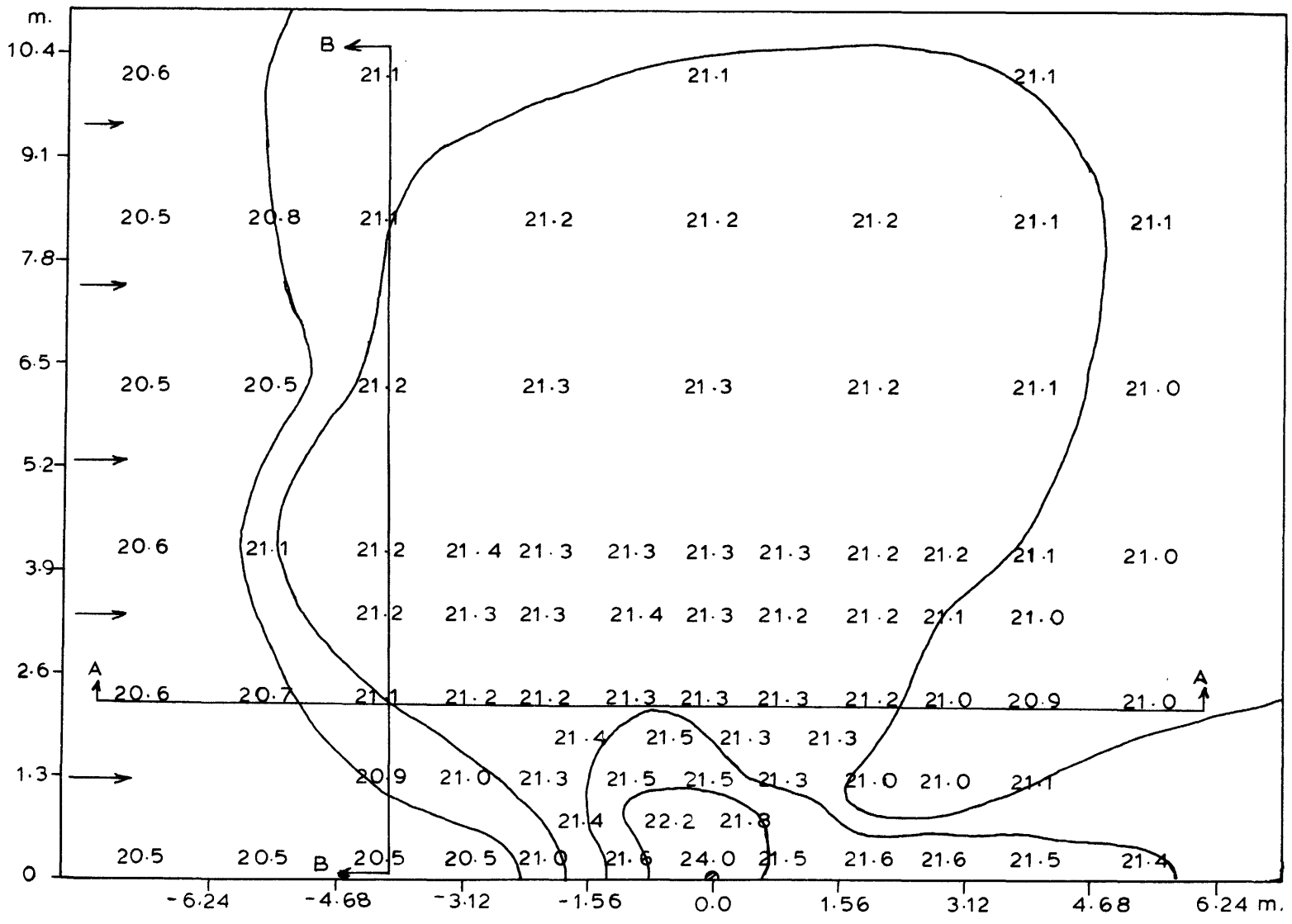

Figure 6.3 Typical Plan View of Surface Isotherms, Cross-Flow Experiment #21
Radial Discharge, Half Model

in the flow and temperature fields of the half model. Multiple scans were taken near the surface to smooth out turbulent fluctuations. The upper level temperatures represent the average of 4 data scans while the lower layer temperatures are taken from only one scan.

Appendix A.3 presents the normalized isotherms, in per cent, for longitudinal transect AA and lateral transect BB shown in Figure 6.2 in addition to the surface plans. Full model experiments actually have two longitudinal transects AA on either side of the model. Only one is presented in Appendix A.3.

Figure 6.3 is a plan view of the uppermost level with the current moving from left to right. The discharge configuration is radial. Isotherms have a distorted shape due to the current effect. The model basin does not contain the discharge jet since some of the surface isotherms extend to the wall opposite the model. As previously mentioned, the discharge jet splits away from the upstream wall for this half model experiment.

6.3 Experimental Correlations of Discharge Behavior

Figure 6.4 is a plot of an average jet dilution as a function of F_o^* at a downstream distance of 5.5 m. Readings of several surface temperature probes at this distance (5 or 6 depending on whether it is a full or half model) were averaged. A dilution was calculated assuming a uniform surface temperature (the average value just mentioned) across

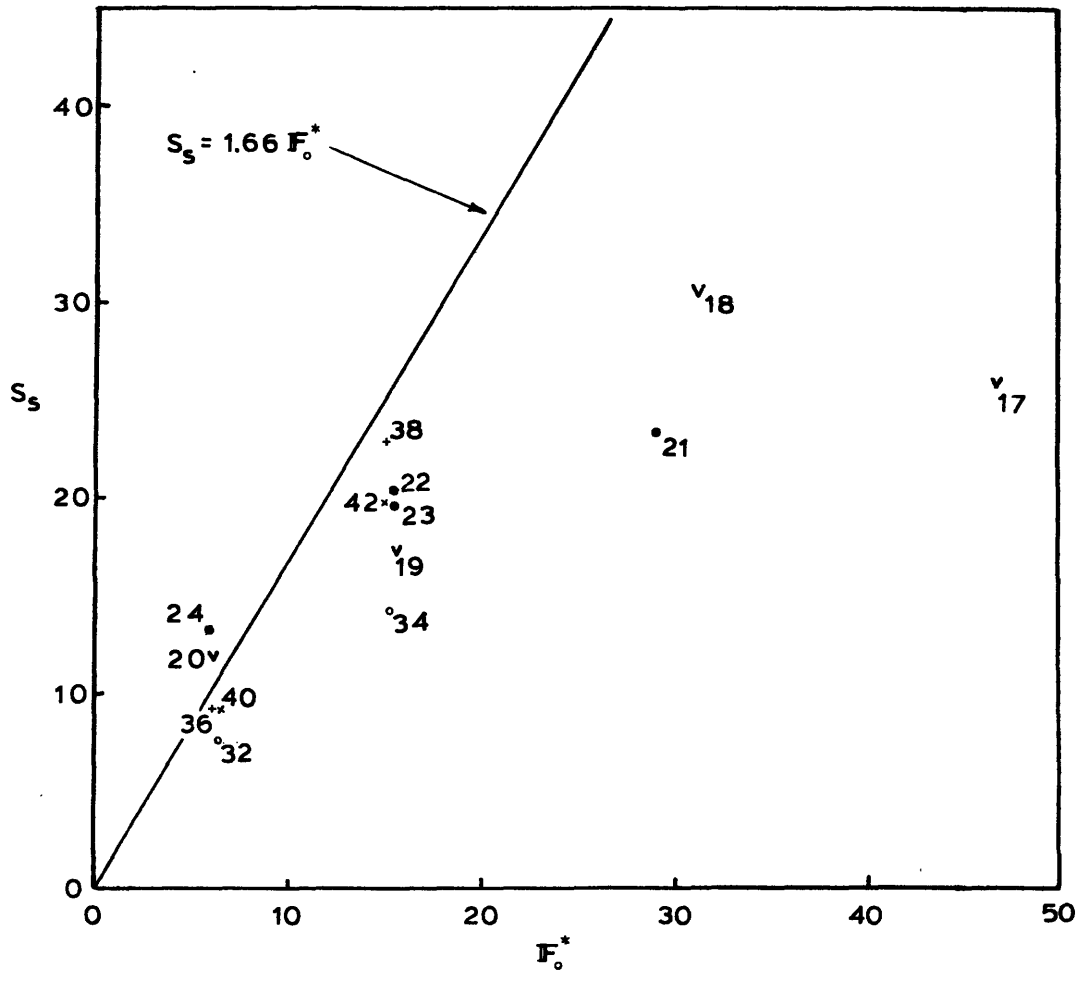

• half model, radial jet

◦ full model, radial jet

ᵛ half model, separate jet

+* full model, separate jet

Figure 6.4 Stable Downstream Dilution vs. Quarter Module "Port" Discharge Froude Number, Ambient Current Experiments

the basin width. The assumption of vertical, polynomial temperature and velocity similarity profiles (as suggested by Abramovich, 1963) allowed a dilution calculation.

The line in Fig. 6.4 is the previously used stable dilution relation, Eq. (5.2), which in principle holds for the stagnant case only. However, the data for the experiments with currents appear to generally agree with the relationship. The lack of agreement for the higher Froude number is similar to the stagnant cases and may be caused by recirculation effects. This agreement between the current and stagnant cases seems to point to the primary conclusion that within the experimental range the OTEC effluent mixing is dominated by the discharge design and not by the current speed. Some secondary effects which may be caused by the presence of the current are discussed in the following.

The slightly lower dilutions could also be caused by several other factors. For example, the interference on the discharge flow field by the experimental basin boundaries might reduce dilution. This effect on full model experiments should be greater than on their half model counterparts. Also, the "blocking" effect, in terms of the upstream density wedge, may cause lower effective dilutions. Discharge waters directed initially upstream will be turned and carried downstream by the current. These discharge waters then served as sources of entrainment for downstream directed jets, lowering their effective

dilution.

Figure 6.5 is a graph of the half temperature depth at the point of maximum, near field penetration of the model discharge. Shown for comparison is the relationship (Eq. 5.3), for maximum penetration of a single jet in stagnant ambient waters. The generally good agreement between the current case data and the stagnant jet correlation shows that the ambient current did not greatly affect the near field mixing process. The increased scatter of data points over those obtained in stagnant experiments is in part due to the difficulties involved in creating and withdrawing a uniform current at either end of the model basin (Section 6.1).

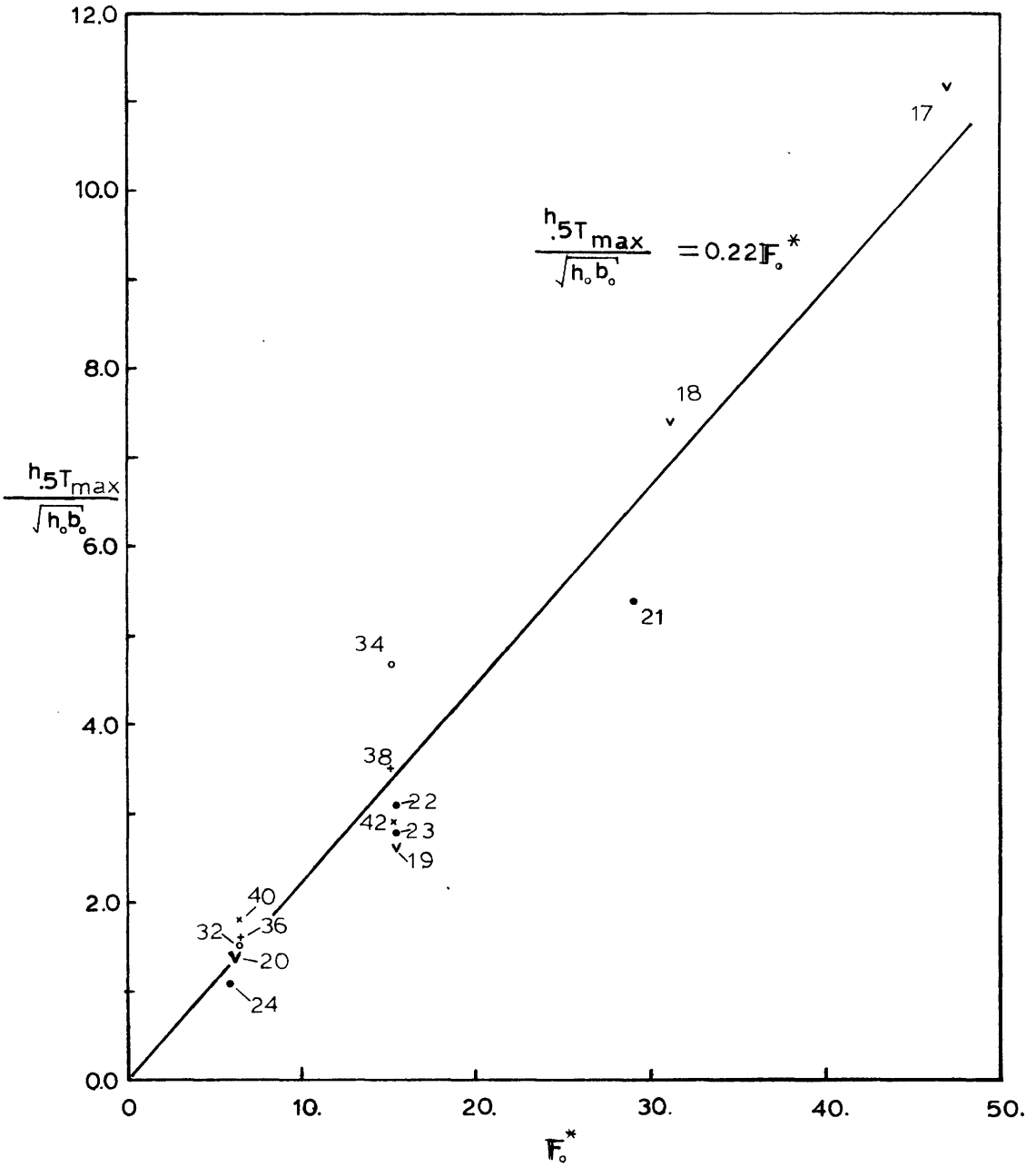

• half mode, radial jet

° full model, radial jet

ᵛ half model, separate jet

+ × full model, separate jet

Figure 6.5 Maximum Half Temperature Depth vs. Quarter Module "Port" Discharge Froude Number; Ambient Current Experiments

CHAPTER VII

RADIAL JET THEORY WITH STAGNANT CONDITIONS

7.1 Method of Analysis

In addition to the physical experiments, theoretical models (based on the conservation equations for mass, momentum and heat) were constructed to examine the external velocity and temperature fields produced by OTEC plants with radial discharge geometry (this chapter) and separate discharge geometry (Chapter 8). In both cases, a stagnant ambient condition is assumed, which appears to represent a critical case regarding the discharge mixing and the potential for recirculation. A fully analytical treatment of the complete flow field is difficult because there are different flow regimes induced throughout the entire region. Therefore, the theoretical models divide the external field into different zones. Each zone is characterized by different aspects of the flow field such that some effects dominate and others are assumed to be negligible. Simplifying assumptions can reduce the complexity of the governing equations within each zone in order to make them more tractable to solution.

Figure 7.1 is a schematic diagram of the zones into which the analytical model has been divided. The induced discharge flow can be divided into a jet zone and a far field zone. The induced intake flow far away from the intake port is accounted for as a return

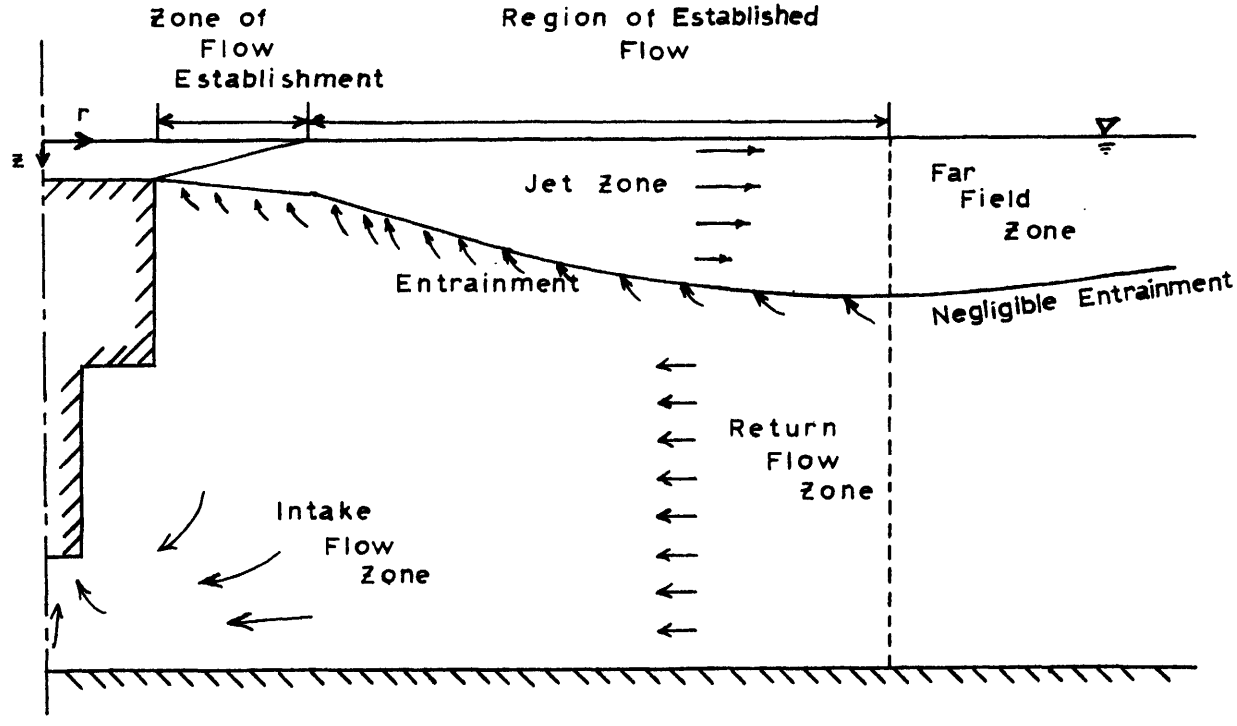

Figure 7.1 Schematic Diagram of the Induced External Flow Field.

flow. These zones are not generally well-defined, but, rather, merge continuously one into another. A fully analytical treatment of the entire induced flow field would require that all boundary conditions linking the different zones be made compatible.

The laboratory experiments indicate that for the design and operating parameter range describing typical OTEC conditions, the controlling mechanism for recirculation of discharged water to the intake is turbulent mixing in the jet zone coupled with return flow to the plant. Thus, for a single plant in a stagnant environment, the stratified flow in the far field apparently has no constraining effect (in the form of a potential thickening of the mixing layer) on the near field. The far field serves primarily as the sink for the discharged mass and heat and probably need not be considered in the analysis of near field recirculation.

The plant intake induces part of the return flow; the other part is caused by jet entrainment. In other words, a double sink flow exists close to the plant due to the intake and turbulent jet entrainment. A detailed accounting for the flow induced by the plant intake would, thus, require an analysis of coupled turbulent source and sink flows in a stratified environment. Analysis and experimental studies of non-turbulent single sink flows in a stratified regime have been carried out by Craya (1949) and Rouse (1956) in a stagnant ambient

field and more recently by Slotta and Charbeneau (1975) in an ambient current. These studies have not considered the presence of entraining turbulent density interfaces with regard to withdrawal, so, do not apply to the OTEC situation.

The thrust of the following analysis is toward a detailed treatment of the turbulent jet discharge which is coupled with a return flow in a confined layer. A thorough examination of the results and properties of these jet equations can reveal information regarding the near-field stability of the OTEC discharge and the potential for recirculation. The analysis does not include the far field zone due to its likely unimportance. By coupling the jet zone to the return flow, the most important effect that the intake has on the induced velocity and temperature fields has been implicitly included. No explicit consideration of the turbulent stratified sink phenomenon is made. The equations for radial jets with return flow are developed for both the surface jet, as represented in the experimental program, and for the interface jet, as typical for the prototype.

7.2 Model for Radial Buoyant Jet Mixing with Return Flow

The jet zone is that region which is dominated by turbulent mixing. In this model, the jet zone has been further subdivided into a zone of flow establishment and a zone of established flow.

7.2.1 Zone of Established Flow

The distinguishing characteristic of fully established jet flow is that the vertical distributions of velocity and temperature can be assumed to be self-similar. That is, the velocity, u, and temperature, ΔT, distributions for uniformly distributed radial flow can be characterized by equations of the form

$$u_r = u_c(r)f(z/h) \tag{7.1}$$

$$\Delta T = \Delta T_c(r)g(z/h) \tag{7.2}$$

The centerline velocity, u_r, and temperature difference, ΔT_c, from ambient are functions of the radial distance, r, only. The functions f and g must be fit from experimental data (Albertson, et. al., 1950; Abramovich, 1963) where h is the "depth" of the jet.

Appendix D presents a derivation of the radial jet equations with and without return flow for the model situation (surface jet). A solution for the prototype discharge at a distinct density interface is also presented in Appendix D. Utilizing the similarity assumption for velocity and temperature and ignoring dynamic pressure effects, the vertically integrated jet quantities in Appendix D can be re-written:

$$\int_0^h u_r dz = u_{r_c} hI_1 = Q \tag{7.3}$$

$$\int_0^h u_r^2 dz = u_{r_c}^2 hI_2 = M \tag{7.4}$$

$$\int_0^h u_r \Delta T dz = u_{r_c} \Delta T_c hIG = J \tag{7.5}$$

where u_r is the velocity relative to the lower layer. u_{r_c}, ΔT_c and h are functions of radial distance only. The integration constants are defined as:

$$I_1 = \int_0^1 f(\eta) d\eta \tag{7.6}$$

$$I_2 = \int_0^1 f^2(\eta) d\eta \tag{7.7}$$

$$IG = \int_0^1 f(\eta) g(\eta) d\eta \tag{7.8}$$

The vertically integrated differential equations for the conservation of mass and momentum, including the effect of return flow, for both the surface and thermocline discharge, D.14 and D. 15, become

Continuity

$$\left(1 - \frac{h}{H}\right) \frac{1}{r} \frac{drQ}{dr} + w\Big|_h = 0. \tag{7.9}$$

Momentum

$$\frac{1}{r}\frac{drM}{dr} - \frac{2}{rH}\frac{drQ^2}{dr} + \frac{1}{rH^2}\frac{drQ^2h}{dr} - \frac{Q^2}{H^2}\frac{dh}{dr} - \frac{Q}{H}\,w|_h = -\frac{1}{\rho}\frac{dP}{dr} \quad (7.10)$$

The pressure term is:

$$\frac{dP}{dr} = \int_o^h \frac{dp}{dr}\,dz \quad (7.11)$$

and is derived for the surface and interface jet situations, respectively, in Appendix D.

The surface and interface discharge jet equations differ in their treatment of the heat transport.

(i) Surface Jet

Substituting for the integral quantities, the surface discharge heat transport equations, (D.16), is:

$$\frac{1}{r}\frac{drJ}{dr} - \frac{1}{Hr}\frac{d}{dr}\left[\frac{rQ^2J}{M}\,\frac{I_2G_1}{IGI_1}\right] = 0 \quad (7.12)$$

where the integration constant

$$G_1 = \int_o^1 g(\eta)d\eta \quad (7.13)$$

The vertically integrated pressure derivative (ignoring the dynamic pressure term) in the momentum equation derived in Appendix E.1 is:

$$\frac{dP}{dr} = \frac{d}{dr}\left[\frac{HQ^3}{M^2}\,\frac{I_2^2 G_2}{I_1^3 IG}\right] \tag{7.14}$$

where

$$G_2 = \int_o^1 \int_\eta^1 g(\eta')d\eta' d\eta \tag{7.15}$$

ii) Interface Jet

For the prototype discharge jet at the density interface, the temperature along the centerline is constant. Under these conditions, the heat transport equation, (D.21), becomes:

$$\frac{\Delta T}{r}\,\frac{dru_r IG}{dr} - \frac{\Delta T}{Hr}\,\frac{dru_b IG}{dr} = 2(w|_{-h})\Delta T \tag{7.16}$$

This is exactly the same as the mass conservation equation provided $IG = 2I_1$. It can be shown that for any anti-symmetric temperature distribution, g(z/h), and any symmetric velocity distribution, f(z/h) (see Figure D.2) this condition holds:

$$IG = \int_{-1}^{1} f(\eta)g(\eta)d\eta = \int_{-1}^{o} f(\eta)(2-g(-\eta))d\eta + \int_o^1 f(\eta)g(\eta)d\eta$$

$$= 2\int_{-1}^{o} f(\eta)d\eta = 2\int_o^1 f(\eta)d\eta = 2I_1 \tag{7.17}$$

Therefore, since the temperature distribution is known, the heat transport equation is redundant.

The vertically integrated pressure derivative in the momentum equation for the interface jet is developed in Appendix D.2. This term is the same as for a surface jet:

$$\frac{dP}{dr} = \frac{d}{dr}\left[\frac{HQ^3}{M^2}\,\frac{I_2^2 G_2}{I_1^3 IG}\right] \tag{7.18}$$

In the surface and submerged discharge cases, the entrainment velocity, $-w|_h$, is modeled in the same manner. The rate of entrainment of water into the jet is assumed to be directly proportional to the jet centerline relative velocity.

$$-w|_h = \alpha u_{rc} \tag{7.19}$$

Ellison and Turner (1959) have shown that for a buoyant jet the entrainment coefficient, α, is a function of the local jet Richardson number, which is the inverse of the square of the local densimetric Froude number, $F_L^2 = u_{rc}^2/g\,\frac{\Delta\rho}{\rho}\,h$. A best fit curve for their experimental data is expressed by the following relationship (Stolzenbach and Harleman, 1971):

$$-w|_h = \alpha \exp(-5/F_L^2)\; u_{rc} \tag{7.20}$$

7.2.2 Zone of Flow Establishment

Equations (7.9), (7.10), (7.12), and (7.20) are the set that describe the surface discharge jet with return flow found in the model situation. Equations (7.9), (7.10), (7.18) and (7.20) form the set which describe the submerged jet discharged at a distinct density interface as found in the schematic prototype.

In both cases, boundary conditions are necessary in order to solve the systems of equations. The region between the discharge opening and the beginning of self-similarity (fully established flow) is the zone of flow establishment. The end of this zone provides the boundary conditions necessary to determine the solution.

The zone of flow establishment is dominated by the discharge momentum and buoyancy can be neglected for the discharge conditions under consideration. It has been found empirically (Albertson, et. al., 1950) that for uniform discharge velocity, the length of the flow establishment region, L_{fe}, is given by

$$L_{fe} = 10.4 h_o \tag{7.21}$$

The jet depth, h_{fe}, at the beginning of established flow is determined from momentum conservation:

$$h_{fe} = \frac{h_o r_o}{I_2 (r_o + L_{fe})} \tag{7.22}$$

Discharge Parameters

Discharge Velocity u_o

Slot Height h_o

Temperature Difference ΔT_o

Plant Radius r_o

Thermocline Depth H

Integral Coefficients (profile dependent)

I_1, I_2, IG, G_1, G_2

Entrainment Coefficient (profile dependent)

α

Table 7.1

INPUT INFORMATION TO ANALYTICAL MODEL FOR RADIAL JET

	Polynomial Profile (Abramovich, 1963)	Gaussian Profile
$f(\eta)$	$(1-\eta^{3/2})^2$	$e^{-\eta^2}$
$g(\eta)$	$(1-\eta^{3/2})$	$e^{-\eta^2}$
I_1	0.45	$\sqrt{\frac{\pi}{2}}$
I_2	0.316	$\sqrt{(\pi/8)}$
IG	0.368	$\sqrt{(\pi/8)}$
G_1	0.6	$\sqrt{\frac{\pi}{2}}$
G_2	0.2143	0.5
α^*	0.0495	0.0682

$\alpha^* = \frac{I_1}{2} \frac{db}{dr}$; where $\frac{db}{dr}$ is derived from experiments,

from Abramovich, 1963, $\frac{db}{dr} = 0.22$ (fit for polynomial profile)

from Albertson, et. al., 1950, $\frac{db}{dr} = 0.154$ (fit for Gaussian profile)

Table 7.2

FUNCTIONS AND COEFFICIENTS FOR ABRAMOVICH AND GAUSSIAN PROFILES

where h_o is the plant slot height and r_o is the plant radius. The centerline temperature at the boundary between the two jet zones is equal to the initial value, ΔT_o.

7.3 Solution Method

The set of vertically integrated ordinary differential equations describing steady uniformly distributed radial jet flow at both the surface and density interface have been solved using a fourth-order Runge-Kutta routine on a digital computer.

The length and depth of the zone of flow establishment are computed to provide the boundary conditions for the fully-established flow region. The centerline velocity and temperatures are predicted as is the depth to half of the temperature difference between the centerline and ambient water. The local jet Froude number and dilution are calculated. For the cases including backflow, the return velocity and depth to zero velocity are provided.

The information necessary to solve the equations is listed in Table 7.1. The discharge parameters are determined by the situation being simulated. The integral coefficients and entrainment coefficient are dependent upon the choice of velocity and temperature profiles. Table 7.2 gives the appropriate values for these coefficients for polynomial (Abramovich, 1963) and Gaussian profiles.

The analysis of the fully established flow region extends from the zone of flow establishment to the radius at which the local

jet densimetric Froude number declines to unity. At this point, the jet zone is arbitrarily terminated and the far field is assumed to begin. In fact, the transition from jet flow to buoyancy driven flow is continuous with the importance of turbulent entrainment decreasing while interfacial friction is increasing. The model sometimes predicts unrealistic oscillatory behavior for the jet thickness as the Froude number approaches unity, indicating the existence of critical stratified flow conditions. However, the actual occurrence of critical conditions would be determined by the behavior of the stratified far field flow (with interfacial friction) which is not treated in the present analysis.

7.4 Model Results

The analysis of the model and the examination of its sensitivity to the discharge parameters; $\mathbb{F}_{r_o}$, r_o/h_o and H/h_o, and the model coefficient, α, has been conducted for the surface jet employing the polynomial distribution for vertical velocity and temperature profiles. This profile was chosen for the cosmetic advantage that a specific depth for zero relative velocity and temperature difference is predicted. The profiles and coefficients are those listed in Table 7.2.

The surface and density interface jets exhibit the same general behavior. Initially, the jet expands linearly since buoyancy does not have much effect on damping turbulent entrainment. As buoyancy becomes more important (i.e., the local jet Froude number,

$F_L \rightarrow 1.0$), the thickness increases more slowly until the jet merges into the far field ($F_L = 1.0$). The computer code continues to calculate jet properties until $F_L = 1.0$, signifying a stable region where entrainment ceases. The surface jet centerline temperature initially declines very rapidly with distance and then levels off when the stable jet region is reached. The density interface jet temperature at the centerline is constant since it entrains water of different temperatures equally from both sides of the jet.

7.4.1 Surface Jet (Laboratory Model) Predictions

7.4.1.1 Discharge Parameter Sensitivity

A set of baseline discharge parameters in the practical range was determined for the purpose of model comparison: $F_{r_o} = 20$, $r_o/h_o = 20$, $H/h_o = 50$.

Figures 7.2a and b show the sensitivity of normalized centerline temperature, $\Delta T_c/\Delta T_o$, and normalized half-temperature depth, $h_{.5T}/h_o$, as a function of normalized distance, r/h_o, to the discharge Froude number. Figure 7.2a illustrates that for increasing F_{r_o} the centerline temperature decreases at any radial distance. For higher F_{r_o}, the centerline temperature sensitivity decreases close to the plant because jet entrainment is not damped by buoyancy so that the maximum amount of mixing takes place. Figure 7.2b shows that for increasing F_{r_o} the depth of the jet increases at any radial distance. This reaction is limited by the fact that if the edge of the jet

extends to the limit of the confining layer, the similarity assumption is no longer valid and the model is not applicable. The formulation implies that recirculation occurs.

Figures 7.3a and 7.3b show the sensitivity of the jet to changes in the relative size of the plant, r_o/h_o. As r_o/h_o gets larger, the flow field undergoes relatively less radial expansion. Theoretically, in the case $r_o/h_o \rightarrow \infty$, the discharge flow becomes a two dimensional plane jet. For larger r_o/h_o, there is less of a decline in the centerline temperature and less sensitivity to a change in r_o/h_o. The depth of the jet is greater for increasing r_o/h_o, since the radial expansion of the diverging flow has proportionately less effect.

Figures 7.4a and 7.4b illustrate the effect that different layer depths have on the same discharge configuration. For small H/h_o, the jet thickens until it extends over the entire layer depth. For H/h_o large enough to allow buoyancy to damp turbulent entrainment and limit the growth of the jet thickness, the predicted centerline temperature and jet thickness are not very sensitive to changes in H/h_o.

7.4.1.2 Model Coefficient Sensitivity

The model employs essentially one empirically derived coefficient once the velocity and temperature profiles are chosen. The entrainment coefficient, α, has been derived from a best fit to experimental data (Abramovich, 1963, and Ellison and Turner, 1959). Figures 7.5a and 7.5b indicate the effect that a small change in α exerts on

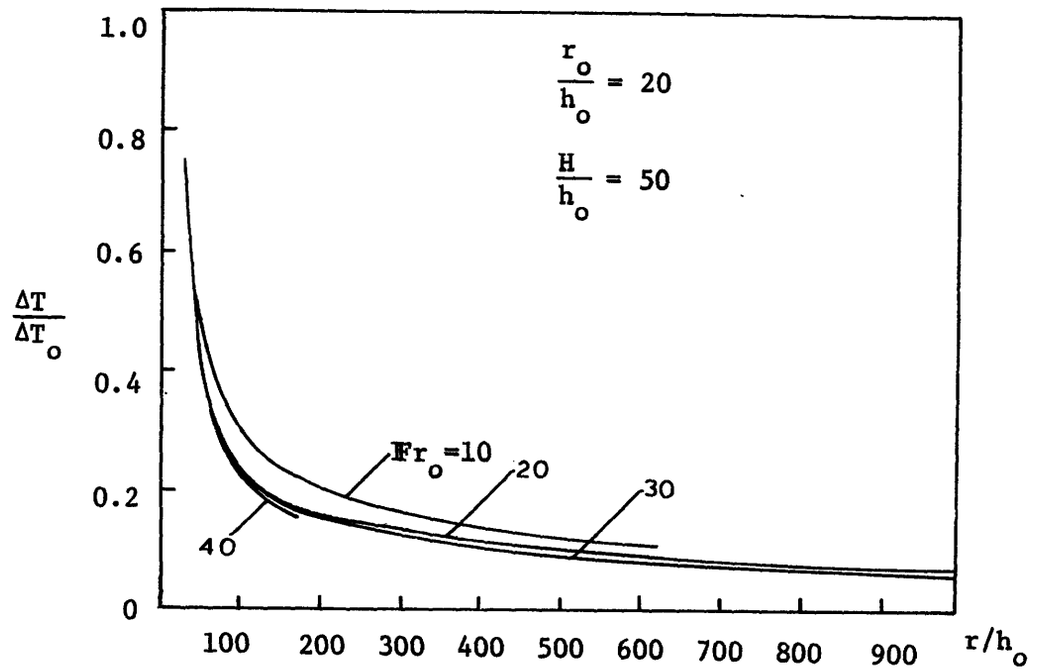

Figure 7.2a Temperature vs. Distance, Varying Fr_o

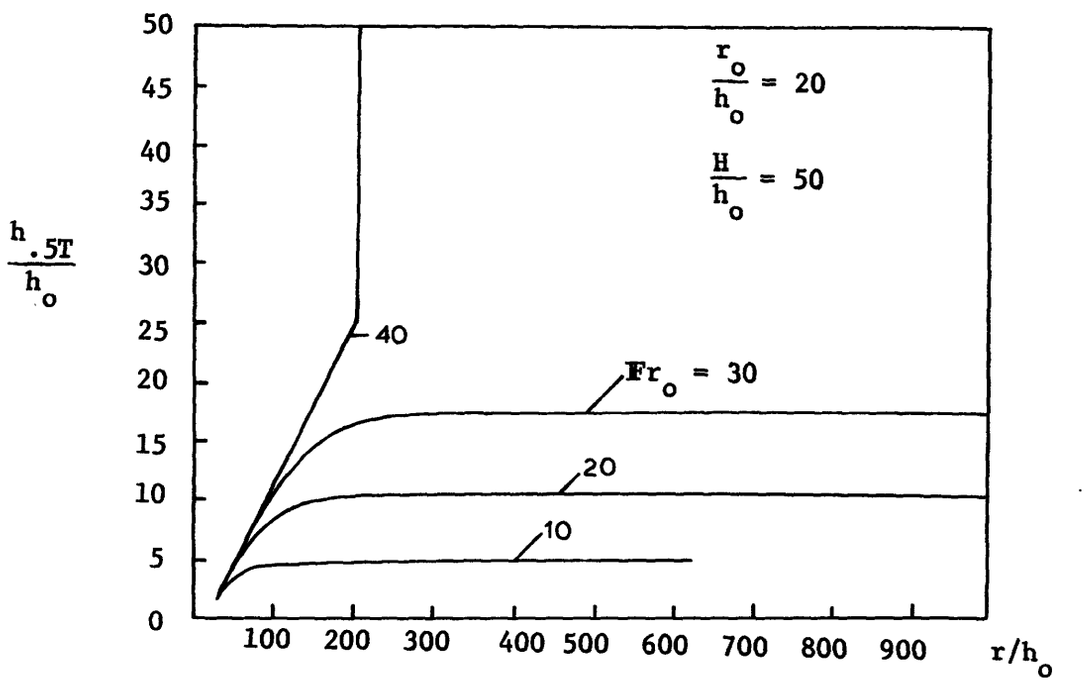

Figure 7.2b Half-Temperature Depth vs. Distance, Varying Fr_o

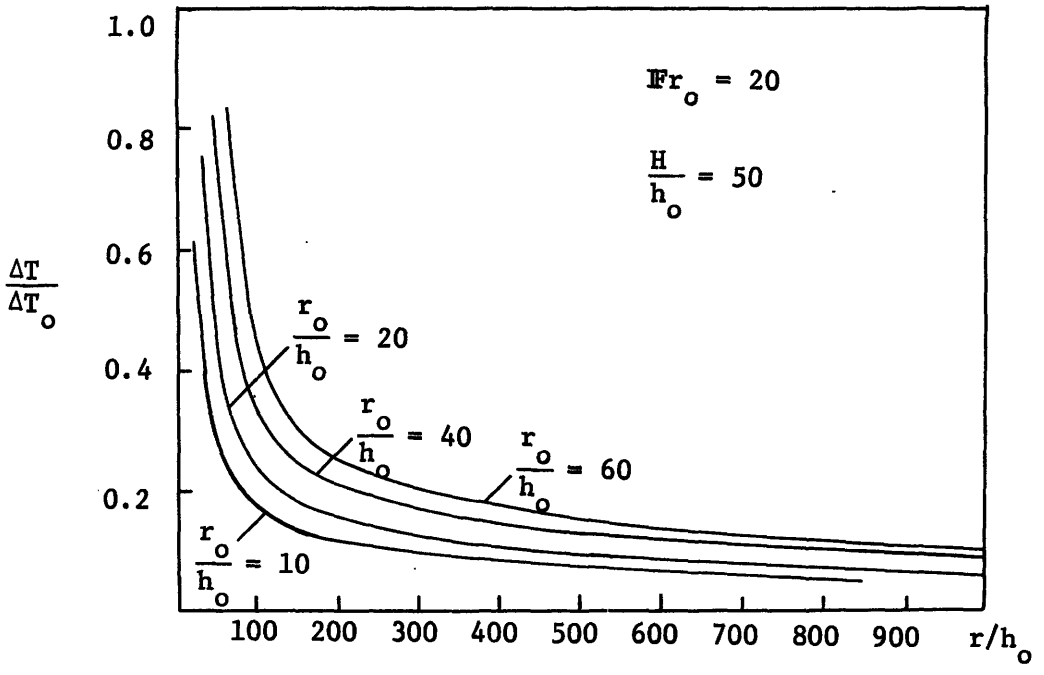

Figure 7.3a Temperature vs. Distance, Varying r_o/h_o

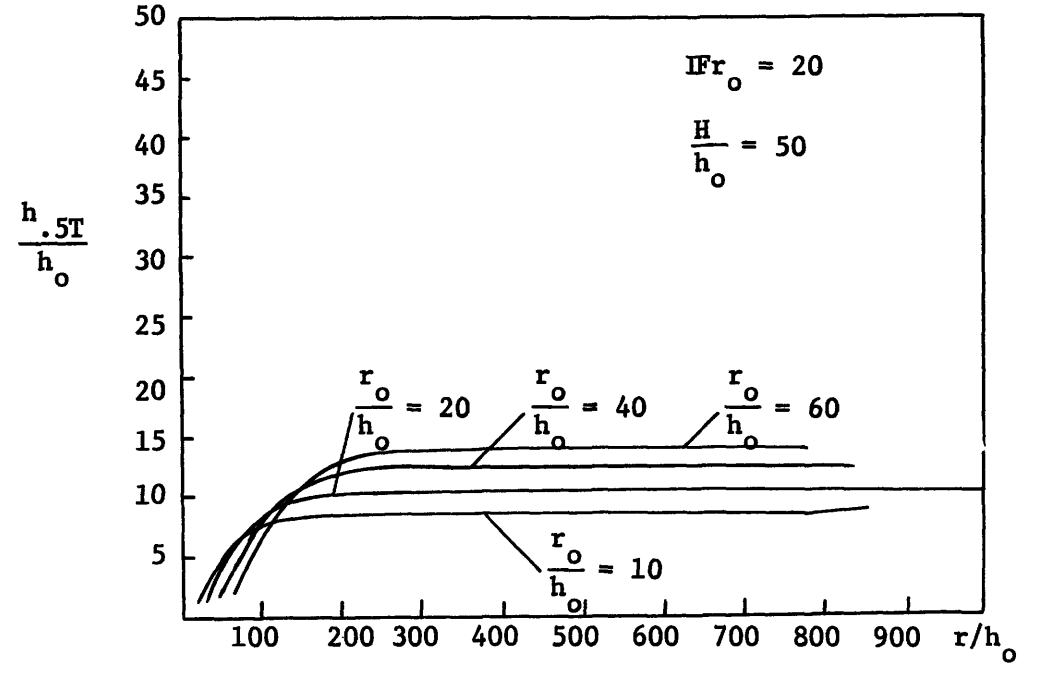

Figure 7.3b Half-Temperature Depth vs. Distance, Varying r_o/h_o

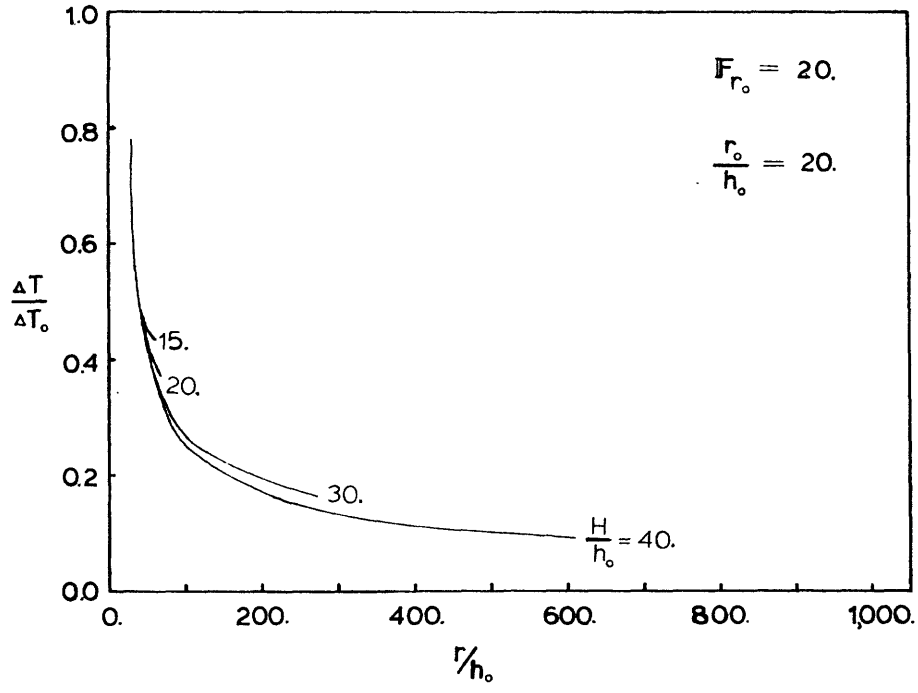

Figure 7.4a Temperature vs. Distance, Varying H/h_o .

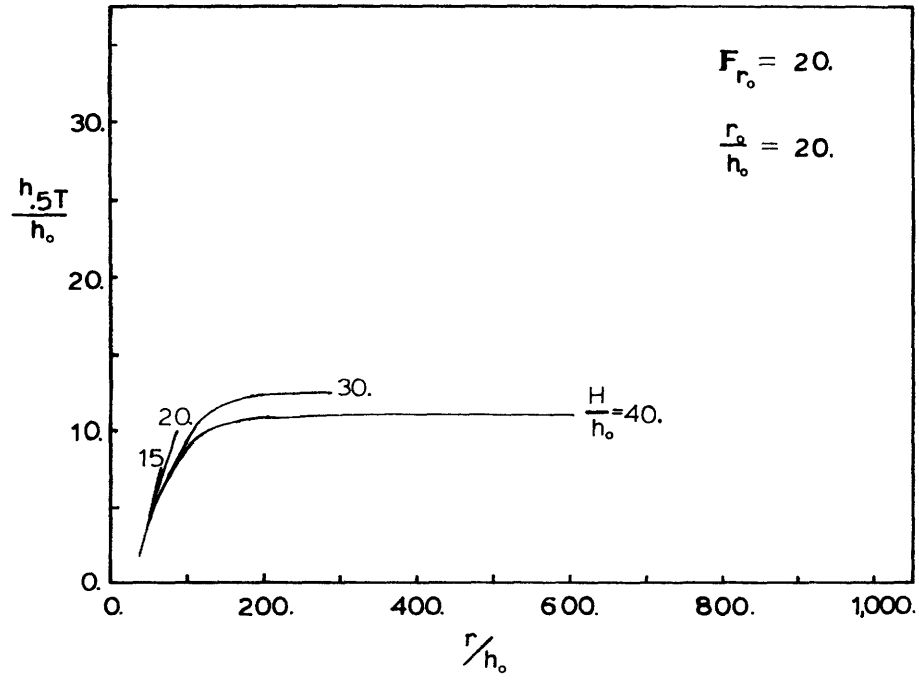

Figure 7.4b Half Temperature Depth vs. Distance, Varying H/h_o .

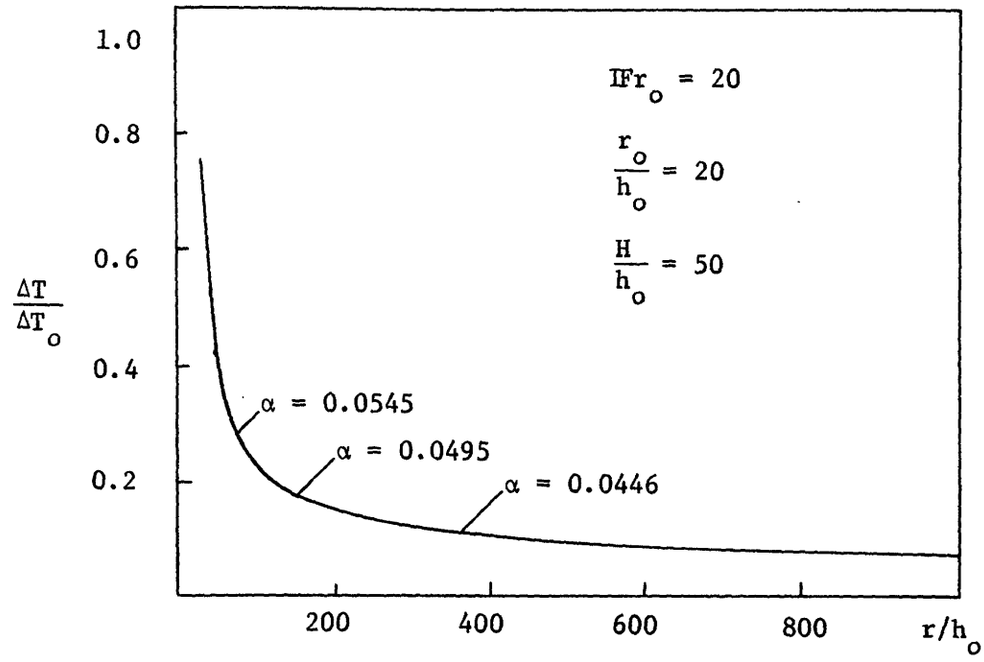

Figure 7.5a Temperature vs. Distance, Varying α

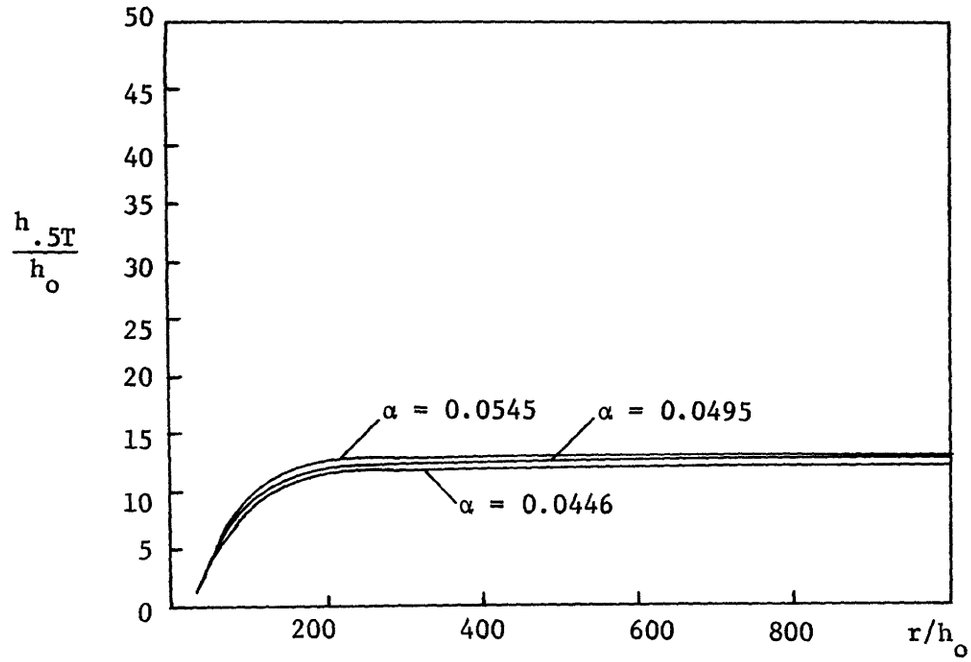

Figure 7.5b Half-Temperature Depth vs. Distance, Varying α

the centerline temperature and jet thickness. The model is not overly sensitive to changes in α.

7.4.2 Interface Jet (Prototype)

The centerline temperature of the radial jet discharged at a distinct density interface does not change since it entrains equally from both sides. The jet thickness responds similarly as a function of radial distance for the same $\mathbb{F}_{r_o}$ as the surface jet except that buoyant damping of turbulence is much more pronounced. For this reason, the interface jets with the same $\mathbb{F}_{r_o}$ as the surface jets expand to a lesser thickness. Fig. 7.6 gives predictions of the jet half depth as a function of $\mathbb{F}_{r_o}$, Fig. 7.7 as a function of r_o/h_o and Fig. 7.8 as a function of H/h_o. In general, the same trends are observed as in the corresponding surface jet plots, however, with lesser penetration depth.

The information of Fig. 7.2b and 7.6 is further summarized by plotting in Fig. 7.9 the maximum predicted (asymptotic) jet depth, h_{max}, (where $h = 1.6 \times h_{.5T}$ for the "Abramovich" distribution) as a function of $\mathbb{F}_{r_o}$, again for the specific case r_o/h_o and $H/h_o = 50$.

The interface jet prediction for maximum jet thickness is less than that for a surface jet of equivalent $\mathbb{F}_{r_o}$. For this combination of parameters, the model predicts the surface jet will expand to half of the available layer thickness at $\mathbb{F}_{r_o} = 25$, whereas the interface jet will not achieve the same condition until $\mathbb{F}_{r_o} = 50$. This graph indicates that predictions for the prototype flow field based on

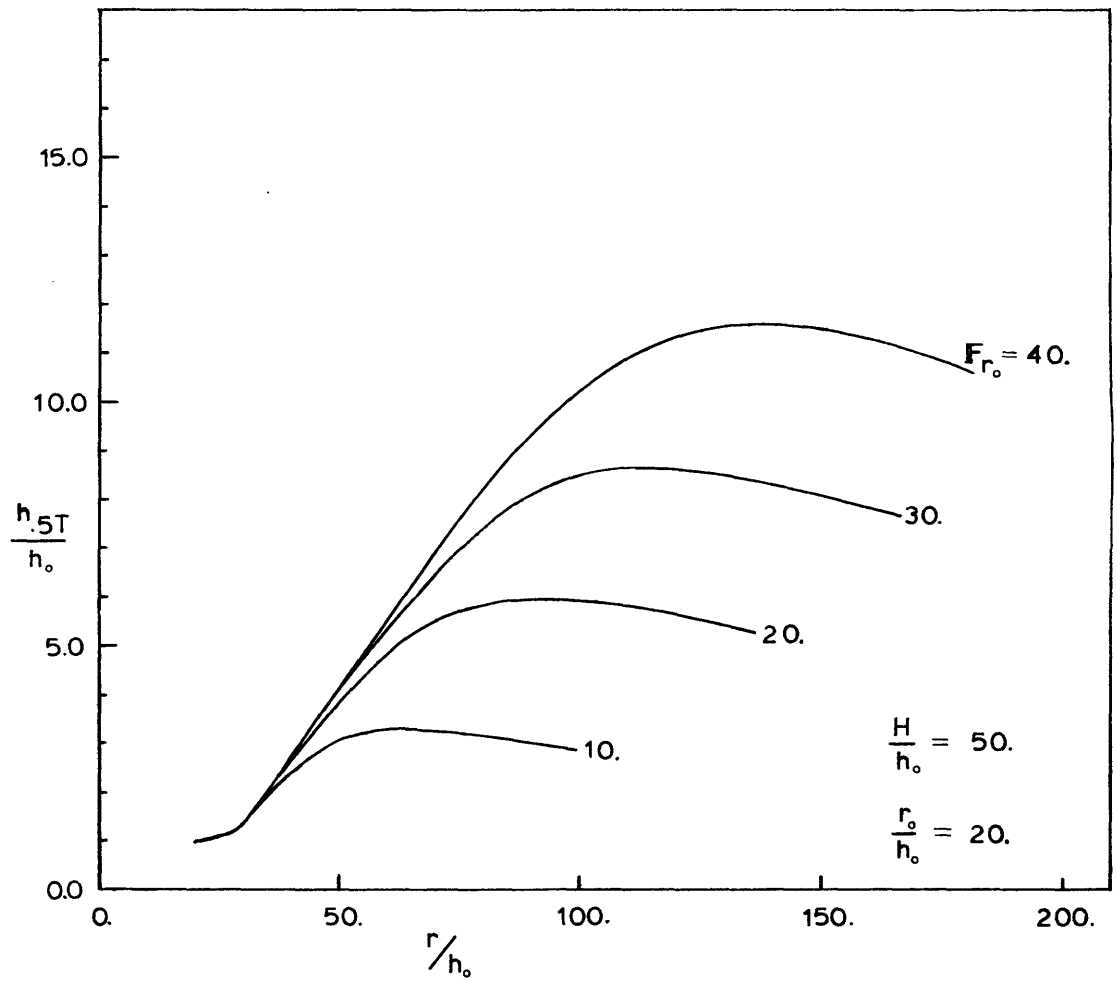

Figure 7.6 Half Temperature Depth vs. Distance, Varying F_{ro}; Radial Interface Jet.

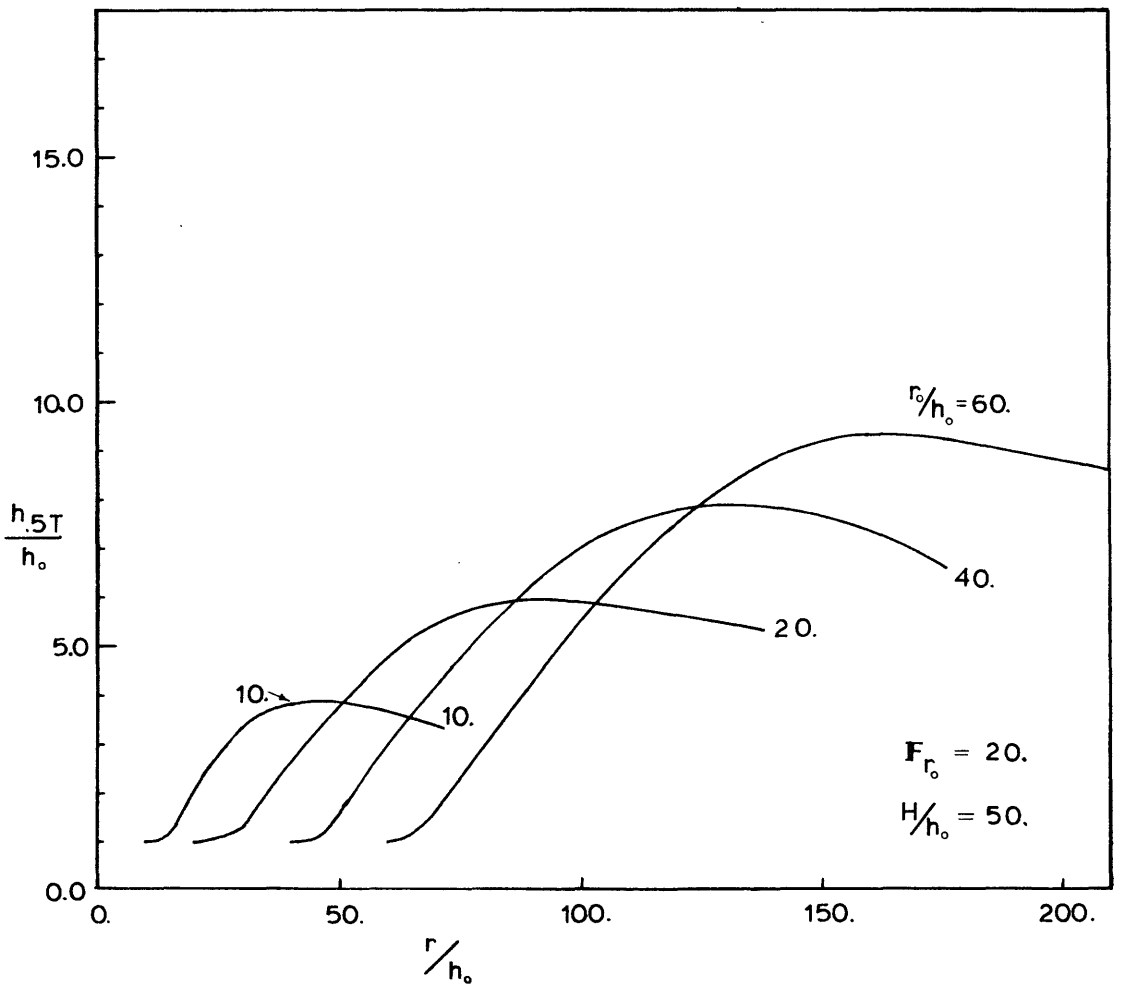

Figure 7.7 Half Temperature Depth vs Distance, Varying r_o/h_o; Radial Interface Jet

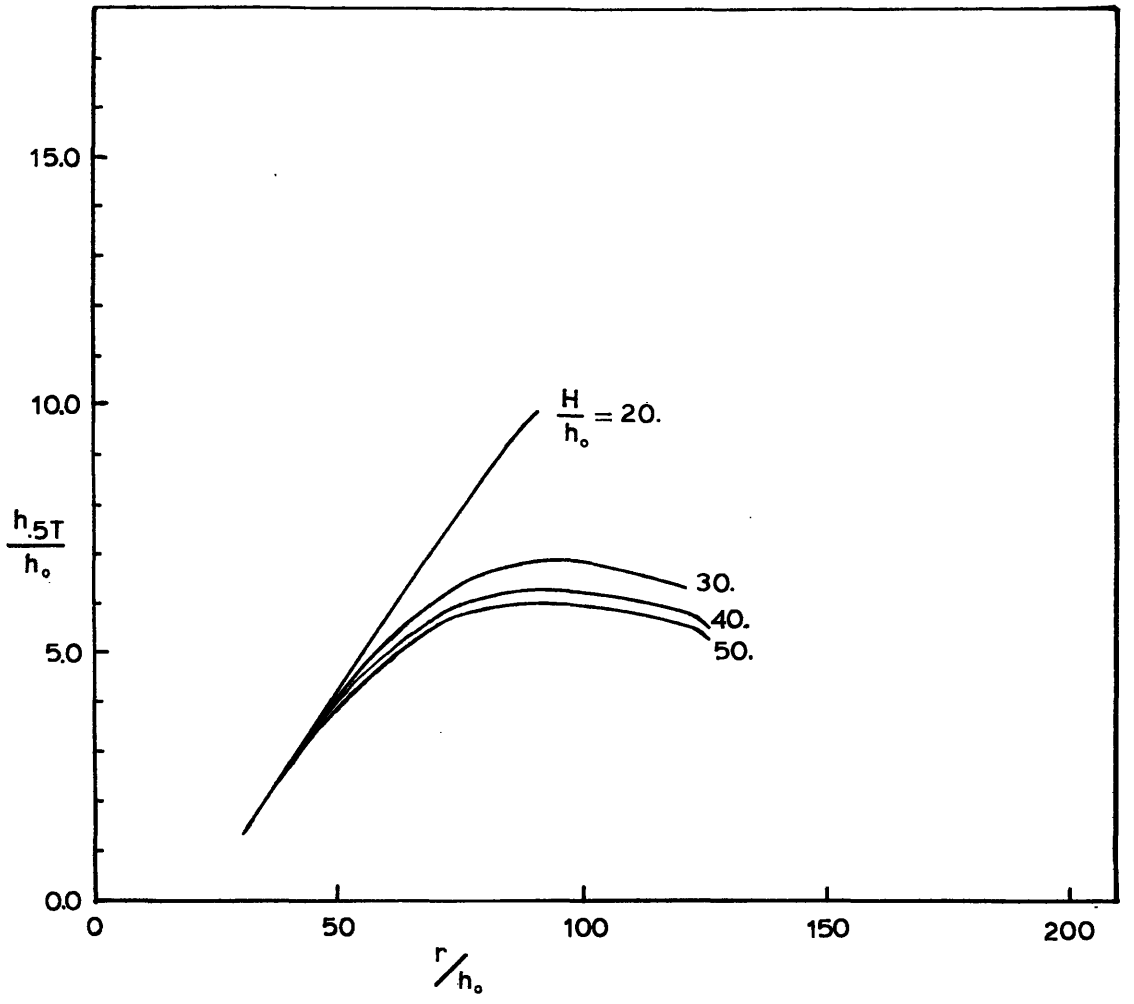

Figure 7.8 Half Temperature Depth vs. Distance, Varying H/h_o ; Radial Interface Jet.

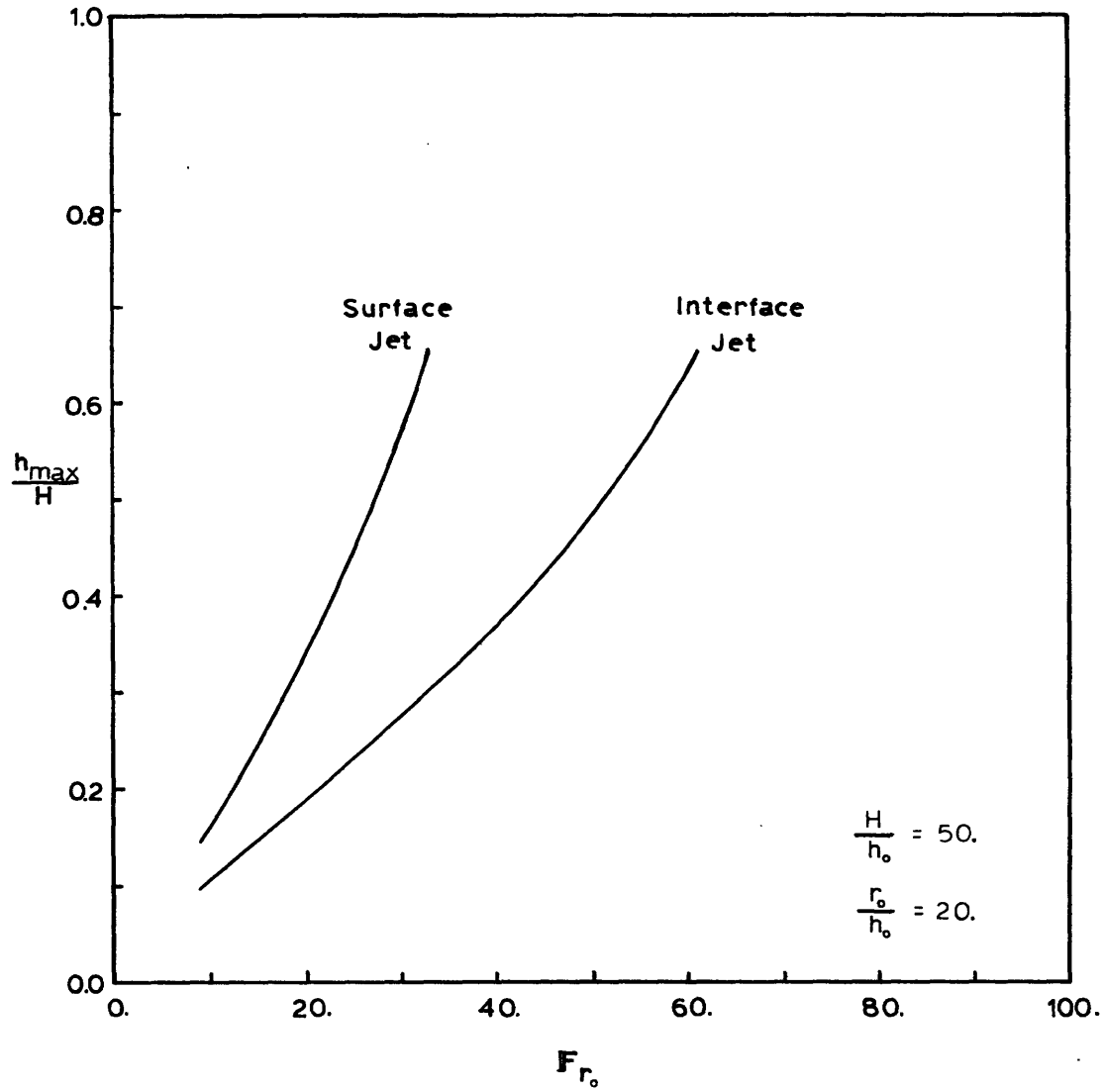

Figure 7.9 Normalized Maximum Jet Thickness vs. Discharge Densimetric Froude Number for Surface Jet and Interface Jet

a surface jet model will be conservative with regard to recirculation of discharged water to the plant intake. At the same time, it must be kept in mind that the model predictions (for both surface and interface) jet will become invalid as the jet thickness approaches the available layer depth $(h_{max})/H \rightarrow 1)$. Under these conditions, dynamic pressure forces will arise which cause flow reversal and which are not included in the present model formulation. This condition can only be evaluated by comparison with experimental observations, as is done in the following.

7.5 Comparison of Analytical and Experimental Results

Figure 7.10 through 7.14 show the predictions and the values found in experiments 1-5, 26, 30, 31 and 33 (conditions of low IF_{r_o}) for the centerline temperature and the depth to half of the centerline temperature difference. The experimental points are from vertical temperature profiles constructed from temperature measurements. For the polynomial distributions, the half temperature depth, $h_{.5T}$, is proportional to the total jet depth, h:

$$h_{.5T} = 0.63h$$

The predictions for experiments 6 and 8 (conditions of high IF_{r_o} and high discharge) are also presented in this section although, as stated in Chapter IV, there are some physical observations indicating that recirculation may have occurred. If recirculation has occurred,

the model formulation of the flow problem becomes invalid, as discussed earlier.

7.5.1 Low Froude Number Experiments (without Recirculation)

The centerline temperature plots (Figures 7.10 to 7.14, "a" series) show that the agreement between the predicted and observed values is very good. This is consistent with the results of the sensitivity study performed in Section 7.4. The analytical model predicts that the centerline temperature is rather insensitive to changes in the discharge conditions. Therefore, slight irregularities in the circumferential distribution of the discharged flow in the plexiglas model are expected to have only a minor effect on the radially averaged centerline temperature.

The agreement between the theoretical predictions and measured values for the half temperature depth, $h_{.5T}$, are satisfactory, as seen in Figures 7.10 to 7.14, "b" series. The sensitivity analysis performed in Section 7.4 for the jet depth shows that it changes almost linearly with a change in the discharge parameters, provided the jet is confined by the layer. Therefore, if the flow is not uniformly distributed, there will be an angular variation in the depth of the jet. A large variation could bias the radially averaged value since the experimental data is taken at discrete points in the external field. A detailed comparison of the vertical temperature structure of the radial jet as predicted by the model and observed in the experiment is given in Fig.

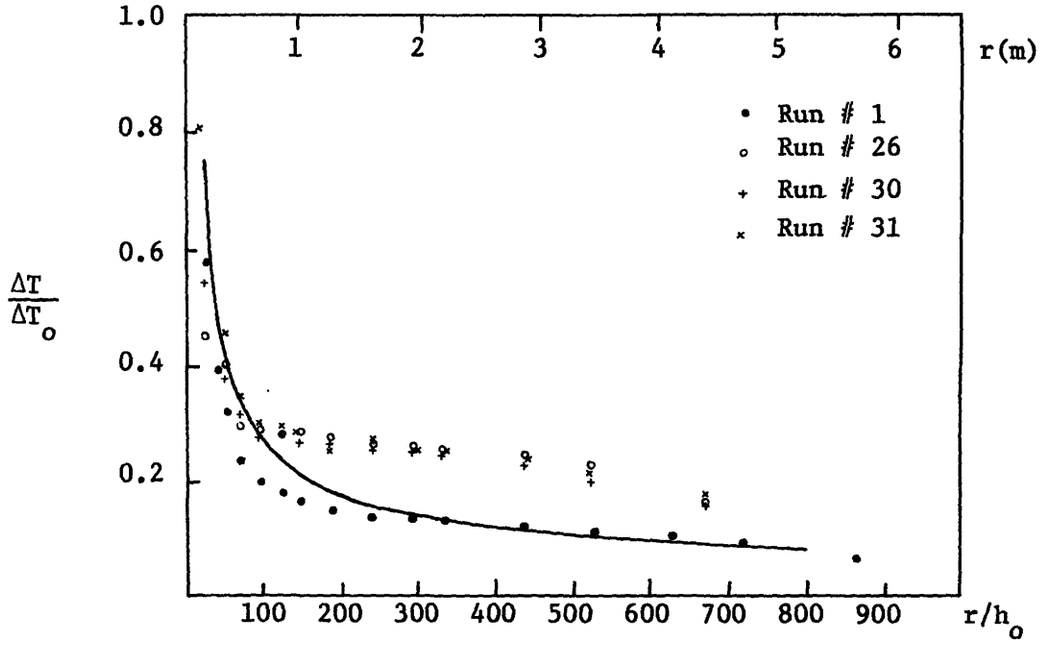

Figure 7.10a Temperature vs. Distance, Experimental Comparison to Model

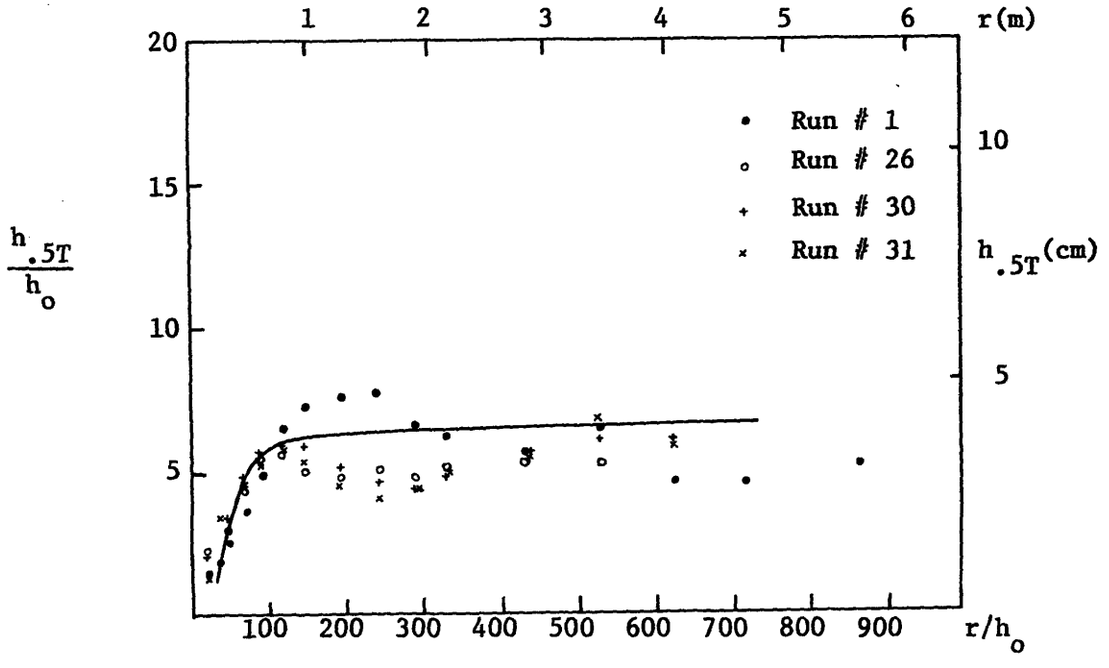

Figure 7.10b Half-Temperature Depth vs. Distance, Experimental Comparison to Model

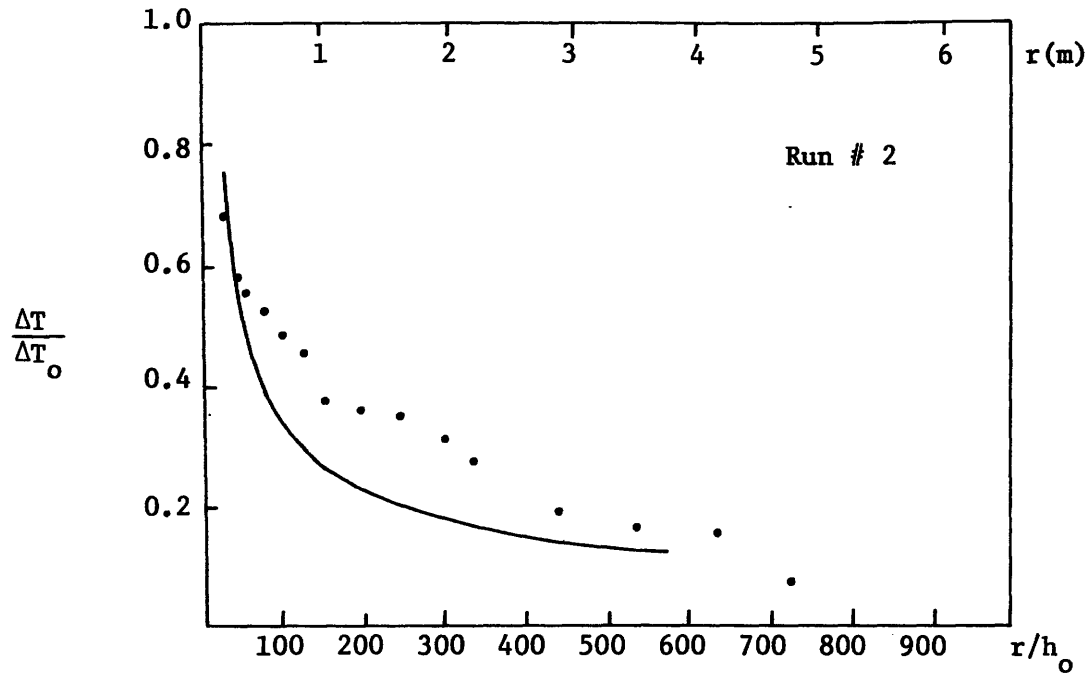

Figure 7.11a Temperature vs. Distance, Experimental Comparison to Model

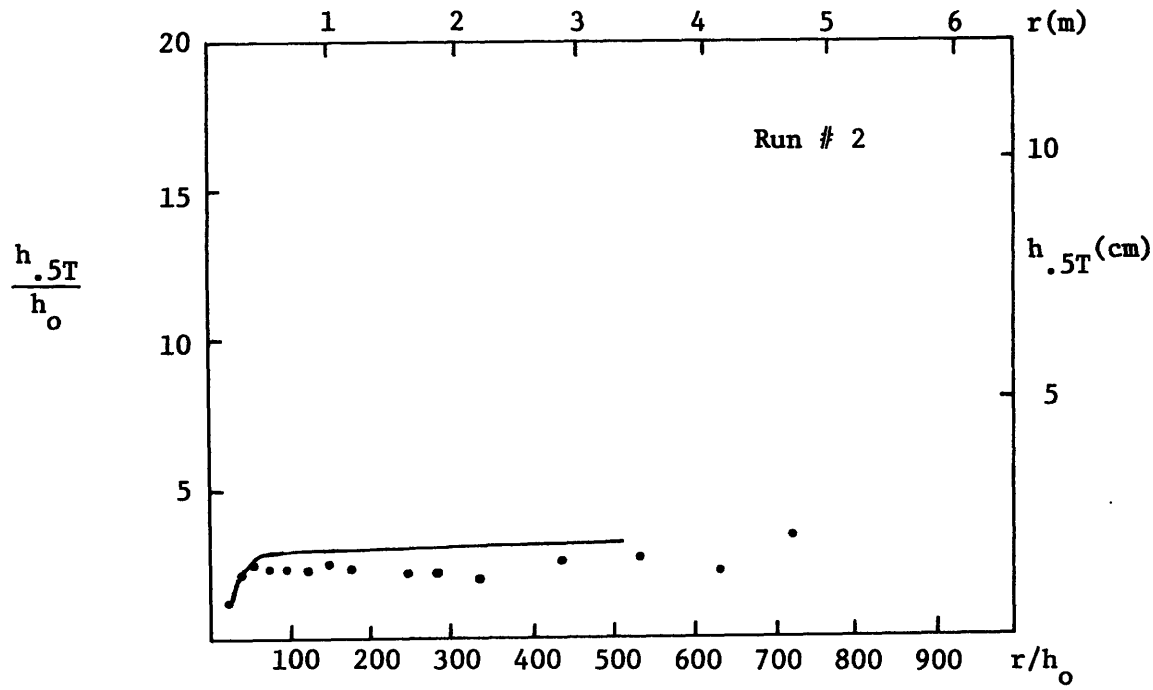

Figure 7.11b Half-Temperature Depth vs. Distance, Experimental Comparison to Model

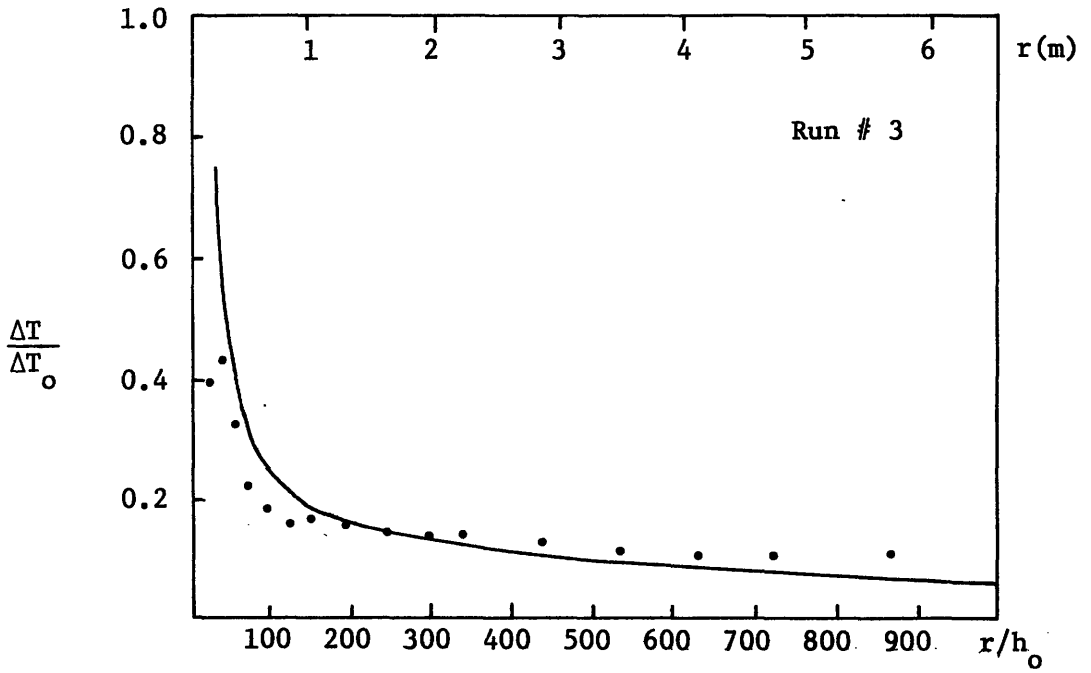

Figure 7.12a Temperature vs. Distance, Experimental Comparison to Model

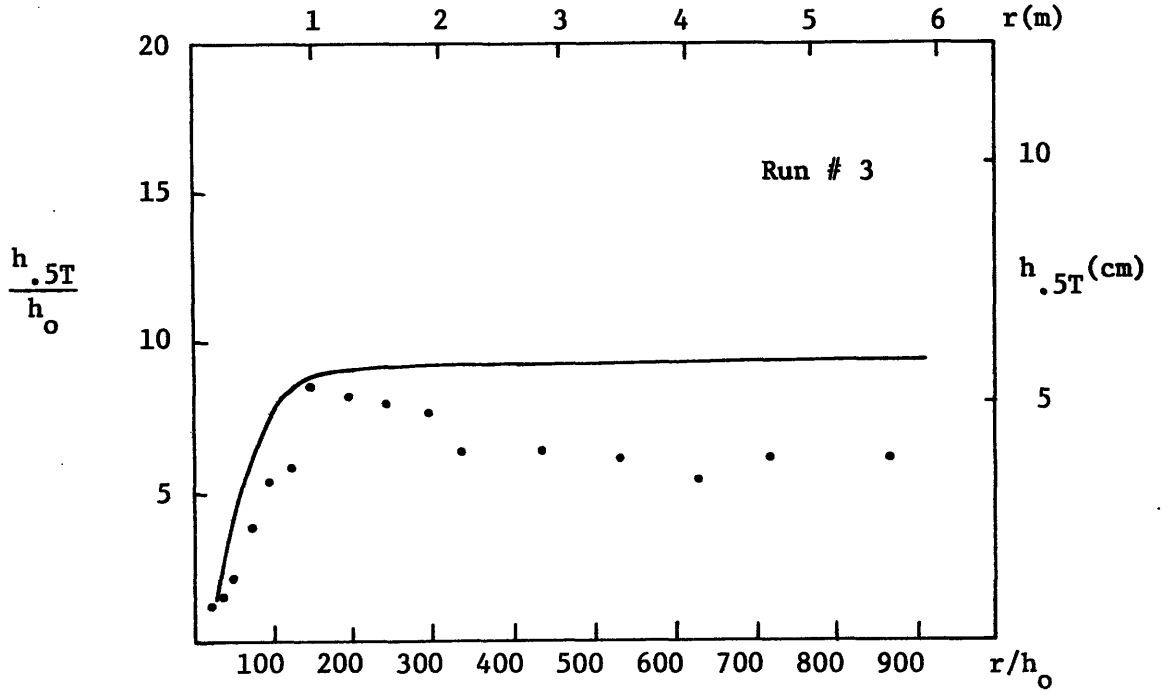

Figure 7.12b Half-Temperature Depth vs. Distance, Experimental Comparison to Model

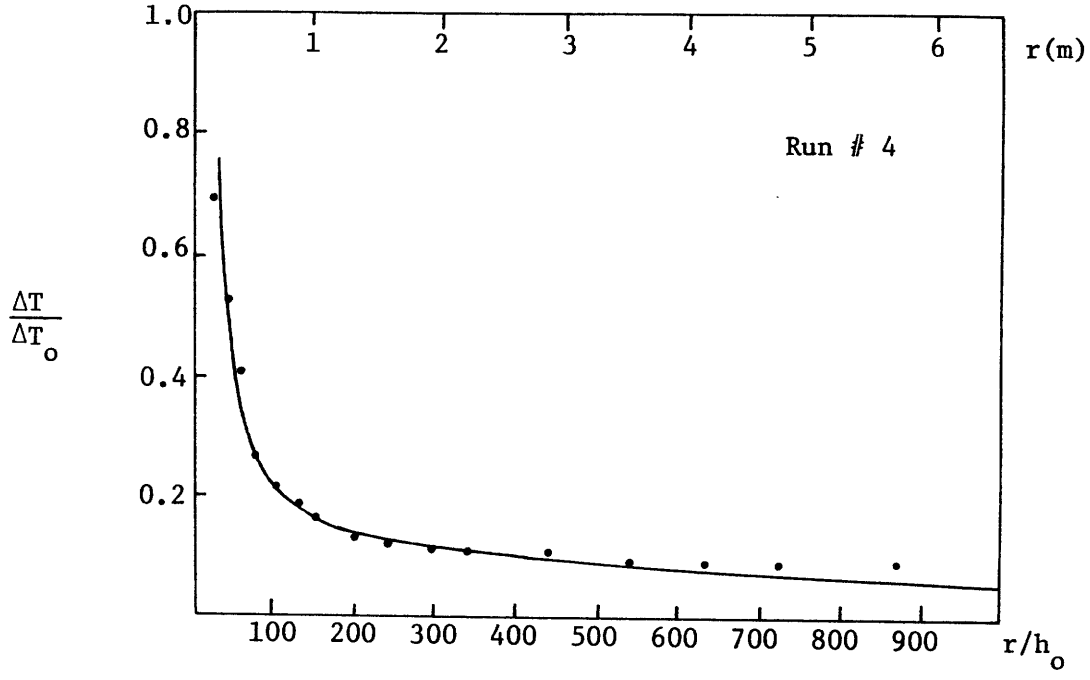

Figure 7.13a Temperature vs. Distance, Experimental Comparison to Model

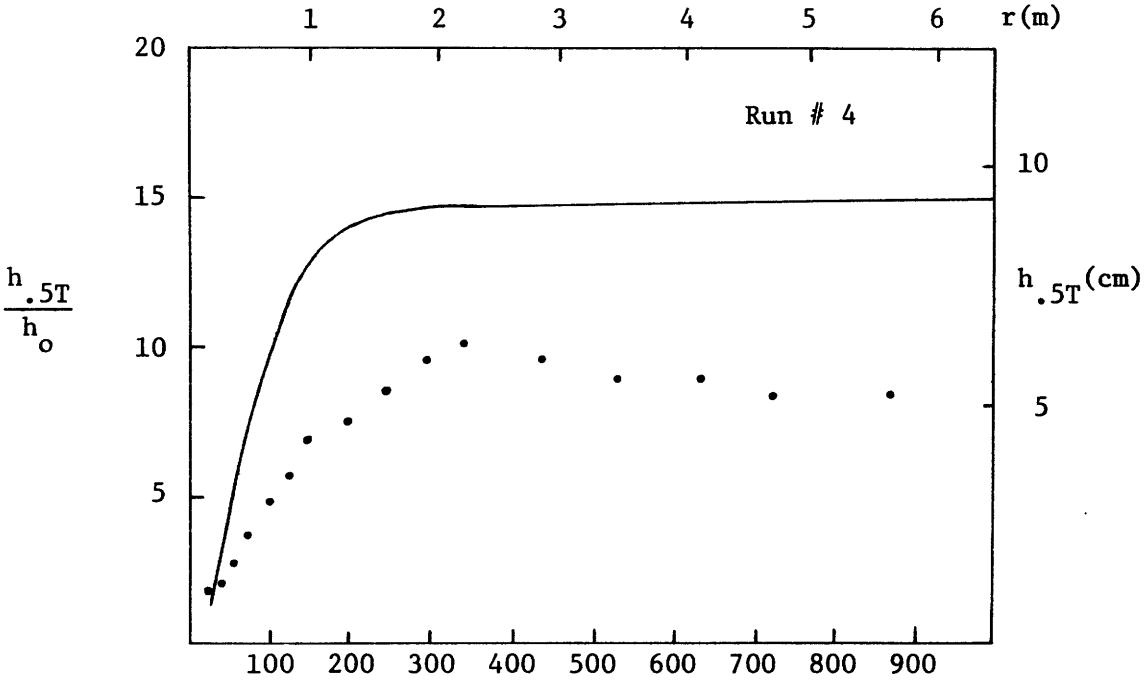

Figure 7.13b Half-Temperature Depth vs. Distance, Experimental Comparison to Model

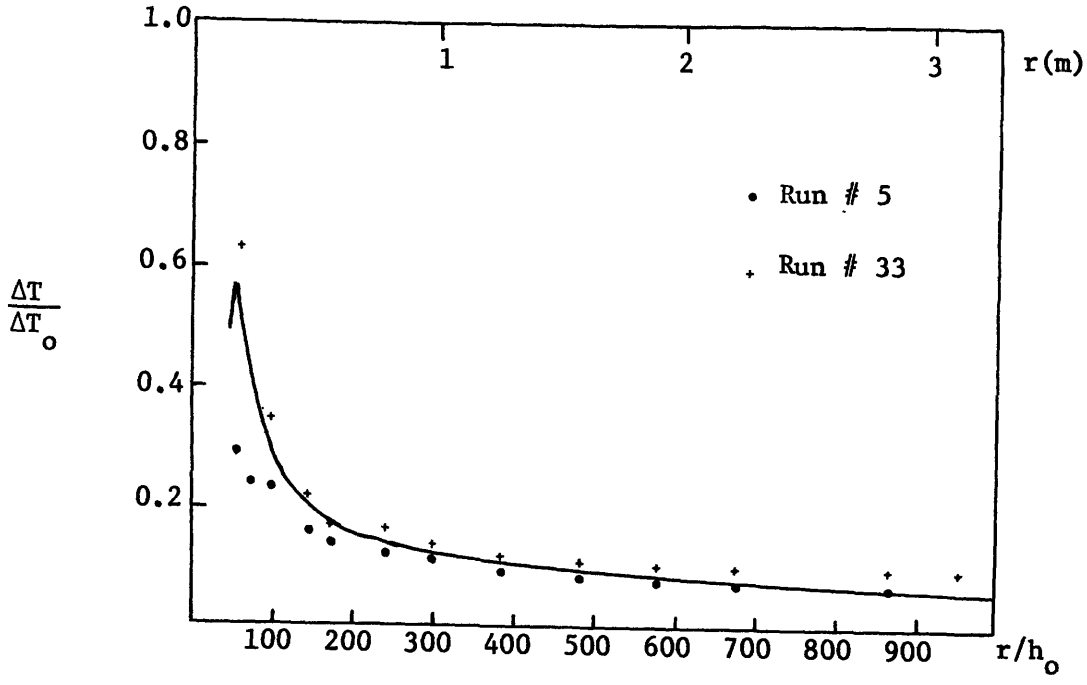

Figure 7.14a Temperature vs. Distance, Experimental Comparison to Model

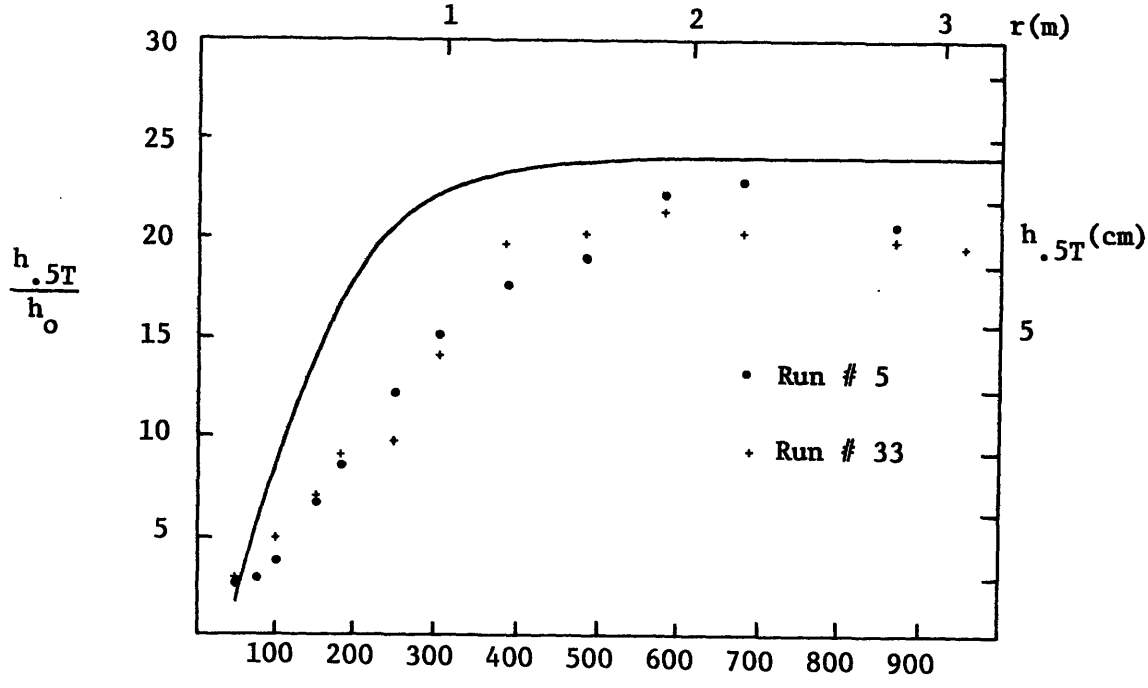

Figure 7.14b Half-Temperature Depth vs. Distance, Experimental Comparison to Model

7.15 for Exp.#33 . The angular variability in the experiment is also indicated.

The error in interpreting the experimental data is 1 to 2 discharge slot heights, h_o, because scans were taken at discrete levels. The fit of a temperature profile to the data is usually imperfect; in which case there is a variance in the estimate of $h_{.5T}$. Furthermore, as the radial distance from the model approaches the length scale of the basin, there is not likely to be any time period within which a steady state approximation is valid, so the data will be biased. Bearing these considerations in mind, the agreement between the analytical model and the experiments on $h_{.5T}$ is good; particularly, closer to the discharge where the major mixing occurs.

In addition to the individual comparison of results for each experiment, other methods for establishing the goodness of fit between the analytical model and physical data were developed. Figure 7.16a is a graph of the centerline temperature (0.5 cm depth) at a fixed radial distance of $\frac{r}{h_o}$ = 148.0 against discharge densimetric Froude number, F_{r_o}, for all the experiments with a layer depth of H/h_o = 53.5 and a plant geometric ratio of r_o/h_o = 18.0. The solid line represents the predictions based on the analytical model and the points are the experimental values. Figure 7.16b is the corresponding graph for the half temperature depth. For both temperature and depth, the agreement is good. The model does not exhibit any trend for either

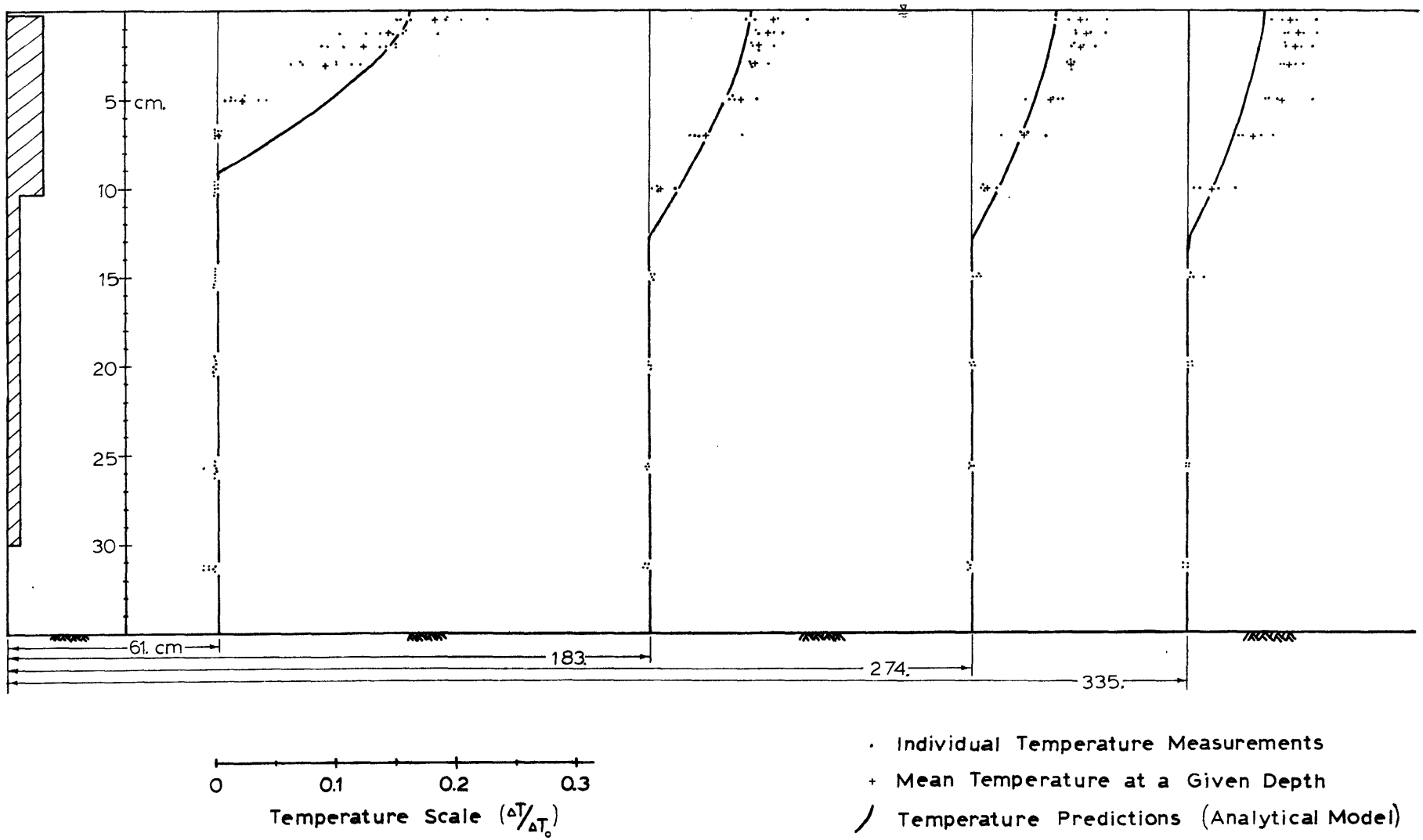

Figure 7.15 Temperature Profile Comparison Between Analytical Model and Data (Experiment #33; Stagnant, Radial Jet Discharge).

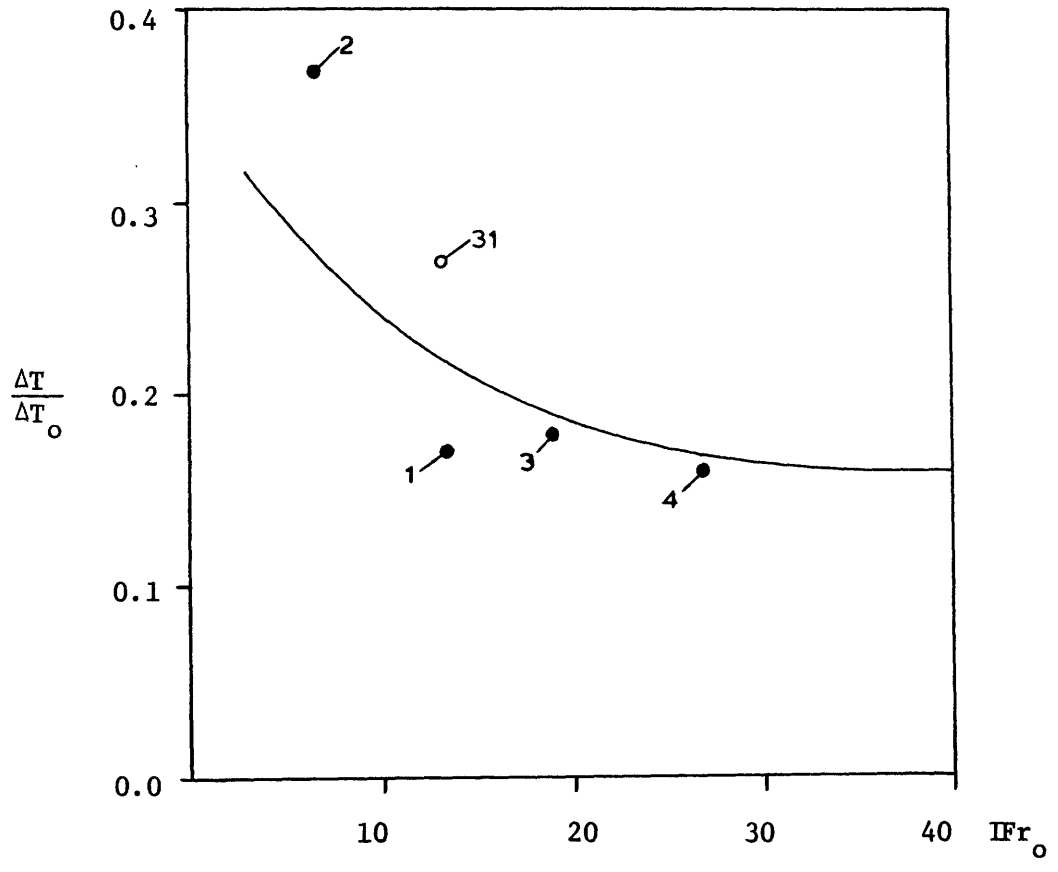

$\frac{r_o}{h_o} = 18.0$ $\frac{r}{h_o} = 148$

$\frac{H}{h_o} = 53.5$

Figure 7.16a Normalized Temperature Difference vs. Discharge Densimetric Froude Number at a Radial Distance $\frac{r}{h_o} = 148$

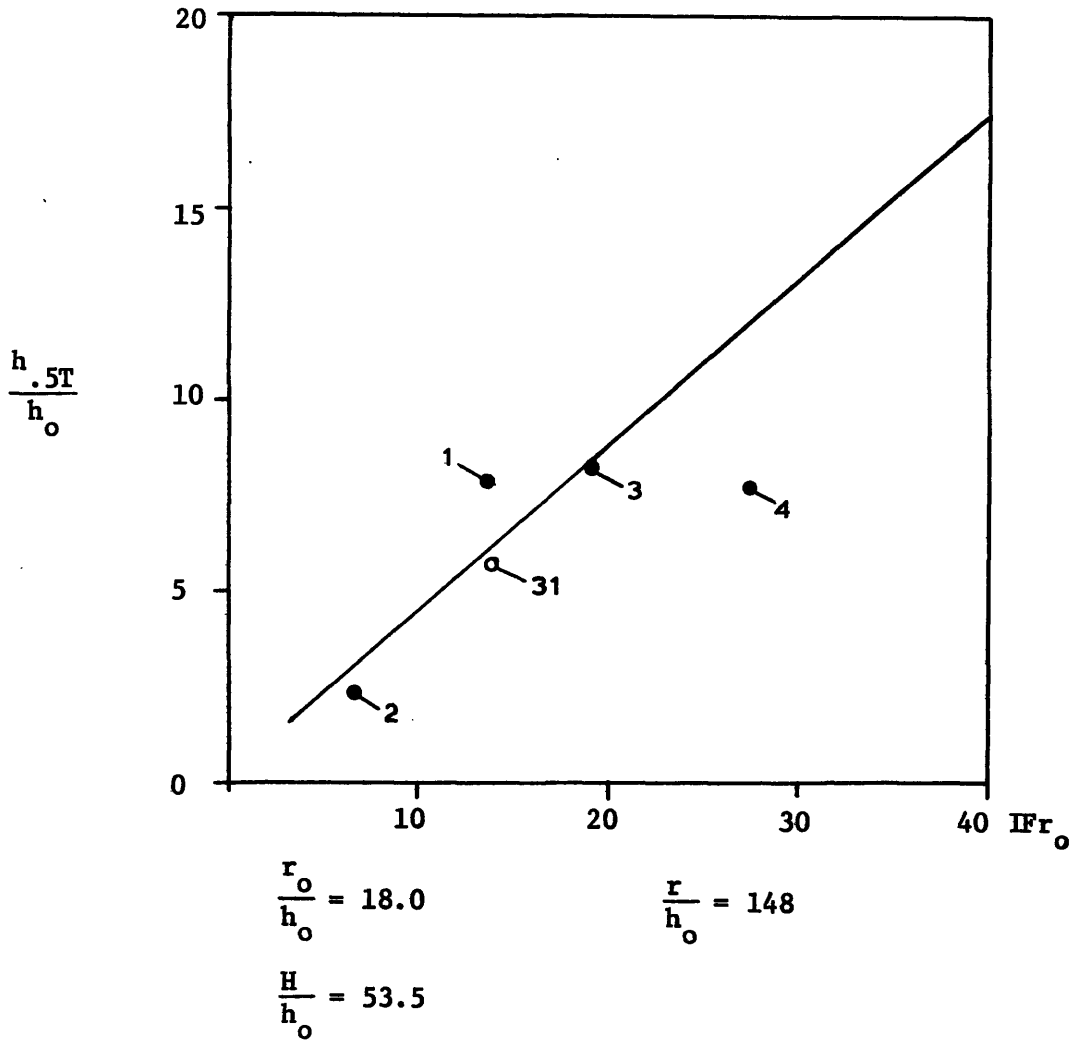

Figure 7.16b Normalized Half-Temperature Depth vs. Discharge Densimetric Froude Number at a Radial Distance $\frac{r}{h_o} = 148$

underprediction or overprediction. Figures 7.17a and 7.17b are similar graphs for those experiments with different geometric properties ($\frac{r_o}{h_o}$ = 36.0 and H/h_o = 107) than in the previous set. Only points for runs 5 and 33 are included since the other experiments with these parameter values appeared to recirculate. The limited agreement shown in these graphs may be due to the experimental inaccuracies discussed earlier.

In general, as the discharge Froude number increases, the flow approaches that of a pure momentum jet in which buoyant damping becomes less important and jet spreading becomes sharper. Figure 7.16a indicates that the centerline temperature approaches a constant value for very high discharge Froude numbers. However, at increasing values of F_{r_o}, the effects of the confined layer also tend to become stronger which can ultimately lead to a breakdown of the jet.

7.5.2 High Froude Number Experiments (with Recirculation)

Figures 7.18a and 7.18b present the comparison of predicted and measured surface temperatures and half-temperature depths for run 6. Figures 7.19a and 7.19b are the corresponding predictions for run 8. Physical observations indicate that recirculation may have occurred in both of these experiments. The analytical model also fails to give a stable jet depth.

For the geometric parameters in these experiments, $\frac{r_o}{h_o}$ = 36.0

and $H/h_o = 107.0$, numerical instabilities interrupt the integral marching procedure of the analytical model when the total jet depth reaches $\sim$ 70% of the total layer depth. Here return flow velocities have a greater magnitude than jet velocities. This is an unstable situation because jet entrainment is significant and the jet depth is increasing. The deeper the jet becomes, the greater is the return flow velocity. The jet velocity relative to the return flow velocity may actually increase (as the model steps out from the discharge point) causing even greater jet depths and entrainment. Also in this situation, the dynamic pressure effects that the return flow exerts on the jet should not be ignored if the formulation is to be accurate.

A conservative estimate of the onset of recirculation would be when the jet depth is approximately half the layer depth. Thus, the following condition can be assumed to hold for the applicability of the radial jet model with return flow:

$$\frac{h_{max}}{H} \lesssim 0.5 \tag{7.23}$$

If inequality (7.23) is not satisfied, near field recirculation can be assumed to occur. However, the model is not able to predict the degree of recirculation. This situation is indicated in Figs. 7.20, which is a revision of Fig. 7.9, combining the experimental observations with the theoretical base. In view of this analysis. run 6 is probably a borderline case of recirculation caused by angular variations of the jet depth arising from non-uniformities of discharge distribution at

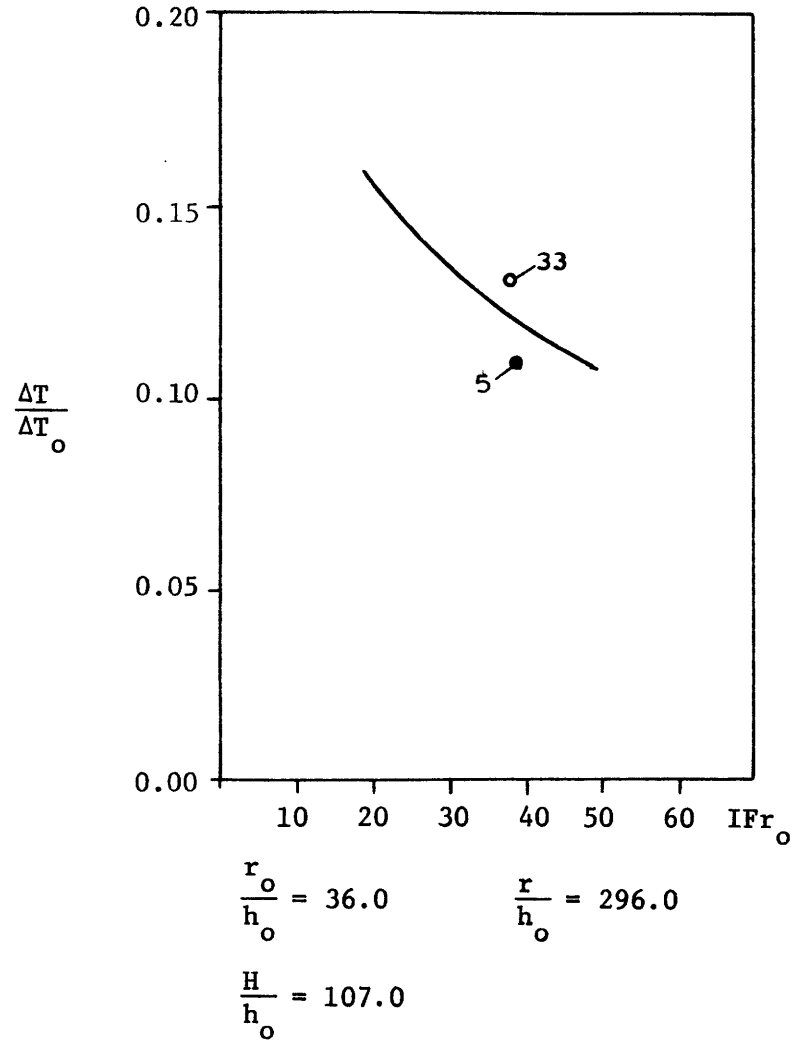

Figure 7.17a Normalized Temperature Difference vs. Discharge Densimetric Froude Number at a Radial Distance of $\frac{r}{h_o} = 296.0$

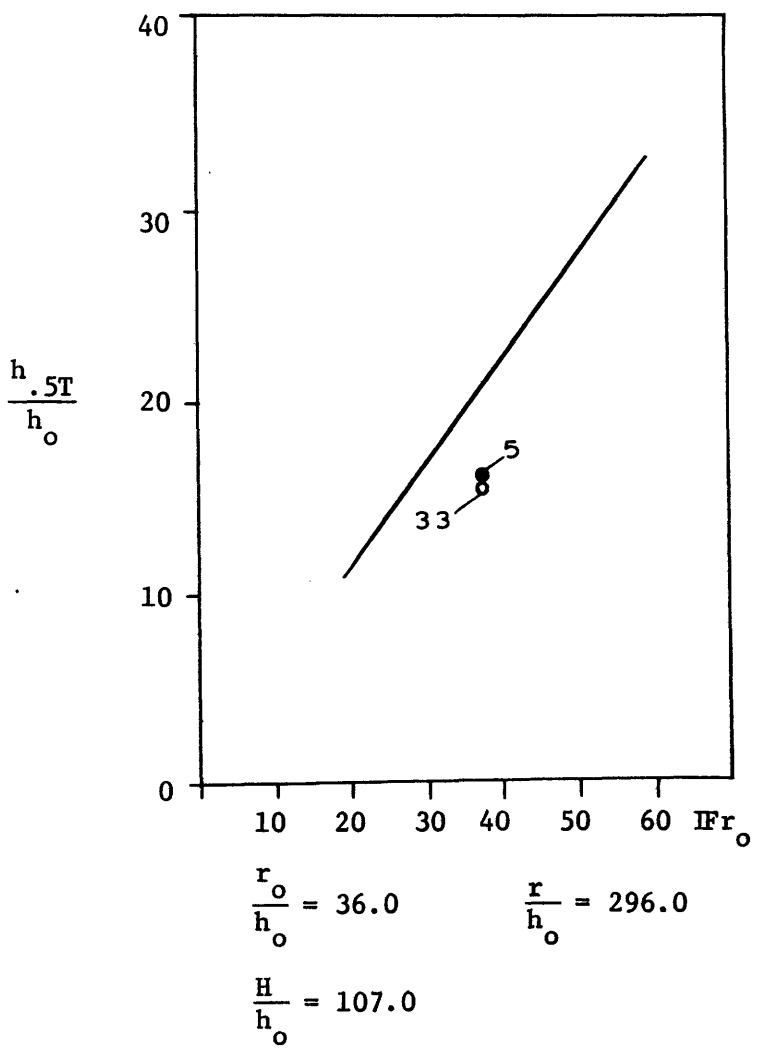

Figure 7.17b Normalized Half-Temperature Depth vs. Discharge Densimetric Froude Number at a Radial Distance of $\frac{r}{h_o}$ = 296.0

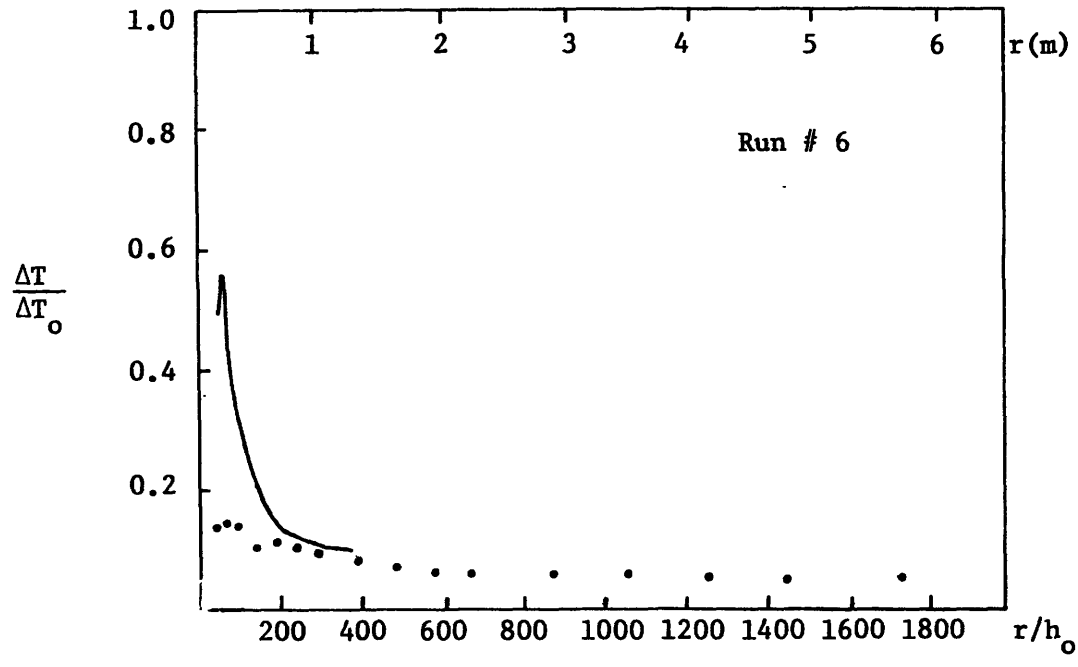

Figure 7.18a Temperature vs. Distance, Experimental Comparison to Model

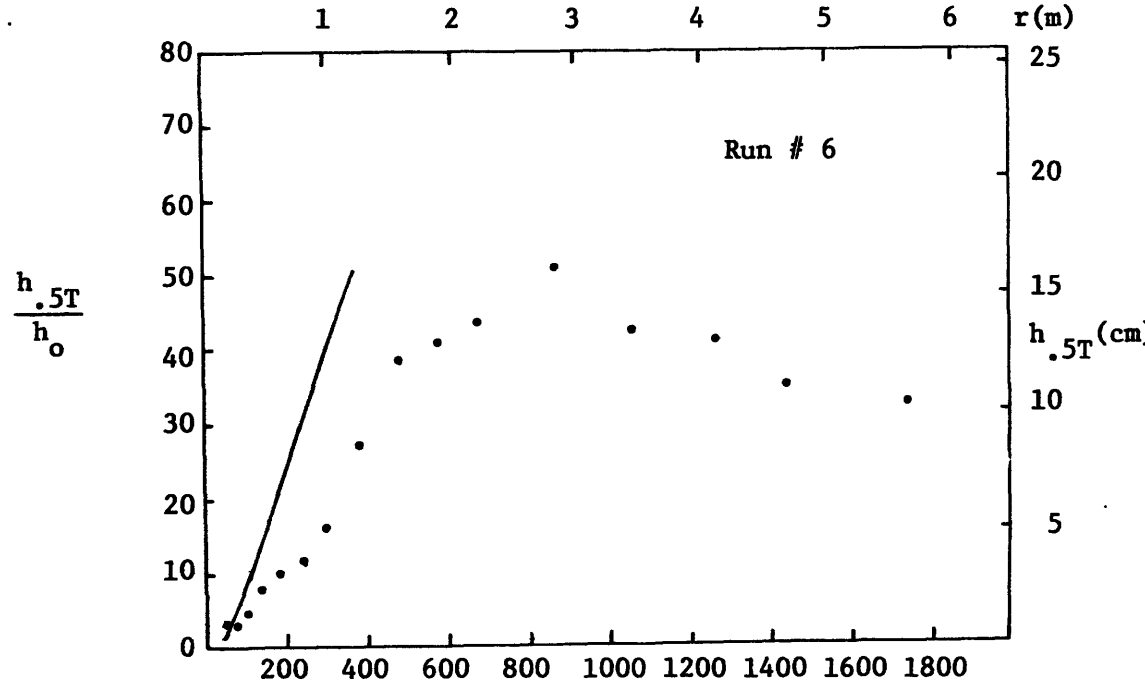

Figure 7.18b Half-Temperature Depth vs. Distance, Experimental Comparison to Model

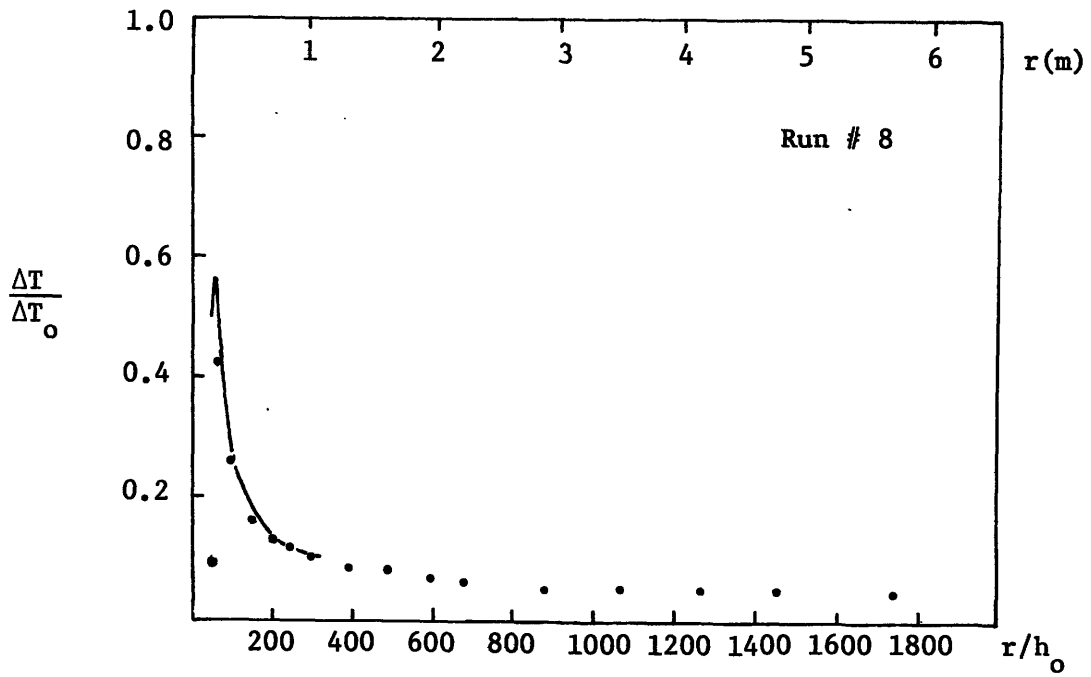

Figure 7.19a Temperature vs. Distance, Experimental Comparison to Model

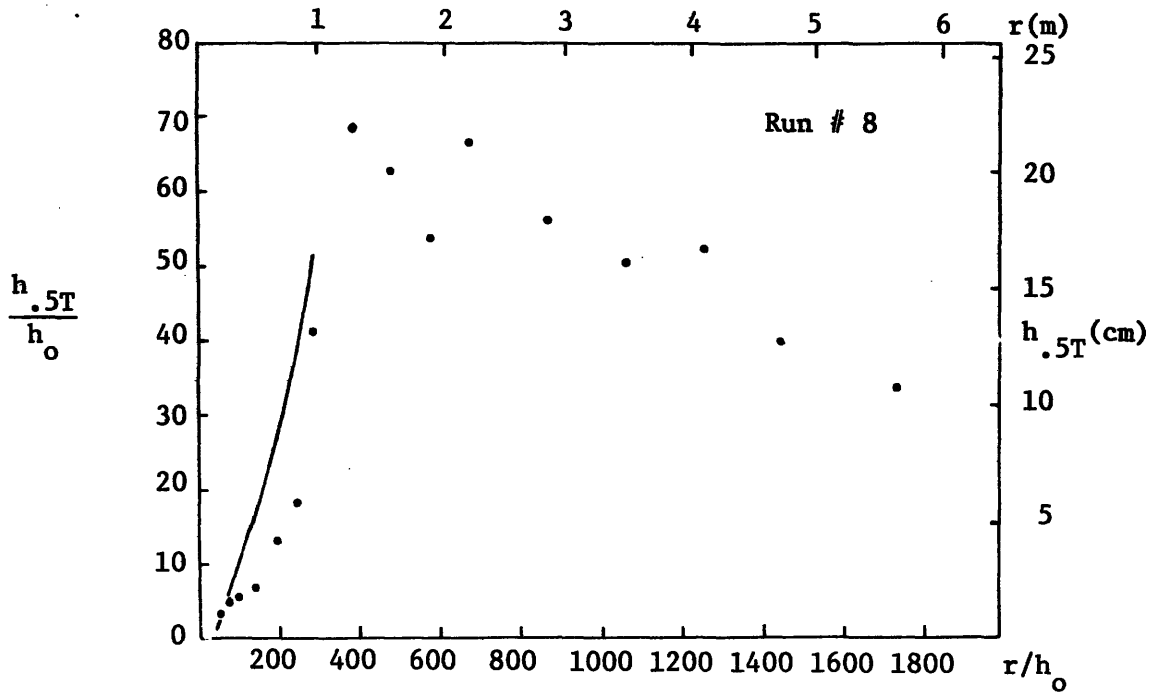

Figure 7.19b Half-Temperature Depth vs. Distance, Model Prediction Only

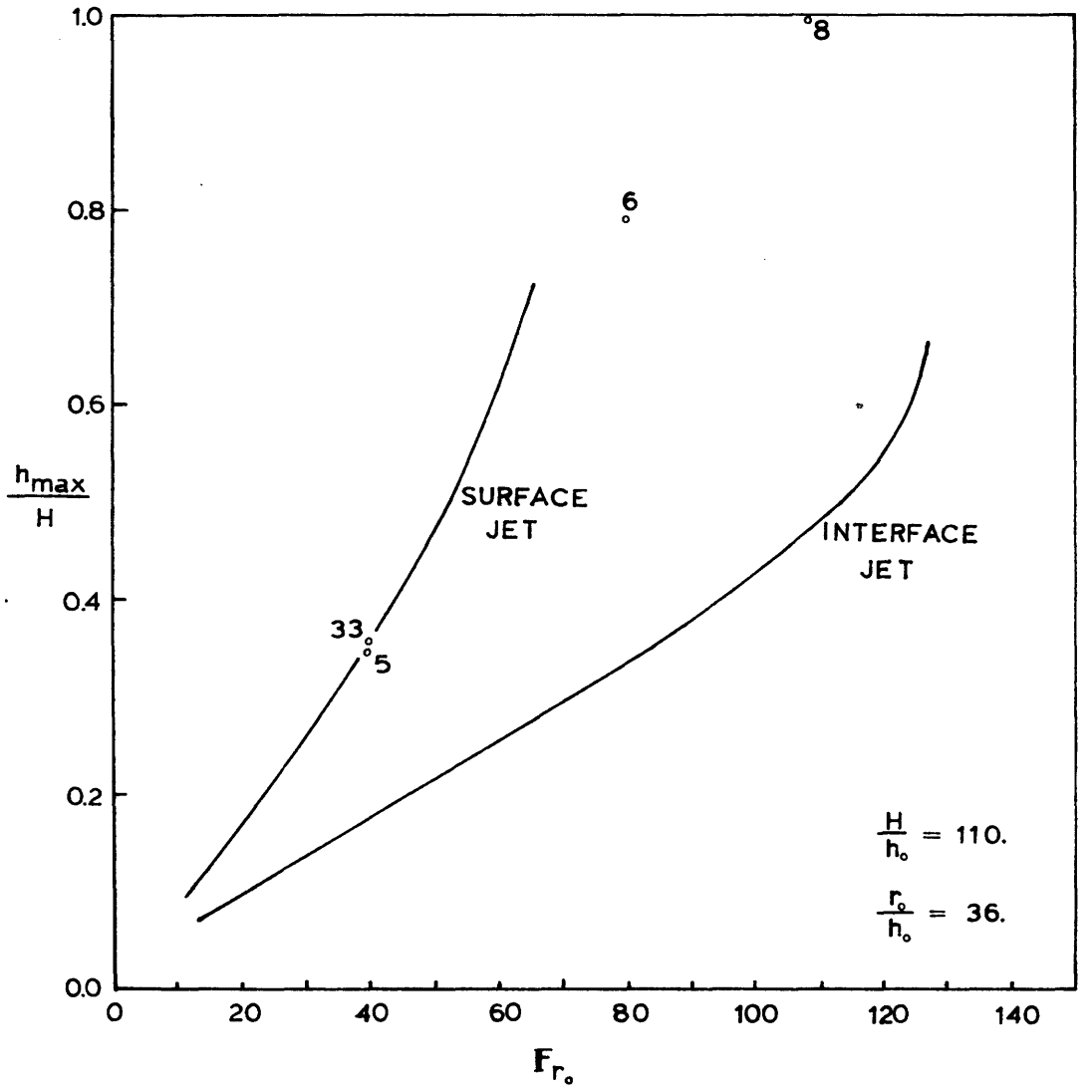

Figure 7.20 Maximum Vertical Penetration vs. Quarter Module Froude Number; (Experimental Surface Jet Data Points are Included).

the plexiglas model. Inequality (7.23) will be used in the final chapter to derive a more general design guideline for the assessment of recirculation with the mixed discharge design.

CHAPTER VIII

SEPARATE JET THEORY WITH STAGNANT CONDITIONS

The analytical buoyant surface jet model of Stolzenbach and Harleman (1971) was chosen for separate discharge jet simulations. A user's manual for this model has also been published (Stolzenbach, Adams and Harleman, 1972).

This integral jet model predicts near field behavior of buoyant surface jets discharged into an isothermal body of water of large depth (Figure 8.1). Several of the characteristics distinguishing the experimentally observed flow field are not included in the formulation. These include: 1. the intake flow zone; 2. the return flow zone; 3. interactions between the multiple jets and 4. the limited depth. Thus, at first, the application of the model to the OTEC case should be exploratory only to determine by comparison with experiments whether (and under what conditions) these characteristics severely limit the model applicability. If not, then the model can be used as a tool to evaluate data trends and give detailed three-dimensional predictions.

8.1 Analytical Background

As in the radial case, the jet dominated near field can be broken up into two zones: the zone of established flow and the zone of flow establishment.

8.1.1 Zone of Established Flow

This zone is characterized by fully developed sheared profiles of velocity and temperature (Figure 8.1). The zone extends out from the zone of flow establishment to the far field region where the discharge flow no longer has turbulent jet type features.

The analysis approach is similar to that used for the radial buoyant jet. The time averaged turbulent momentum, heat conservation, and continuity equations are reduced to ordinary differential equations through a series of assumptions and integration over the jet's cross-sectional area. These assumptions are typical for integral analysis of buoyant jets:

1. Steady flow: $\frac{\partial}{\partial t} = 0$
2. Large Reynolds number: viscous terms negligible
3. Boussinesq approximation: density differences are only important in pressure terms
4. Hydrostatic pressure
5. No jet induced motion at large depths: $\frac{\partial p}{\partial x} = \frac{\partial p}{\partial y} = 0$ as $z \to -\infty$
6. Boundary layer flow $\frac{\partial}{\partial x} << \frac{\partial}{\partial y}$ and $\frac{\partial}{\partial z}$
7. Small density differences $\frac{\Delta\rho}{\rho_{amb.}} << 1$

The assumption of self-similarity of vertical and lateral profiles of velocity and temperature allows the cross-sectional integration of the equations resulting in the equations of Table 8.1. These equations

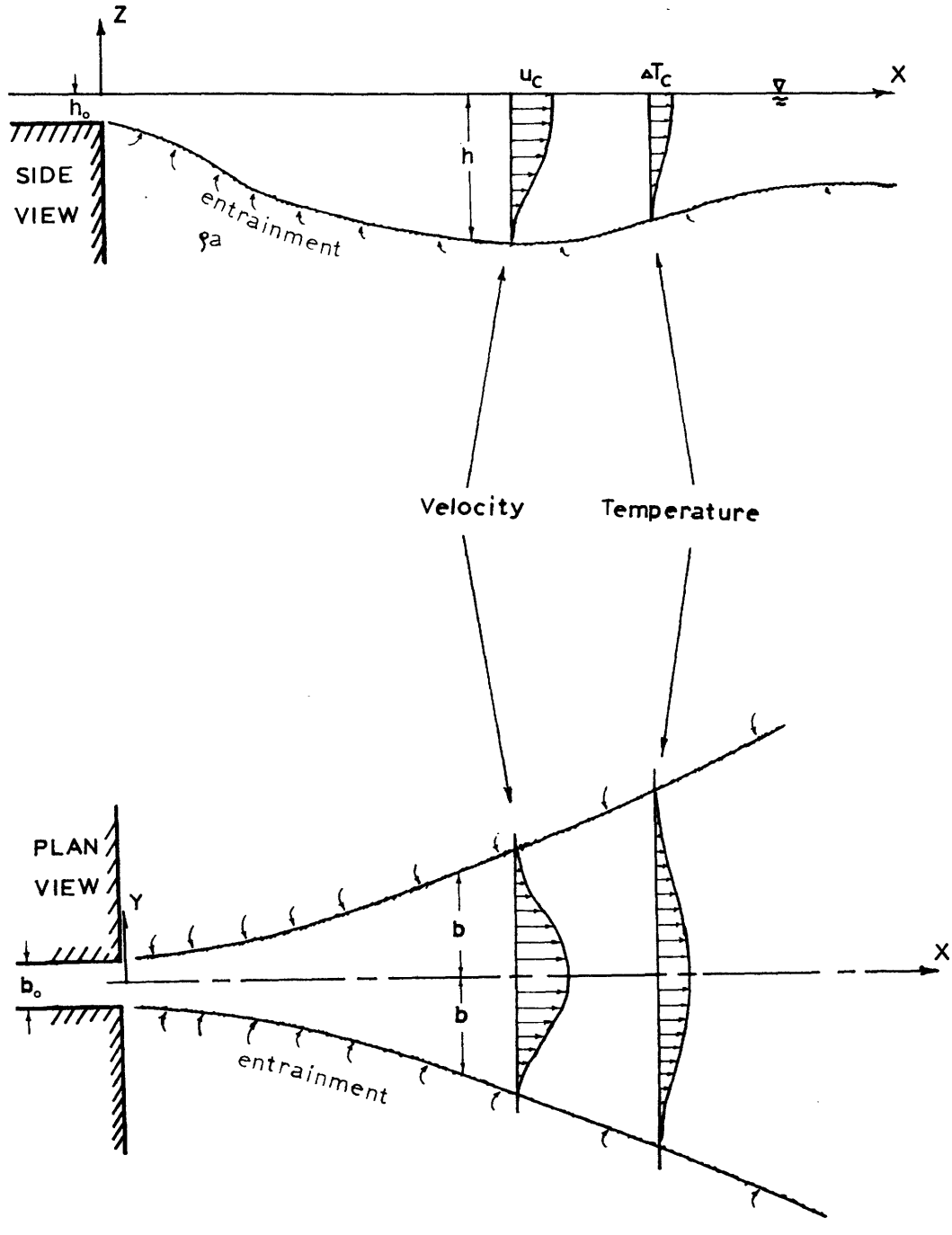

Figure 8.1 Schematic for Buoyant Surface Jet

can be solved numerically using given flow conditions at the beginning of the zone.

The particular similarity functions chosen for this model are polynomials as assumed by Abramovich (1963) for sheared buoyant jets.

$$u = u_c \; f(y/b) \; f(z/h)$$

$$\Delta T = \Delta T_c \; t(y/b) \; t(z/h)$$

where:

$$f(\zeta) = [1 - \zeta^{3/2}]^2$$

$$t(\zeta) = [1 - \zeta^{3/2}]$$

Two features are particular to the Stolzenbach-Harleman surface jet model. First of all, entrainment velocities are assumed proportional to the jet centerline velocity. Separate proportionality coefficients are assumed for lateral and vertical entrainment. The lateral entrainment coefficient is a constant, 0.0495. The vertical entrainment coefficient is reduced to a function of local Froude number (see Eq. 7.20).

The second feature concerns the lateral velocity, V. It is analogous to some sort of lateral spreading assumption often employed in other formulations. The local lateral velocity due to buoyant spreading is assumed proportional to: 1. the local normalized density gradient $\left(\frac{\partial t}{\partial \zeta_y}\right)$; 2. the local longitudinal velocity, u; 3. the lateral

Table 8.1

GOVERNING EQUATIONS AND INTEGRAL QUANTITIES

FOR SURFACE JET MODEL BY STOLZENBACH AND HARLEMAN (1971)

Governing Equations

Conservation of Mass

$$\frac{dQ}{dx} = c_1 \alpha_o u_c h + c_2 \alpha_v u_c b$$

Conservation of x -Momentum

$$\frac{dM}{dx} = \frac{dP}{dx}$$

y-Momentum Spreading Equation

$$\frac{d}{dx}\left[\left(\frac{db}{dx} - k_j\right) u_c^2 \, bhc_4\right] = (\mathbb{F}_o^*)^{-2} \, \Delta T_c h^2 c_5$$

Conservation of Heat Flux (Surface Jet)

$$\frac{dH}{dx} = -c_3 \, K' \, \Delta T_c b$$

Centerline Temperature Boundary Condition (Interface Jet)

$$\frac{d(\Delta T_c)}{dx} = 0$$

Integral Quantities

Volume Flux: $$Q = \int_A u d\eta d\zeta$$

Momentum Flux: $$M = \int_A \rho_a u^2 \, d\eta d\zeta$$

Pressure Force: $$P = \int_A \left[\int_{-\infty}^{\zeta} g \Delta\rho d\rho \right] d\eta d\zeta$$

Temperature Flux: $$H = \int_A \Delta T u d\eta d\zeta$$

Table 8.1 (Continued)

Parameters

A = cross-sectional area of jet

η = y/b

ζ = z/h

c_i = profile dependent coefficients

K' = $K/\rho c_p$ = kinematic surface heat loss coefficient [L/T]

k_j = $\left[\frac{db}{dx}\right]_{NB}$ = lateral spreading rate of a non-buoyant surface jet typically taken as .22

spreading rate in excess of a non-buoyant jet $\left(\left|\frac{\partial b}{\partial x}\right|_B\right)$ This assumption is important in the formulation of the y-momentum spreading equation.

8.1.2 Zone of Flow Establishment

This zone extends from the discharge point out to the zone of established flow. The mean velocity and temperature profiles are characterized by central portions that are unsheared. The zone is basically a transition from the approximately uniform velocity of the discharge port to the free-shear velocity distribution in the jet.

The model of Stolzenbach and Harleman carries out a detailed analysis of this zone which is necessary in cases where the zone of flow establishment encompasses a significant portion of the near-field zone. The large port sizes proposed for OTEC power plants contribute to the size and significance of the zone.

The solution approach divides the jet cross-section into 4 regions of sheared, partially sheared, and unsheared velocity profiles (Figure 8.2). The system of governing equations then contains four individual equations of continuity and longitudinal momentum linked through transfer conditions. The detailed equations and their development can be found in Stolzenbach and Harleman (1971).

8.1.3 Interface Jet

For the prototype discharge jet at the density interface, the temperature along the centerline is constant. Only the heat flux equation needs changing for this case. It was replaced by the boundary

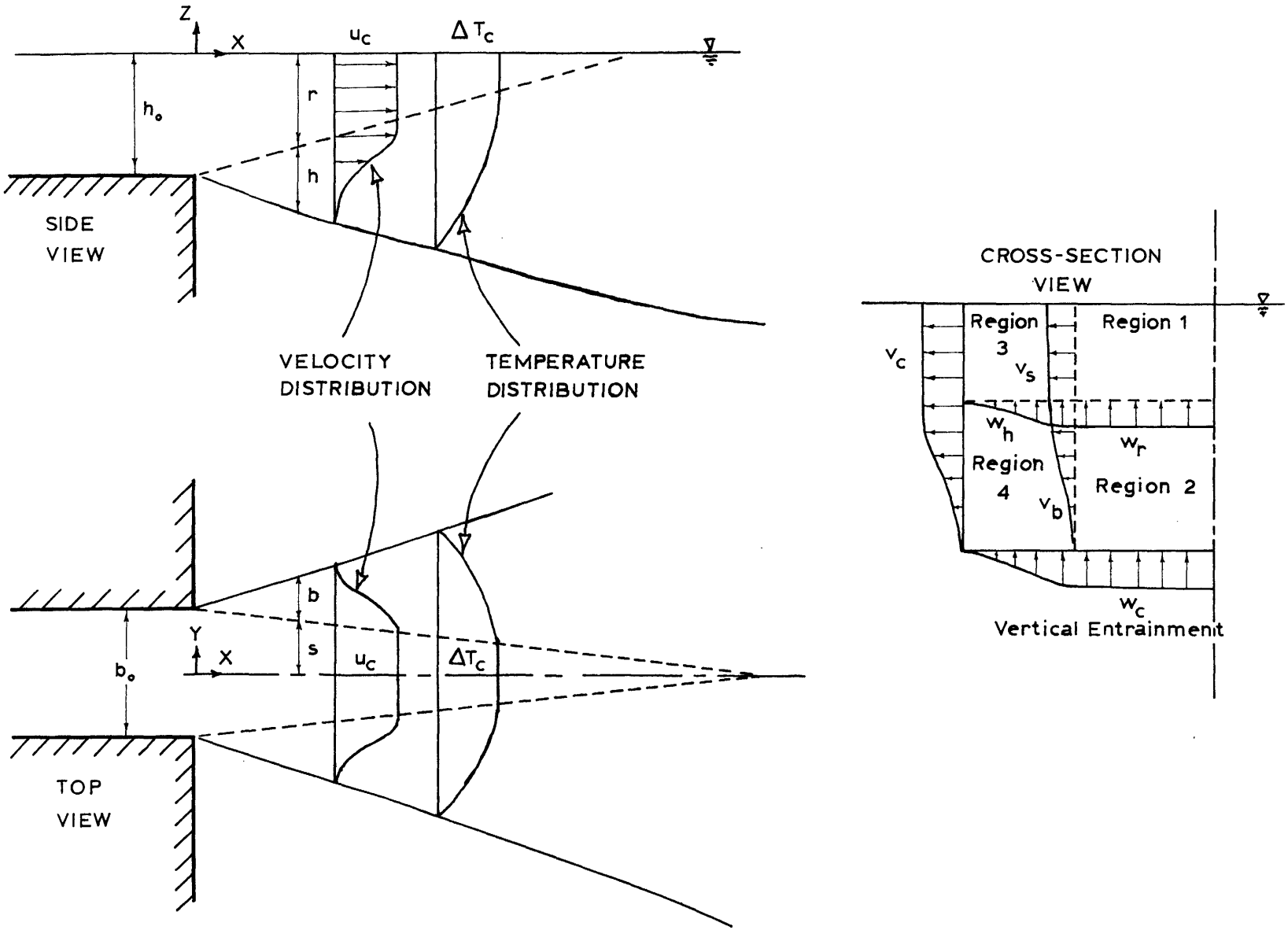

Figure 8.2 Detailed Jet Structure in Zone of Flow Establishment

condition $\frac{d\Delta T_c}{dx} = 0$. The same polynomial profile shapes of the surface jet are used in these simulations as well.

8.2 Solution Method

The governing equations are solved by a fourth order Runge-Kutta integration technique supplied by the IBM Fortran Scientific Subroutine Package. The routine was modified slightly to prevent physically positive variables from ever taking on negative values.

The program chooses a step size to meet an inputted error bound. The solution is stepped out from the discharge point until a specified distance is reached or until the low velocity and low local Froude number flow can no longer be considered to exhibit jet-like behavior.

The results of the calculations are printed out in dimensionless form with u_o, ΔT_o, and $\sqrt{h_o b_o}$ being the normalizing velocity, temperature and length scales.

8.3 Model Results

The analysis of the model and the examination of its sensitivity to the discharge parameters F_o^* and h_o/b_o have been conducted.

8.3.1 Surface Jet

The surface jet behavior and parameter sensitivity have been examined thoroughly by Stolzenbach, Adams and Harleman (1972). Figure 8.3 illustrates typical model predicted jet behavior. The jet mixes

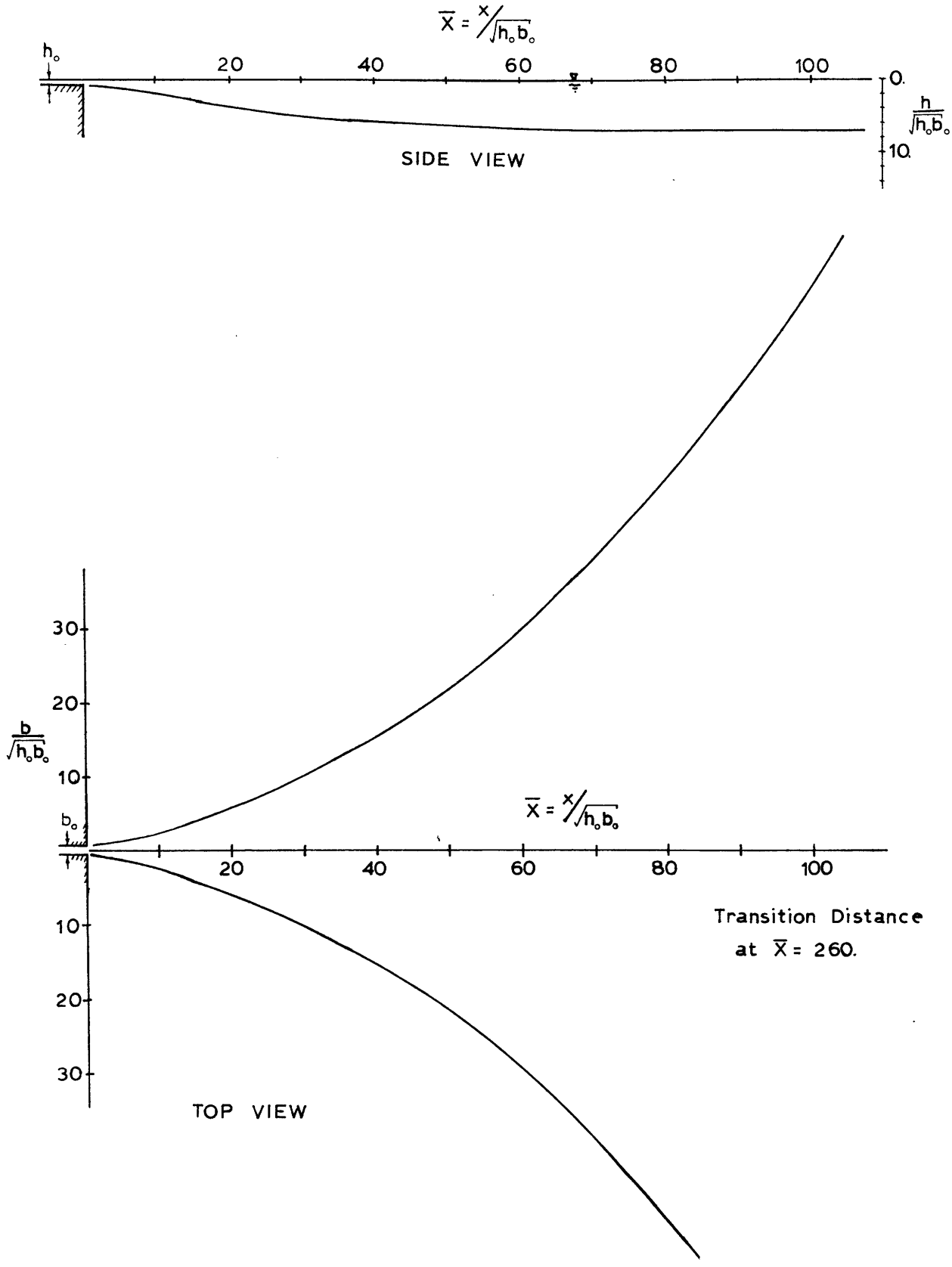

Figure 8.3 Surface Jet Model Preditions for Vertical and Lateral Jet Dimensions (Discharge Conditions Correspond to Experiment #13).

down to a maximum depth and then gets shallower as lateral spreading becomes more important. Lateral spreading is at first moderate but then increases strongly as buoyant spreading dominates the x momentum of the jet. A transition distance, x_t, where the local Froude number equals one, has been defined (Eq. 5.1). This appears to be the limit of strict applicability of the model. Buoyant spreading and far field phenomena rather than jet behavior can be expected to dominate beyond this distance. The model continues its calculations beyond x_t, until the predicted centerline velocity is .02 of its original value. For the conditions encountered in the laboratory, the inclusion of surface heat loss had little effect on jet behavior for distances in the order of x_t.

Figures 8.4 and 8.5 illustrate the sensitivity of centerline depth and temperature to changes in the Froude number, $\mathbb{F}_o^*$, and the aspect ratio, h_o/b_o. The depths and temperatures are nondimensionalized by $[h_o\ b_o]^{\frac{1}{2}}$ and T_o, respectively. Higher discharge Froude numbers cause more mixing and deeper jets. However, jet solutions for $\mathbb{F}_o^*$ equals 15.0 are insensitive to changes in the aspect ratio over the range of .2 to 1.5. The difference in solution for all aspect ratios in this range is less than the thickness of the curves drawn in Figures 8.5a and 8.5b.

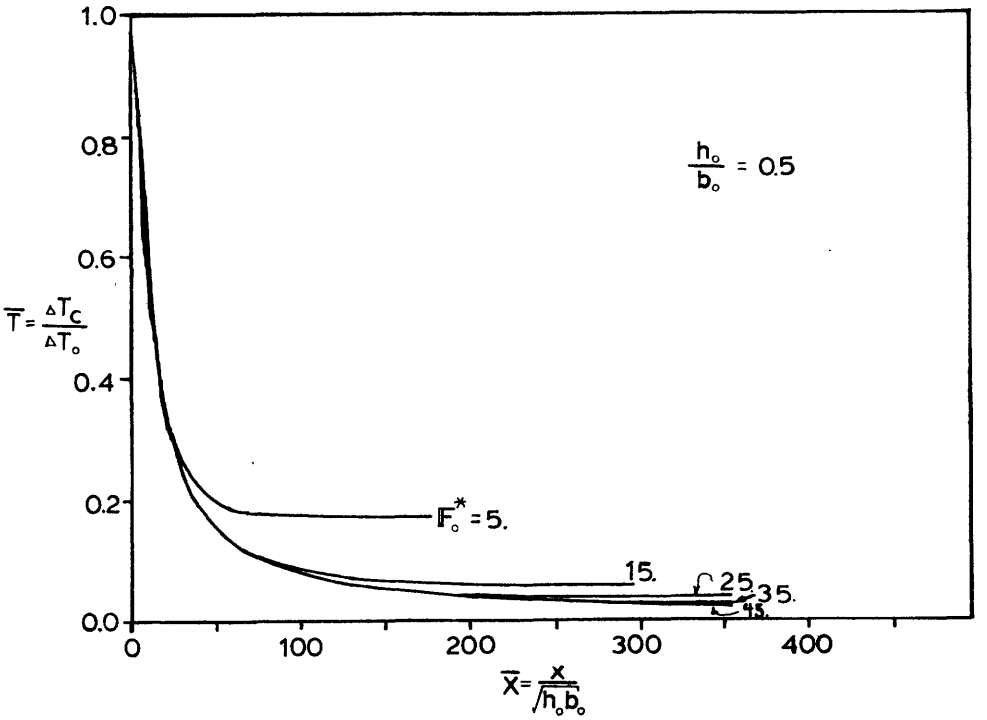

Figure 8.4a Centerline Temperature vs. Distance, Varying F_o^*

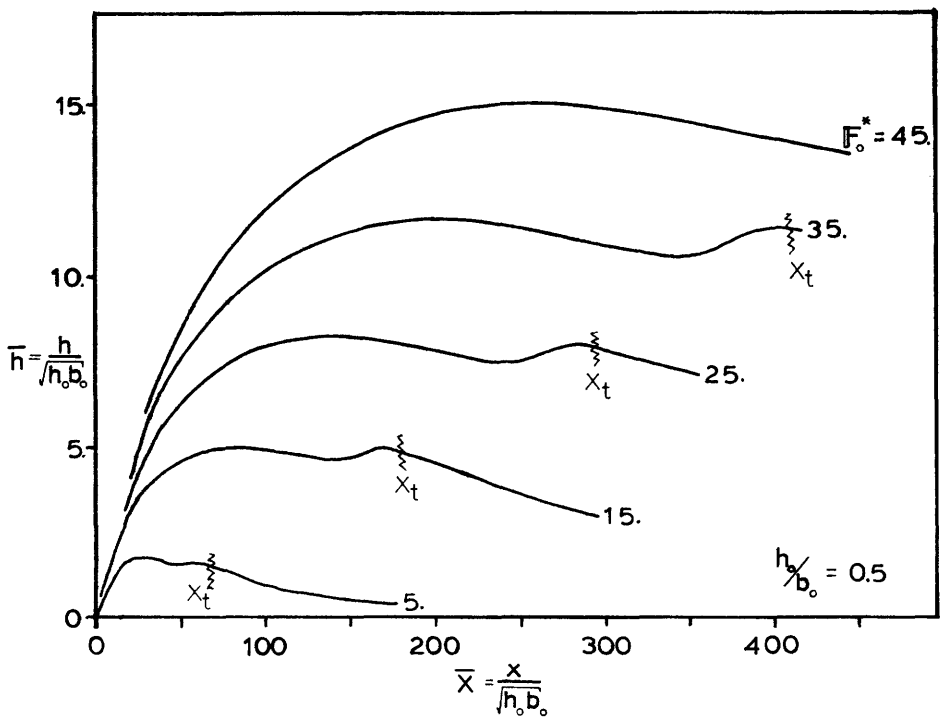

Figure 8.4b Jet Depth vs. Distance, Varying F_o^*

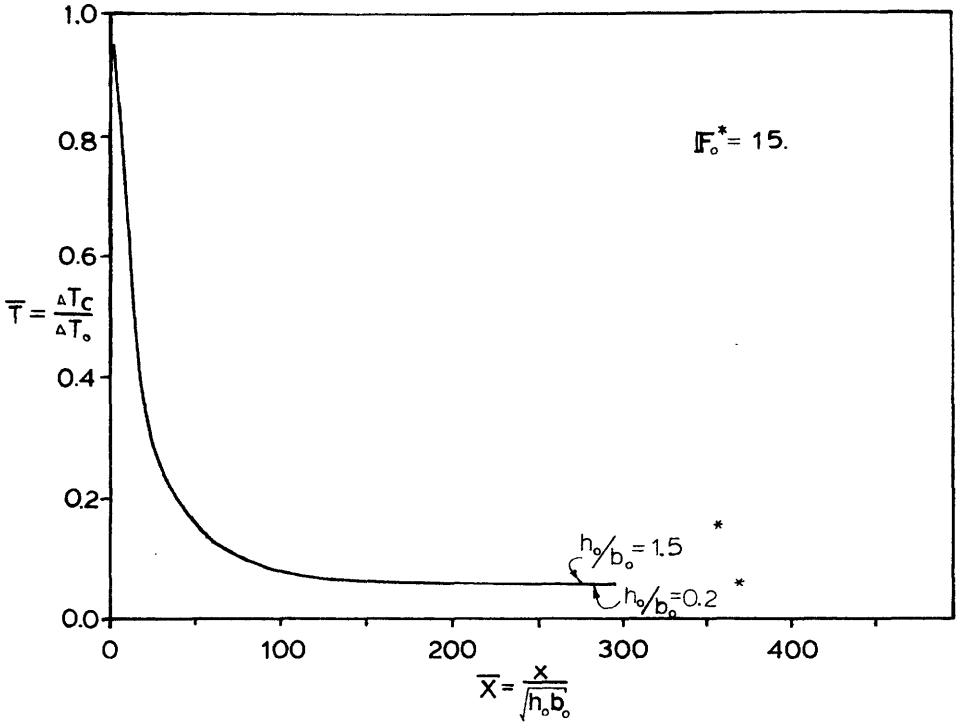

Figure 8.5a Centerline Temperature vs. Distance Varying h_o/b_o

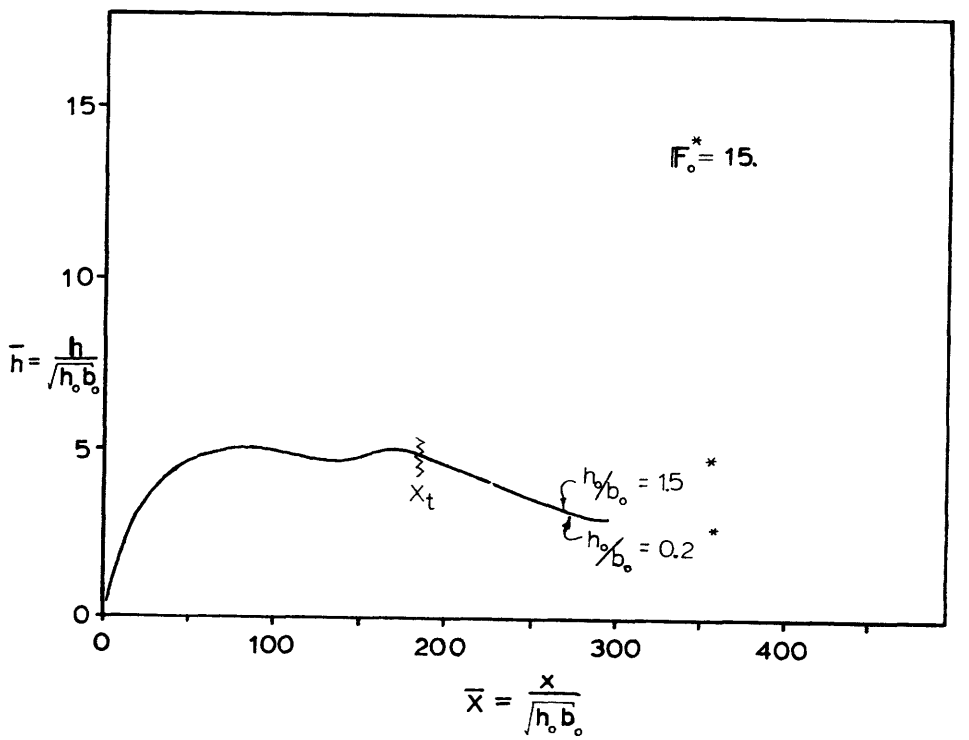

Figure 8.5b Jet Depth vs. Distance, Varying h_o/b_o

*The curves for the range $0.2 \leq h_o/b_o \leq 1.5$ lie within the thickness of the line drawn.

8.3.2 Interface Jet (Prototype)

The centerline temperature of the interface jet (as described in 2.2) does not change, since it entrains equally from both sides of the density interface. The jet thickness responds similarly as a function of distance from the same $\mathbb{F}_o^*$ as the surface jet except that buoyant damping of turbulence is much more pronounced. The interface jet is thinner, has more pronounced buoyant spreading, and loses its jet properties much sooner (smaller x_t) than the surface jet.

Figure 8.6 and 8.7 illustrate the sensitivity of the jet thickness prediction to $\mathbb{F}_o^*$ and h_o/b_o. Actually, a dimensionless "half" thickness or the jet penetrating above the density interface is plotted. High discharge Froude numbers indicate a thicker, better mixing jet. As was the case in surface jets, there is no sensitivity (less than graphs line thickness) to h_o/b_o over the range of 0.2 to 1.5.

The information of Fig. 8.4b and 8.6 is further summarized by plotting in Fig. 8.8 the maximum predicted jet thickness, h_{max}, as a function of $\mathbb{F}_o^*$. The plot is good for any aspect ratio h_o/b_o in the range 0.2 to 1.5. Predictions of vertical penetration based on the surface jet are conservative with respect to prototype conditions (interface jet). The important parameter, recirculation, should be directly related to the discharge jet's vertical penetration or thickness.

8.4 Comparison of Analytical and Experimental Results

Even though the experiments for the separate jet discharge

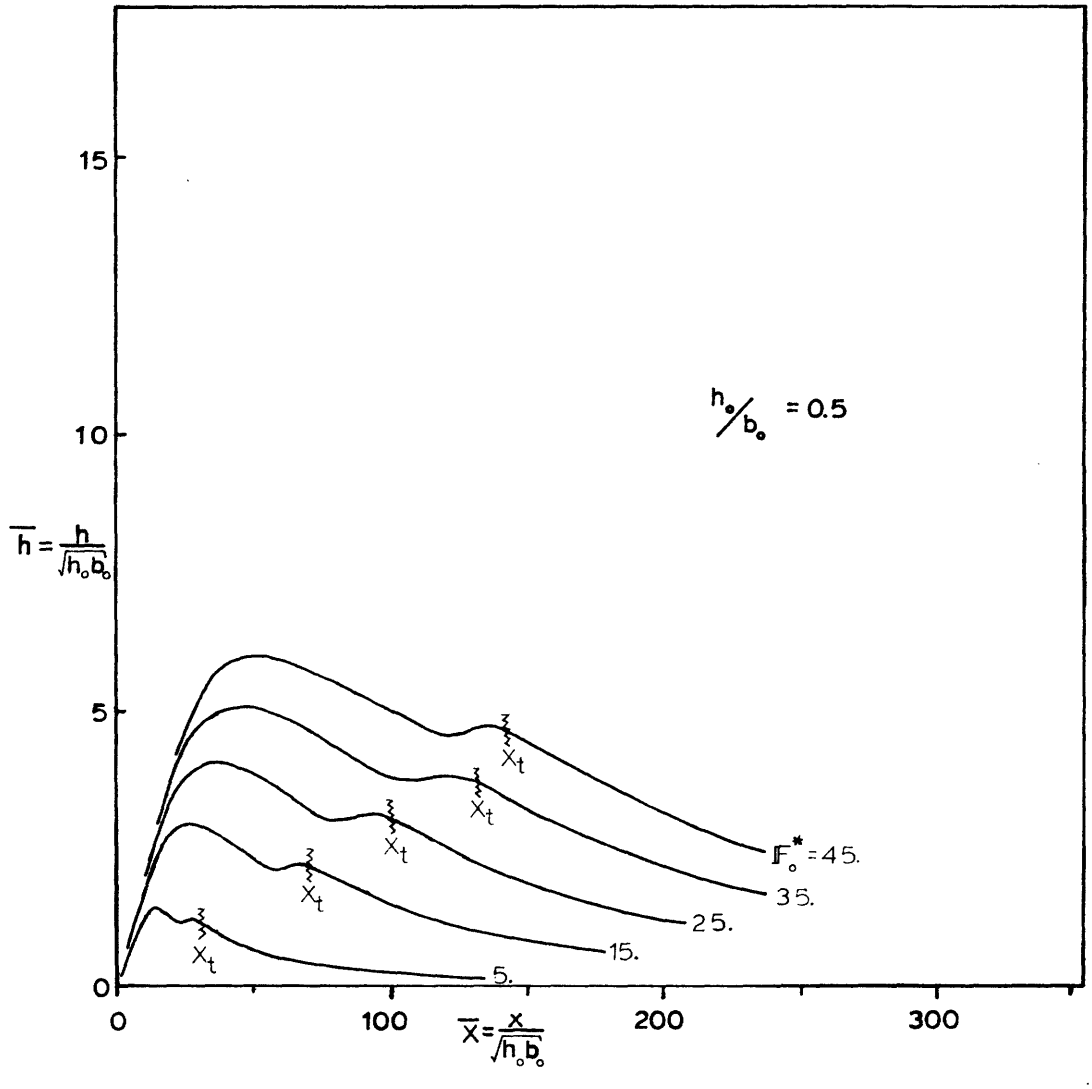

Figure 8.6 Interface Jet Depth vs. Distance, Varying F_o^*

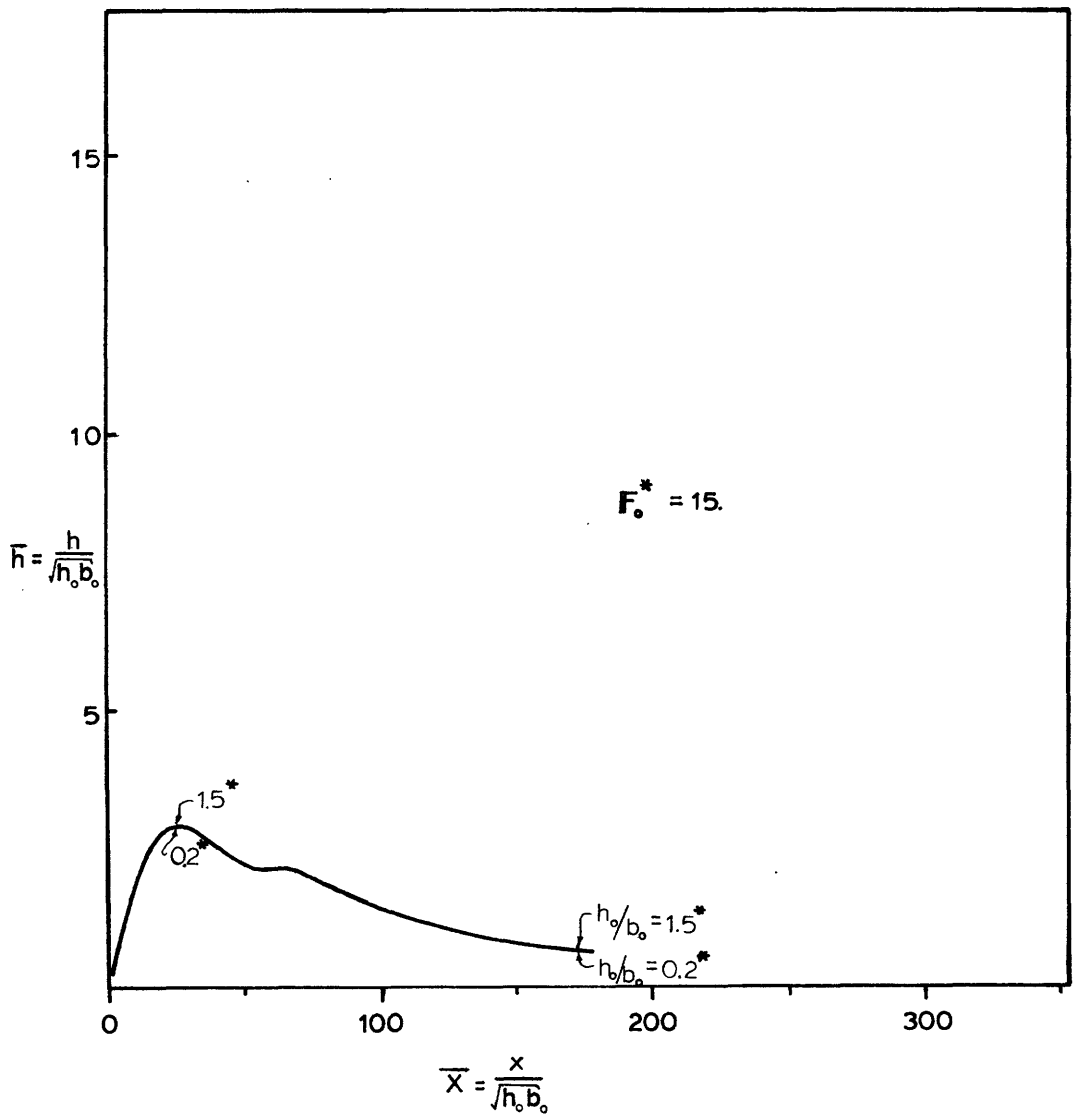

Figure 8.7 Interface Jet Depth vs. Distance Varying h_o/b_o

*The range of $0.2 \leq h_o/b_o \leq 1.5$ is contained in the thickness of the curve drawn.

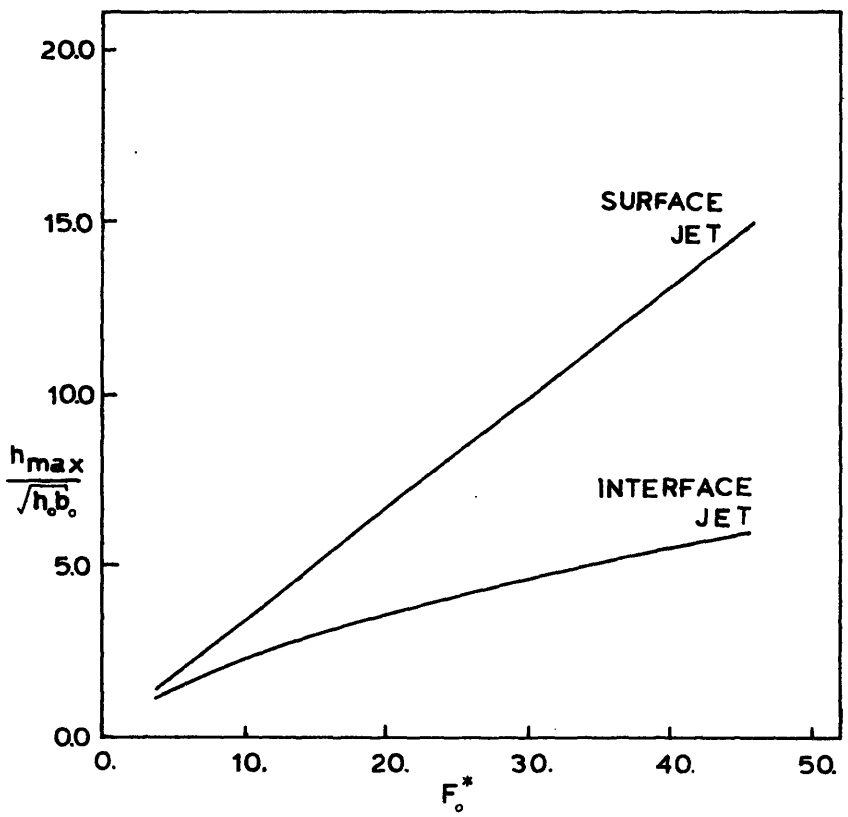

Figure 8.8 Dimensionless Maximum Jet Thickness vs. Discharge Densimetric Froude Number for Surface Jet and Interface Jet.

configuration do not allow a direct classification into cases without and with recirculation, the comparison is carried out in two sections (analogous to the radial jet case, Section 7.5): First, experiments with low Froude number conditions and no recirculation; second, experiments with high Froude number conditions showing some tendency for recirculation (based on the observations in Section 5.3).

8.4.1 Low Froude Number Experiments

The centerline temperature plots (Figures 8.9 to 8.12, "a" series) show that the agreement between the predicted and observed values is very good. Data points appear for each individual jet of the half or full model experiment. There is a slight tendency to underpredict the temperature. This could be due to the model not accounting for the heat entrained from the lateral return flow. The underprediction tendency is slight, indicating that the importance of this effect is only secondary.

The agreement between theoretical predictions and measured half temperature depths is satisfactory. The scatter is partly due to the turbulent fluctuations in the temperature field. Experimental steady state durations did not always allow sufficient data to be taken for good estimates of mean temperature. The fit also depends significantly on the temperature similarity profile assumed in the model. Figure 8.13 illustrates the correctness of this profile assumption for experiment #37.

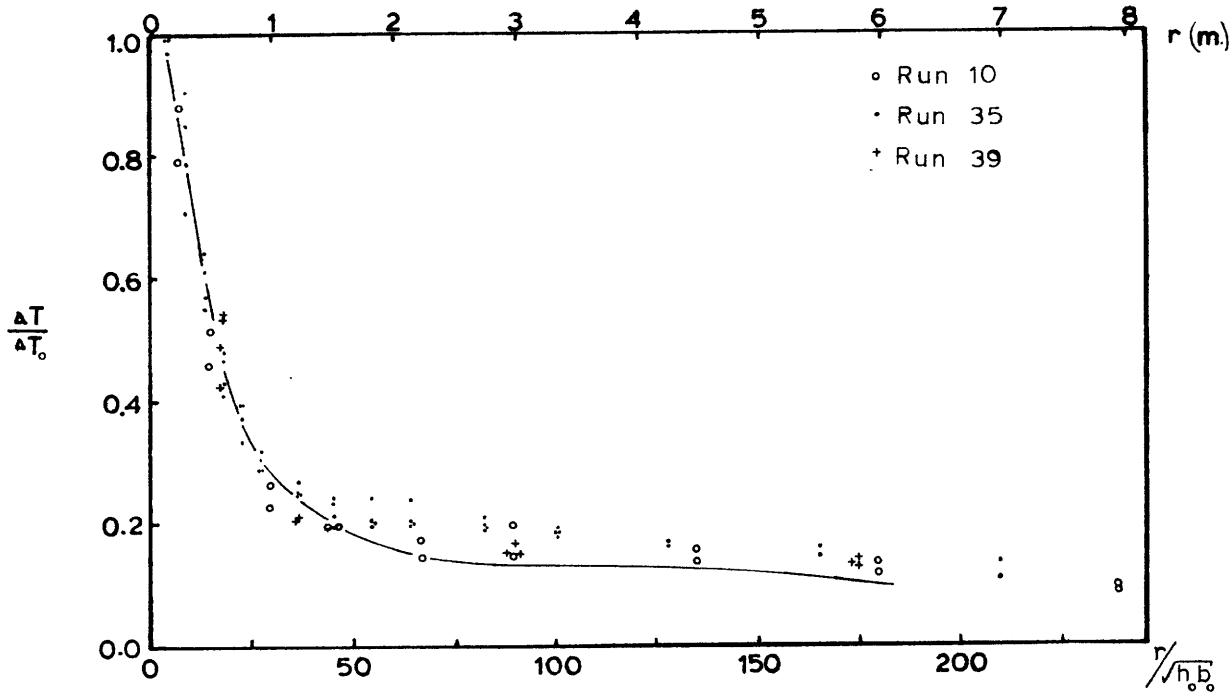

Figure 8.9a Temperature vs. Distance, Experimental Comparison to Model

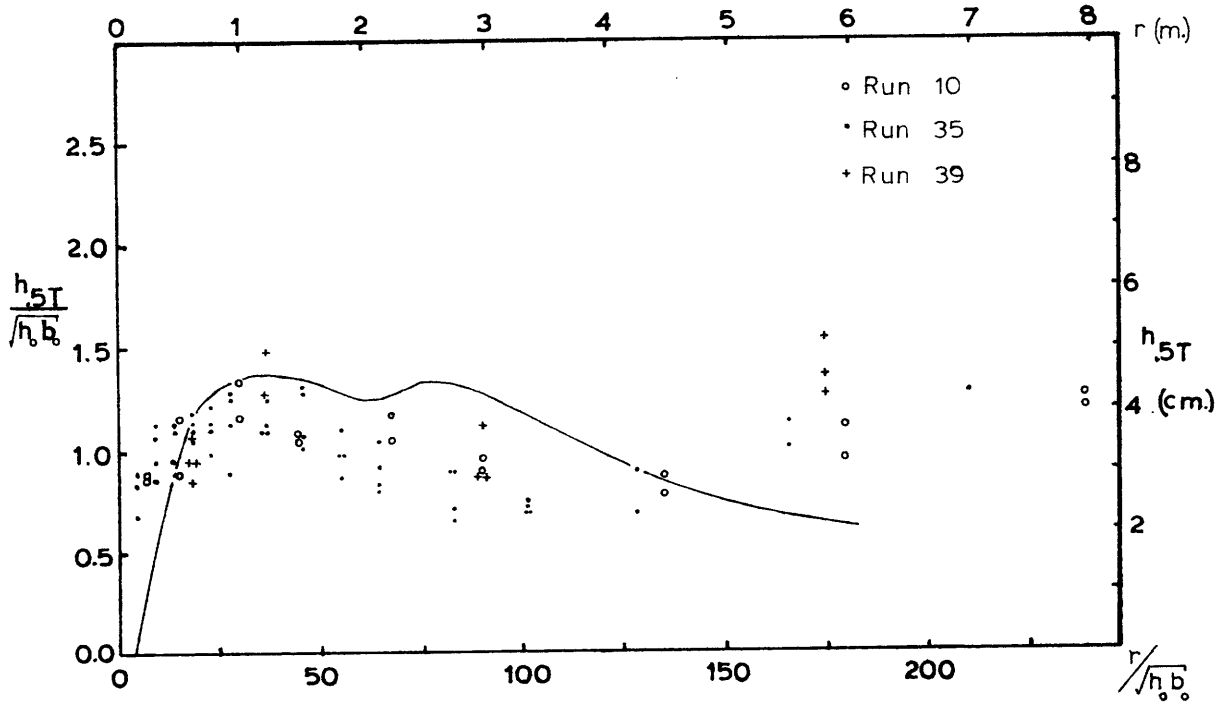

Figure 8.9b Half Temperature Depth vs. Distance, Experimental Comparison to Model

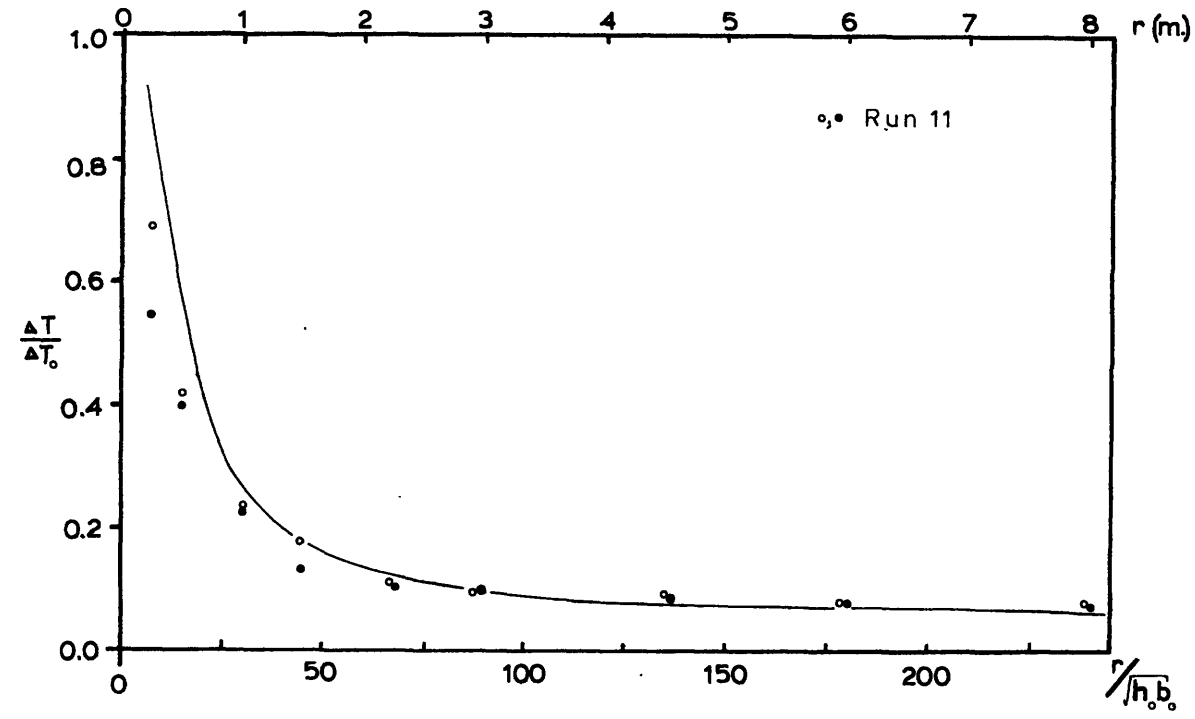

Figure 8.10a Temperature vs. Distance, Experimental Comparison to Model

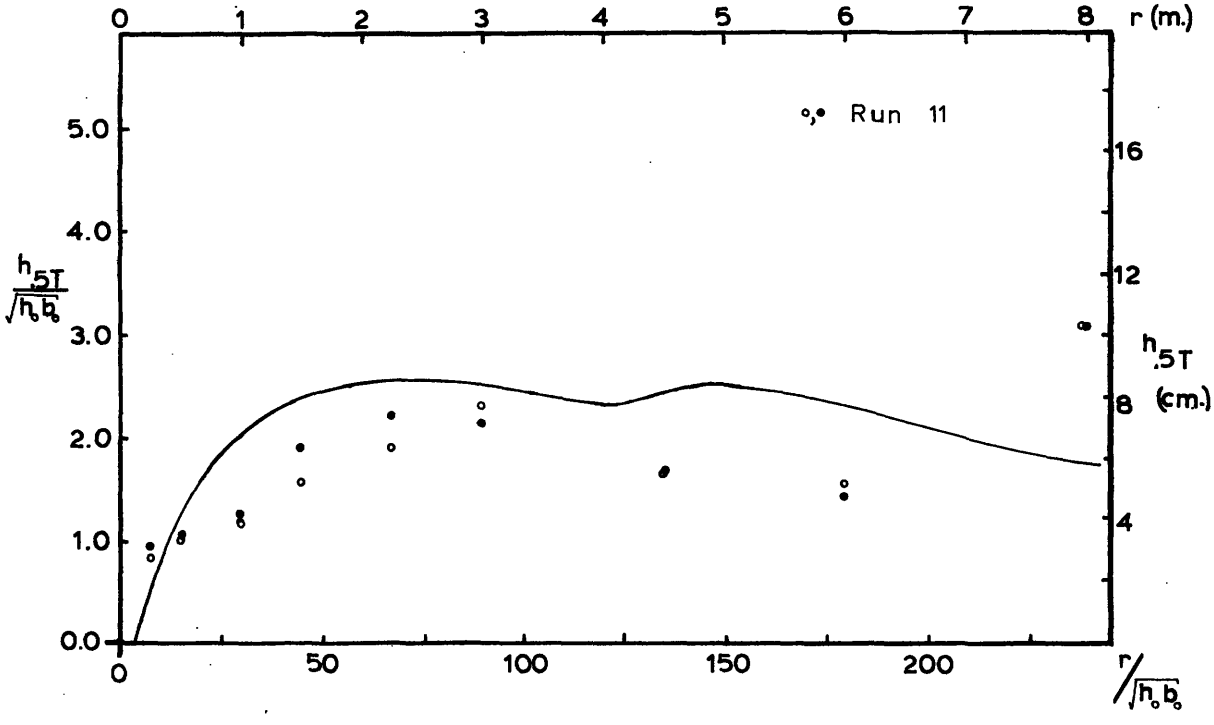

Figure 8.10b Half Temperature Depth vs. Distance, Experimental Comparison to Model

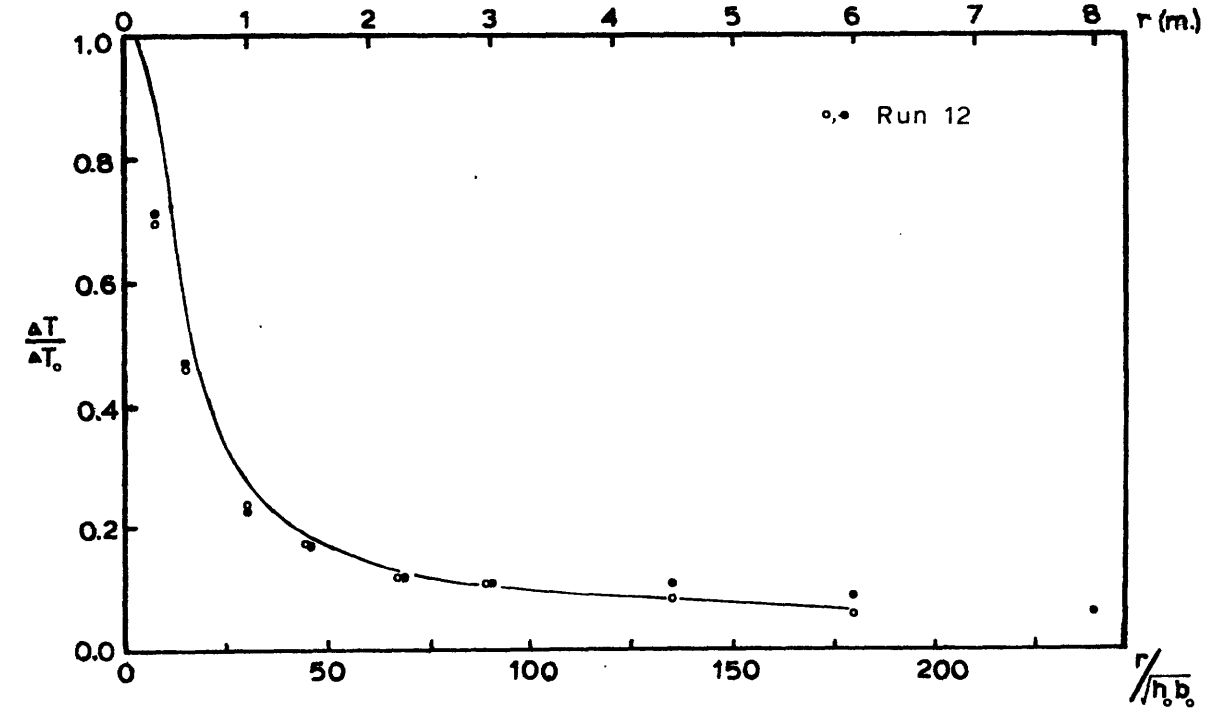

Figure 8.11a Temperature vs. Distance, Experimental Comparison to Model

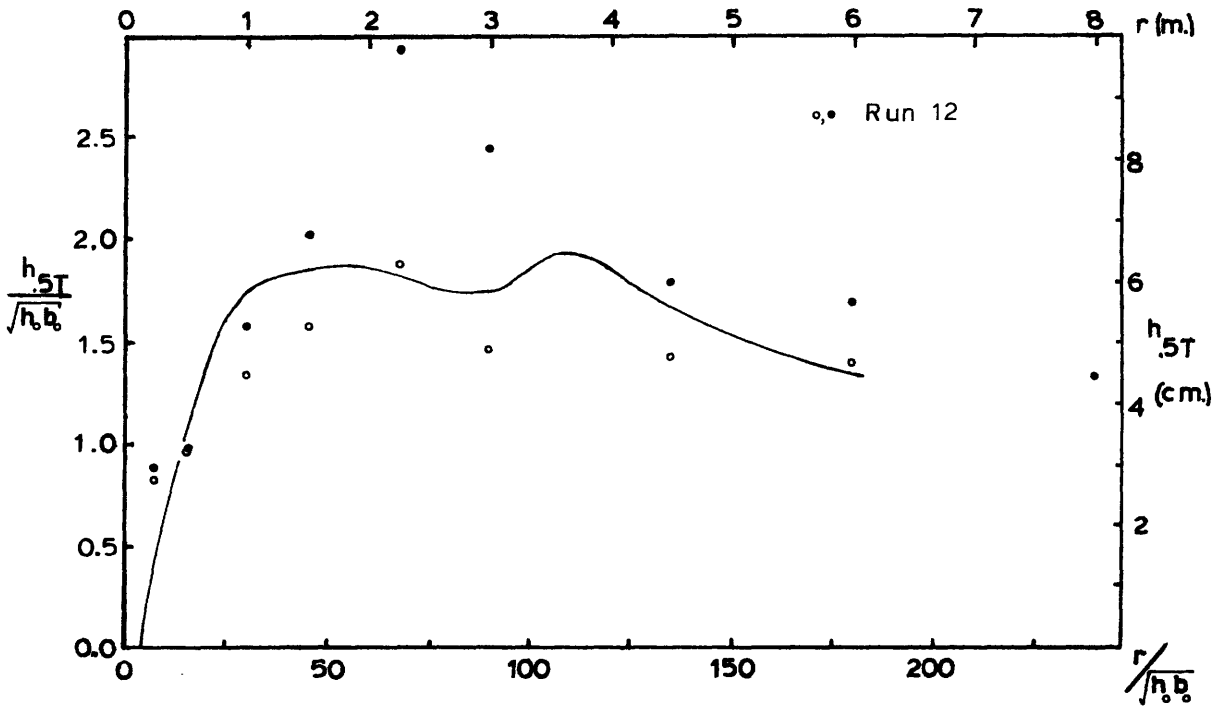

Figure 8.11b Half Temperature Depth vs. Distance, Experimental Comparison to Model

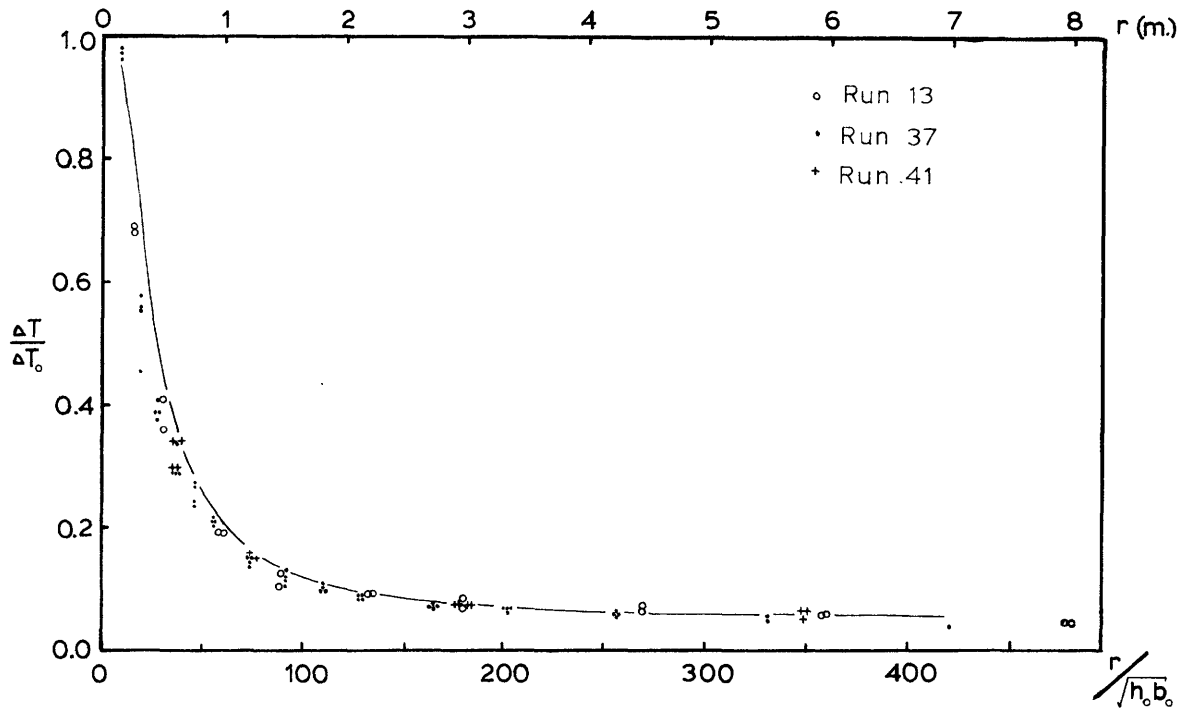

Figure 8.12a Temperature vs. Distance, Experimental Comparison to Model

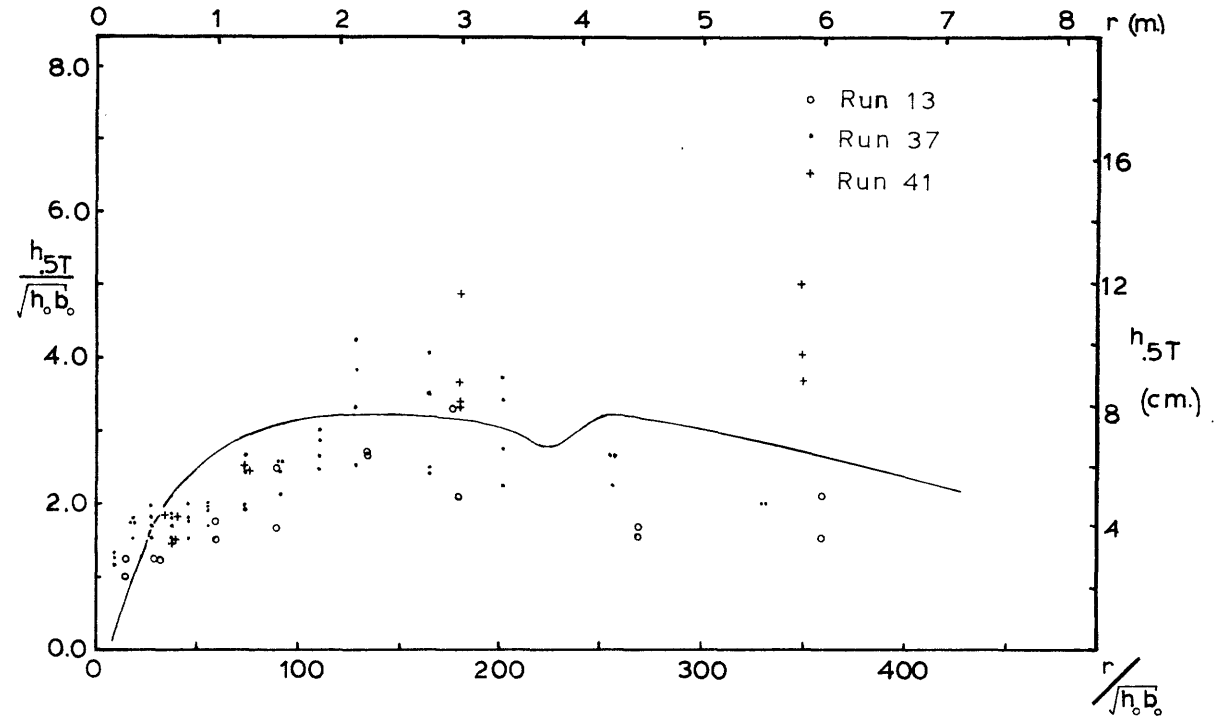

Figure 8.12b Half Temperature Depth vs. Distance, Experimental Comparison to Model

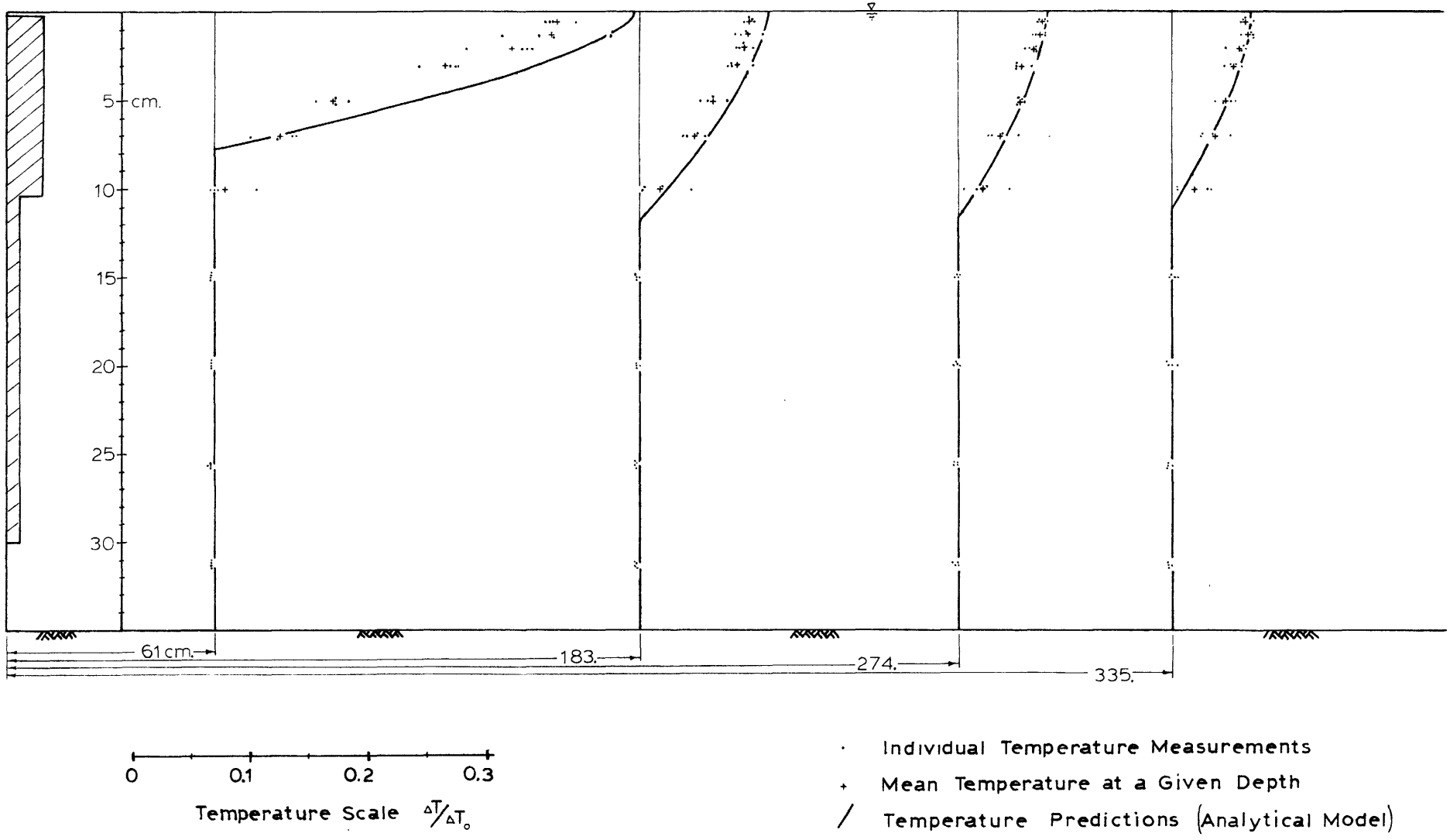

Figure 8.13 Temperature Profile Comparison Between Analytical Model and Data (Experiment # 37; Stagnant, Separate Jet Discharge).

All experimental values of centerline temperature and half temperature depth are based on data similar to that displayed in Figure 8.13.

8.4.2 High Froude Number Experiments

The centerline temperature plots (Figures 8.14 to 8.15, "a" series) show good agreement between predicted and observed values. The half temperature depth plots (Fig. 8.14 to 8.15, "b" series) also show good agreement, though with more experimental scatter. This is in contrast to radial experiments for which the maximum jet depth was not predictable for the high Froude number range. The important difference in radial experiments is the absence of a lateral return flow zone. If a radial jet at some point penetrates more than half of the basin depth, less than 50% of the cross-sectional area at that radius is available for return flow. The average return flow velocity exceeds that of the discharge flow.* This is not the case for separate jets. The lateral return flow zone provides a large cross-sectional area for return flow even when the jet reaches the basin floor. The dynamic pressure effects of a fast underlying return flow are not present.

The analytical jet model considers only an infinitely deep receiving water body. Since the discharge jets of experiment 15 did reach the basin floor, the analytical surface jet predictions will become less appropriate for higher discharge Froude numbers. Empirical

*By continuity, the magnitude of flow moving away from the model must be equal to the returning flow.

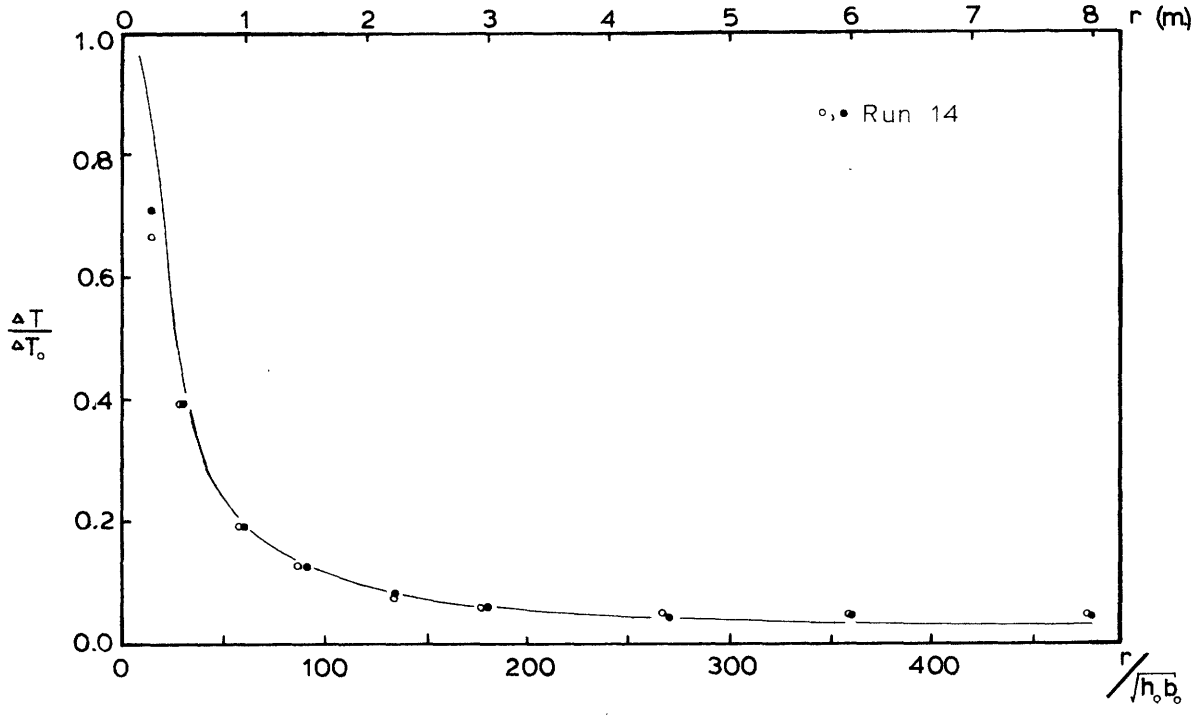

Figure 8.14 a Temperature vs. Distance, Experimental Comparison to Model

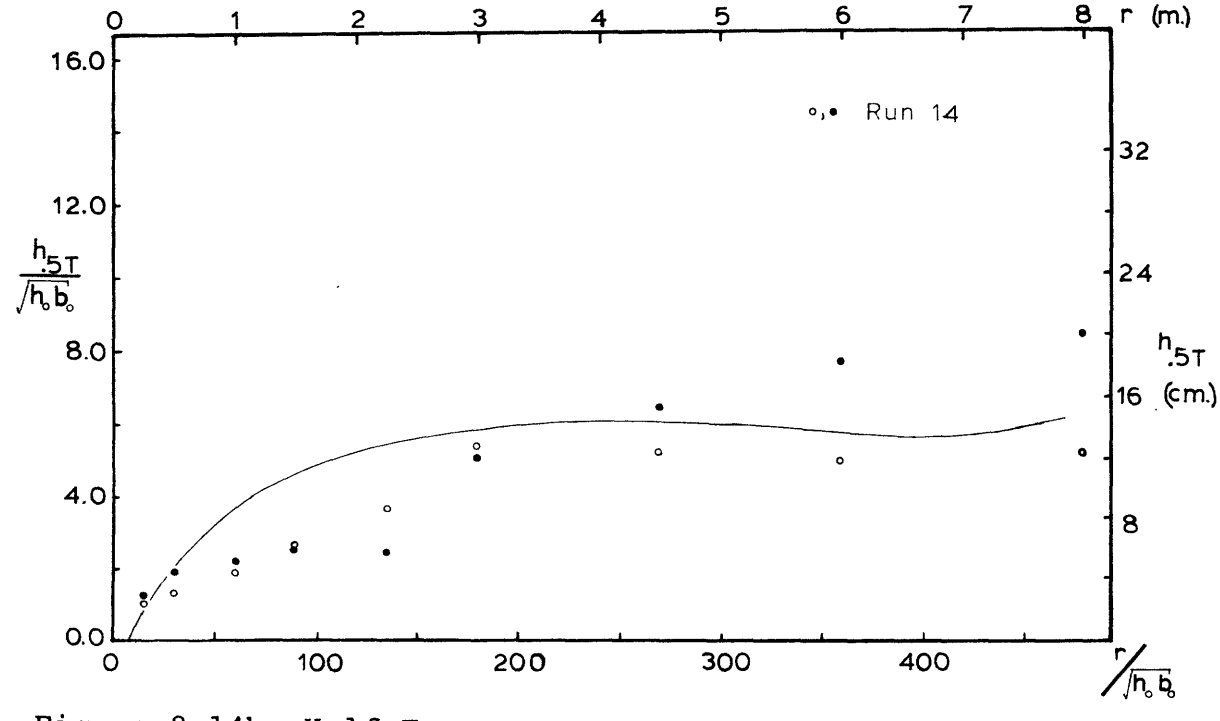

Figure 8.14b Half Temperature Depth vs. Distance, Experimental Comparison to Model

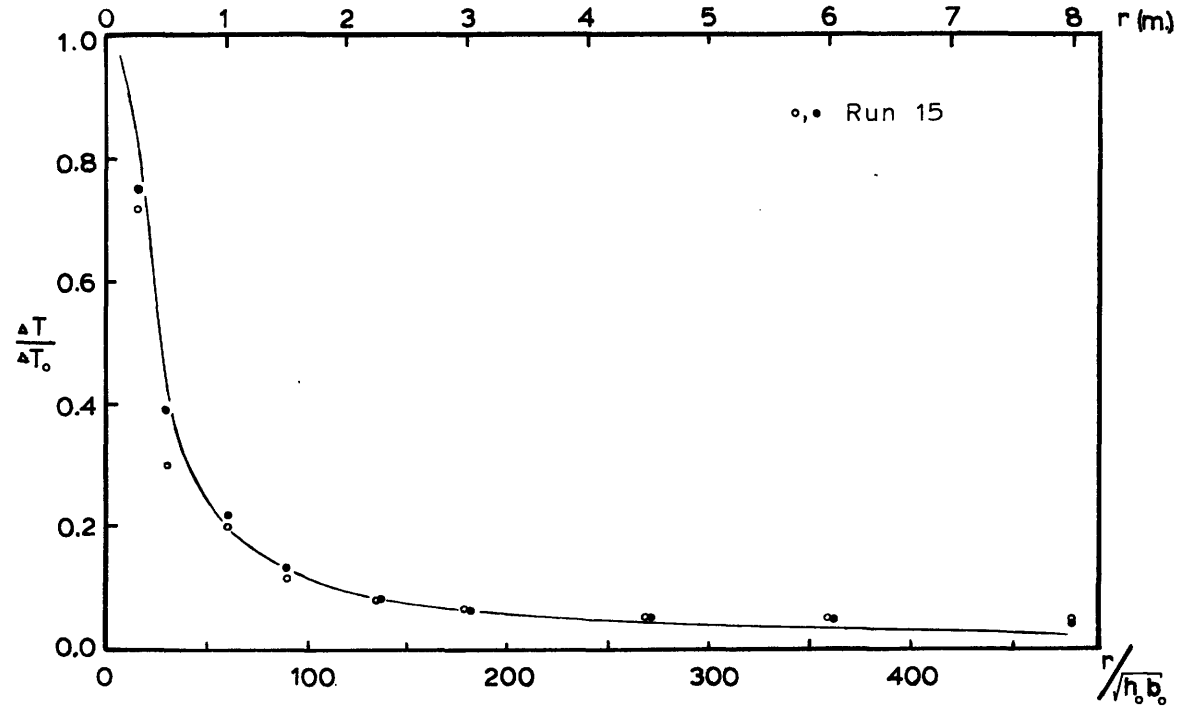

Figure 8.15a Temperature vs. Distance, Experimental Comparison to Model

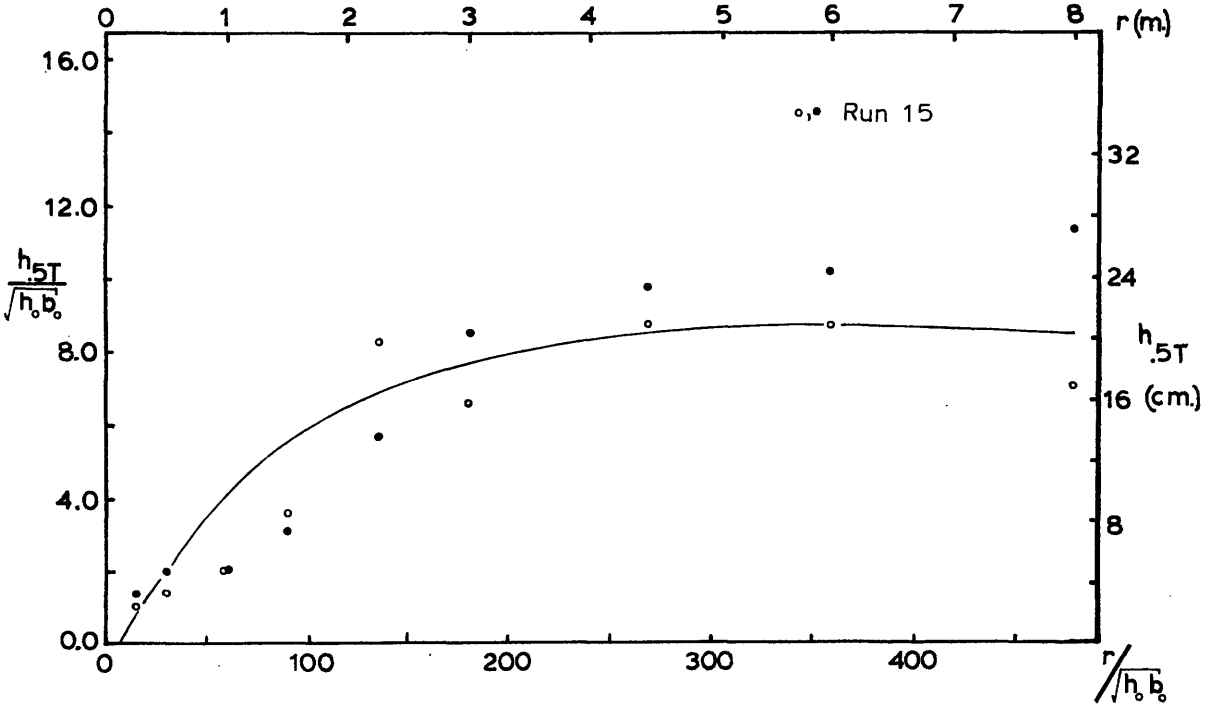

Figure 8.15b Half Temperature Depth vs. Distance, Experimental Comparison to Model

methods exist to take into account the effect of interaction with the bottom (Jirka, Abraham and Harleman, 1975).

8.4.3 Discharge Froude Number Sensitivity

In the analytical model, the local densimetric Froude number, F_L, is indicative of the local jet behavior. This is caused by the dependence of vertical entrainment on F_L (Eq. 7.20). For example, the transition from the near field jet zone to the far field zone is signaled by a F_L of 1.0. Maximum jet penetration occurs for F_L in the range 2.1 to 2.4.

It was desired to compare the model to experimental data at a location of similar behavior for all the stagnant separate jet experiments. Therefore, a local Froude number value was chosen. The analytical model was used to predict at which location each of the experimental runs would reach this value of F_L. Figures 8.16 to 8.18 are the result of comparing experimental jet surface temperature and half temperature depth at these locations with the values predicted by the model. The non-dimensionalized depths and temperatures appear as functions of the discharge Froude number, F_o^*. (As Section 8.3 demonstrated, there should be little or no dependence on the port aspect ratio, h_o/b_o). The solid line is the analytical model prediction. These points are averages of the data taken from each of the jets in the experiment.

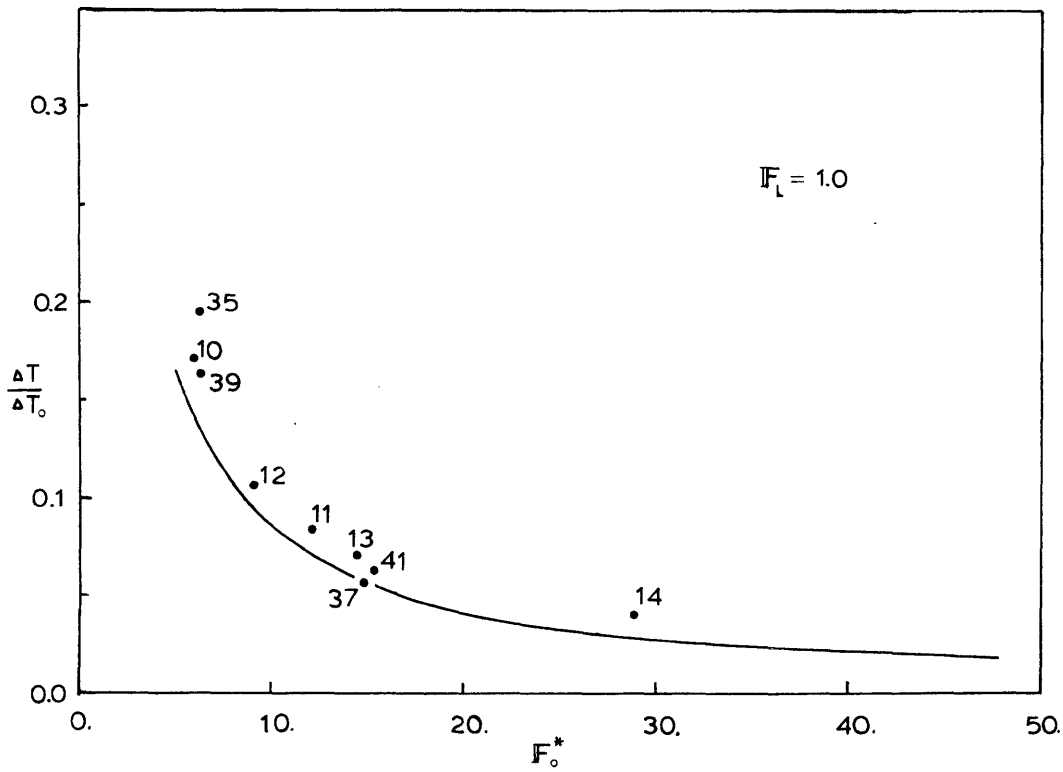

Figure 8.16a Jet Centerline Temperature vs. Discharge Froude Number at the Position of F_L = 1.0

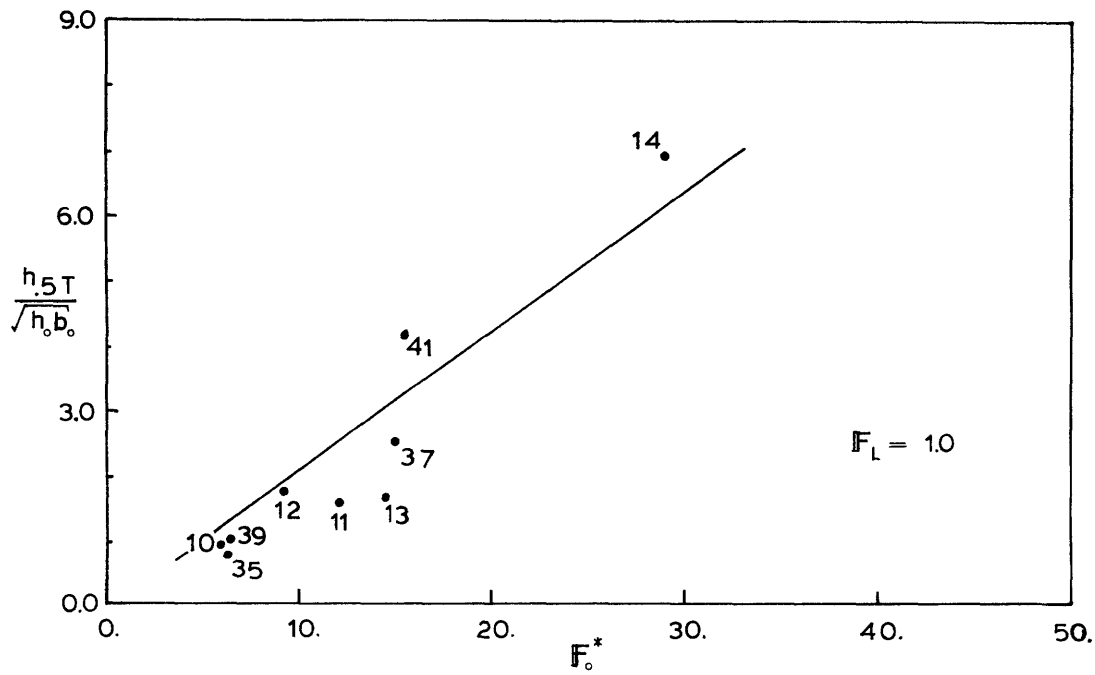

Figure 8.16b Jet Penetration Depth vs. Discharge Froude Number at the Position of F_L = 1.0

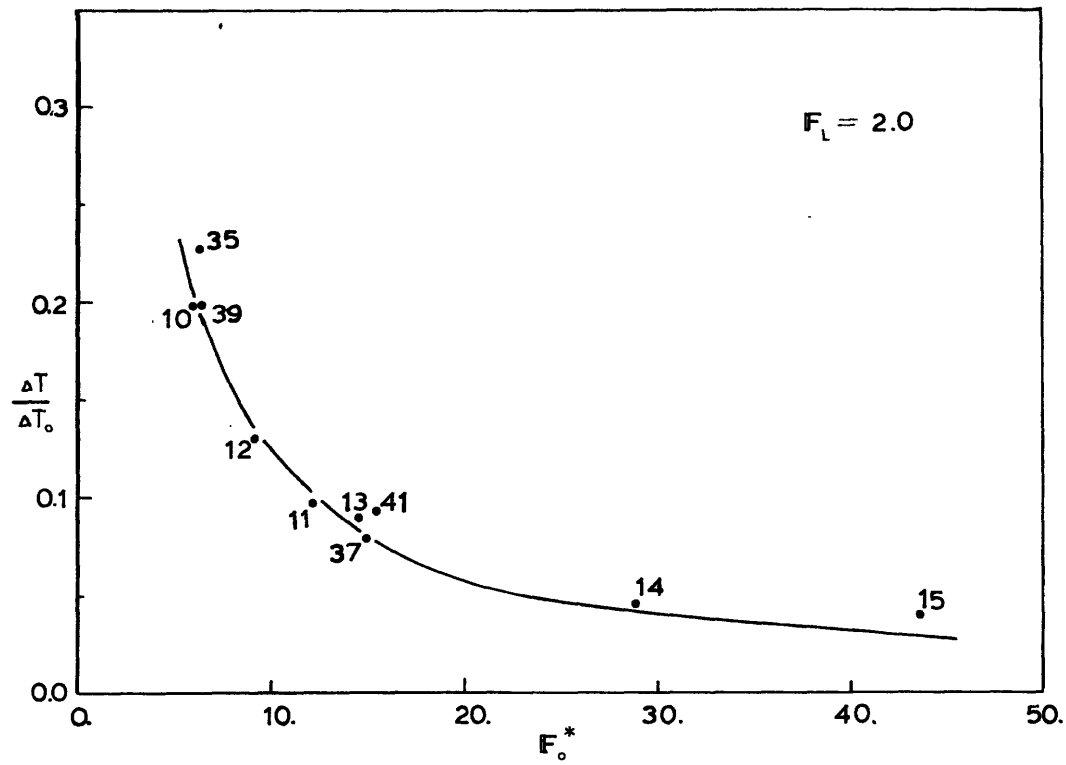

Figure 8.17a Jet Centerline Temperature vs. Discharge Froude Number at the Position of F_L = 2.0

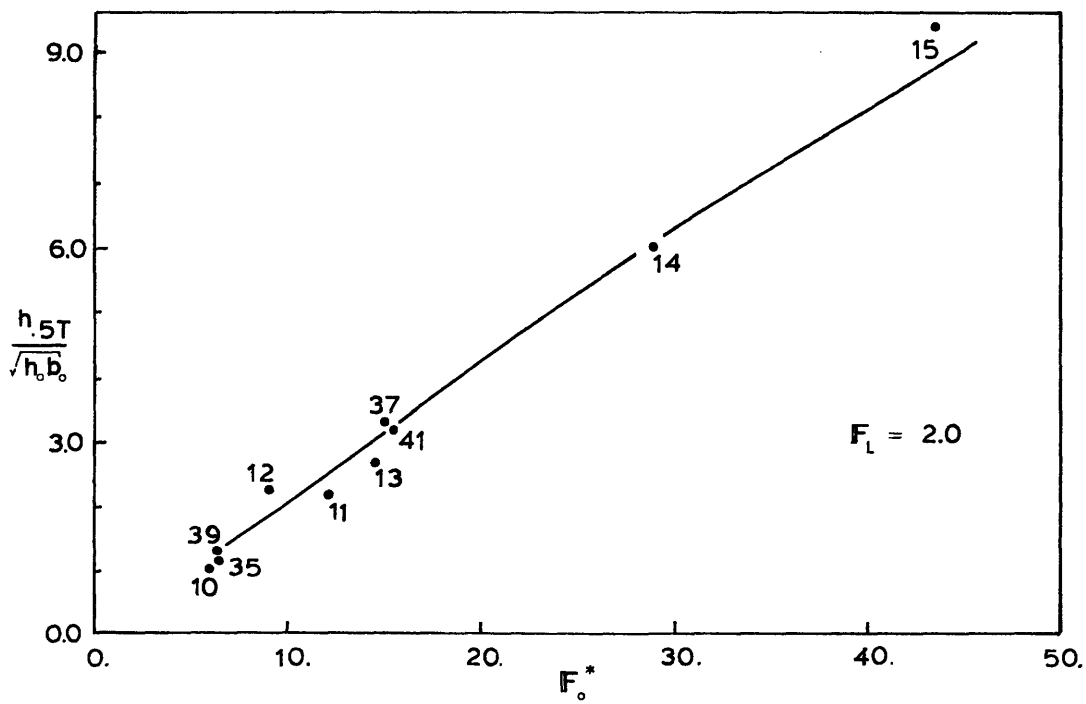

Figure 8.17b Jet Penetration Depth vs. Discharge Froude Number at the Position of F_L = 2.0

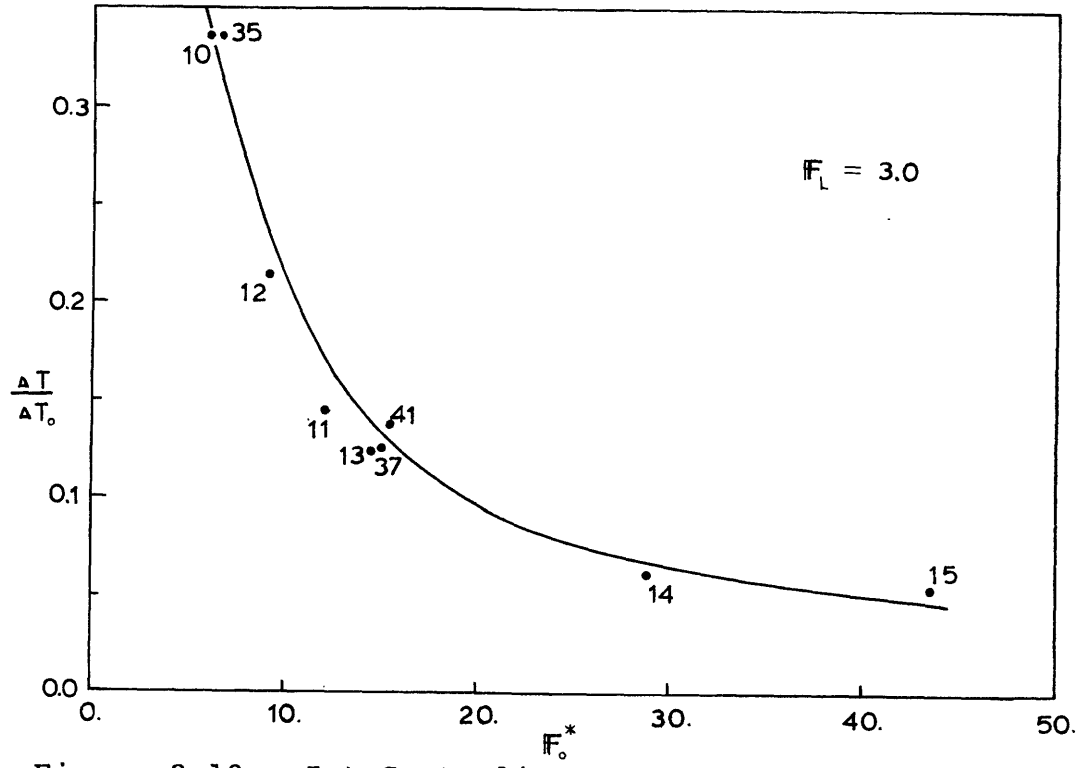

Figure 8.18a Jet Centerline Temperature vs. Discharge Froude Number at the Position of $F_L = 3.0$.

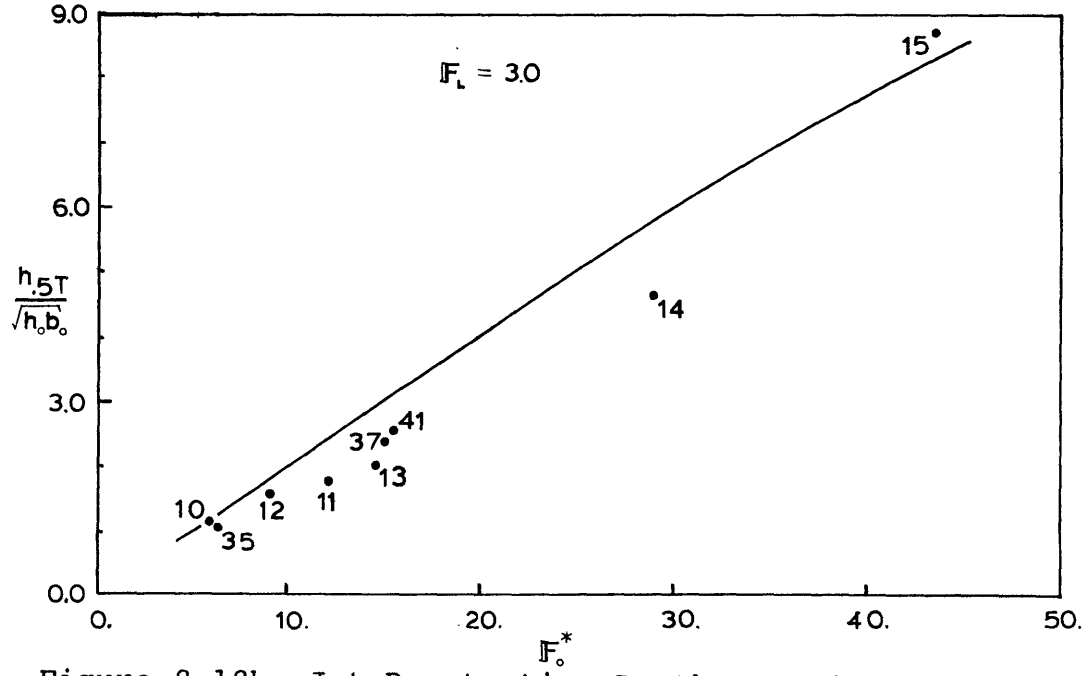

Figure 8.18b Jet Penetration Depth vs. Discharge Froude Number at the Position of $F_L = 3.0$.

Experimental data and analytical predictions are in good agreement in each case. There is a trend in the temperature plot for $\mathbb{F}_{\ell}$ = 1.0 [at the transition to the far field]. Measured temperatures exceed the predicted values indicating reduced dilution probably caused by the lateral return flow (Section 5.3.2). Also, there seems to be a trend to overpredict the penetration depth for $\mathbb{F}_{\ell}$ = 3.0 [while the jets are still deepening].

CHAPTER IX

CONCLUSIONS AND DESIGN CONSIDERATIONS

9.1 Summary

Experimental and analytical studies have been carried out to determine the characteristics of the temperature and velocity fields induced in the surrounding ocean by the operation of an OTEC plant. In particular, the condition of recirculation, i.e., the re-entering of mixed discharge water back into the plant intake, was of interest due to its adverse effect on plant efficiency. The studies were directed at the mixed discharge concept, in which the evaporator and condenser water flows are exhausted jointly at the approximate level of the ambient ocean thermocline. The ocean was assumed to be distinctly stratified and to have a uniform current velocity.

The studies were aimed at a 100 MW "standard" OTEC plant operating at a thermocline depth of about 70 m (see Section 2.2). Considerable variations in the size and the design and operating conditions of this plant were considered. The two major types of discharge geometries were a radial slot around the periphery of the plant and four separate ports at a 90° angle with each other.

In order to simplify the procedure, the experimental program (at an approximate scale of 1:200) was carried out by considering the

flow in the upper layer of the ocean only. The surface layer was modeled in an inverted manner and the actual OTEC discharge at the ocean thermocline was simulated by a model discharge at the surface. The conservativeness of this procedure, regarding the prediction of any recirculation, was demonstrated by analytical techniques.

The analytical studies consisted of the formulation and application of integral jet models for both the radial jet case and the separate jet case. The models predictions are in good agreement with the experimental data and can be used for understanding the discharge behavior (data trends) and for establishing design strategies.

9.2 Conclusions

Based on the combined experimental and analytical results, the following conclusions are made:

i) The major characteristic zones of the temperature and flow field of the OTEC plant are a jet mixing zone and an intake flow zone in the near field (of the order of a few hundred meters in extent) and density and ambient current zones in the far-field. Of these, the jet discharge mixing zone is probably the most important one. Effective jet entrainment causes the accumulation of large quantities of mixed water at the edge of this near-field zone.

ii) This accumulation of fluid masses, which ultimately may result in intake recirculation, is counteracted by two mechanisms:

buoyant convection in the form of density currents and convection by ambient ocean current. The role of the first seems to be the more critical one: the recirculation potential seems highest for the stagnant ocean. Small currents ($\sim$ 0.10 m/s) approach this condition.*

iii) The jet mixing is predominantly controlled by the discharge velocity (i.e. by the discharge area for a given flow rate). The shape of the discharge opening ports appears to have a secondary effect (with radial jets and separate jets representing extremes in the shape effect). This is reflected in the definition of the governing discharge parameter, a densimetric Froude number

$$F_o^* = \frac{u_o}{\sqrt{\frac{\Delta\rho_o}{\rho} g A_o^{\frac{1}{2}}}} \qquad (9.1)$$

where u_o = discharge velocity

$\frac{\Delta\rho_o}{\rho}$ = relative density difference between discharge and upper ocean layer (i.e., one half of the total relative density difference between the upper and lower layer for the mixed discharge concept).

g = gravitational acceleration

*The experimental program was limited to this current range. The conclusion is based in part on the expected reduced recirculation potential for strong ocean currents due to its adequate convection mechanism.

A_o = characteristic area* of discharge =

= area* of one of the four discharge ports or area* of a quarter section of radial discharge slot.

iv) The strength of the intake flow is given by another densimetric Froude number,

$$\mathbb{F}_i = \frac{Q_i}{\sqrt{\frac{\Delta\rho_o}{\rho} g H^5}} \qquad (9.2)$$

where Q_i = intake flow (equal to evaporator flow)

H = upper layer depth

v) A condition of recirculation is generally associated with a high degree of jet discharge mixing and high intake flow rate, i.e., a combination of large values for $\mathbb{F}_o^*$ and $\mathbb{F}_i$. (Alternatively, this situation is described by another set of dependent parameters, namely $\mathbb{F}_{r_o}$ and H/h_o as has been done in the analytical model for the radial jet).

vi) It appears that a "standard" 100 MW OTEC plant under baseline stratification conditions can be designed to operate without near-field recirculation by using a low velocity (low $\mathbb{F}_o^*$) mixed discharge mode at the ocean thermocline. In fact, this recirculation-free operating condition appears to be possible up to the 200 MW range.

*In each case, the area is taken as the "half area" above the thermocline for the symmetric discharge geometry.

9.3 Design Considerations

At this point in time, it appears that the primary design objective for the interaction of an OTEC plant with the ocean environment must be the prevention of a degree of recirculation that would cause a "significant" loss of heat engine efficiency. An efficiency loss carries a considerable economic burden. Based on an analysis of early OTEC engineering designs Lavi (1975) proposed the following relationship between plant unit costs C and the thermal resource ΔT_o.

$$C \sim \Delta T_o^{-2.5} \tag{9.3}$$

As an example, if the base parameter is $\Delta T_o = 20^oC$, a steady recirculation which results in a thermal resource depression by 1^oC (5%) would require an investment increase of 13% per unit power produced. Thus, even modest recirculation influences can have a significant economic impact.

Other OTEC design objectives concerning environmental impacts and plant costs are not as well defined at this time. For example, possibly desirable nutrient enrichment would be caused by the lodging of the condenser discharge somewhere in the photosynthetic mixed layer. But this strategy may be at odds to possibly detrimental effects of thermocline changes and drops in the mixed layer temperature.

Plant construction costs implied by different sized ports and levels of discharge are not obvious. The economy of scale for constructing larger capacity (e.g., 200-300 MW plants) plants is not

known. Deeper discharge levels would seem to mean greater costs due to the need of placing the heat exchangers and heat engine machinery further from the ocean surface. Larger ports imply more piping (greater material costs) and slower discharge velocities (lower pumping costs). As in the case of environmental impacts, the importance of these combinations (in designing an optimal OTEC power plant) have not been quantified.

The desirable strategy of exactly where in the stratified ocean, the OTEC discharge waters should have their sink is not clear. The answer is largely dependent on the analysis of the intermediate field behavior (of order 10 km), its associated phases of buoyant spreading and mass transport and possible interaction with adjacent plants and the far-field behavior (of order 100 km to basin scale) with its effects on thermocline dynamics, surface heat transfer and basin-wide circulations.

Thus, the following design considerations are restricted to the primary objective, namely control of near-field recirculation. However, the experimental and analytical results of this report can be used for the assessment of other design issues as well.

9.3.1 Mixed versus Non-Mixed Discharges

The most basic design choice involves the relative orientation of the condenser and the evaporator discharge flows. In the "mixed mode" concept, the flows are either combined before being discharged close enough together so that the jets merge near the outlet. In the

"unmixed mode", the discharge flows are separated such that there is little or no interaction between them.

It is of utmost importance to differentiate between the consequences of recirculation (usually given as a percentage value) for these two discharge modes. The factor of interest is the temperature decrease δT of the available thermal gradient ΔT (see Eq. 9.3). Simple mass and heat balances for the two design cases yield the following relationships between the normalized resource decrease $\frac{\delta T}{\Delta T}$ and the recirculation fraction, r, of discharged water back into the evaporator intake:

Mixed Discharge:

$$\delta T = r \left\{ \frac{\Delta T_e Q_e + (\Delta T - \Delta T_c) Q_c}{Q_e (1-r) + Q_c} \right\} \tag{9.4a}$$

where Q_e = evaporator flow rate

Q_c = condenser flow rate

ΔT_e = temperature drop of evaporator flow

ΔT_c = temperature drop of condenser flow.

For the usual case of $Q_e \approx Q_c$ and $\Delta T_e \approx \Delta T_c$

$$\frac{\delta T}{\Delta T} = \frac{r}{2-r} \tag{9.4b}$$

Unmixed Discharge (only evaporator flow recirculating):

$$\frac{\delta T}{\Delta T} = \left(\frac{r}{1-r}\right) \frac{\Delta T_e}{\Delta T} \tag{9.4c}$$

Example:

The disparate consequences of discharge recirculation for the two cases is demonstrated for the case, $\Delta T = 20^{o}C$, $\Delta T_e = 2^{o}C$ and $r = 25\%$.

For the mixed discharge,

$$\frac{\delta T}{\Delta T} = 14.3\% \qquad \text{or } \delta T = 2.86^{o}C$$

For the unmixed discharge,

$$\frac{\delta T}{\Delta T} = 3.3\% \qquad \text{or } \delta T = 0.66^{o}C$$

The considerably stronger sensitivity of the mixed discharge mode to agiven value of recirculation is contrasted by its much lower likelihood of occurence. In fact with proper design, the mixed mode can be made to have zero recirculation, while recirculation seems much more likely in the unmixed mode. The experimental results can be used as evidence for this conclusion:

The major part of the experimental program was devoted to the mixed mode of discharge. In this mode, the discharge waters have a $\sim 11^{o}C$ temperature differential from the evaporator intake water. It is the buoyancy effects of this temperature differential that counteracts recirculation tendencies. The basic result of the experimental program was that near-field recirculation could be wholly prevented for this mode discharging into a stagnant or slow current environment. There would be no loss of plant efficiency for plant sizes up to 200 MW.

The "unmixed mode" discharge, on the other hand, has a greater tendency for evaporator intake recirculation than the "mixed mode." This is because of lower temperature and density differentials (2 or $3^{o}C$ rather than $11^{o}C$) between evaporator intake and discharge water. Three of the experiments conducted with smaller temperature differences (Exp. 8, 54 and 55, see Chapter 4) showed definite recirculation based on dye measurements and visual observations. The observed temperature rise, however, was small (less than $0.03^{o}F$) and would not suggest a complete disqualification of the "unmixed" discharge mode from further consideration. The data, however, suggest that in the OTEC range of up to 200 MW the "mixed" mode can be designed with a much higher confidence regarding the prevention of recirculation than the "unmixed" mode.

9.3.2 Design Formula

In Chapter 7, the analytical model for discharge mixing was used in conjunction with the experimental results to determine a criteria for the onset of recirculation

$$\frac{h_{max}}{H} \gtrsim 0.5 \qquad (9.5)$$

In essence, the formula states that recirculation of mixed discharge water back into the evaporator intake will occur if the jet zone, h_{max}, occupies more than 50% of the available mixed layer depth, H. This can be interpreted as a "blocking" of the ambient water flow toward the intake. Since both the analytical studies (Chapter 8) and the experi-

mental data (Chapters 4 and 5) have demonstrated that similar discharge mixing occurs regardless of jet discharge geometry (radial or separate), Eq. 7.23, can be applied in either case as long as h_{max} is given as a function of a Froude number $\mathbb{F}_o^*$. As noted earlier $\mathbb{F}_o^*$ is a Froude number which only depends on the jet discharge area but is independent of its geometry.

Using analytical predictions of jet thickness and assuming simple dependences on the parameters $\mathbb{F}_{r_o}$, r_o/h_o and H/h_o, Eq. 9.5 is modified to

$$8.7\ \mathbb{F}_{r_o}\ [\frac{r_o}{h_o} + 6.3][(\frac{h_o}{H})^{5/2} + 2.6 \times 10^{-5}] \leq 1 \qquad (9.6)$$

applicable for the radial jet geometry and experimental parameter ranges (Table 2.5). With the definition of the discharge Froude number $\mathbb{F}_o$*, Eg. 9.1, the intake Froude number, Eq. 9.2, and the identity $h_o = (2/\pi)(A_o/r_o)$ a more general formula is derived:

$$[1 + 4.0\ (\frac{r_o}{\sqrt{A_o}})^{-2}][1.4\ \mathbb{F}_i + 4.4 \times 10^{-4}\ \mathbb{F}_o^*\ (\frac{r_o}{\sqrt{A_o}})^{5/2}] \leq 1 \qquad (9.7)$$

applicable for <u>any symmetric discharge geometry</u>. Eq. 9.6 can be modified by using the actual design parameters

$$1.39\ [\frac{u_o^3\ r_o}{Q_i\ \frac{\Delta\rho_o}{\rho}\ g}]^{1/2}\ [\frac{r_o^2 u_o}{Q_i} + 1]\ [(\frac{Q_i}{u_o r_o H})^{5/2} + 2.6 \times 10^{-3}] \leq 1 \qquad (9.8)$$

where u_o = discharge velocity

Q_i = evaporator flow rate

r_o = plant radius at discharge ports

H = upper layer depth

$\frac{\Delta\rho_o}{\rho}$ = relative density difference of a mixed discharge with respect to the upper ocean layer

g = gravitational acceleration.

The set of operating parameters above is complete in the sense of determining the recirculation potential of an OTEC plant with a radial, mixed, discharge jet. Recirculation sensitivities can then be studied from Eq. 9.8 by varying one of the parameters while leaving the others fixed:

Recirculation potential increases	Increased discharge velocity,	"u_o"
	Increased flow rate (i.e., plant size)	"Q_i"
Recirculation potential decreases	Increased mixed layer depth,	"H"
	Increased thermal gradient,	"$\frac{\Delta\rho_o}{\rho}$"
Secondary* Recirculation potential changes	Plant radius,	"r_o"

*The range of the other design parameters determine the sensitivity of this parameter.

Thus Eq. 9.8 can be used to assess the recirculation likelihood for specific design concepts and choices of design parameters and

to estimate the effect of variable conditions (such as the seasonal changes in $\Delta\rho_o/\rho$ and H). The restriction to the mixed discharge concept has to be kept in mind, however.

The following examples illustrate the use of the design formula:

A) Standard 100 MW Plant (see Table 2.2):

r_o = 23 m, Q_i = 500 $m^3/5$, u_o = 2 m/s, $\Delta\rho_o/\rho$ = 0.003 (11°C), H = 50 to 100 m.

The left hand side of Eq. 9.8 is denoted by C.

C = 0.4 to 0.1 (as H = 50 to 100 m)

$C \ll 1$ No recirculation likely.

B) 200 MW Plant:

Q_i = 1000 m^3/s, u_o = 8 m/s (comparable to discharge velocities for submerged diffusers), r_o = 23 m

C = 0.9 to 0.5 (as H = 50 to 100 m)

$C < 1$ No recirculation likely, although critical value would be approached for small H and decreases in ΔT_o.

C) 400 MW Plant:

Q_i = 2000 m^3/s, u_o = 8 m/s , r_o = 23 m

C = 1.5 to 0.4 (as H = 50 to 100 m)

$C \sim 1$ Incipient recirculation likely.

On the basis of such perliminary calculations it might be concluded that a maximum possible OTEC plant size which carries a degree of conservativeness (e.g., for the effect of weak currents) would be on the order of 200 MW. Although note that Eq. 9.8 does not predict the degree, r, of

recirculation but only whether recirculation takes place or not.

9.3.3 Intake Design

The sensitivity of the external flow field to evaporator intake design was not treated in the experimental program or the analytical models. The optimal intake level would appear to be as close to the surface as possible (above discharge ports) without causing excessive flow velocities and surface drawdown.

Due to its potential flow characteristics, the flow field is expected to be nearly independent of the intake opening dimensions and horizontal location except in the immediate vicinity of the intake. The intake induced flow accounts for only a portion of the double sink return flow. Specific intake design parameters will only effect that portion and only near the intake opening.

The portion of return flow eventually reaching the plant intake is small. If at a certain distance, a discharge jet has reached dilution of 10, then only 10% of the return flow at that point will eventually enter the intake. Considering the stable dilutions encountered in experiments (Fig. 4.7, 5.6 and 6.4), the intake induced return flow is overwhelmed by that induced by jet entrainment.

For low Froude number discharge configurations, dilution is small and the intake induced return flow is more important. Single sink studies which account for intake geometry and variable stratification (such as Katavola, 1975) may be useful in predicting intake design sensitivities.

REFERENCES

1. Abramovich, G.N., The Theory of Turbulent Jets, M.I.T. Press, M.I.T., Cambridge, Massachusetts, (1963)

2. Albertson, M.L., Dai, Y.B., Jensen, R.A., Rouse, H., "Diffusion of Submerged Jets", Trans. ASCE, 115 (1950)

3. Bathen, K.H., Kamins, R.M., Kornreich, D., Mocur, J.E.T., "An Evaluation of Oceanographic and Socio-Economic Aspects of a Nearshore Ocean Thermal Energy Conversion Pilot Plant in Subtropical Waters", NSF-RANN Grant No. AER74-17421 A01, (1975)

4. Carnahan, B., Luther, H.A., Wilkes, J.O., Applied Numerical Methods, John Wiley and Sons, Inc., New York (1969)

5. Craya, A., "Recherches Theoriques sur L'Ecoulent de Couches Superposees de Fluides de Densites Differntes", LaHouille Blanche, Jan.-Feb. (1949)

6. Daily, J.W. and Harleman, D.R.F., Fluid Dynamics, Addison-Wesley Publishing Co., Reading, Massachusetts (1973)

7. Dugger, G.L. (ed.), "Proceedings, Third Workshop on Ocean Thermal Energy Conversion (OTEC)", Houston, Texas, May 8-10, 1975, Johns Hopkins University, Applied Physics Laboratory, SR75-2 (1975)

8. Fuglister, F.C., Atlantic Ocean Atlas, Temperature and Salinity Profiles and Data from the International Geophysical Yeat of 1957-1958, The Woods Hole Oceanographic Atlas Series, Vol. 1, Woods Hole, Massachusetts (1960)

9. Jirka, G.H., Abraham, G., and Harleman, D.R.F., "An Assessment of Techniques for Hydrothermal Prediction", R.M. Parsons Laboratory for Water Resources and Hydrodynamics, Department of Civil Engineering, M.I.T., Technical Report No. 203 (1975)

10. Katavola, D.S., "An Experimental Study of Three-Dimensional Selective Withdrawal from a Thermally Stratified Fluid System", S.M. Thesis, Department of Ocean Engineering, M.I.T. (1975)

11. Koh, R.C.Y, and Fan, L.N., Mathematical Models for the Prediction of Temperature Distributions Resulting from the Discharge of Heated Water into Large Bodies of Water, EPA Water Pollution Control Research Series 16130 DWO (1970)

12. Lavi, A., "Final Report: Solar Sea Power Project," Carnegie-Mellon University, January 1975.

13. Lee, J.H.W., Jirka, G.H. and Harleman, D.R.F., "Stability and Mixing of a Vertical Round Buoyant Jet in Shallow Water", R.M. Parsons Laboratory for Water Resources and Hydrodynamics, Department of Civil Engineering, M.I.T., Technical Report No. 195 (1974)

14. Schlicting, H., Boundary Layer Theory, McGraw-Hill Book Co., (1968)

15. Slotta, L.S. and Charbeneau, R.J., "Ambient Current Effects on Vertical Selective Withdrawal in a Two-Layer System", Final Project Report, OWR Proj. No. A-025-ORE, Office of Water Research and Technology, U.S. Department of the Interior (1975)

16. Stolzenbach, K.D. and Harleman, D.R.F., "An Analytical and Experimental Investigation of Surface Discharges of Heated Water", R.M. Parsons Laboratory for Water Resources and Hydrodynamics, Department of Civil Engineering, M.I.T., Technical Report No. 135 (1971)

APPENDIX A

EXPERIMENTAL ISOTHERM* DATA

*Isotherms labeled in percent of discharge temperature difference: $(\Delta T/\Delta T_o)*100$

APPENDIX A.1

RADIAL STAGNANT EXPERIMENTS

(see Tables 4.1 & 4.2 for discharge parameter values)

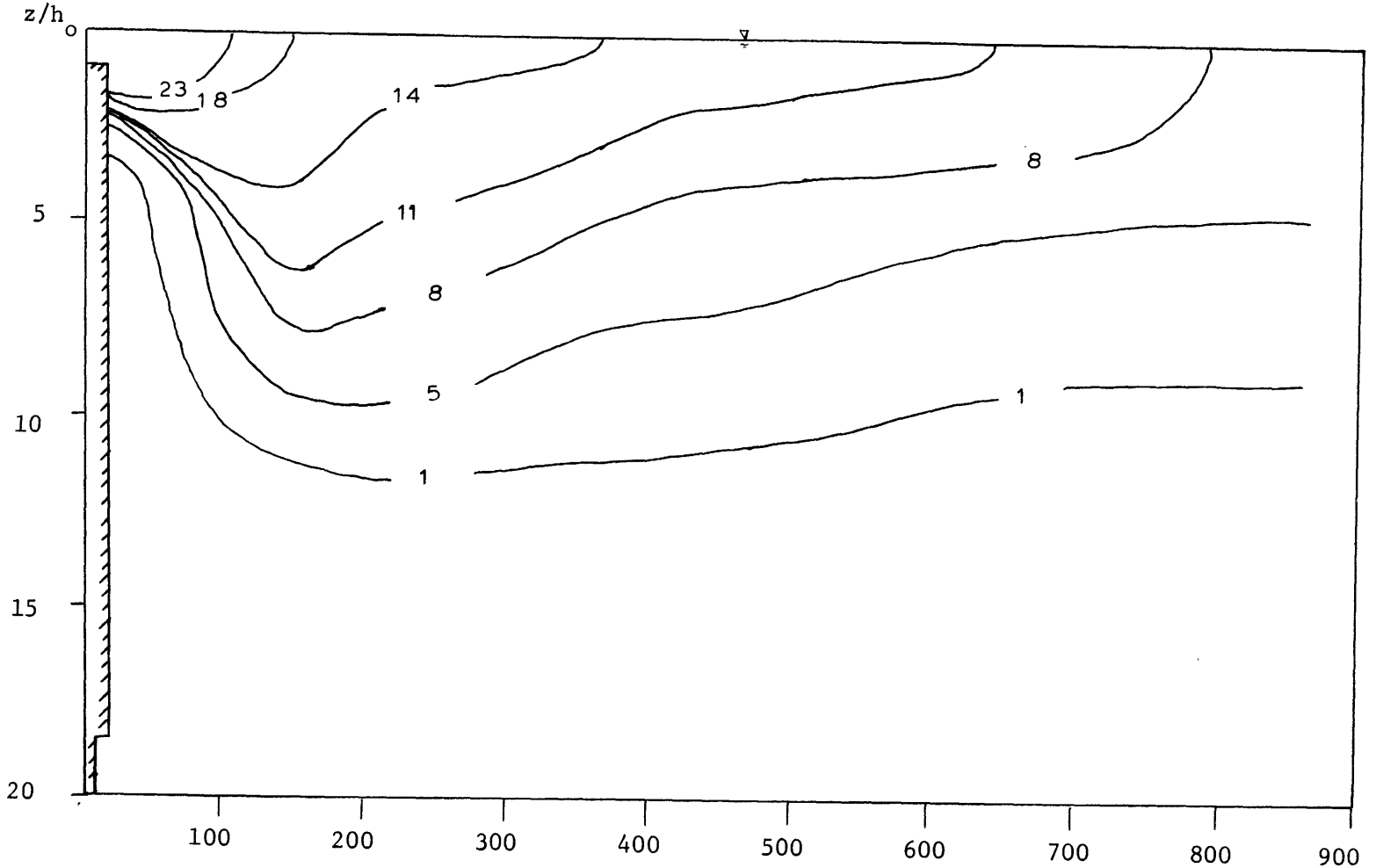

Figure A.1.1 Radially Averaged Cross-Section. Run # 1

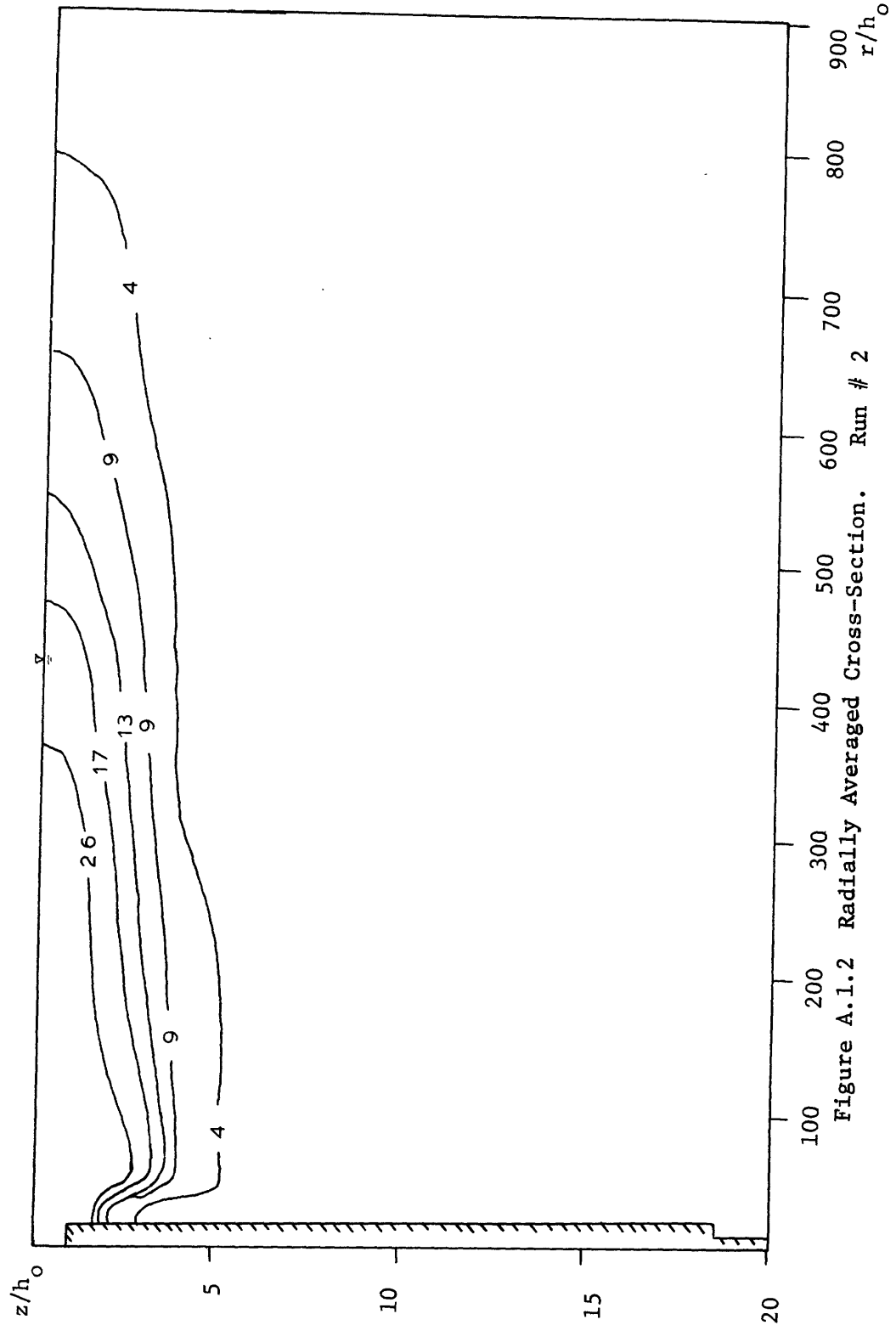

Figure A.1.2 Radially Averaged Cross-Section. Run # 2

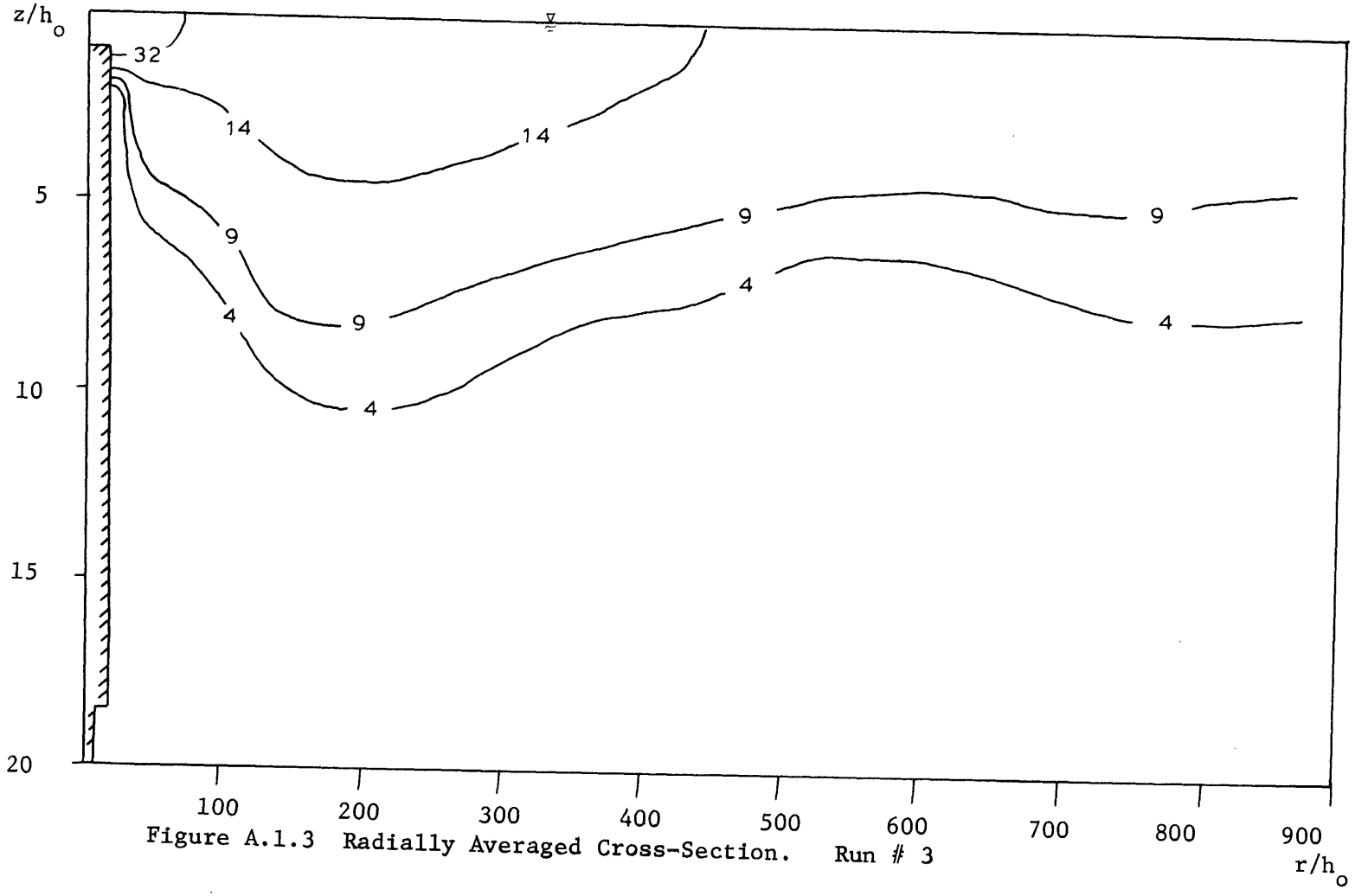

Figure A.1.3 Radially Averaged Cross-Section. Run # 3

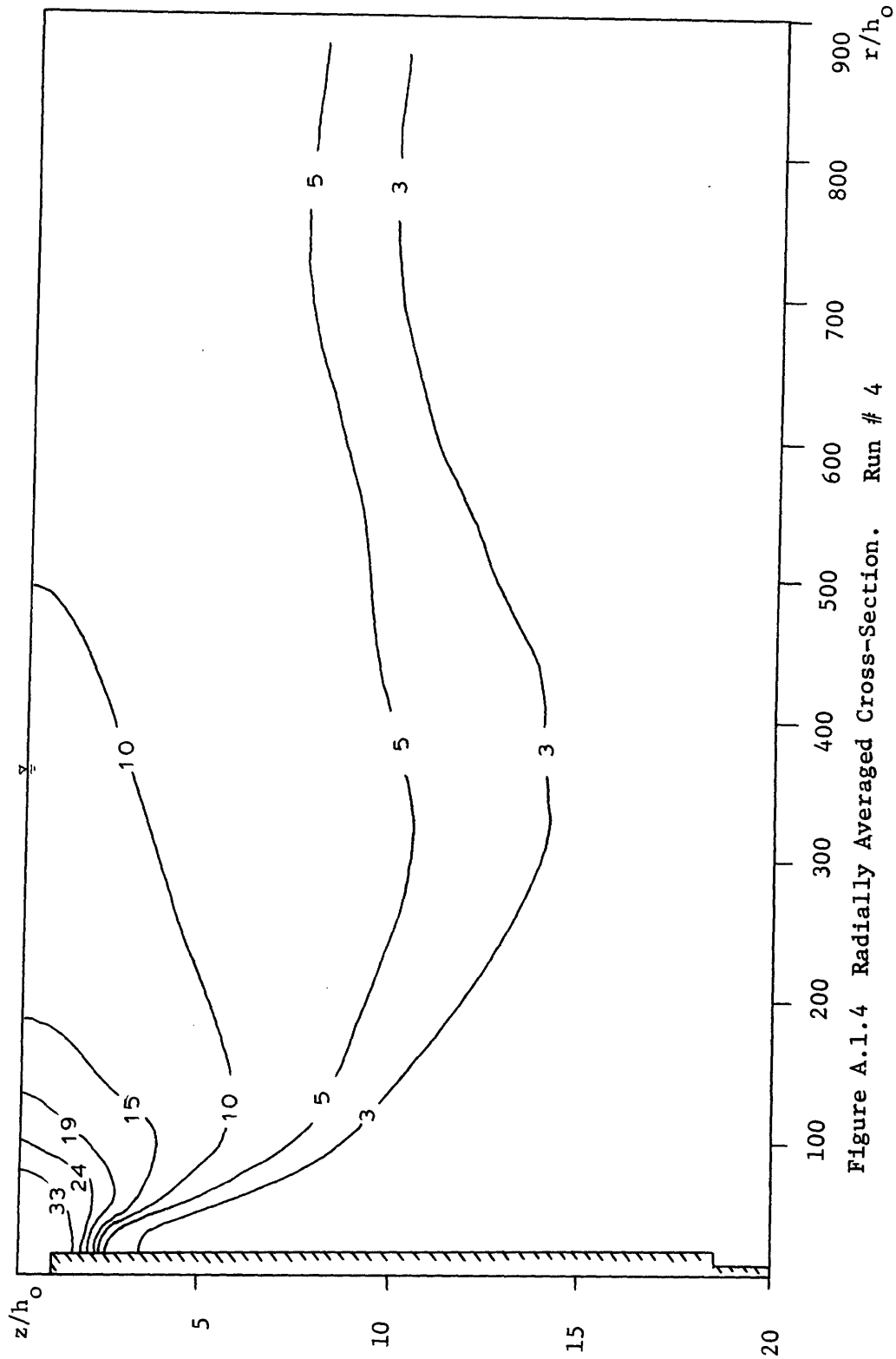

Figure A.1.4 Radially Averaged Cross-Section. Run # 4

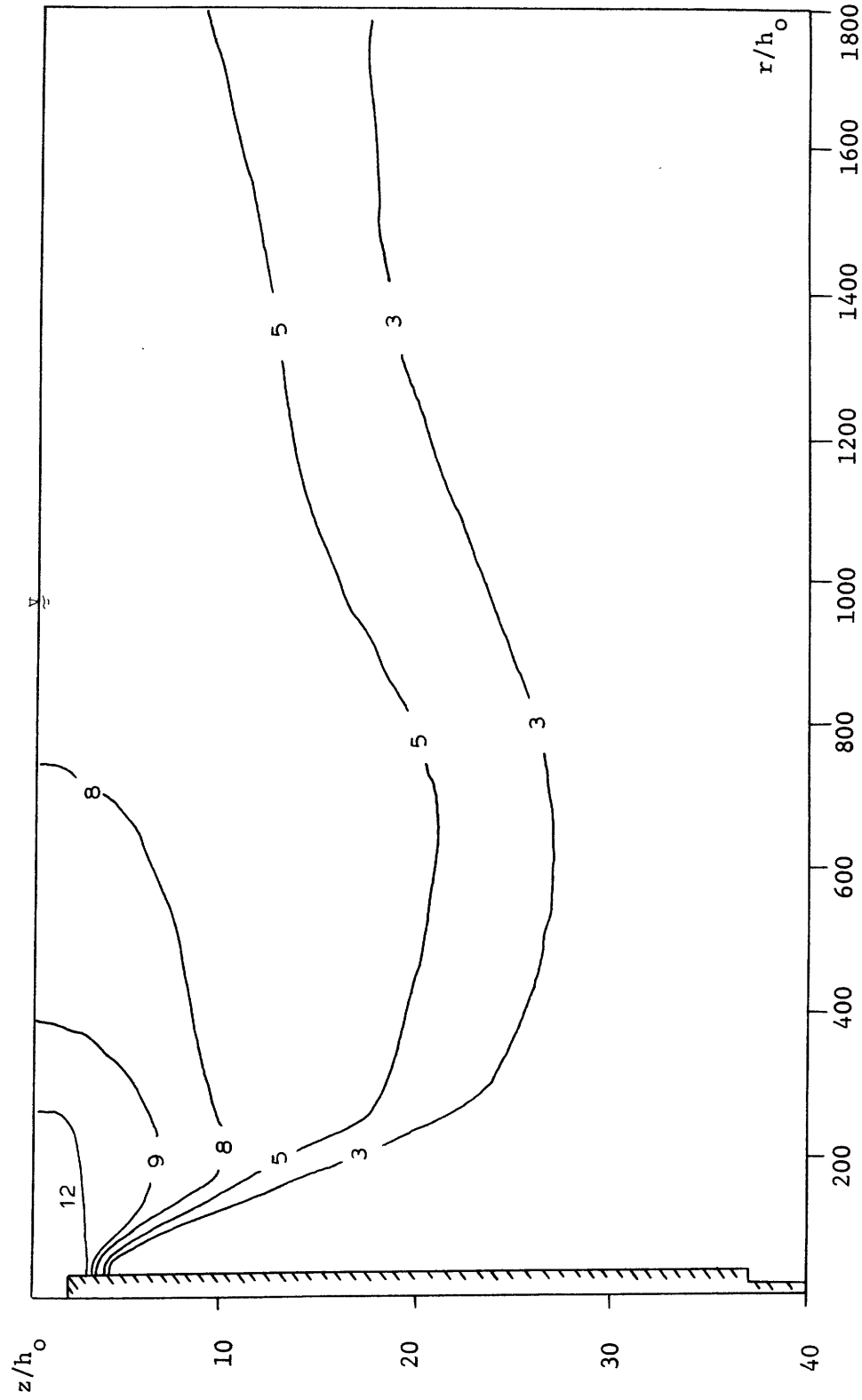

Figure A.1.5 Radially Averaged Cross-Section. Run # 5

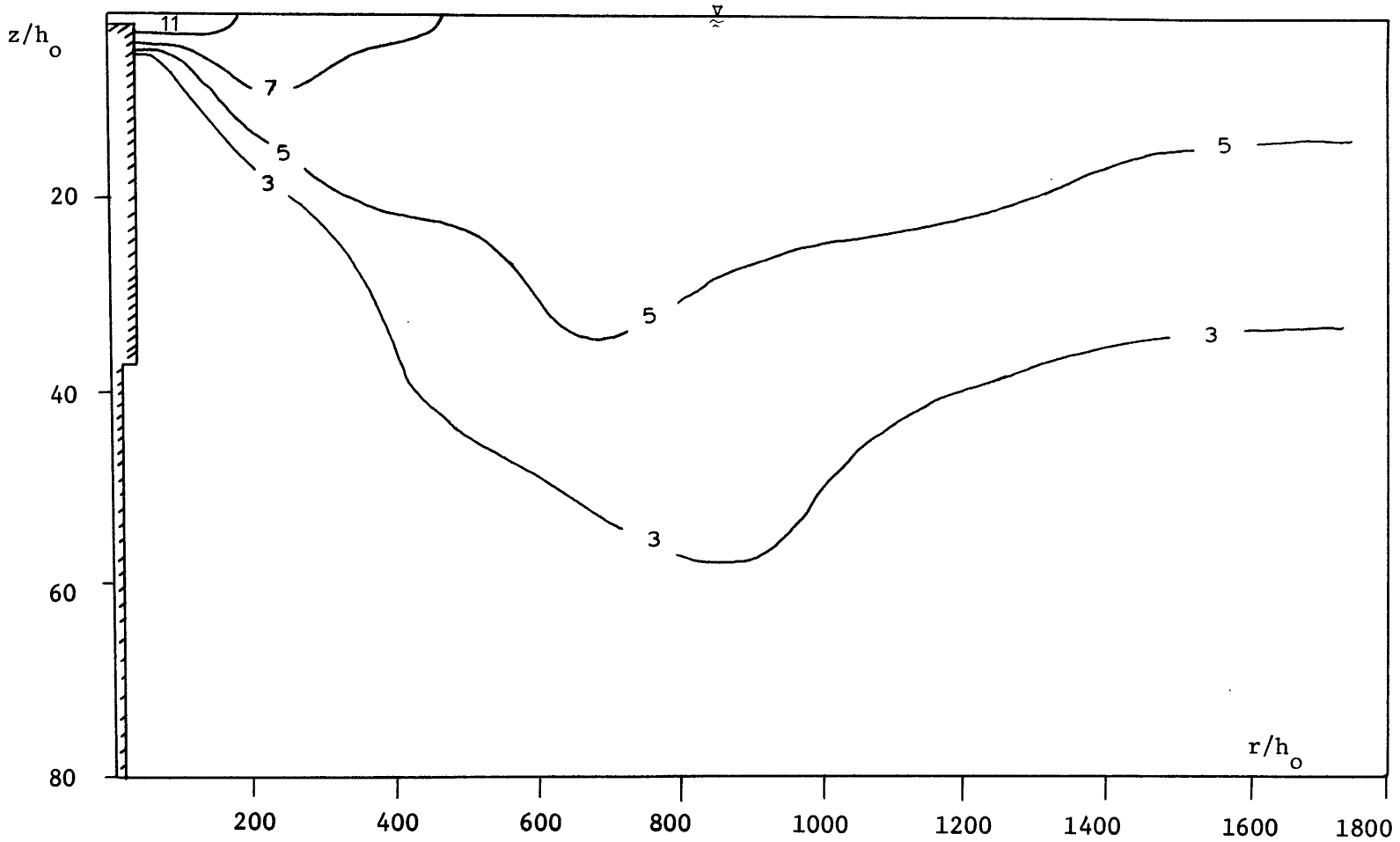

Figure A.1.6 Radially Averaged Cross-Section. Run # 6

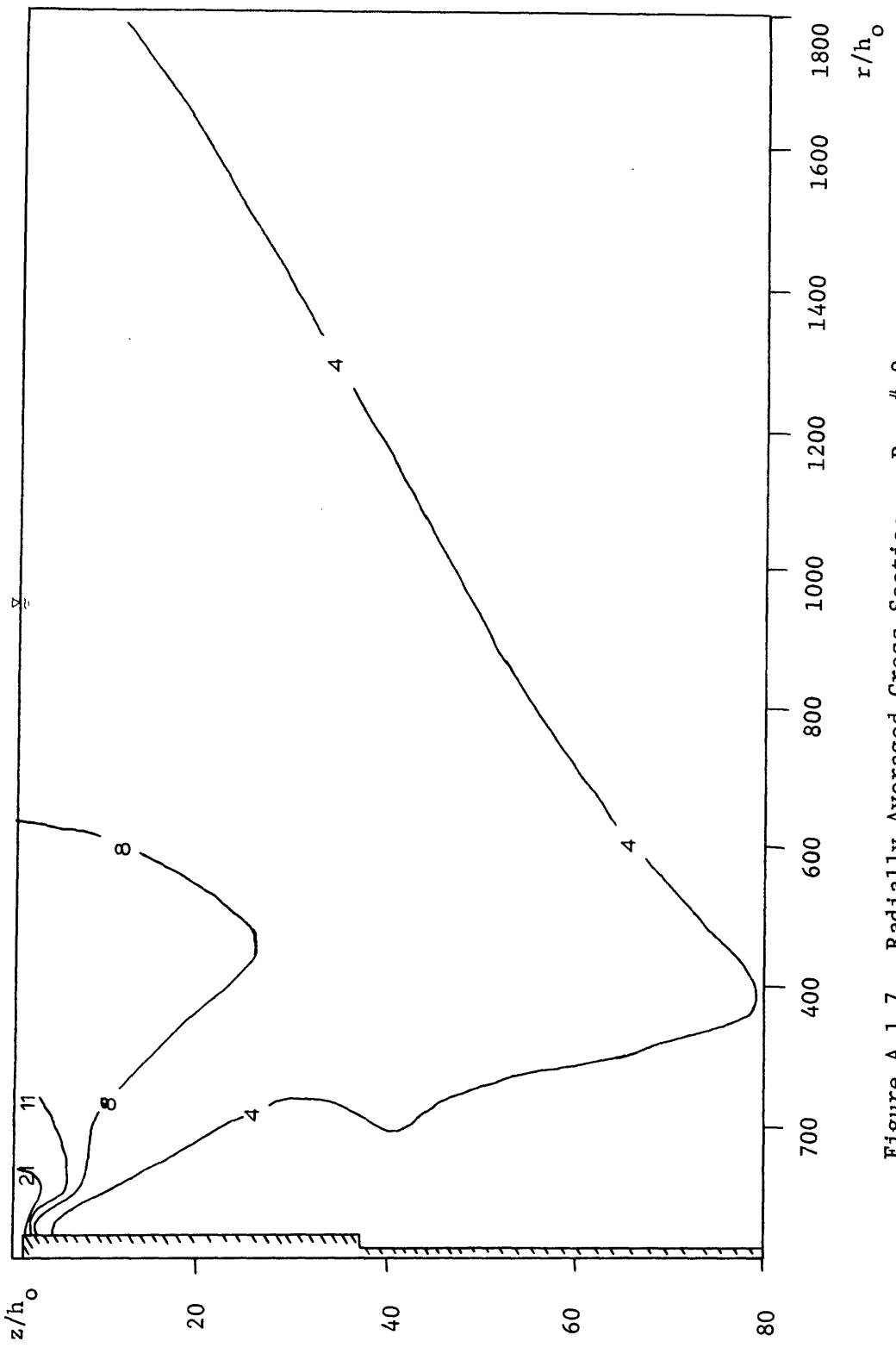

Figure A.1.7 Radially Averaged Cross-Section. Run # 8

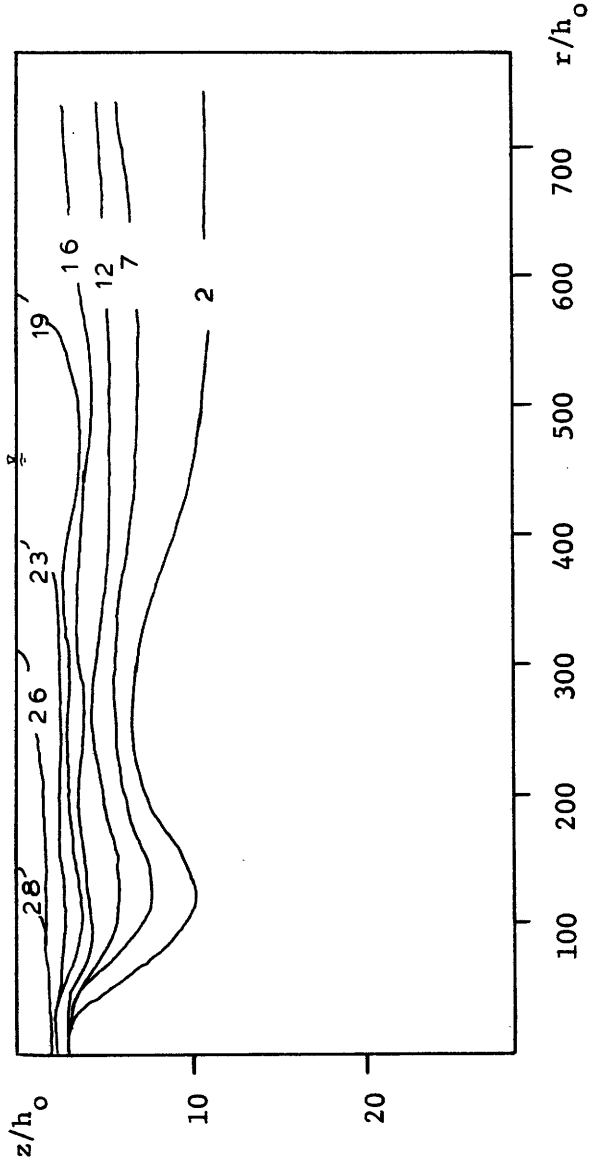

Figure A.1.8 Radially Averaged Cross-Section. Run # 31

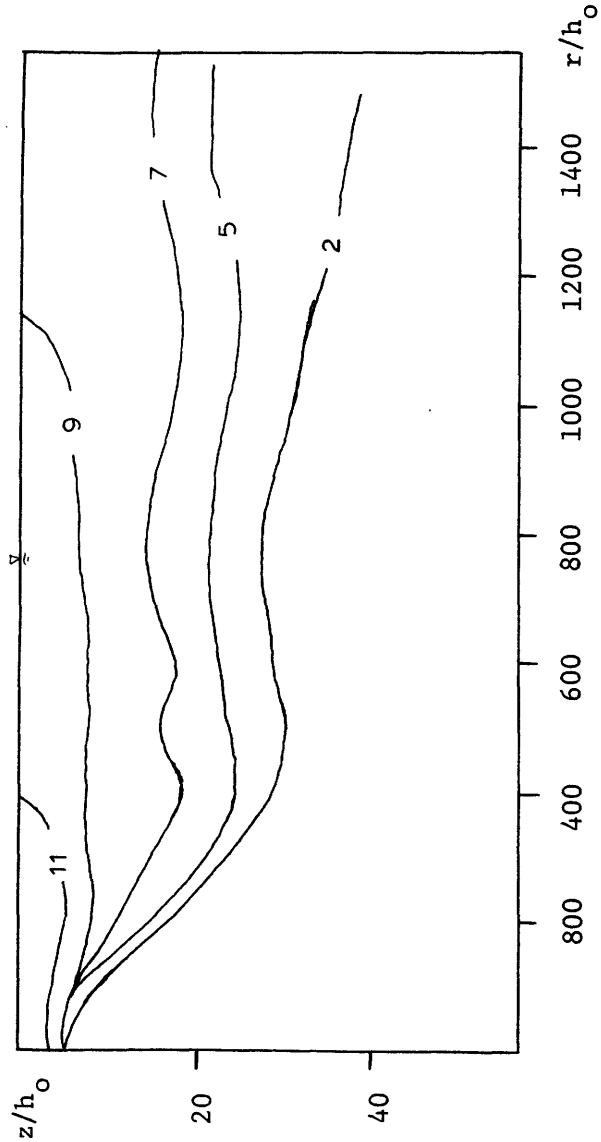

Figure A.1.9 Radially Averaged Cross-Section. Run # 33

APPENDIX A.2

SEPARATE JET*o STAGNANT EXPERIMENTS

(see Tables 5.1 & 5.2 for discharge parameter values)

*The "X" axis in centerline section figures is in the jet centerline direction

cIn the plan views "Jet #1" is directed to the right and "Jet #2" is to the left

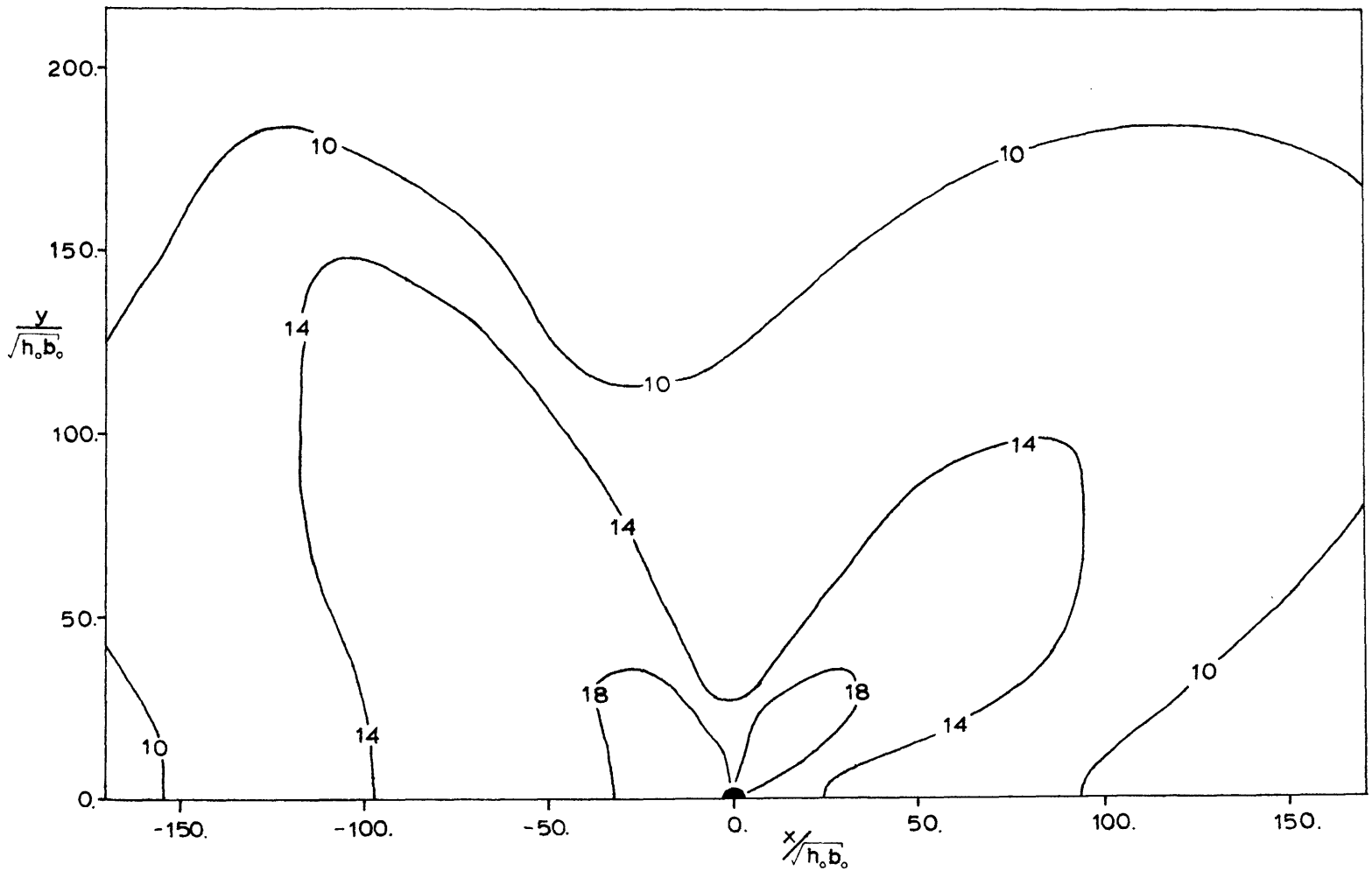

Figure A.2.1 Plan View. Run #10

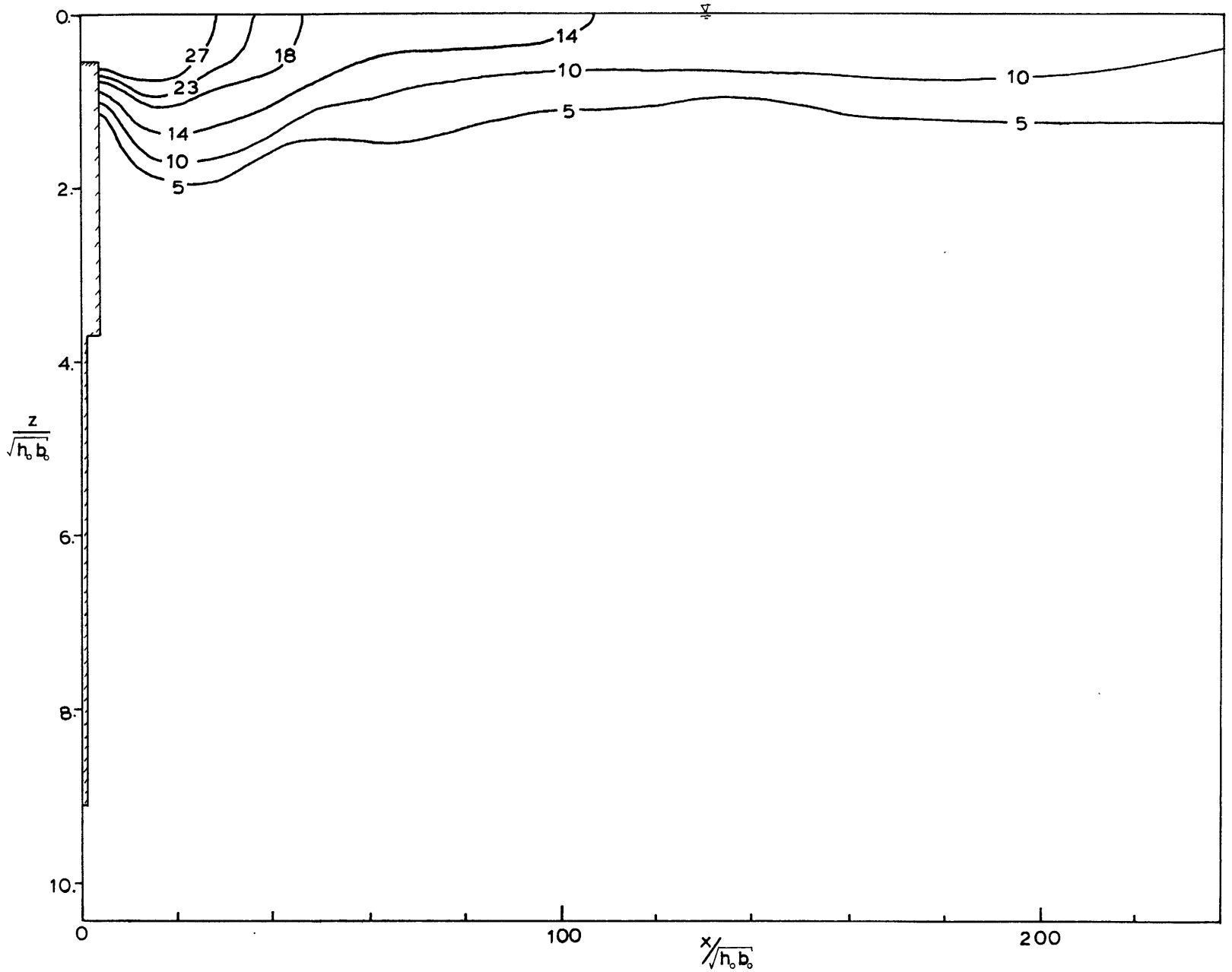

Figure A.2.2 Centerline Section Jet #1. Run #10.

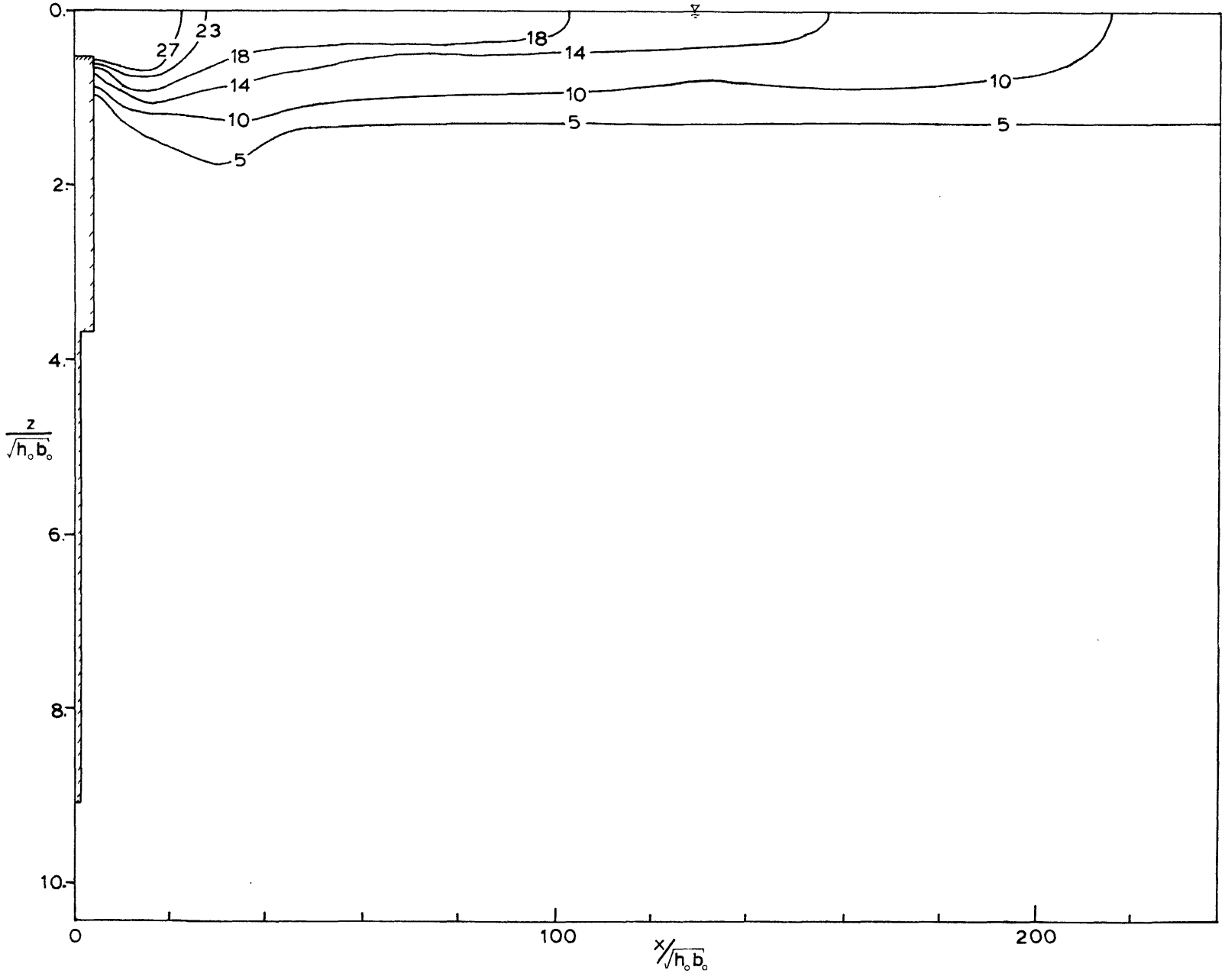

Figure A.2.3 Centerline Section Jet #2. Run #10.

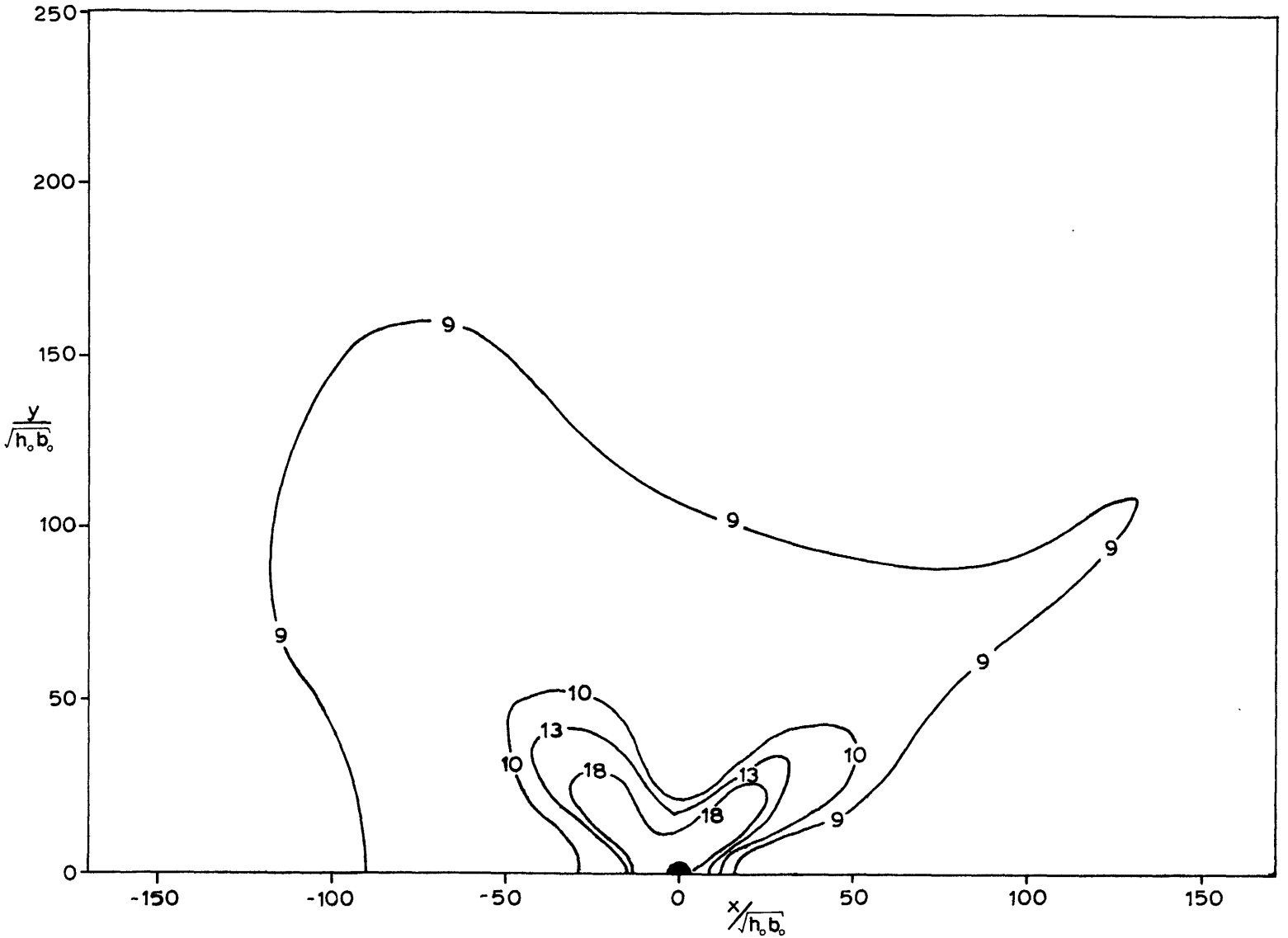

Figure A.2.4 Plan View. Run #11.

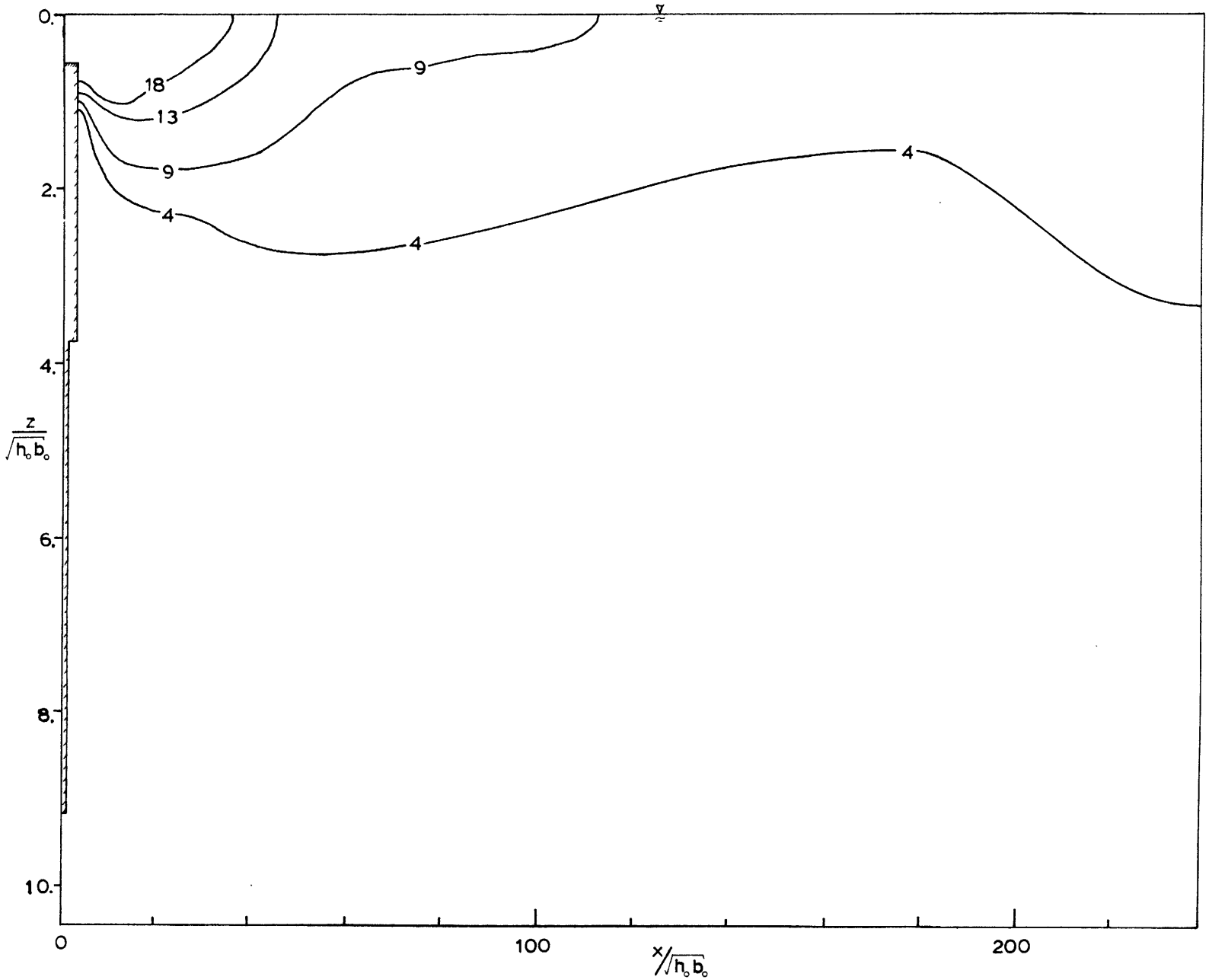

Figure A.2.5 Centerline Section of Jet #1. Run #11.

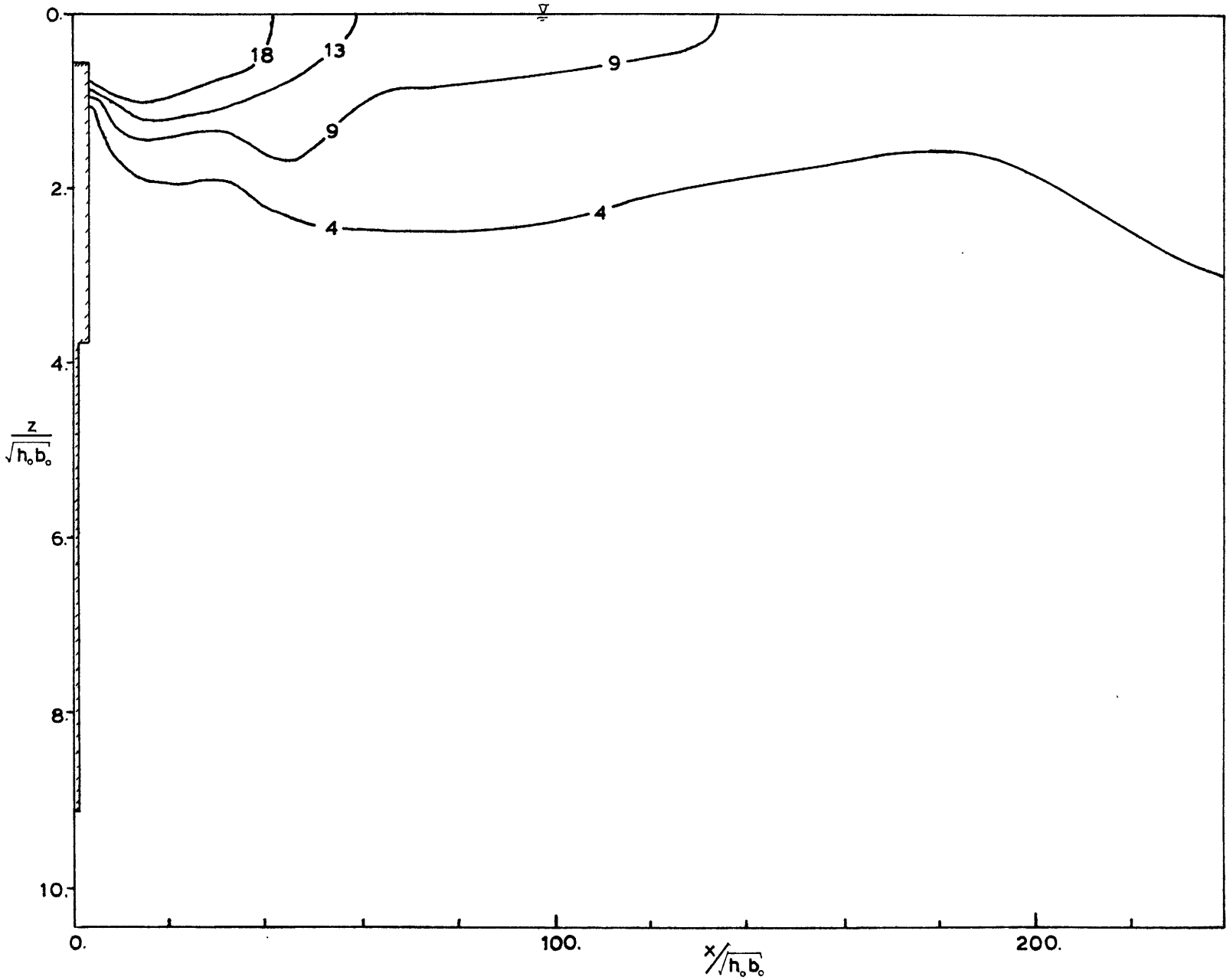

Figure A.2.6 Centerline Section of Jet #2. Run #11.

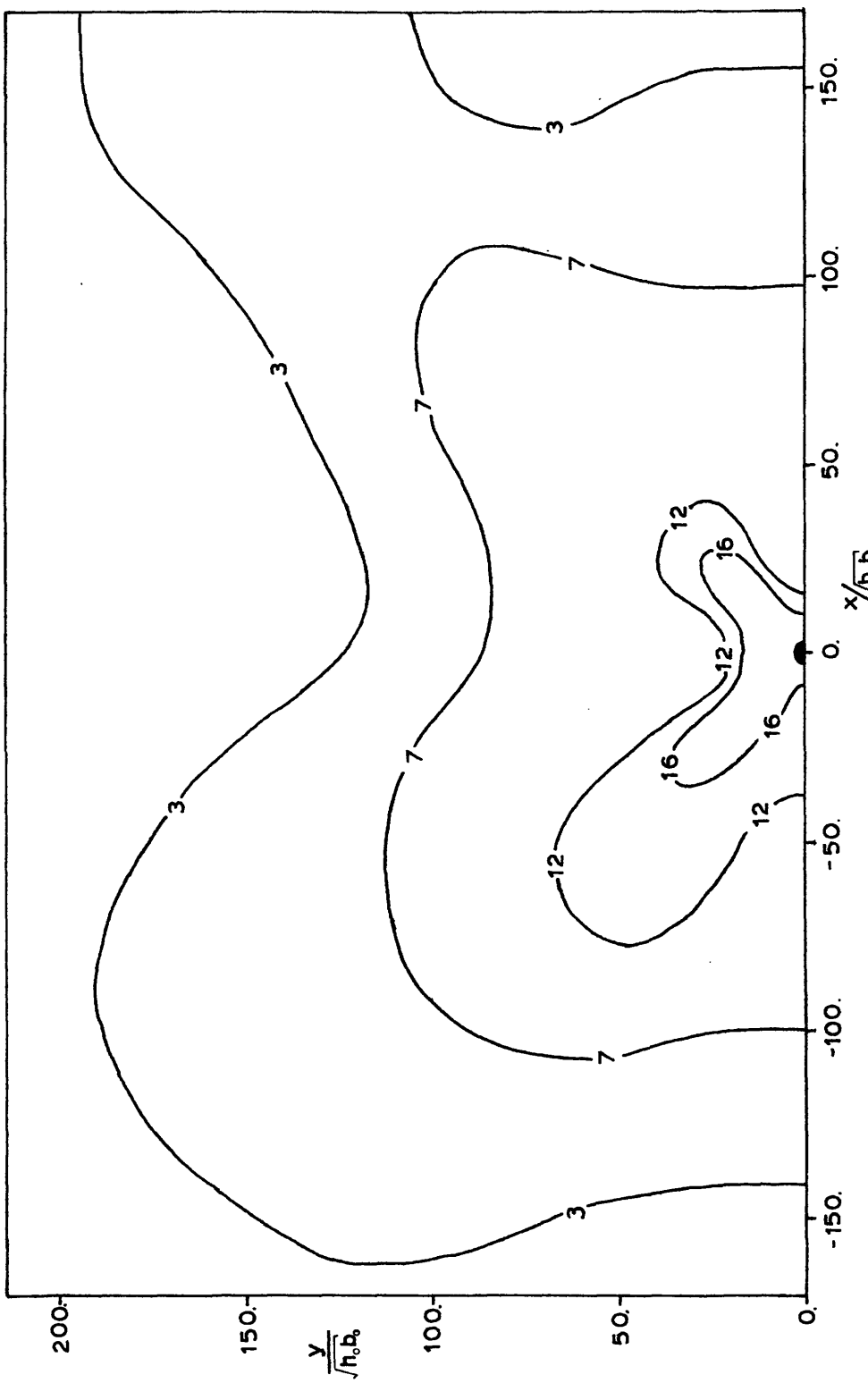

Figure A.2.7 Plan View. Run #12.

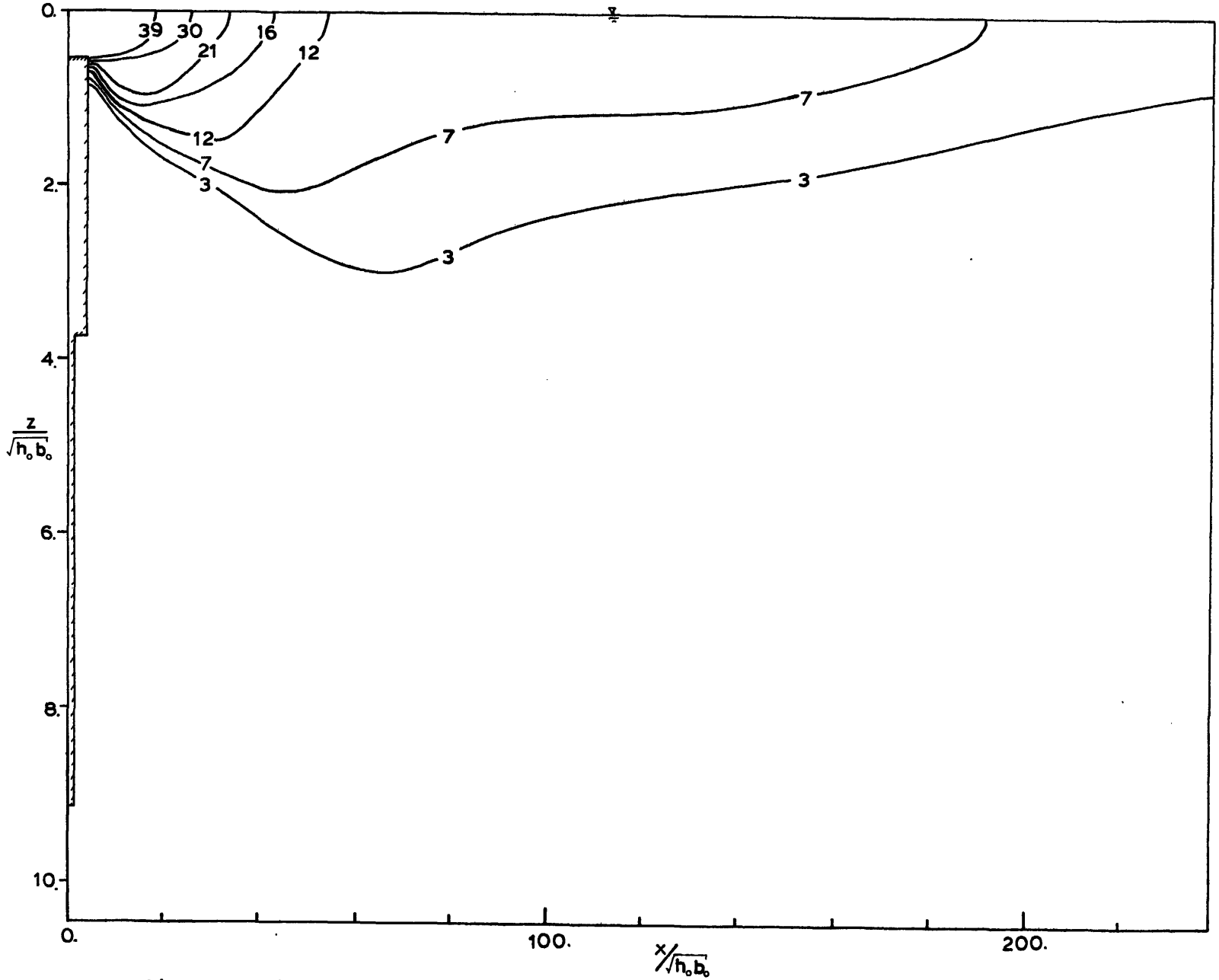

Figure A.2.8 Centerline Section Jet #1. Run #12.

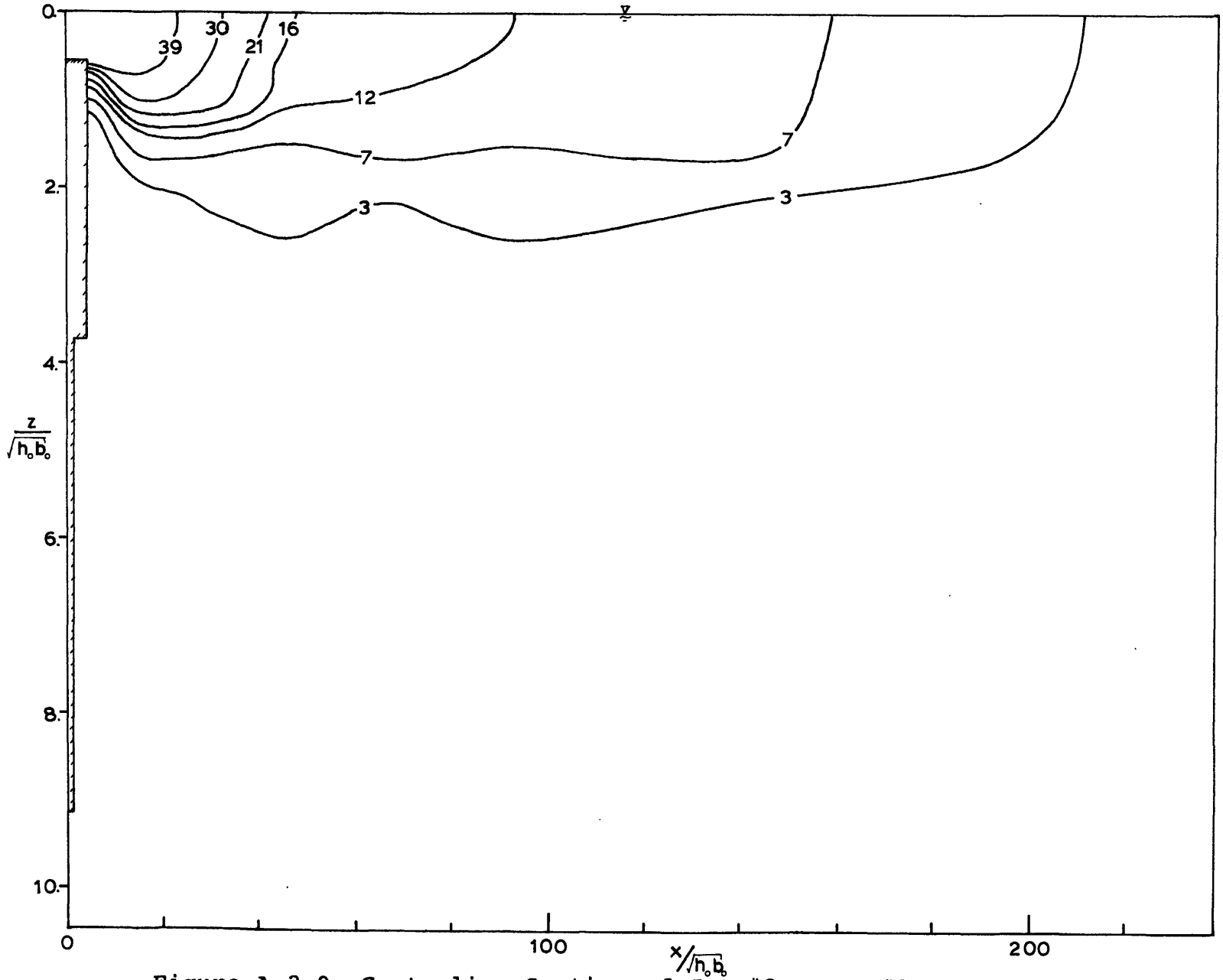

Figure A.2.9 Centerline Section of Jet #2. Run #12.

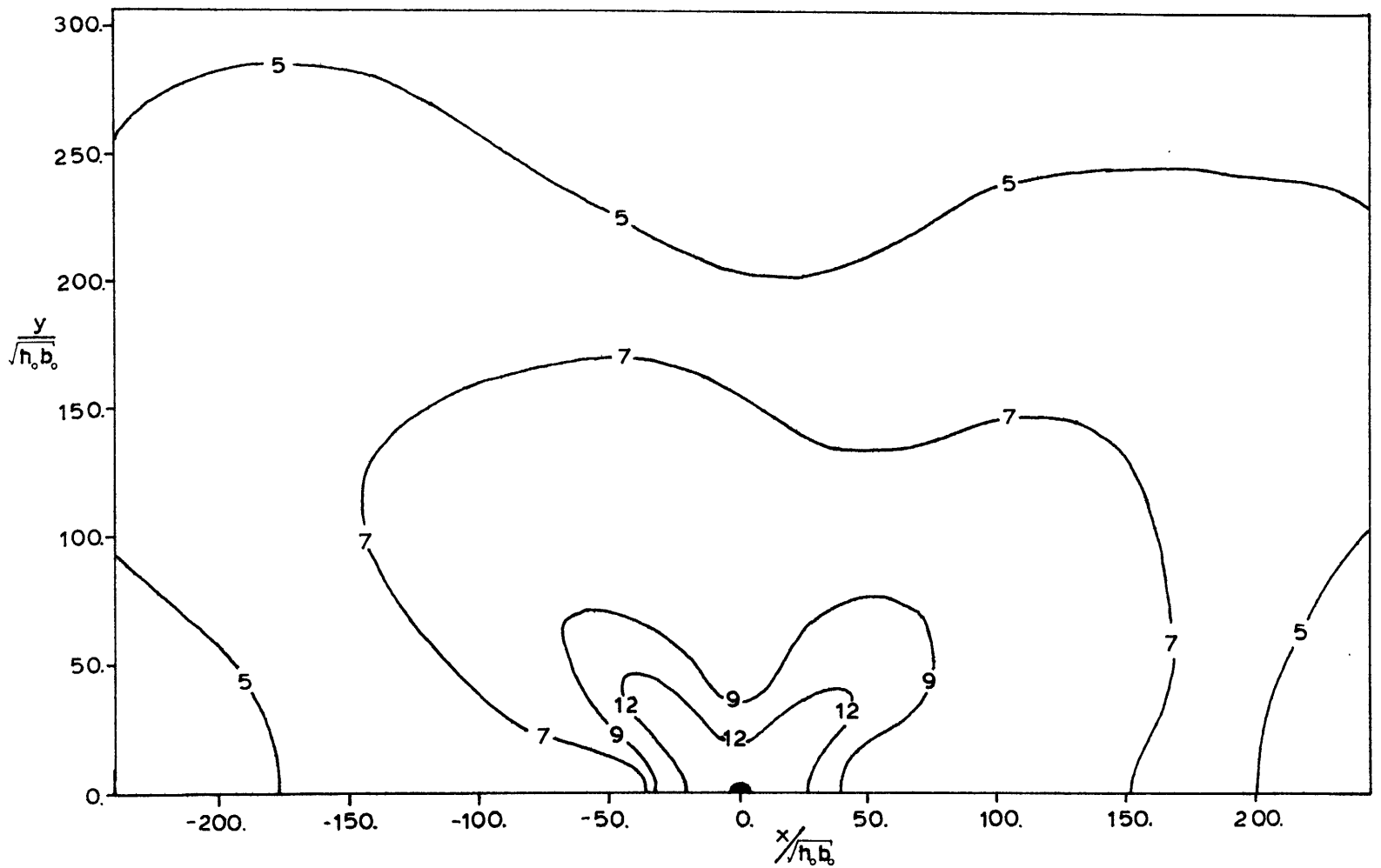

Figure A.2.10 Plan View. Run #13.

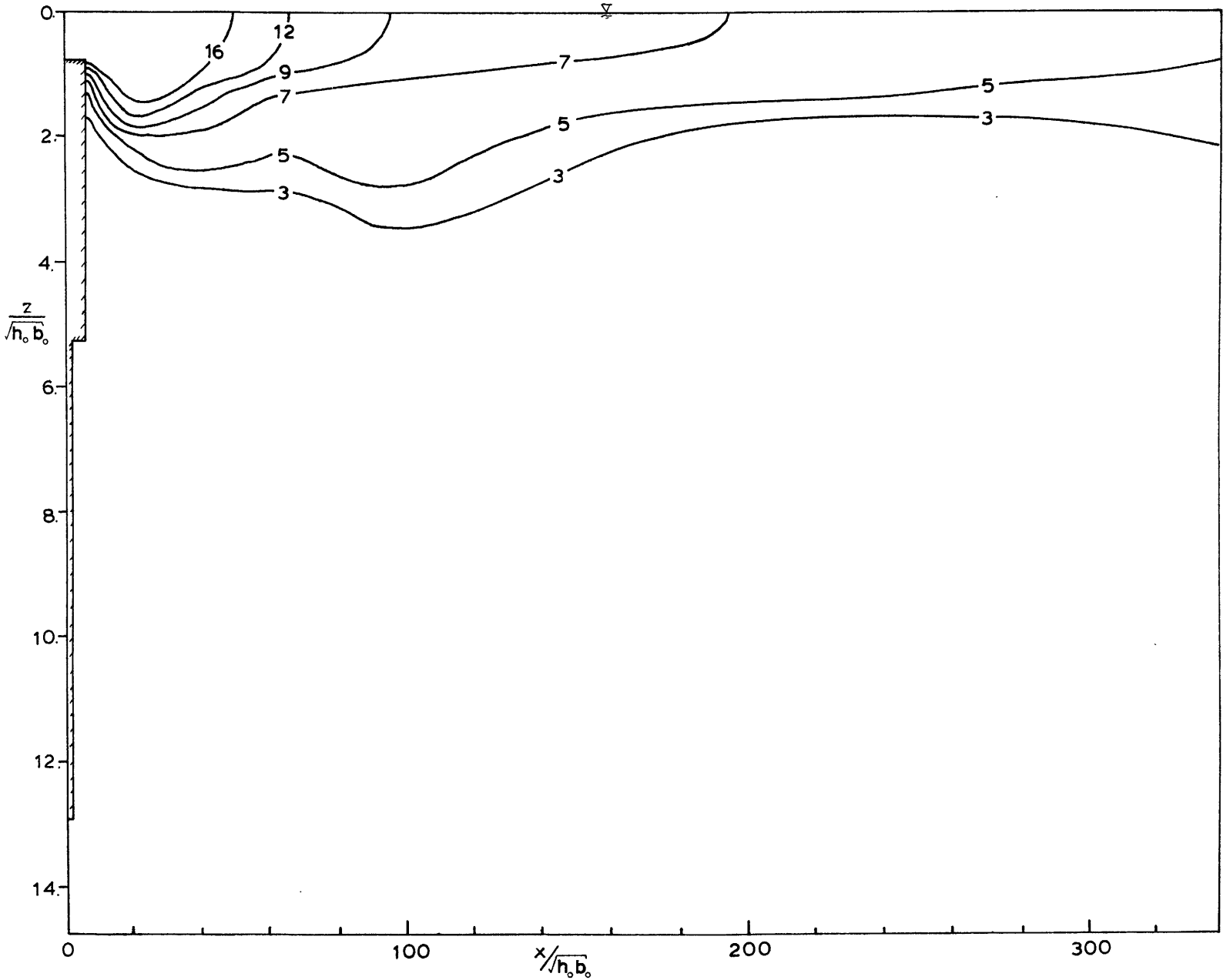

Figure A.2.11 Centerline Section of Jet #1. Run #13.

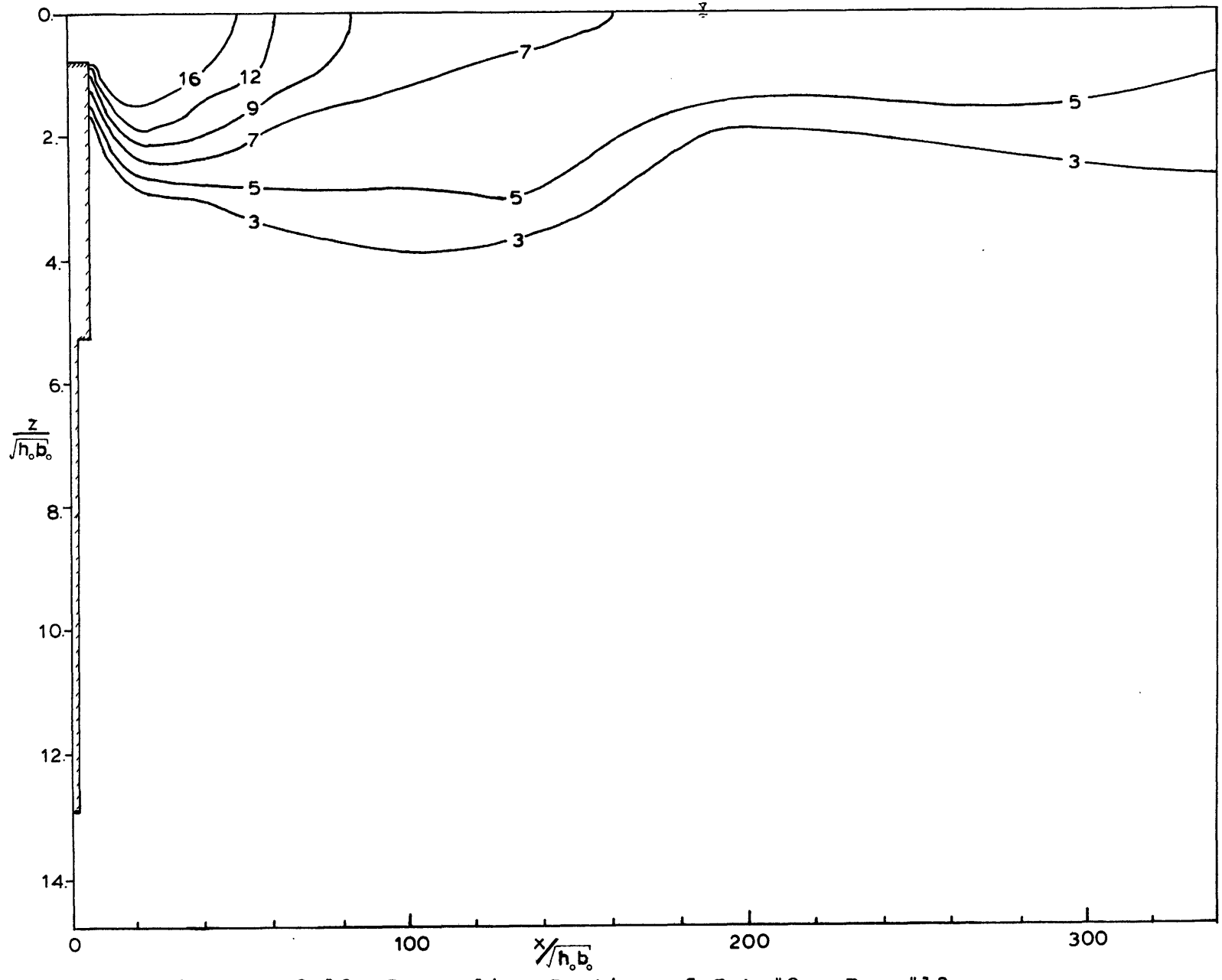

Figure A.2.12 Centerline Section of Jet #2. Run #13.

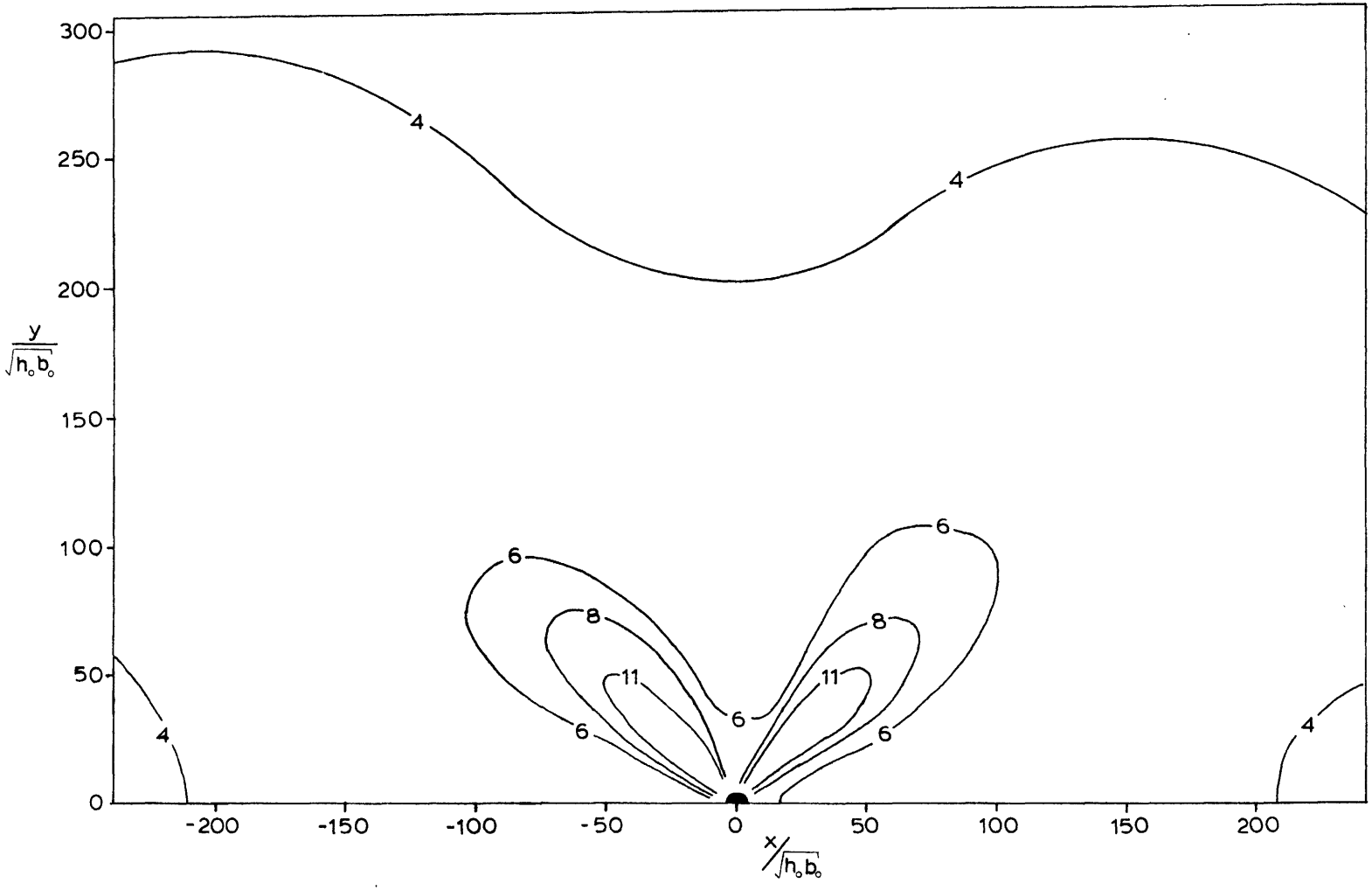

Figure A.2.13 Plan View. Run #14.

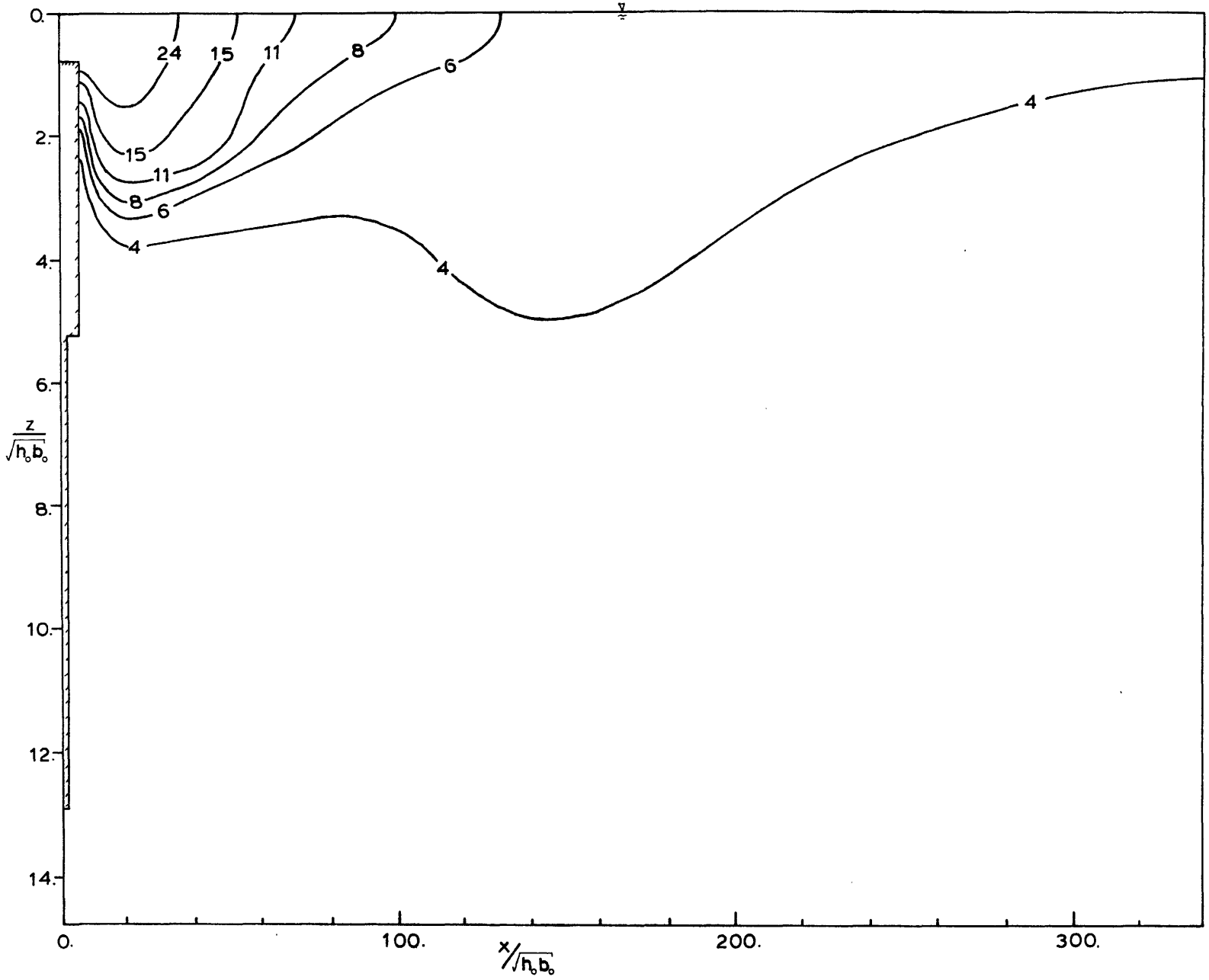

Figure A.2.14 Centerline Section of Jet #1. Run #14.

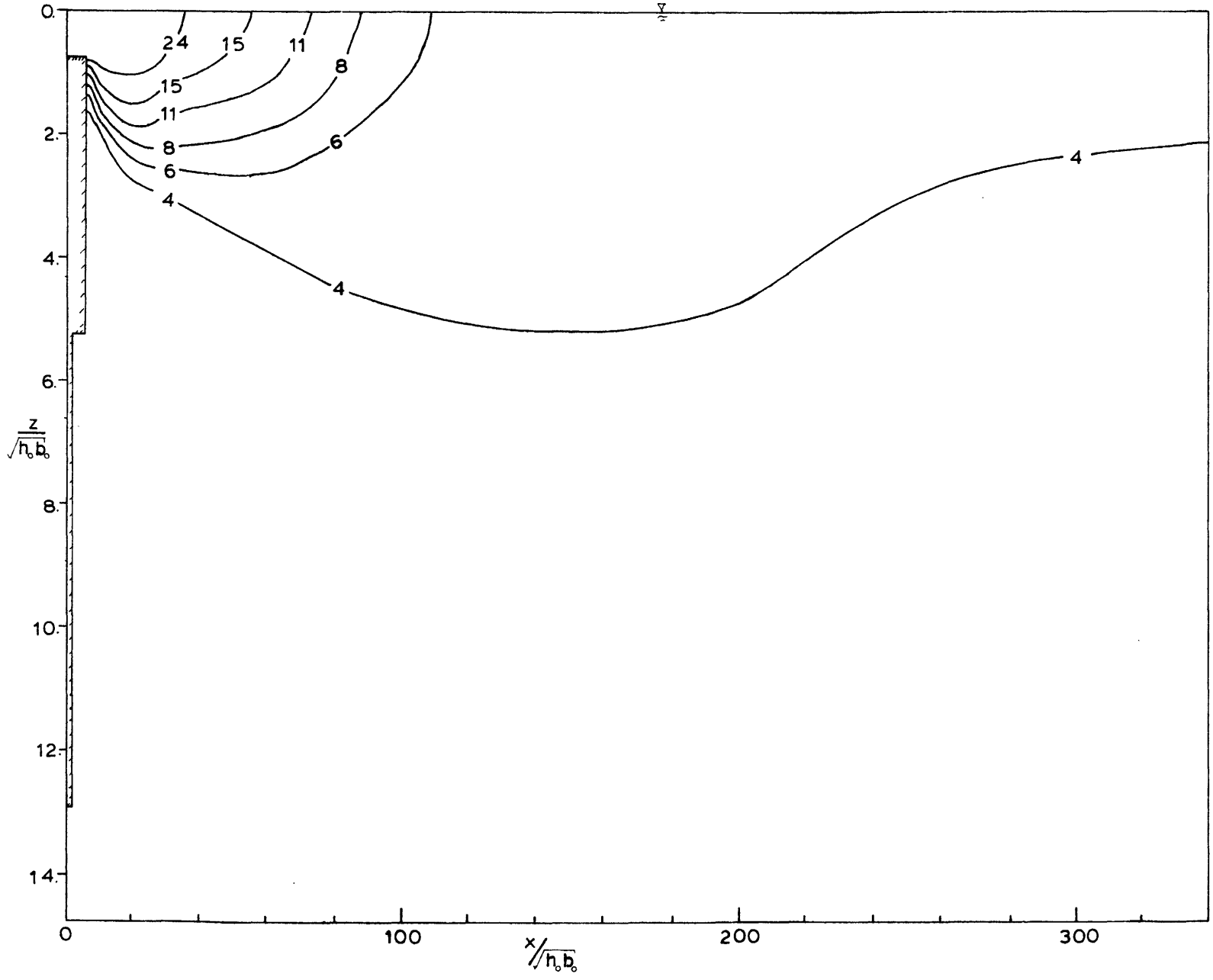

Figure A.2.15 Centerline Section of Jet #2. Run #14.

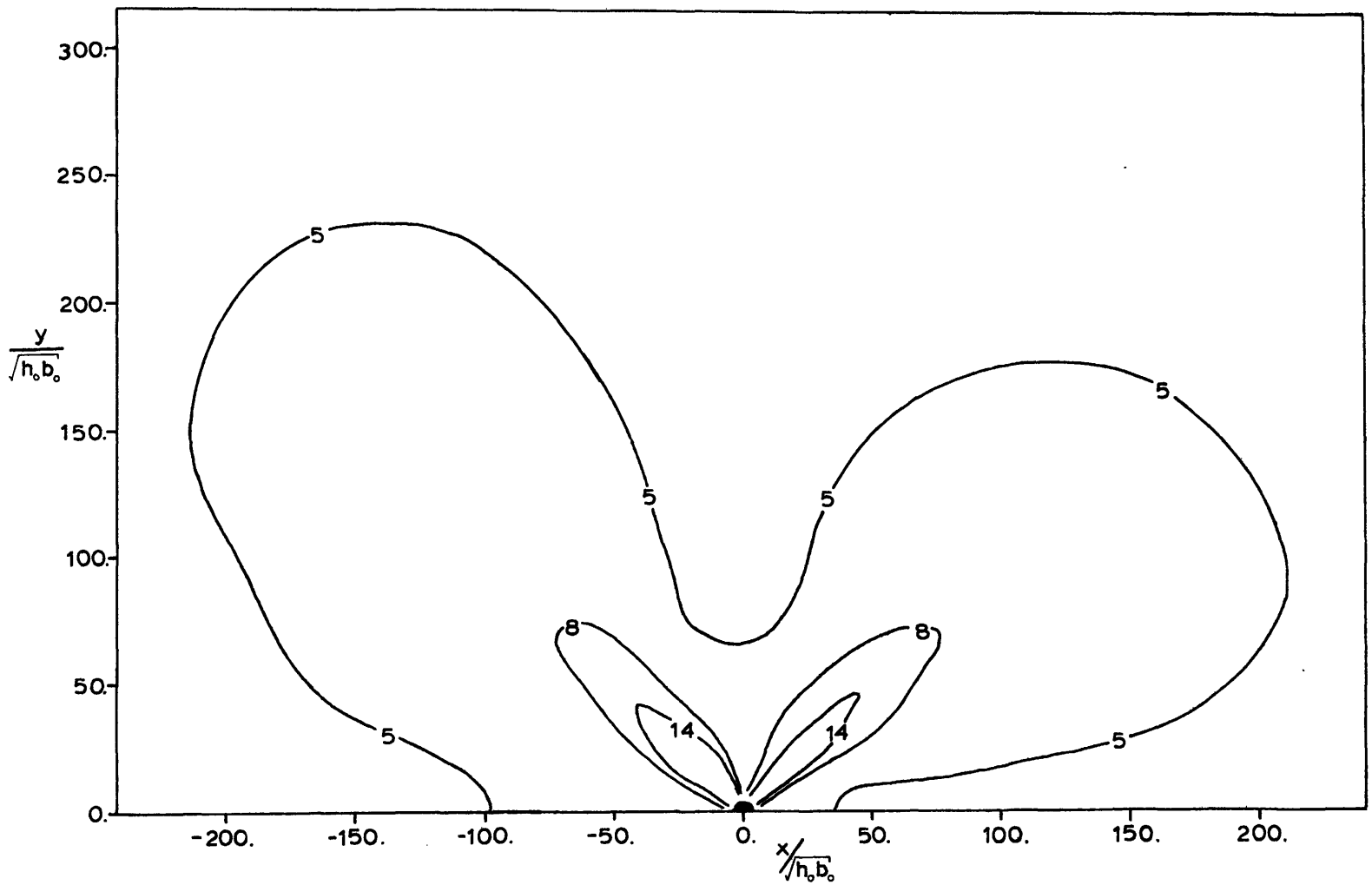

Figure A.2.16 Plan View. Run #15.

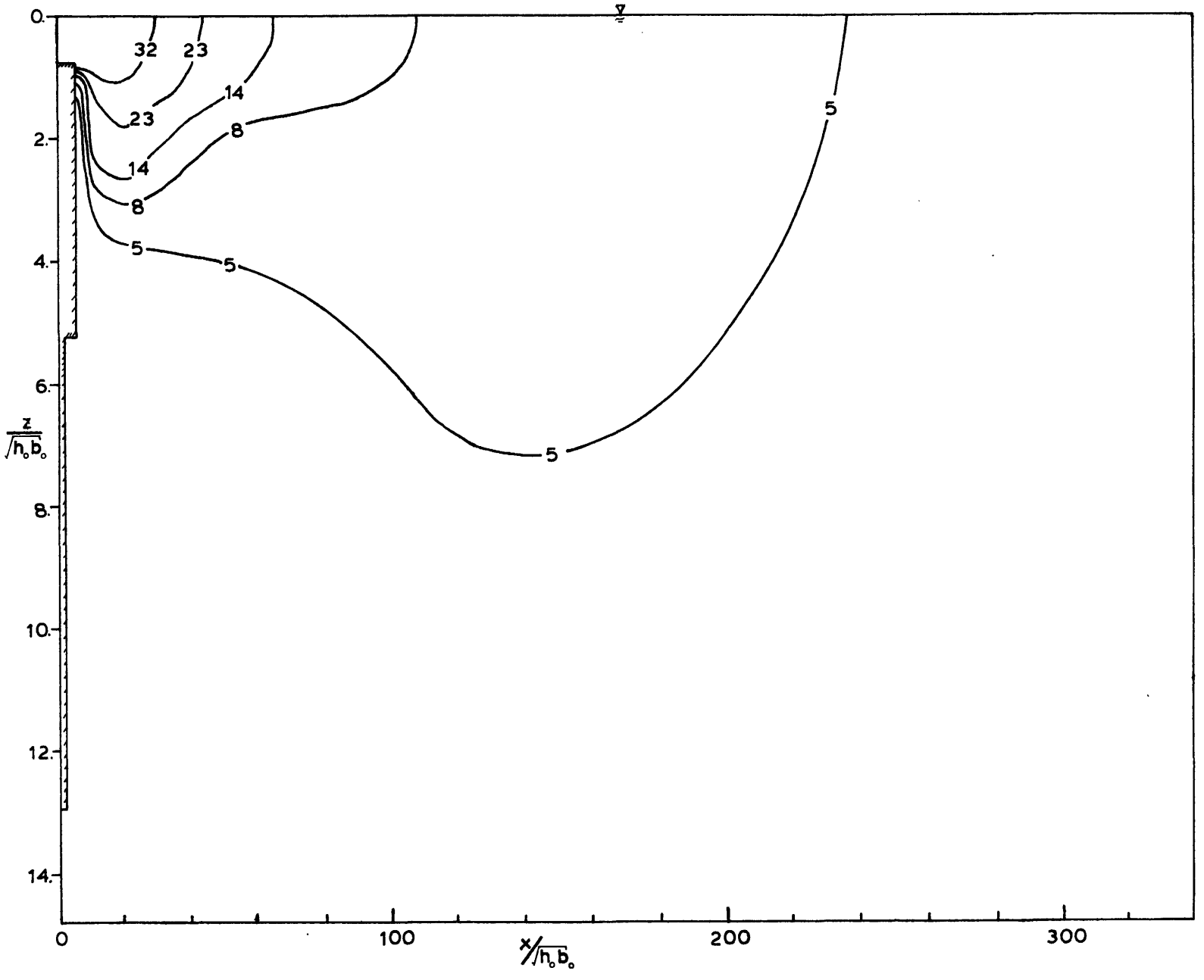

Figure A.2.17 Centerline Section of Jet #1. Run #15.

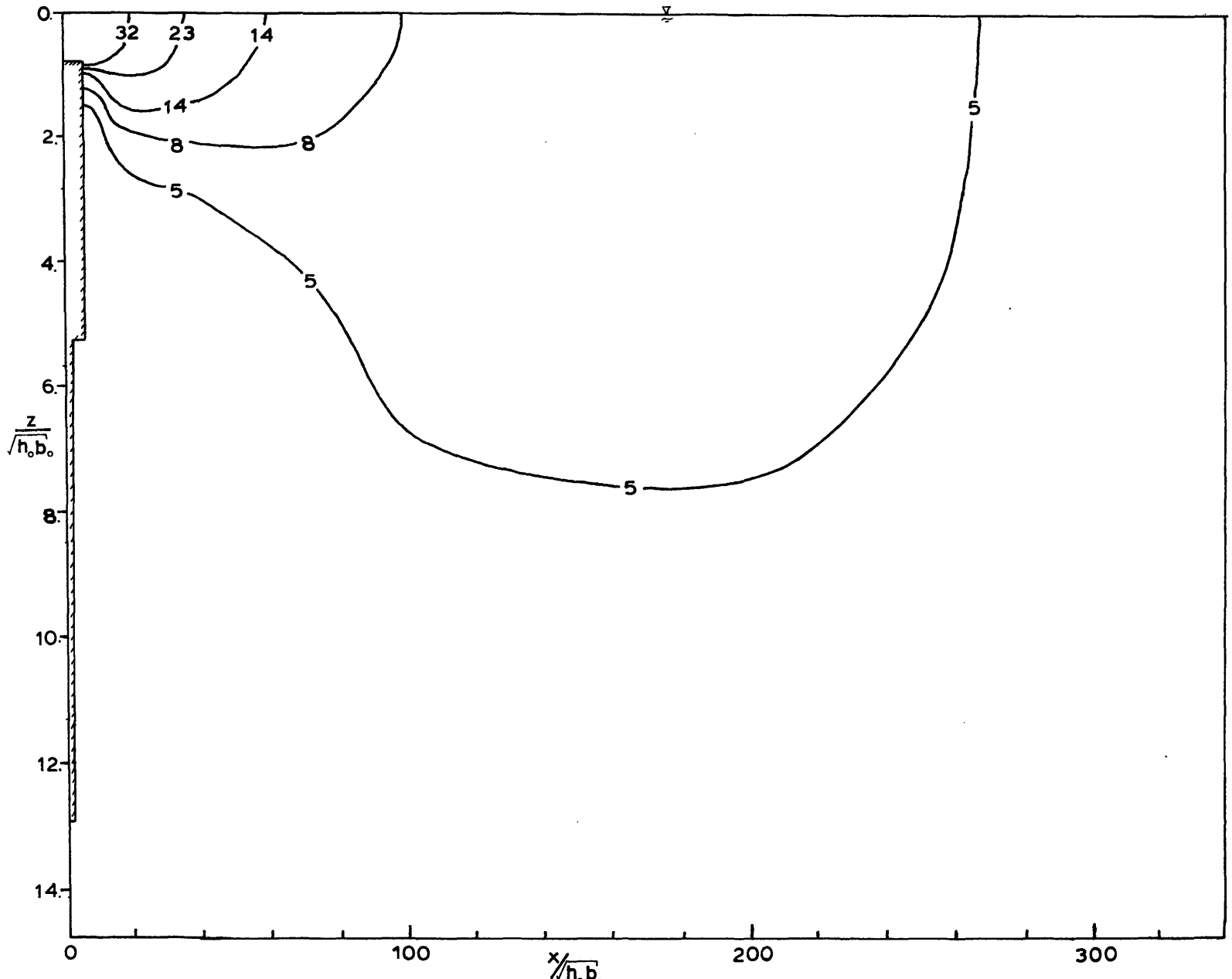

Figure A.2.18 Centerline Section of Jet #2. Run #15.

APPENDIX A.3

EXPERIMENTS WITH AN AMBIENT CURRENT*

(see Tables 6.1 and 6.2 for discharge parameter values)

*The "x" axis is parallel to the current. The "y" axis is perpendicular to the current.

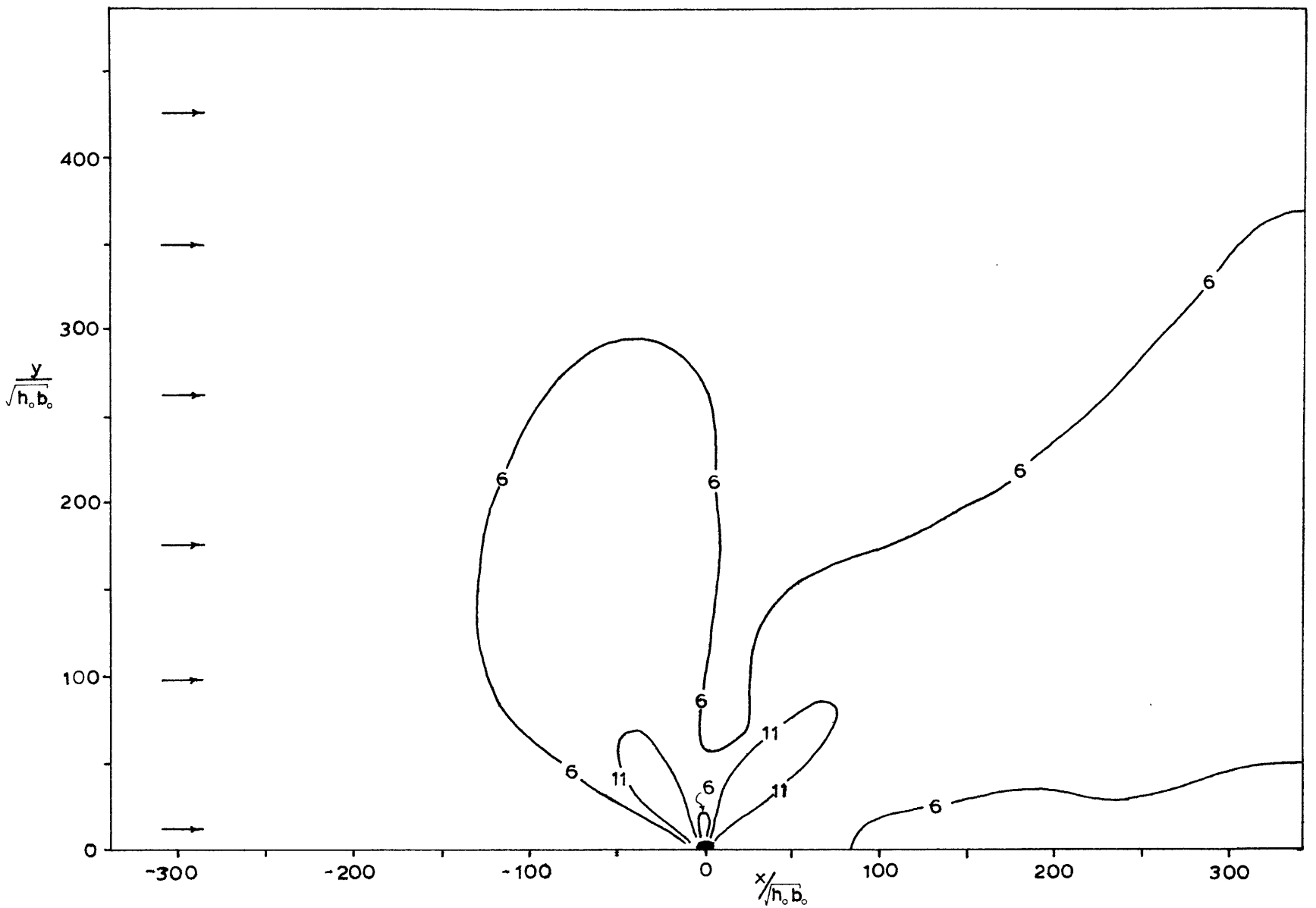

Figure A.3.1 Plan View of Run #17, Separate Jet Discharge.

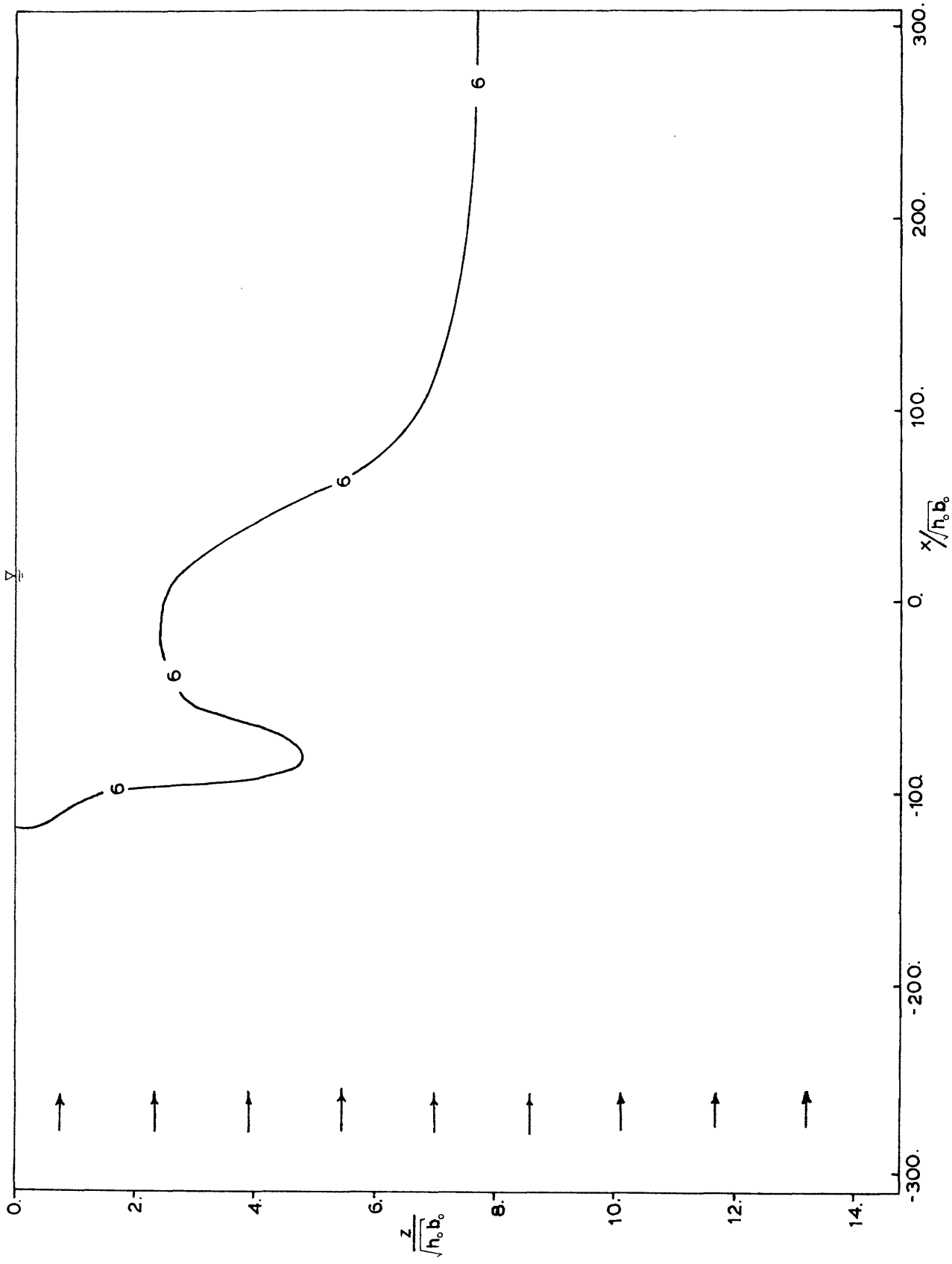

Figure A.3.2 Longitudinal Transect A-A, Run #17.

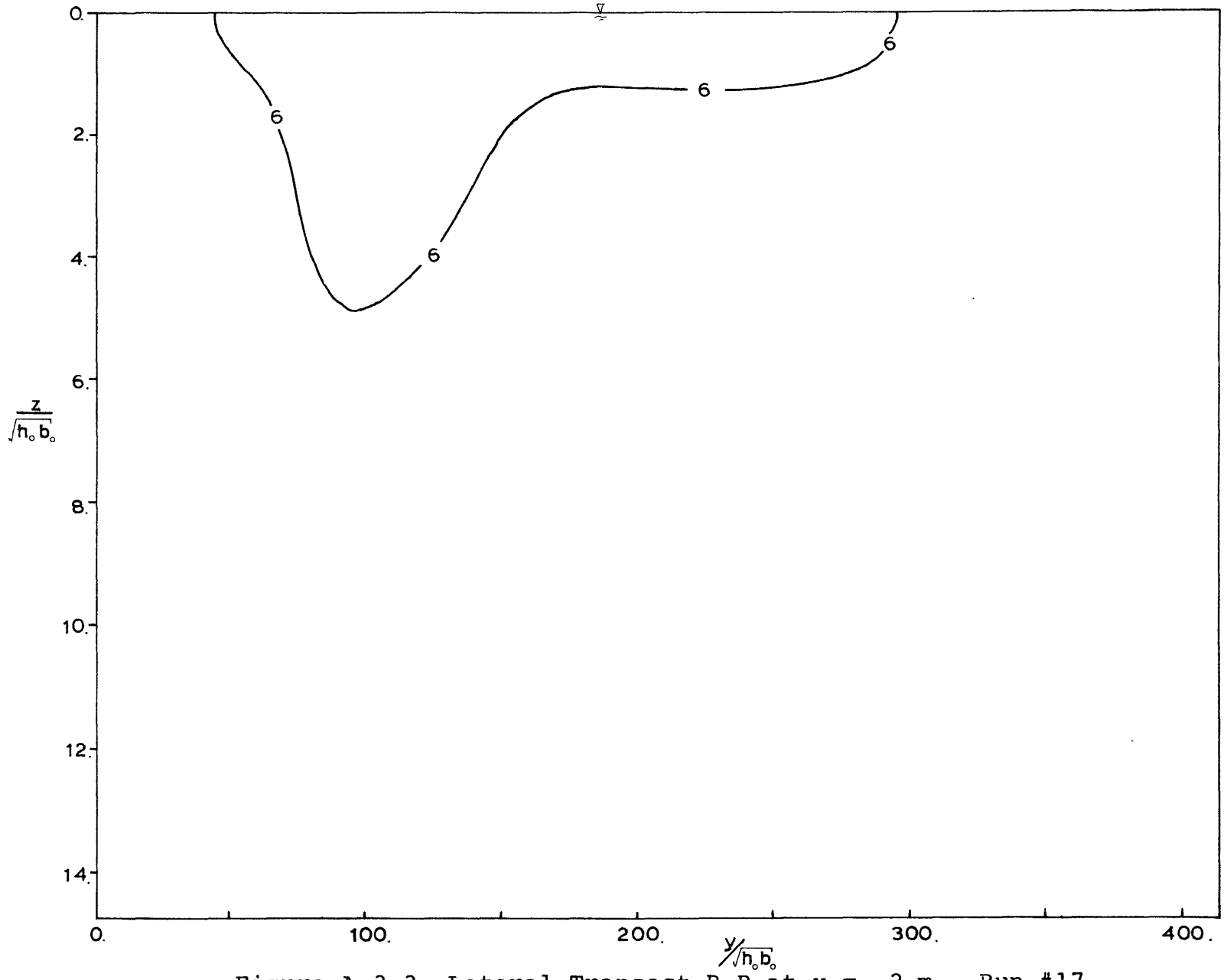

Figure A.3.3 Lateral Transect B-B at x = -2 m. Run #17.

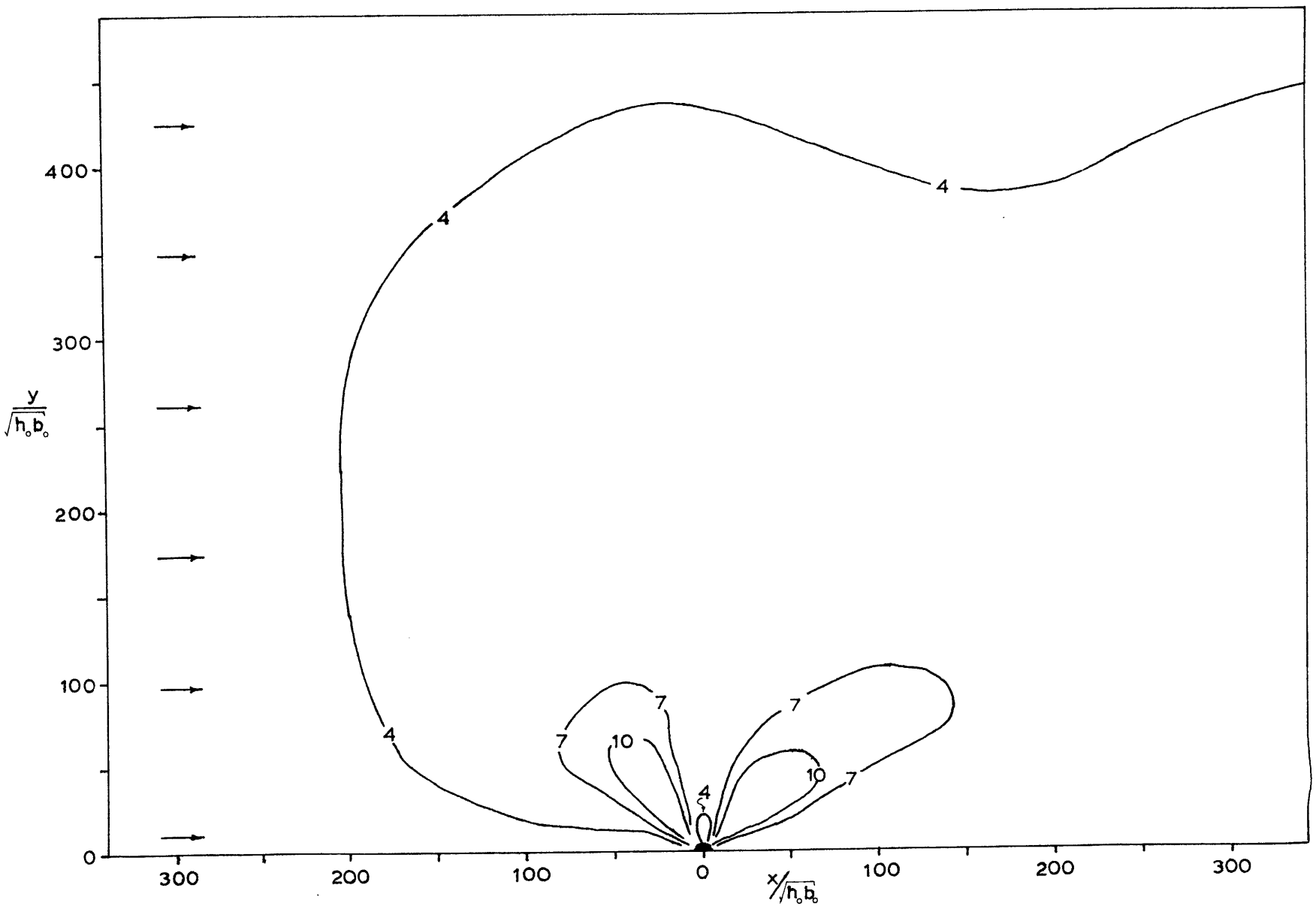

Figure A.3.4 Plan View. Run #18, Separate Jet Discharge

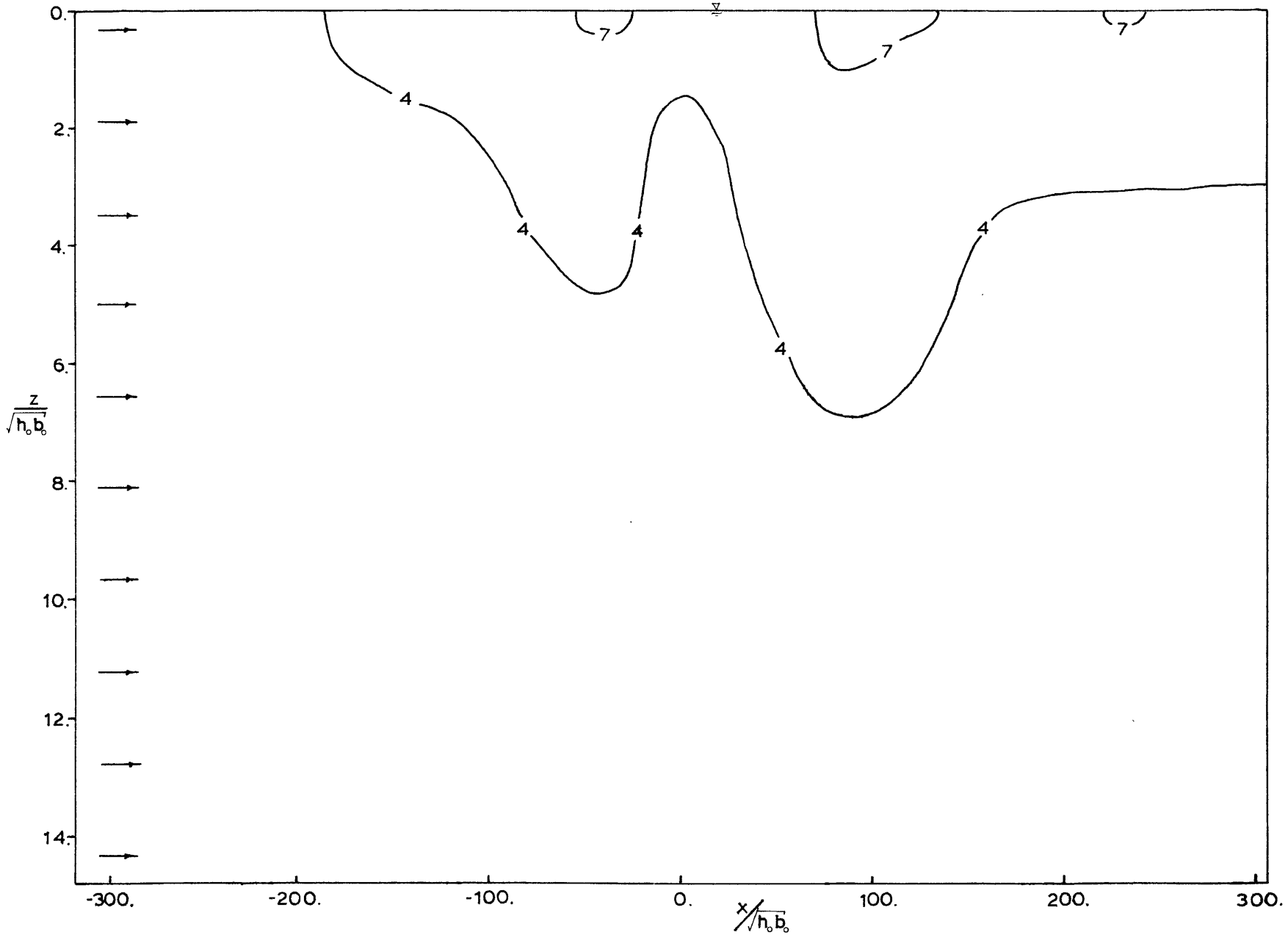

Figure A.3.5 Longitudinal Transect A-A. Run #18.

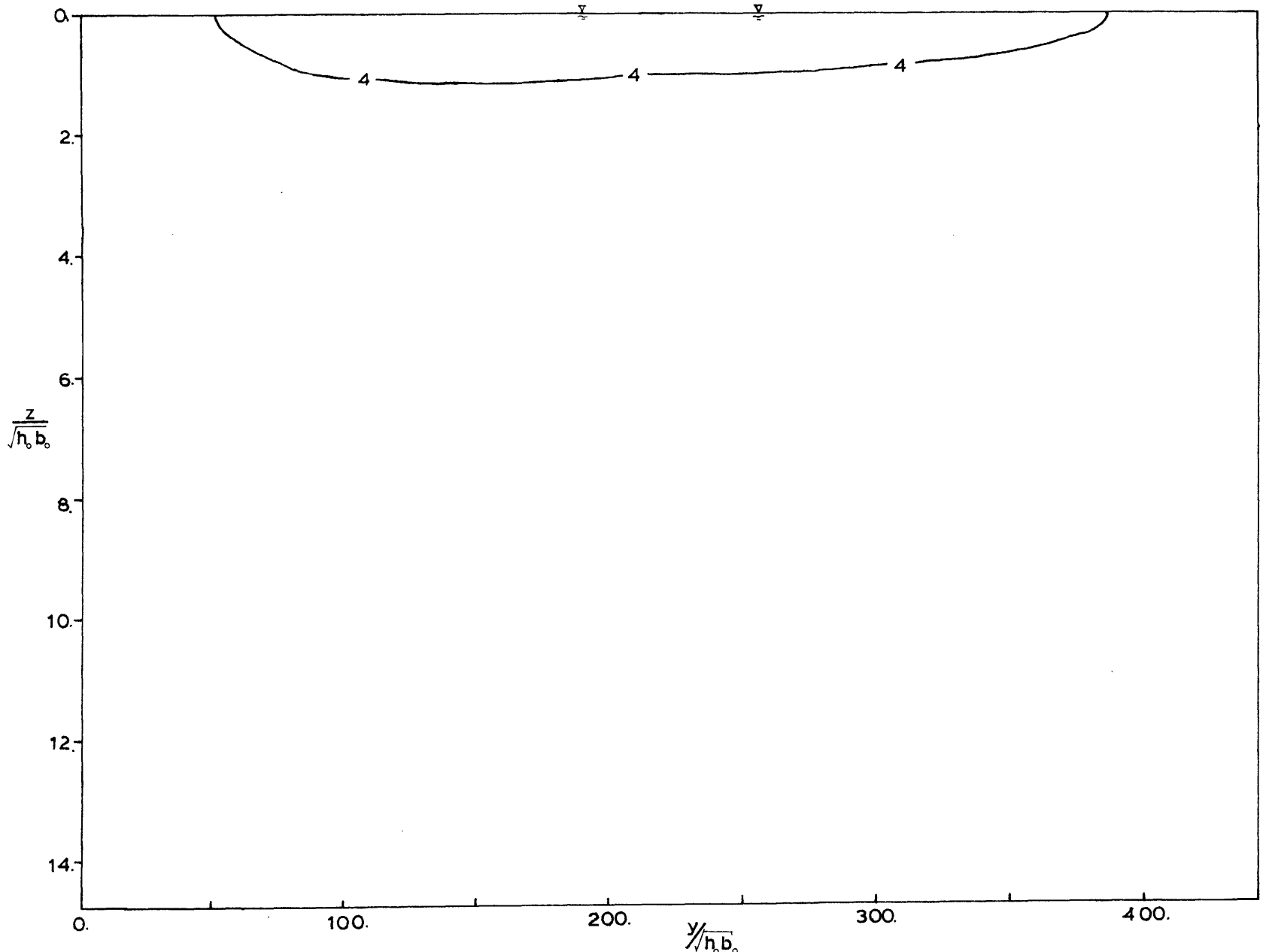

Figure A.3.6 Lateral Section B-B at x = -4m., Run #18.

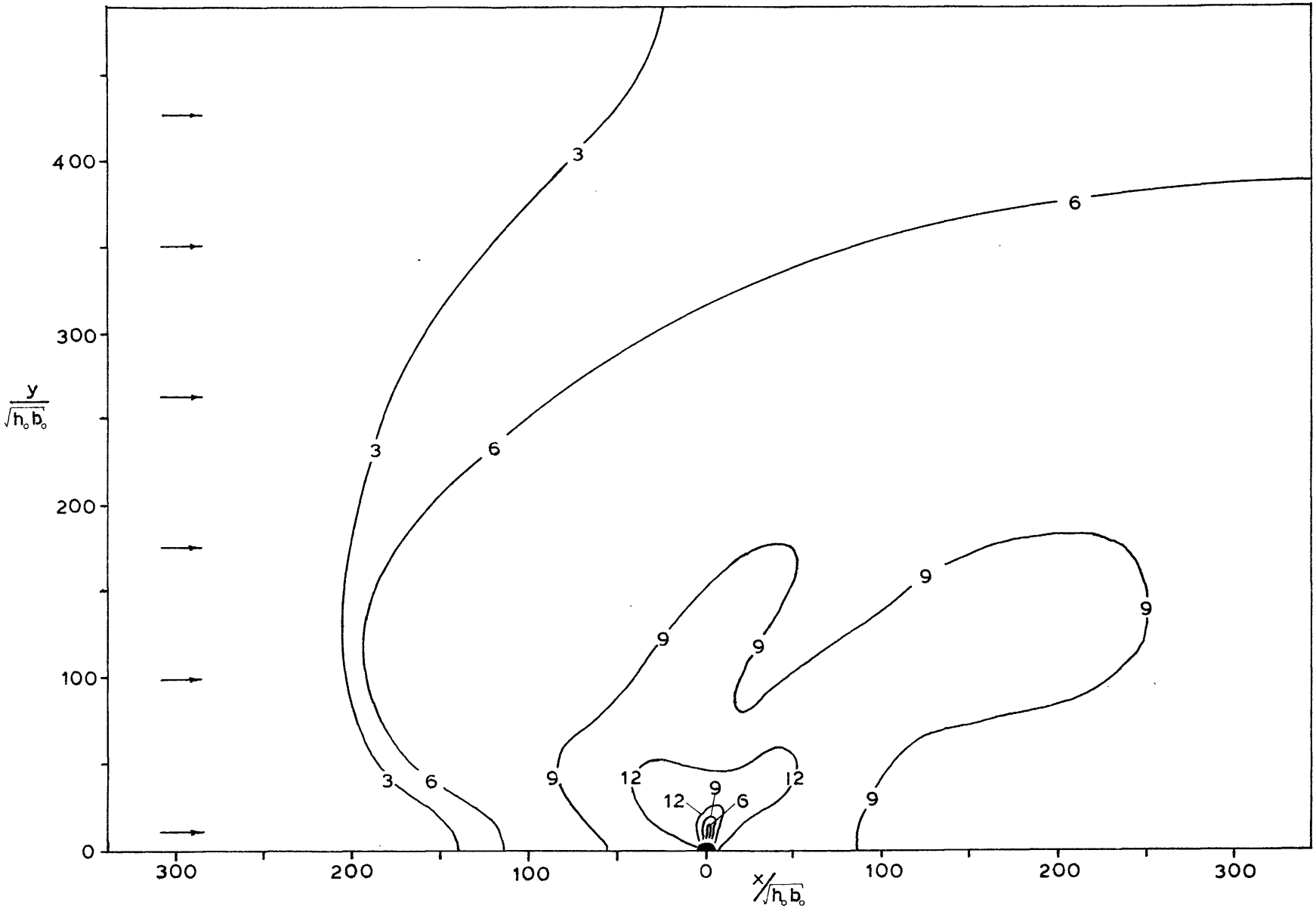

Figure A.3.7 Plan View of Run #19, Separate Jet Discharge

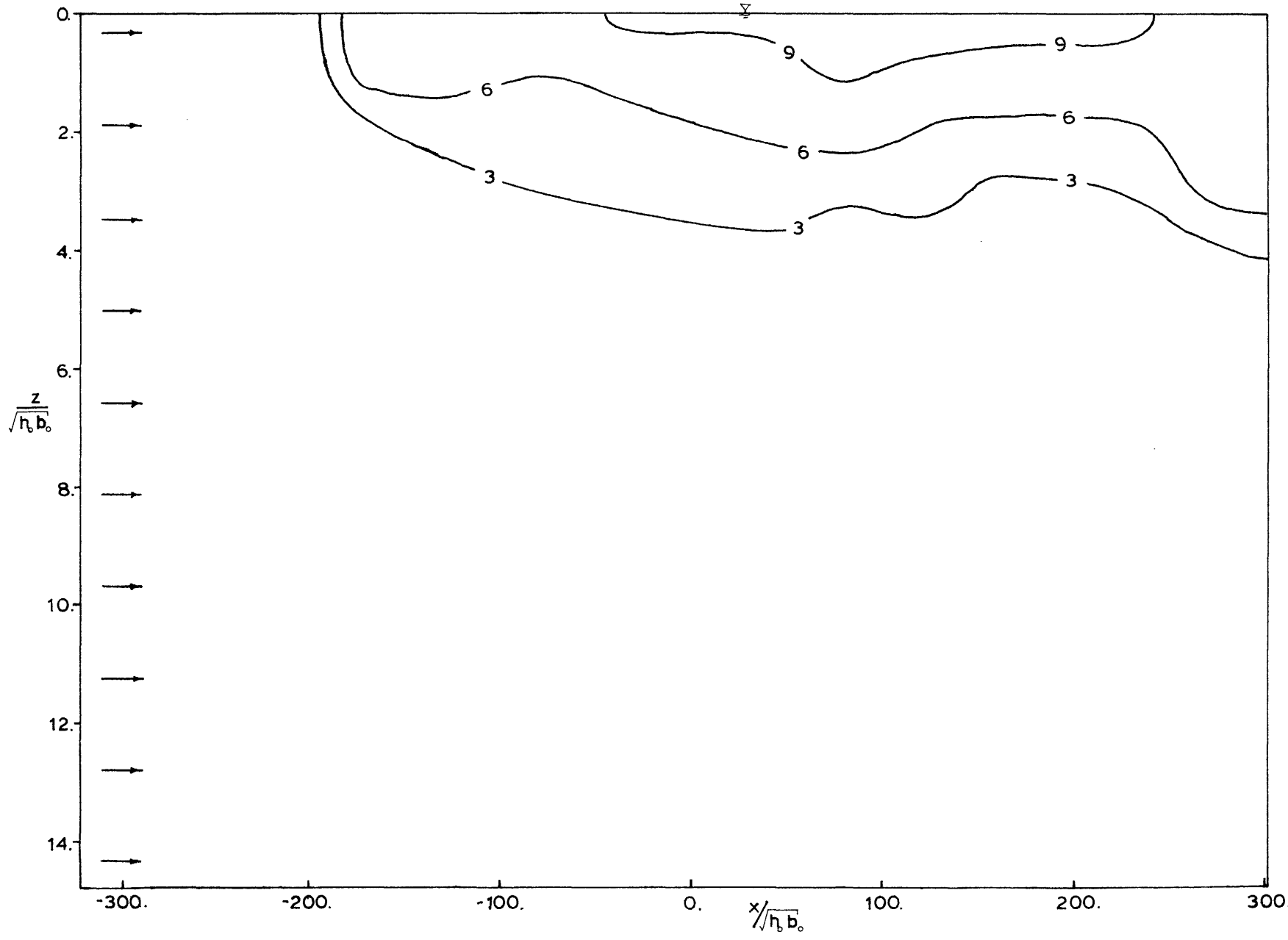

Figure A.3.8 Longitudinal Transect A-A at y = 2.25m, Run #19.

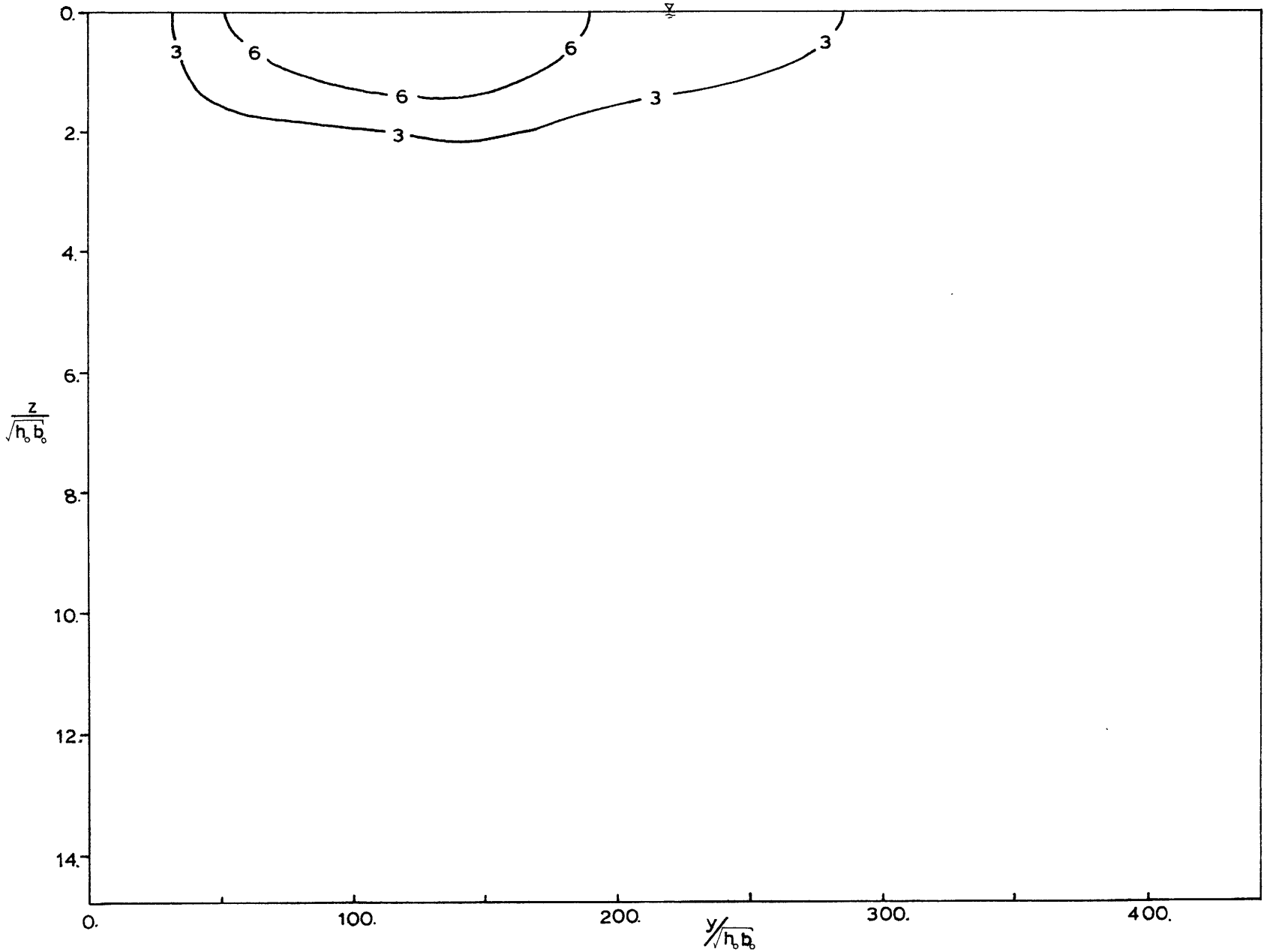

Figure A.3.9 Lateral Transect B-B at x = -4m, Run #19.

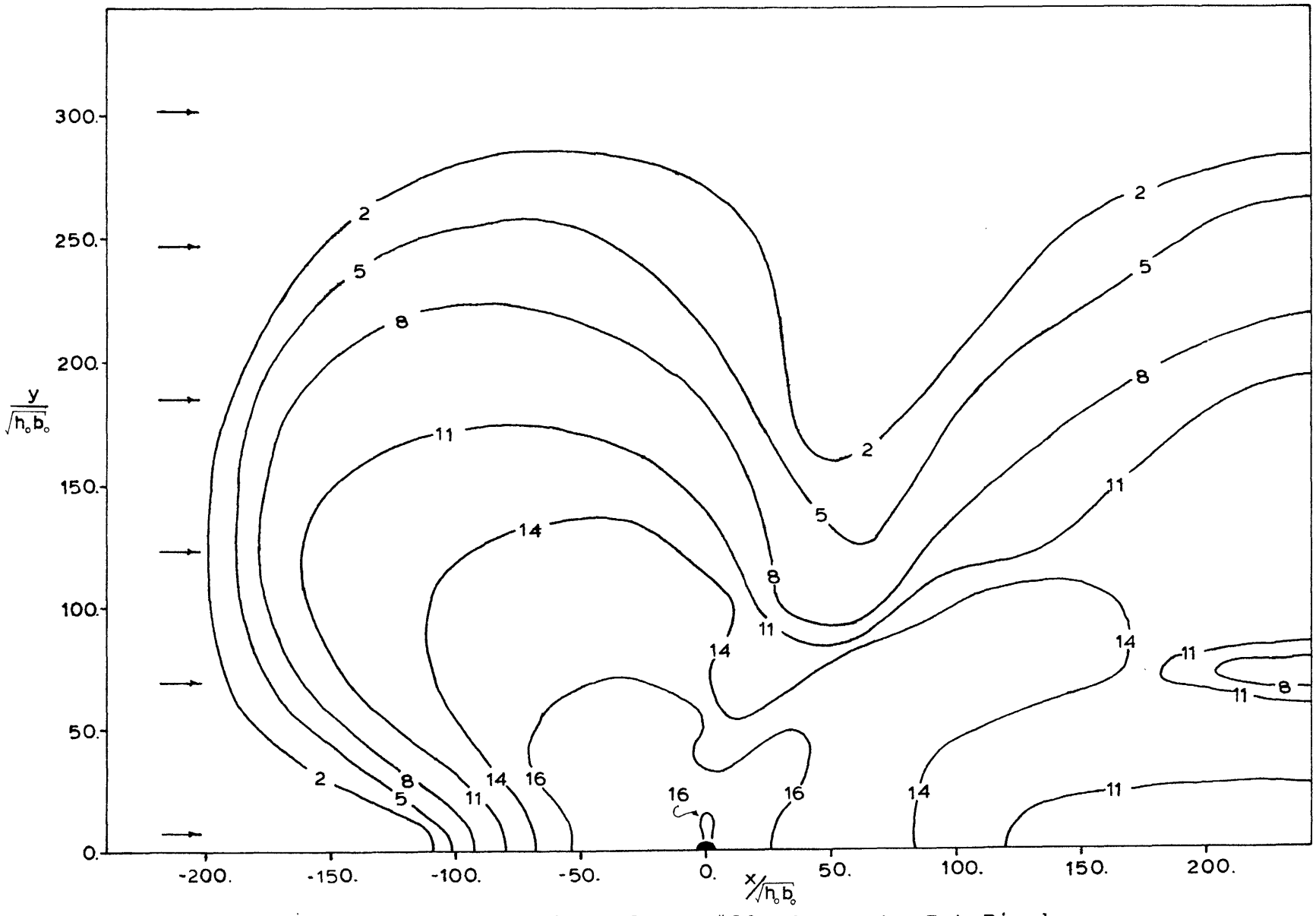

Figure A.3.10 Plan View of Run #20, Separate Jet Discharge.

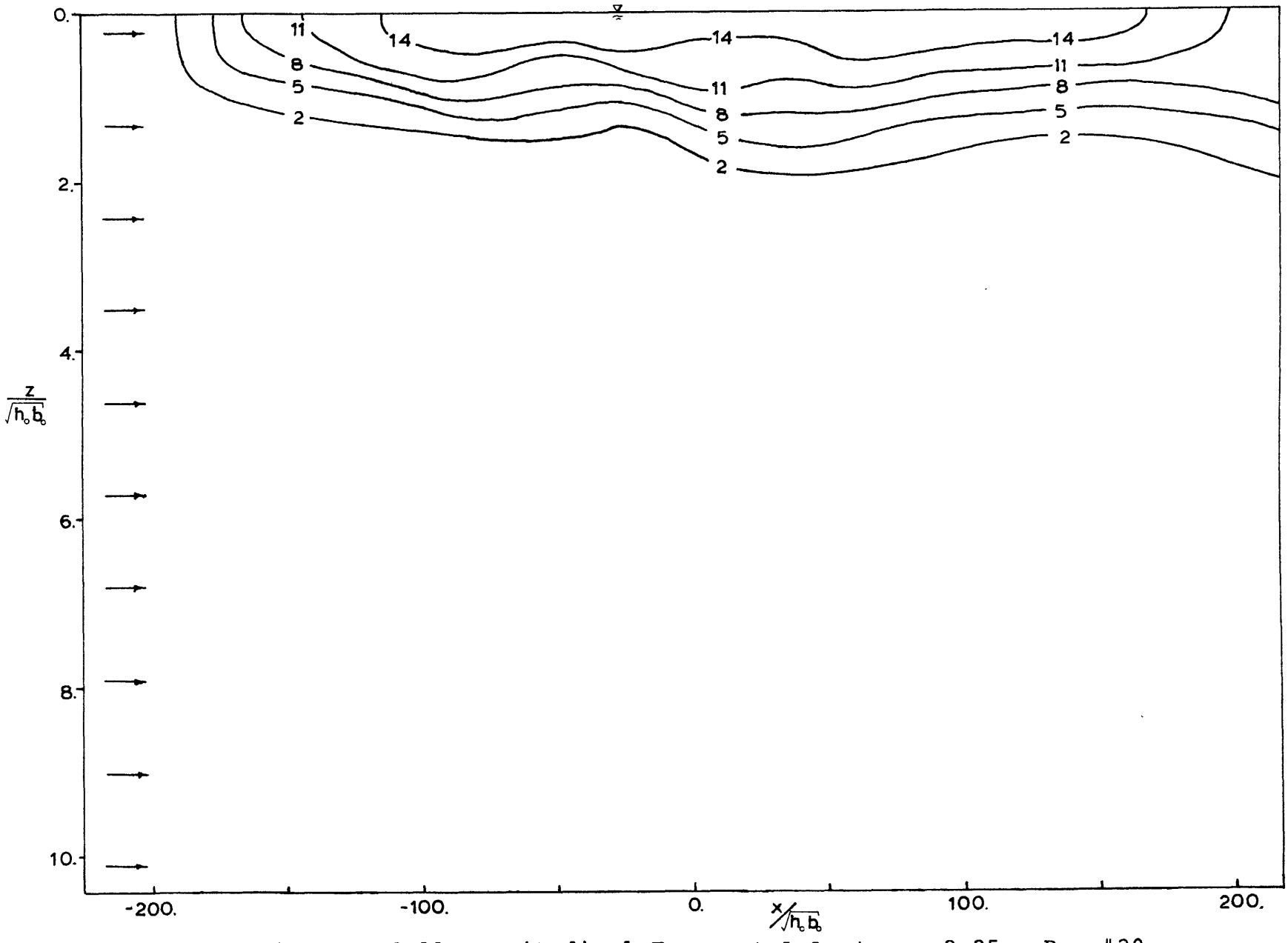

Figure A.3.11 Longitudinal Transect A-A at y = 2.25m, Run #20.

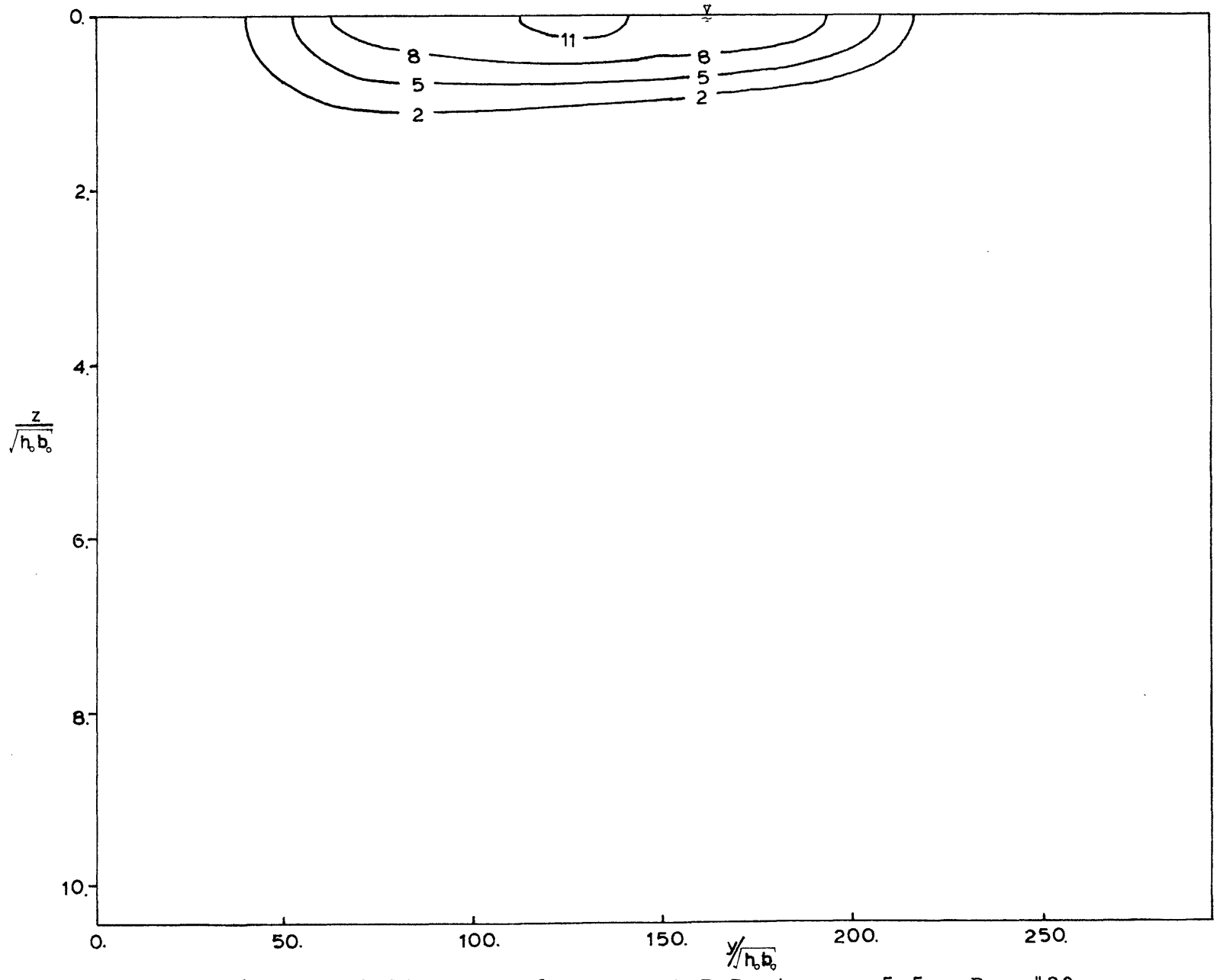

Figure A.3.12 Lateral Transect B-B at x = -5.5m, Run #20.

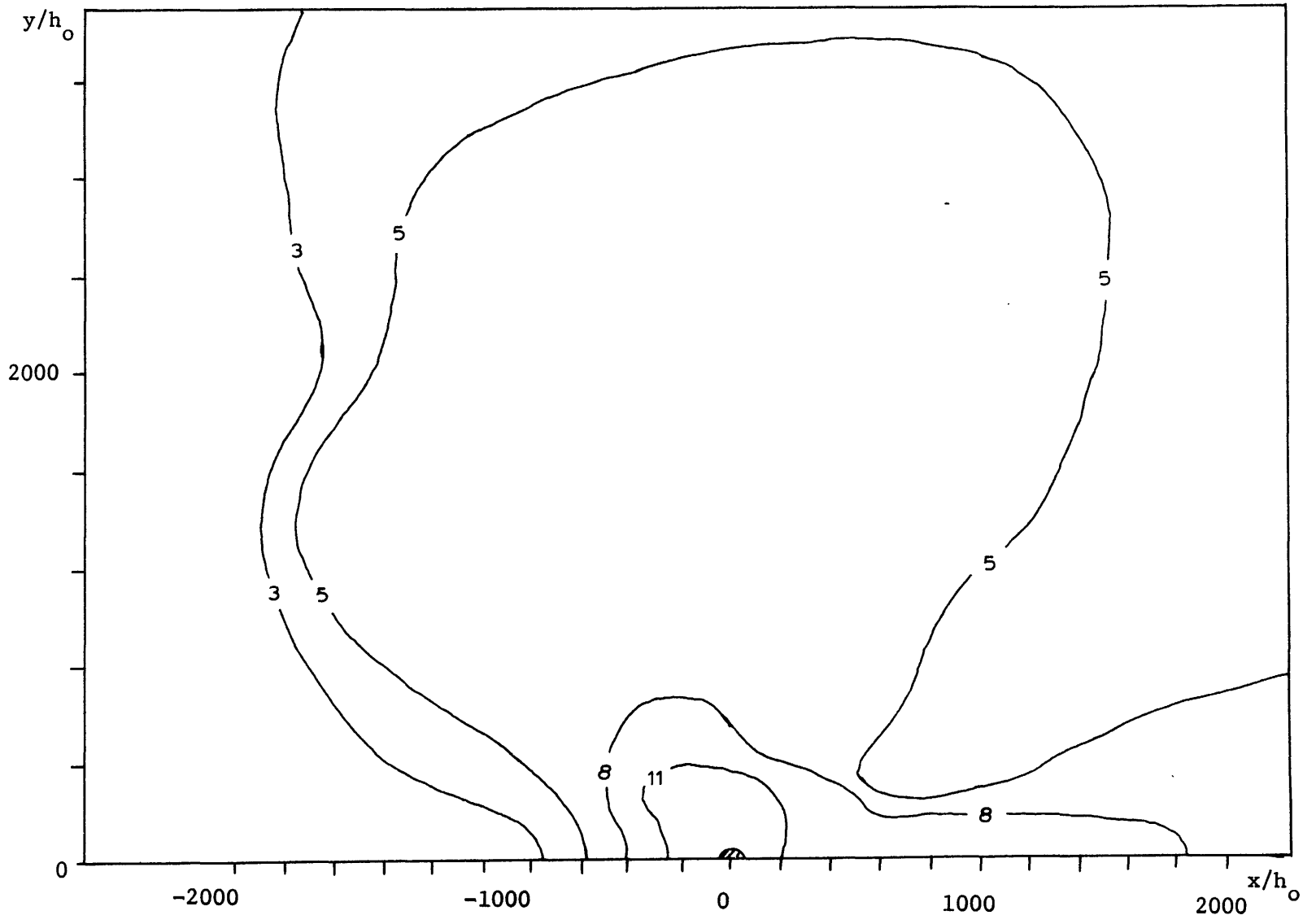

Figure A.3.13 Surface Plan, Run #21, Radial Jet Discharge

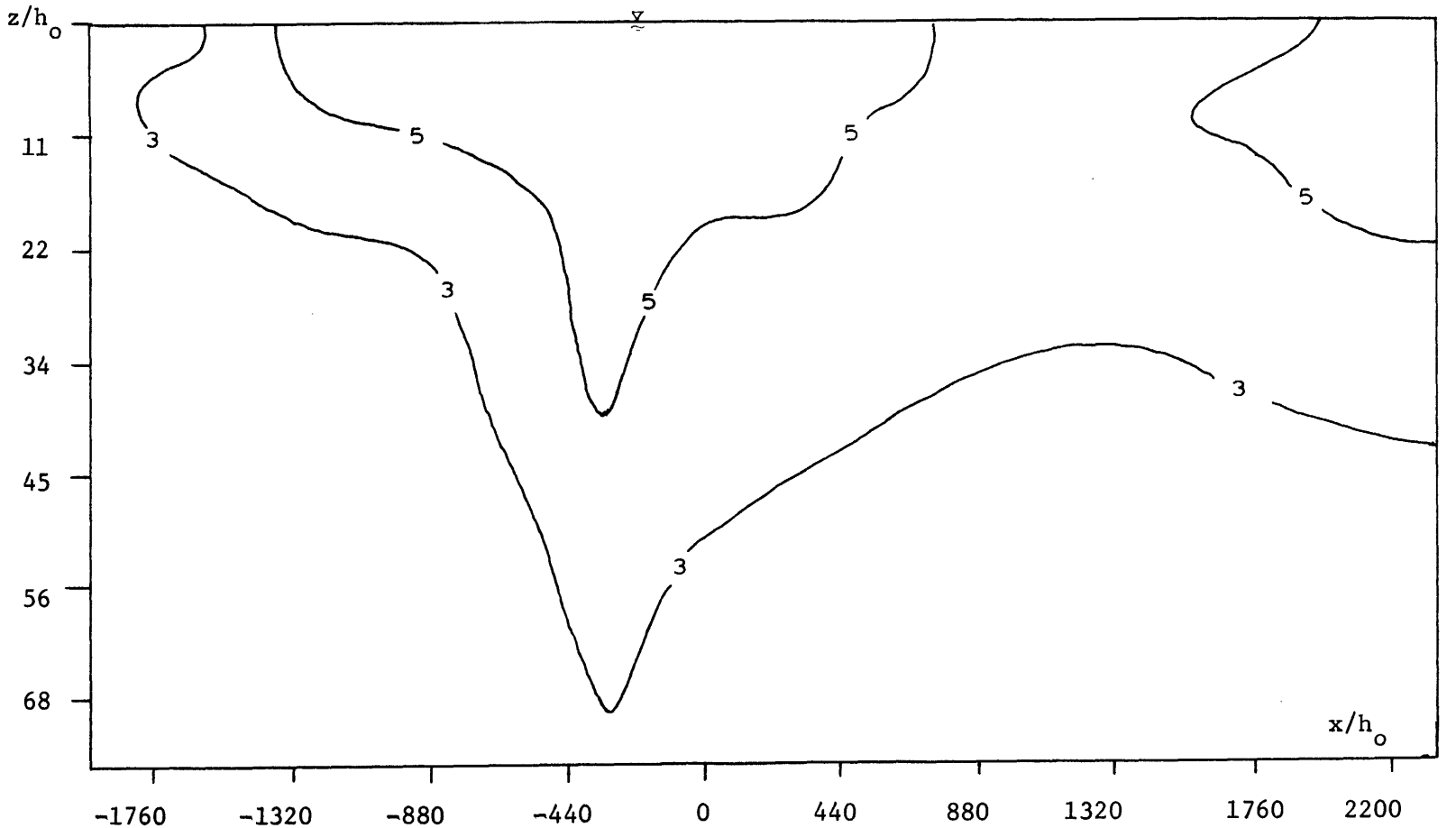

Figure A.3.14 Longitudinal Transect A-A at y = 2.25m, Run #21.

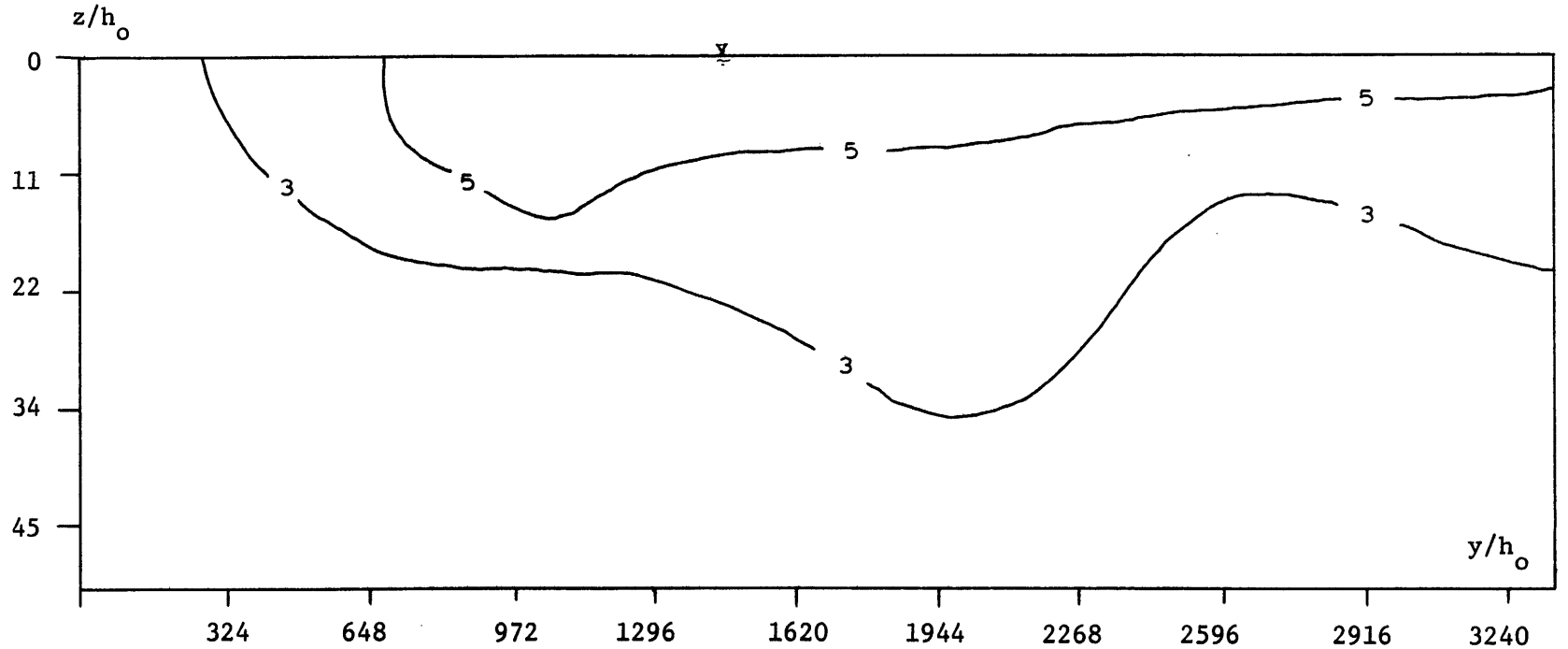

Figure A.3.15 Lateral Transect B-B at x = -4.0m, Run #21.

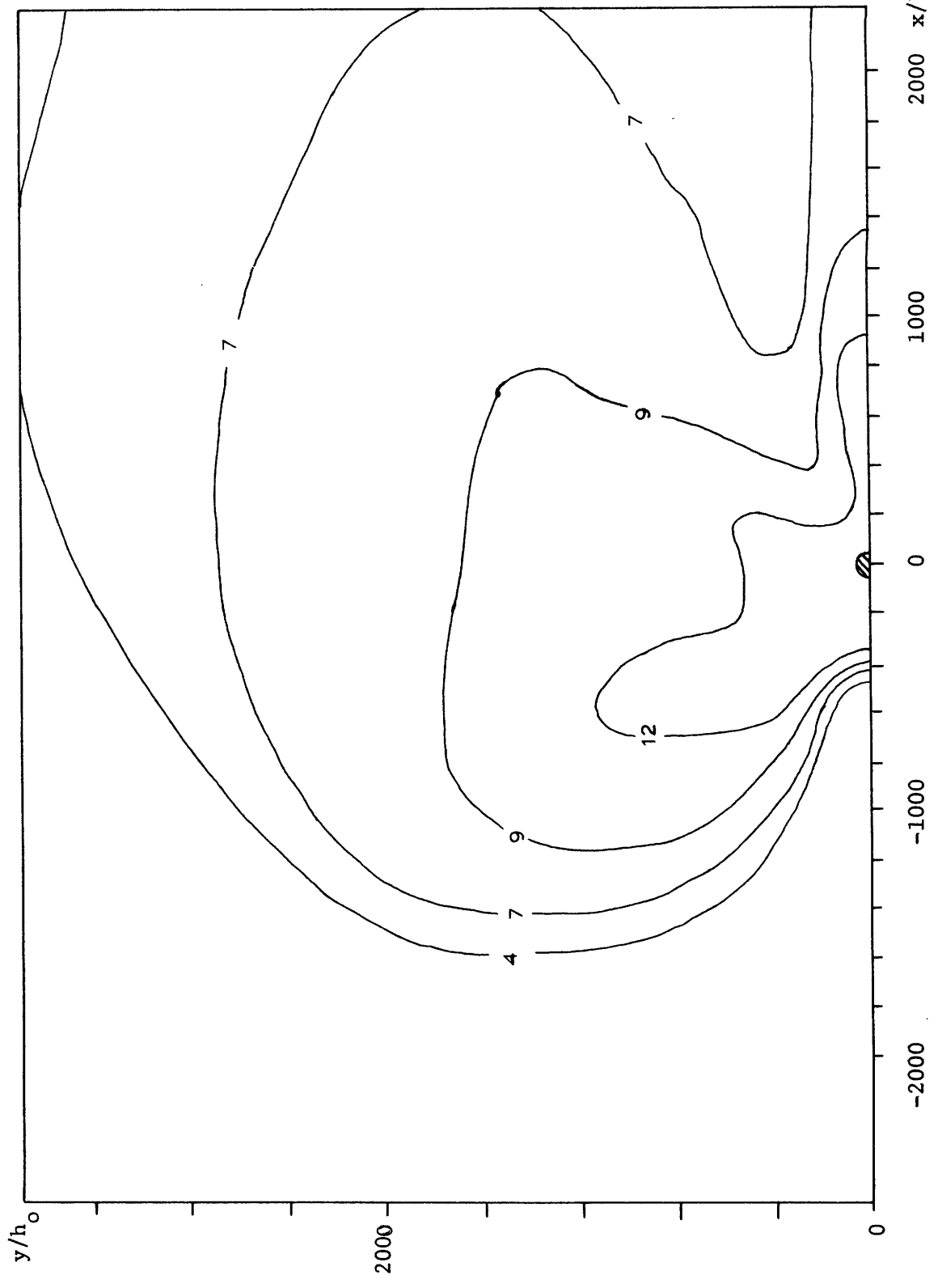

Figure A.3.16 Surface Plan, Run #22.

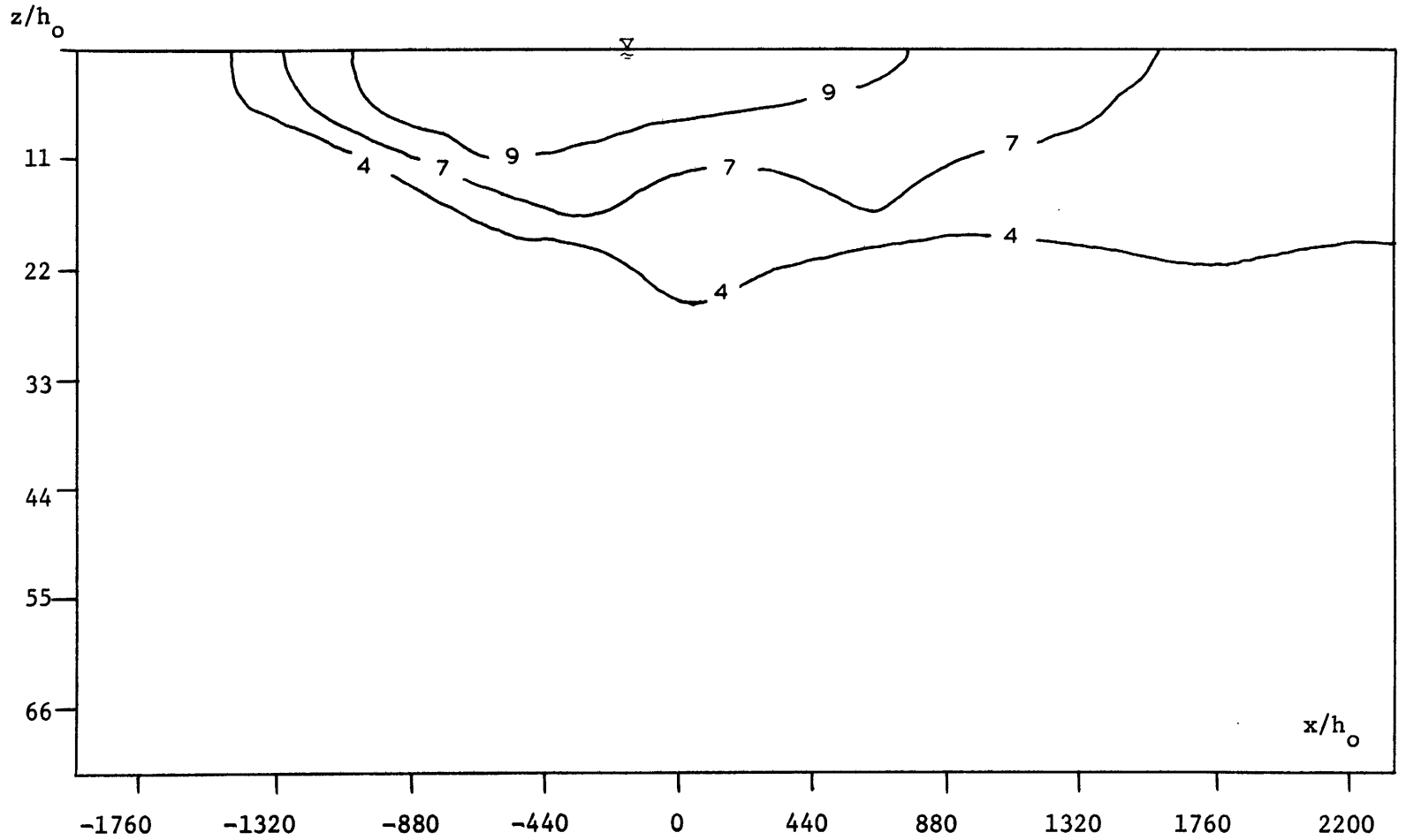

Figure A.3.17 Longitudinal Transect A-A at y = 2.25m, Run #22.

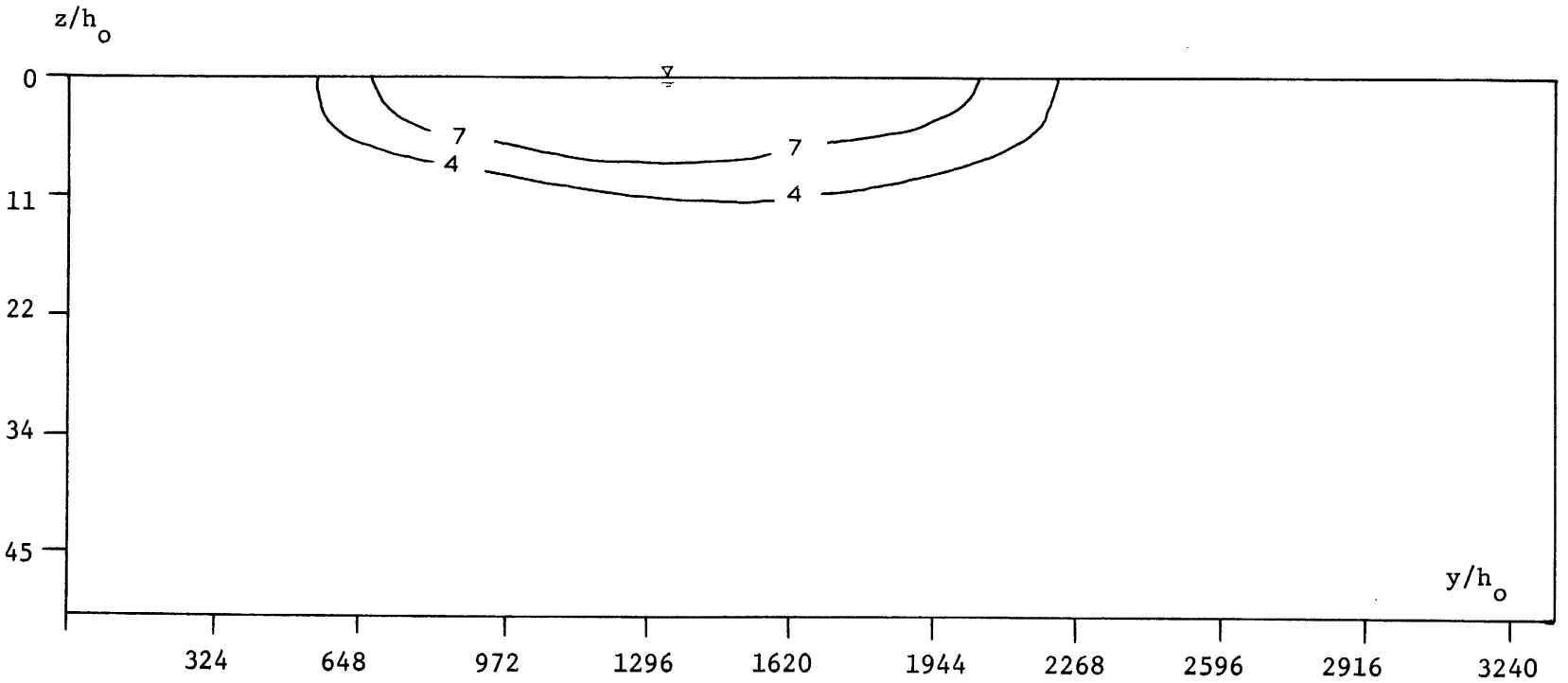

Figure A.3.18 Lateral Transect B-B at x = -4m, Run #22.

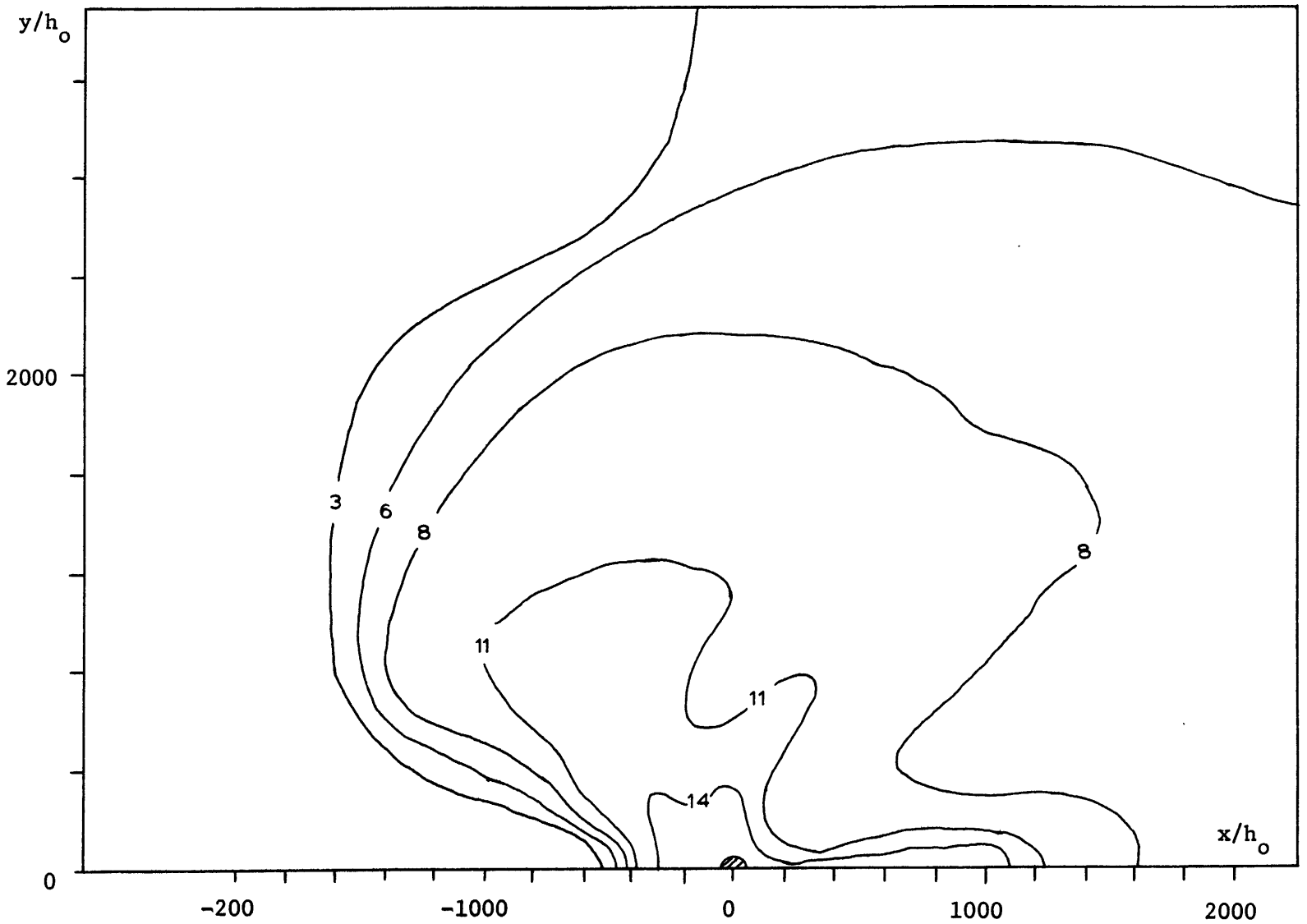

Figure A.3.19 Surface Plan, Run #23, Radial Jet Discharge.

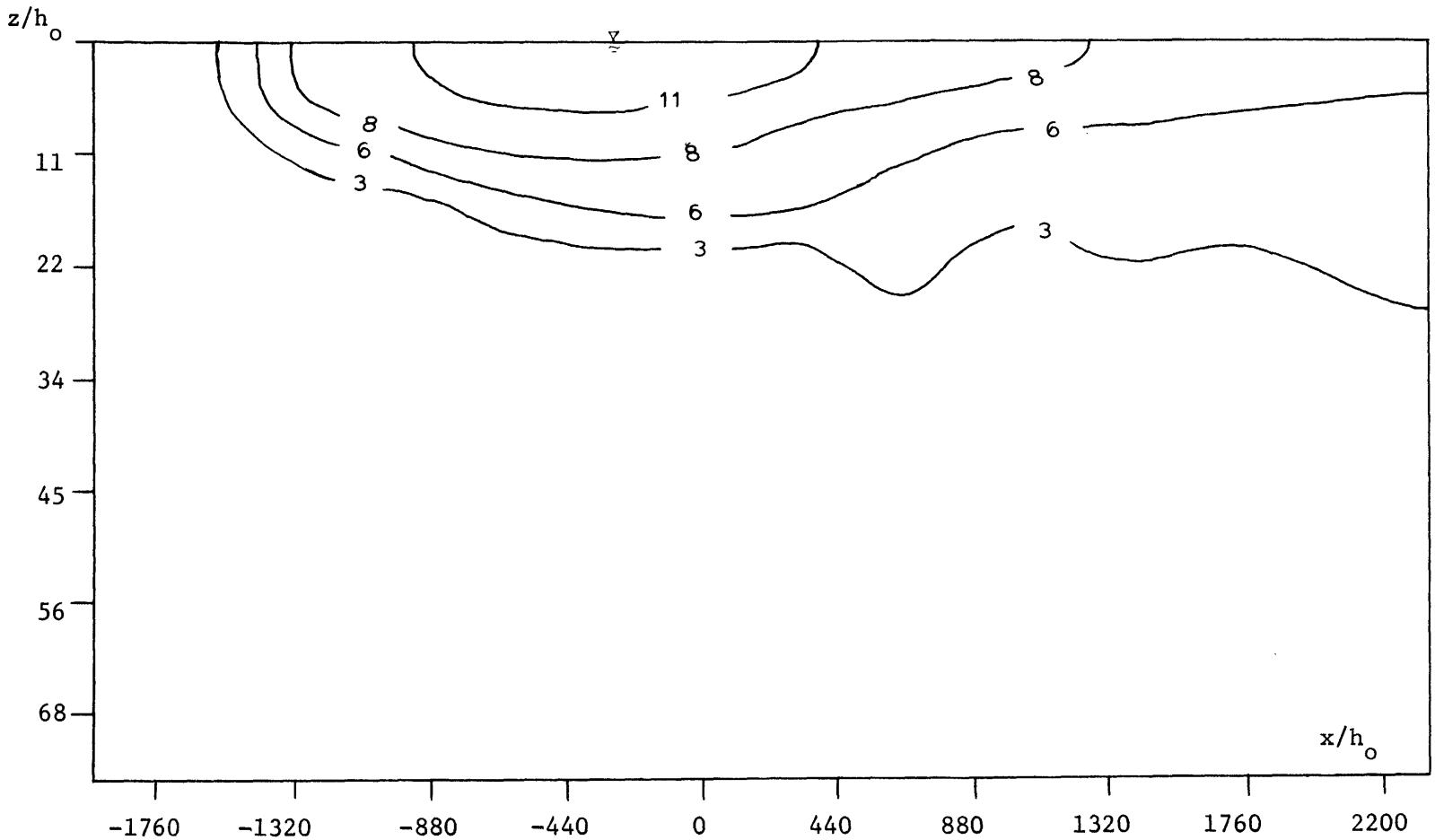

Figure A.3.20 Longitudinal Transect B-B at y = 2.25m, Run #23.

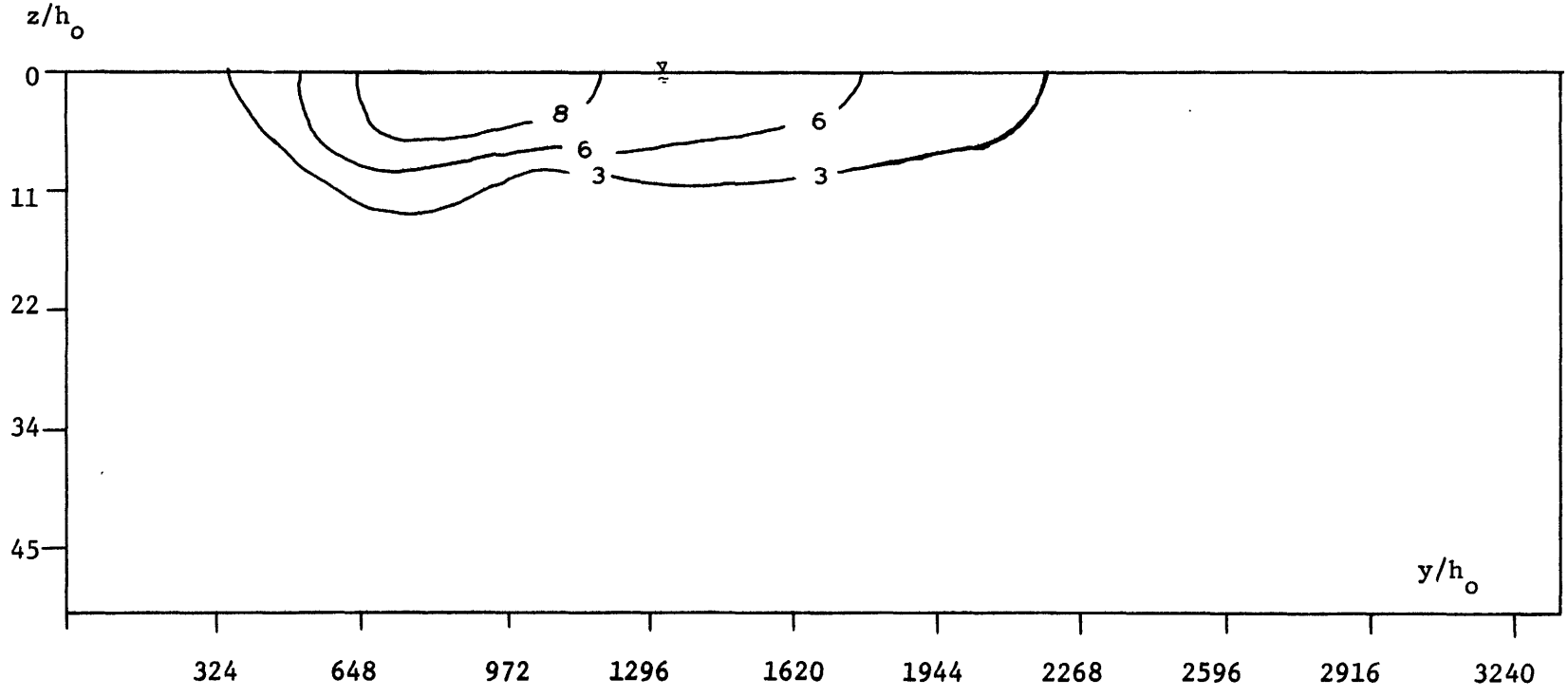

Figure A.3.21 Lateral Transect B-B at x = -4m, Run #23.

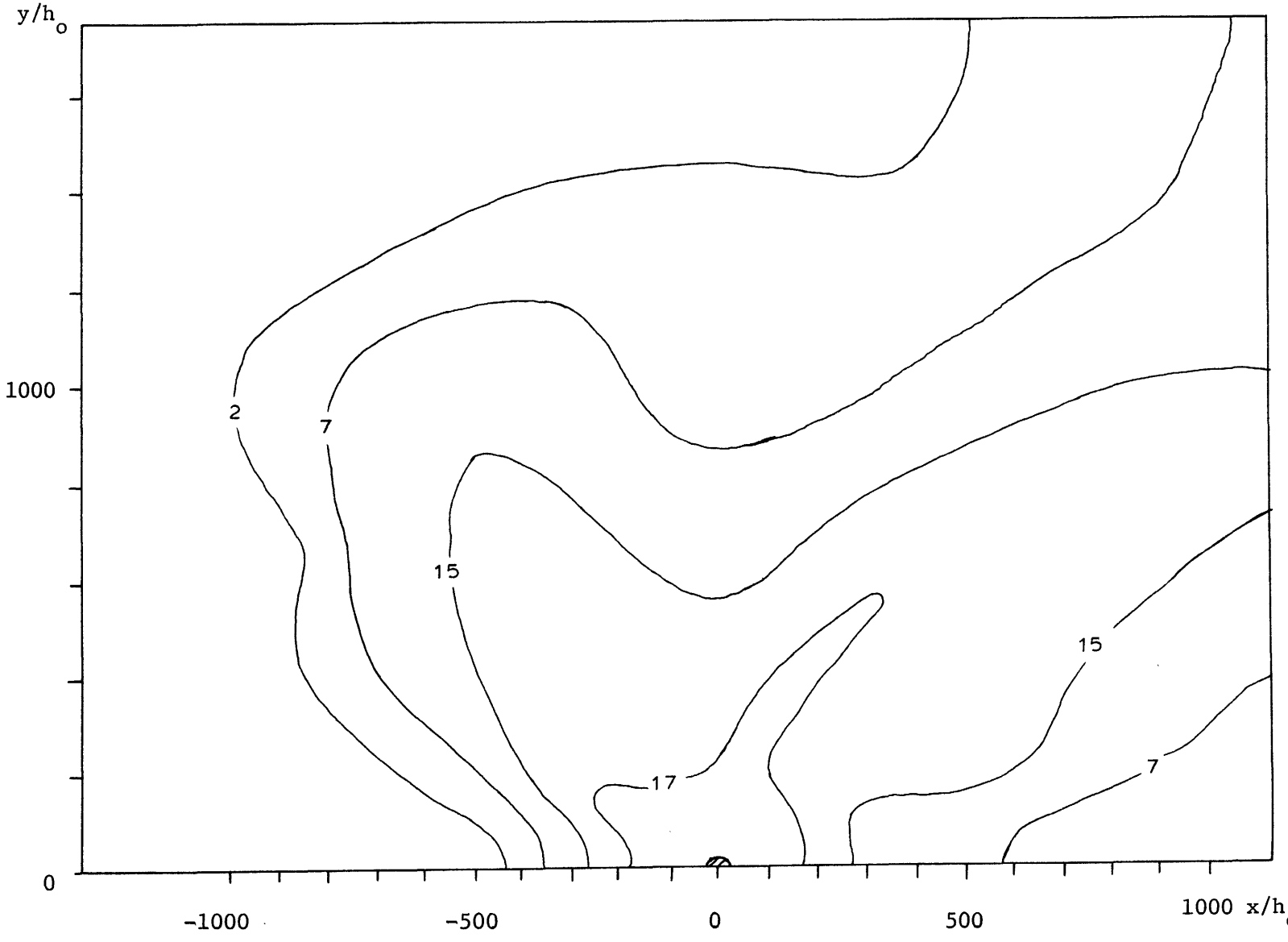

Figure A.3.22 Surface Plan, Run #24, Radial Discharge.

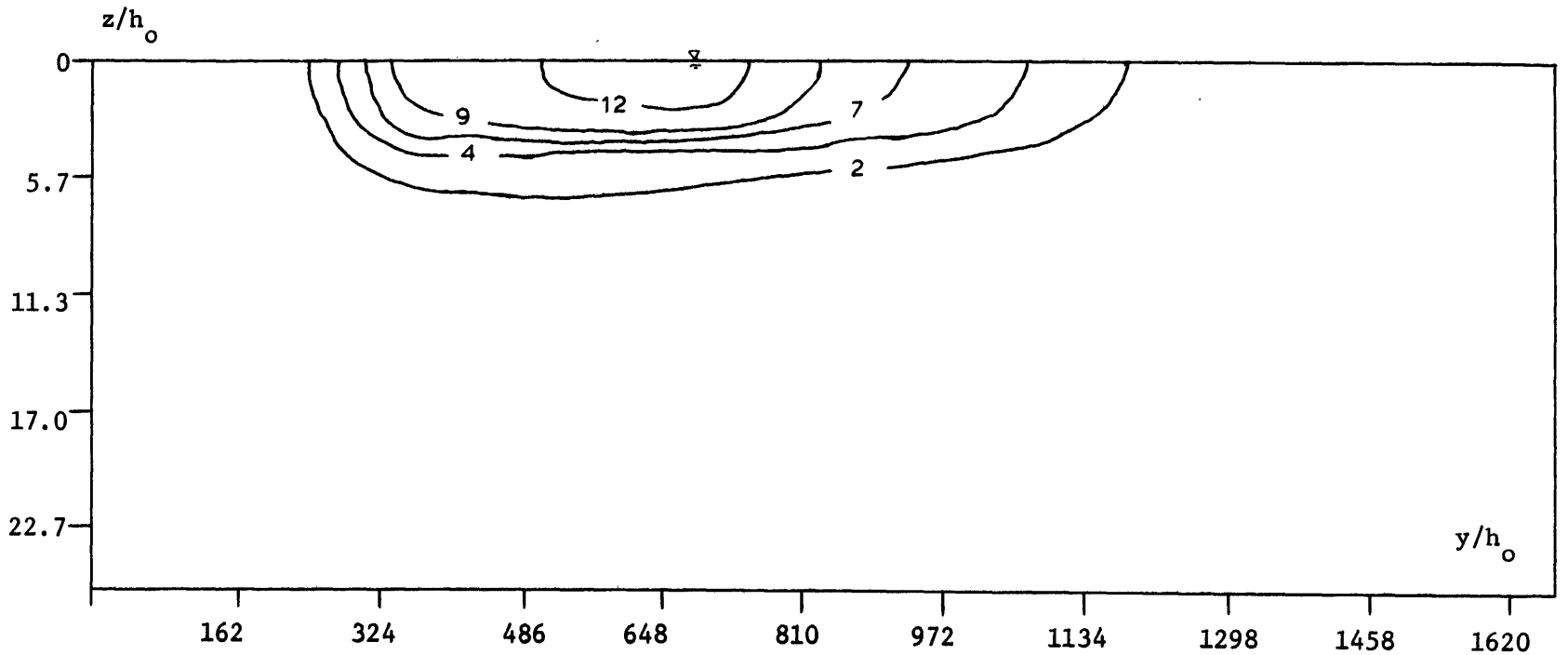

Figure A.3.24 Lateral Transect B-B at x = -4.0m, Run #24.

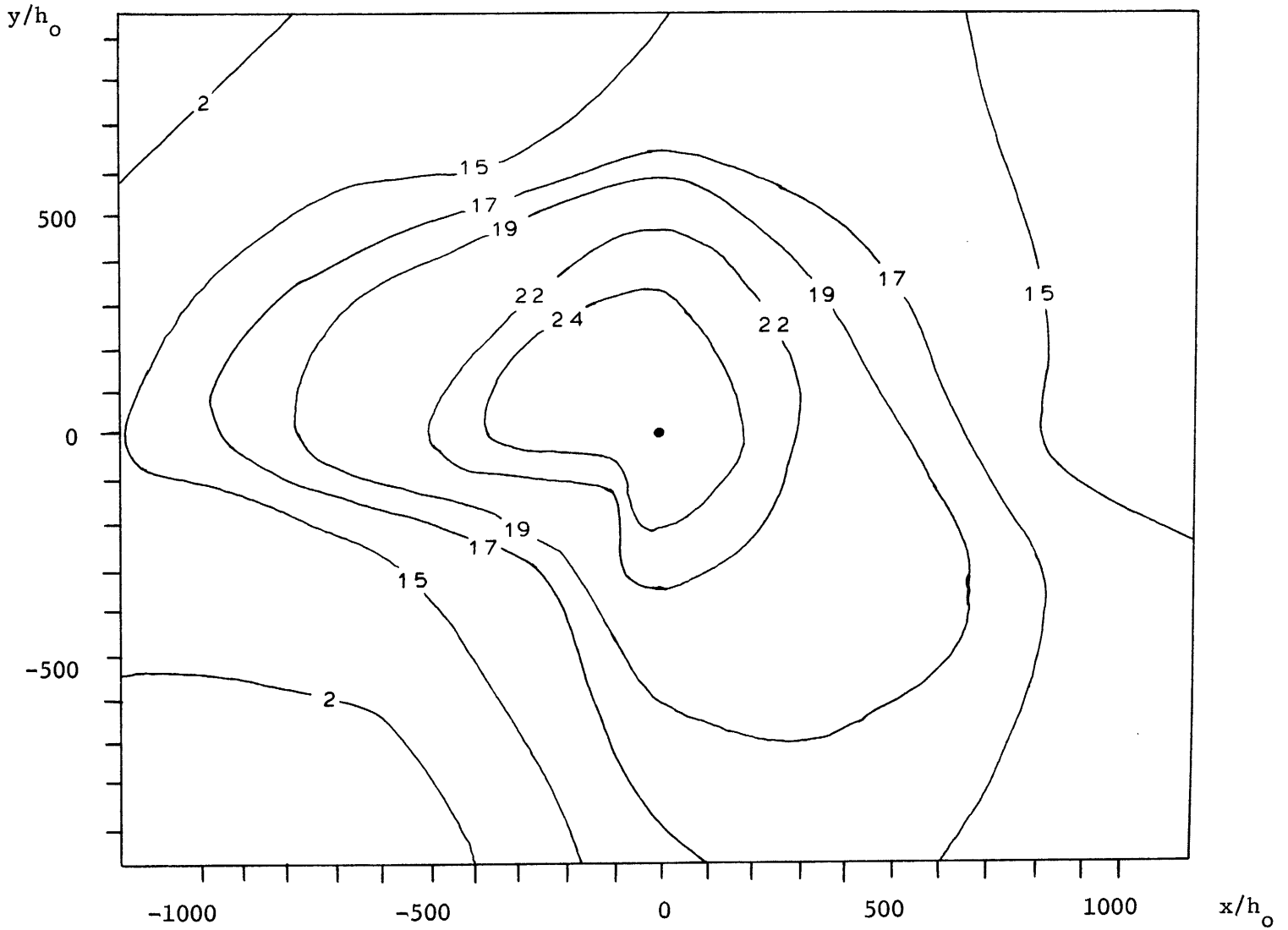

Figure A.3.25 Surface Plan, Run #32, Radial Jet Discharge.

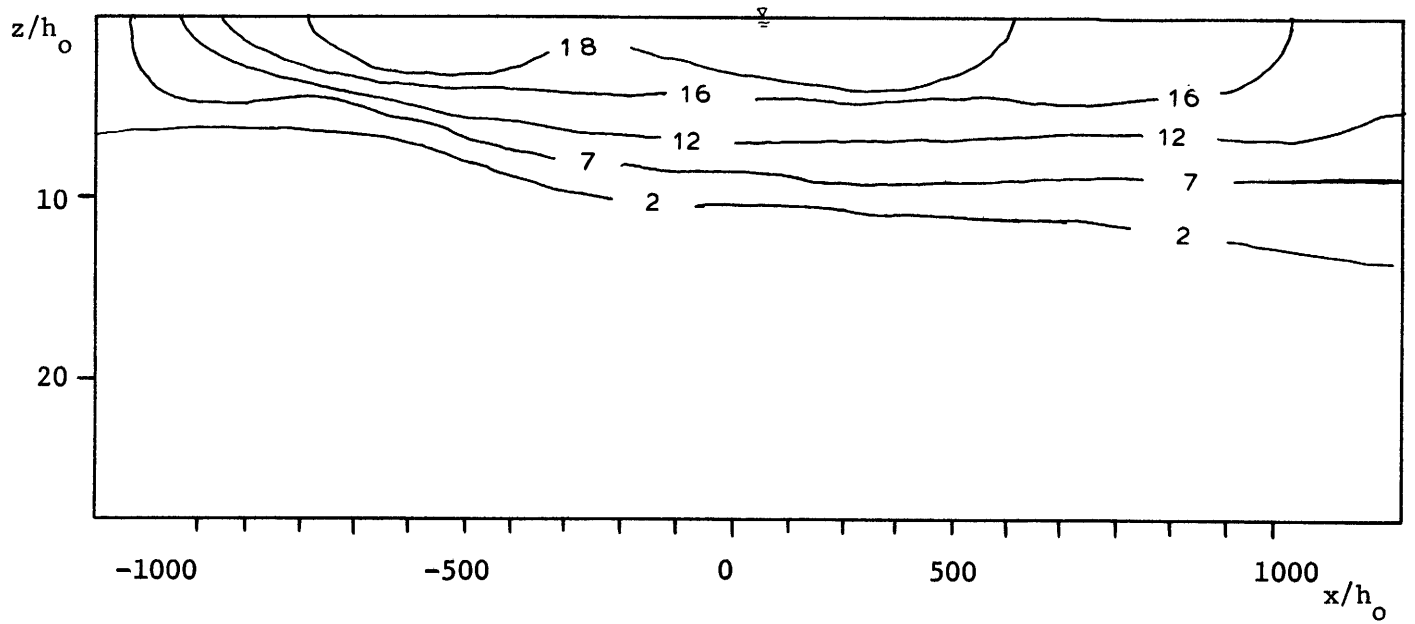

Figure A.3.26 Longitudinal Transect A-A at y = 2.25m, Run #32.

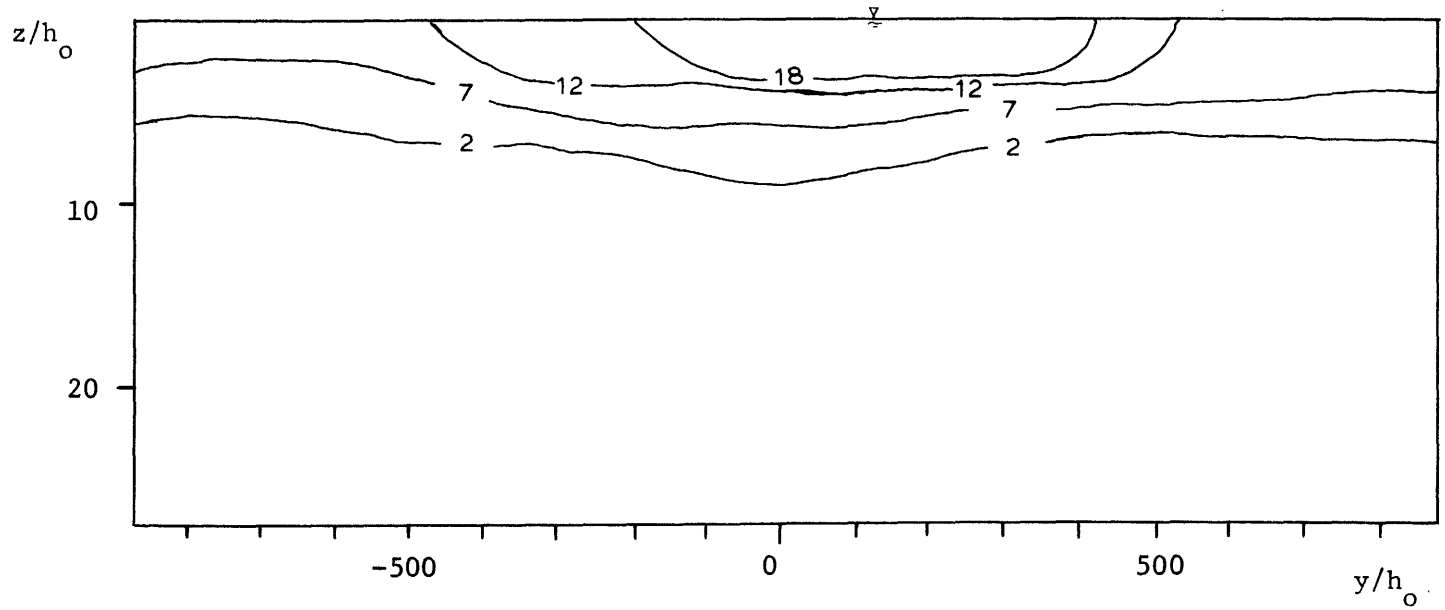

Figure A.3.27 Lateral Transect B-B at x = -4m, Run #32.

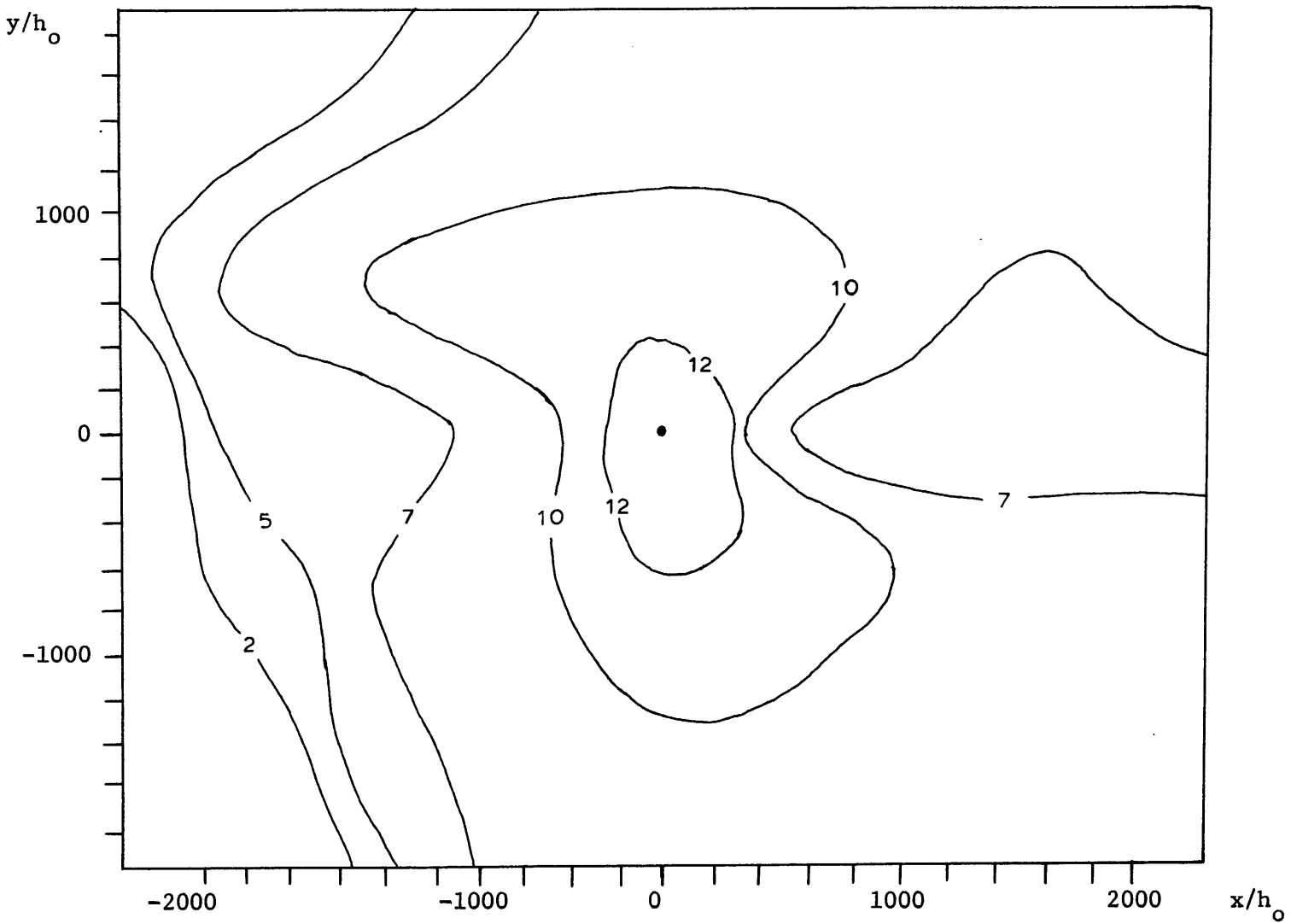

Figure A.3.28 Surface Plan, Run #34, Radial Jet Discharge.

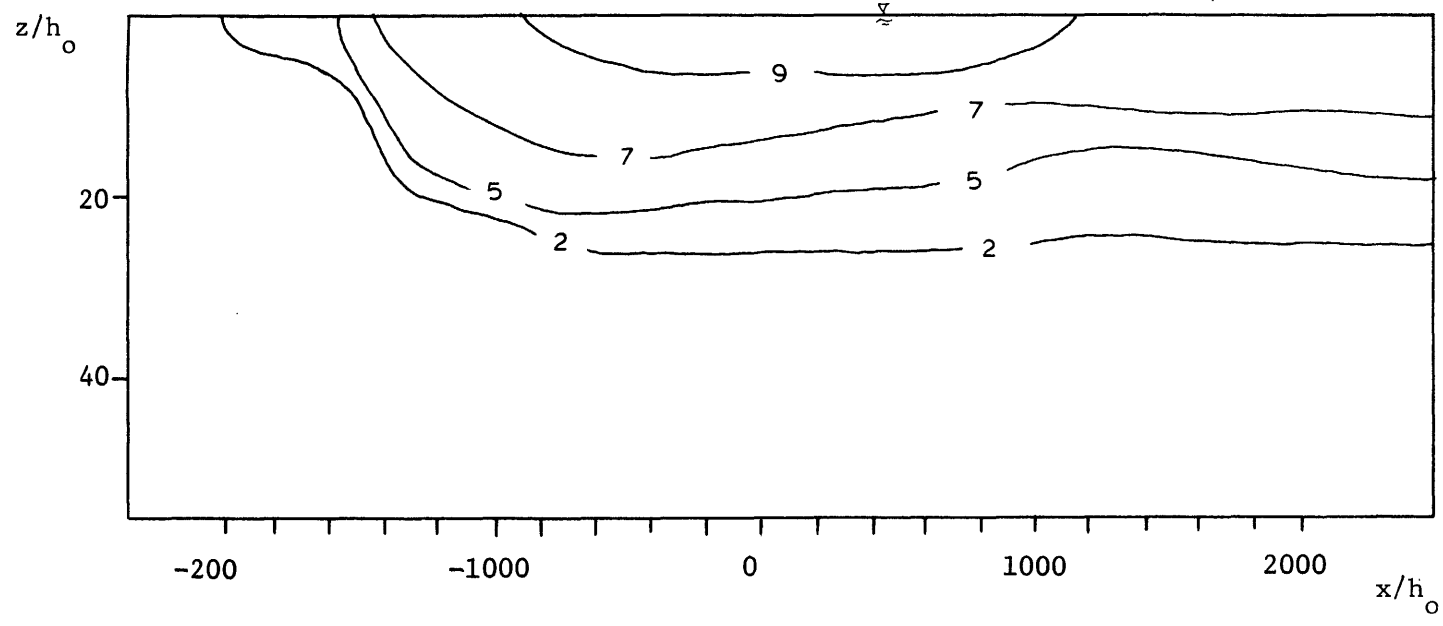

Figure A.3.29 Longitudinal Transect A-A at y = 2.25 m, Run #34.

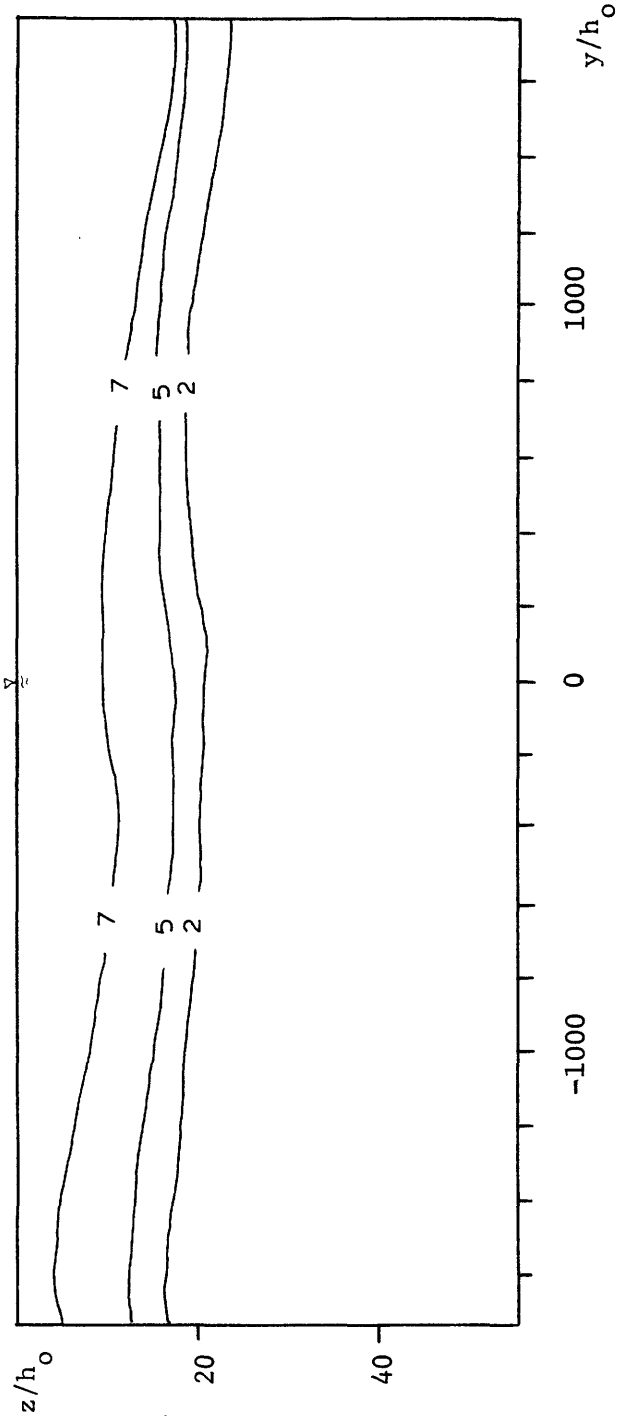

Figure A.3.30 Lateral Transect B-B at x = -4.m, Run #34.

APPENDIX B

VELOCITY MEASUREMENT THROUGH DYE PHOTOGRAPHY

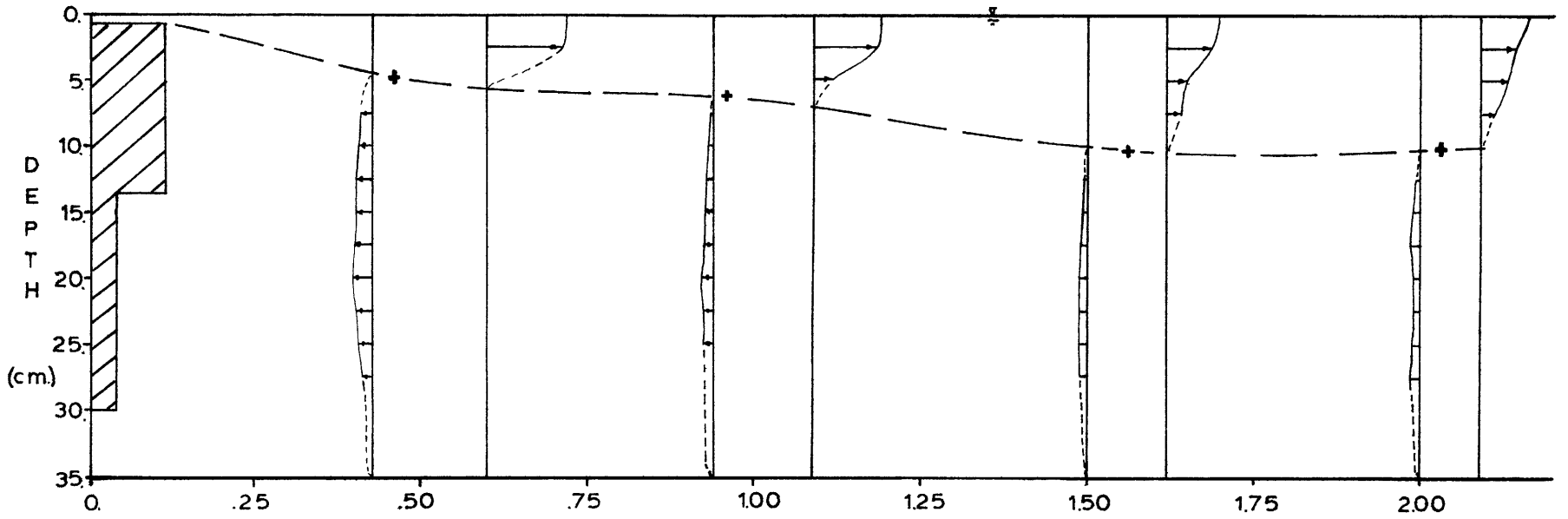

Figure B.1 Photographic Velocity Measurements Exp #60

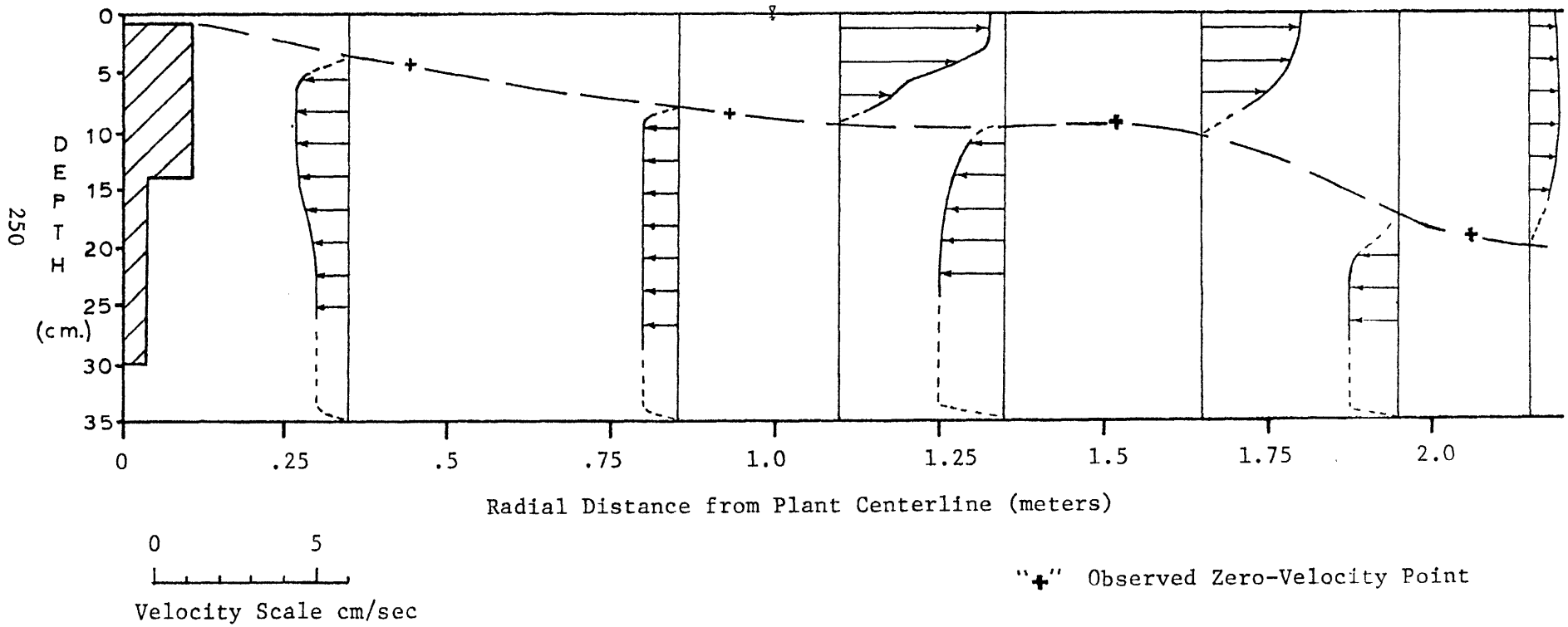

Figure B.2 Photographic Velocity Measurement Exp #51

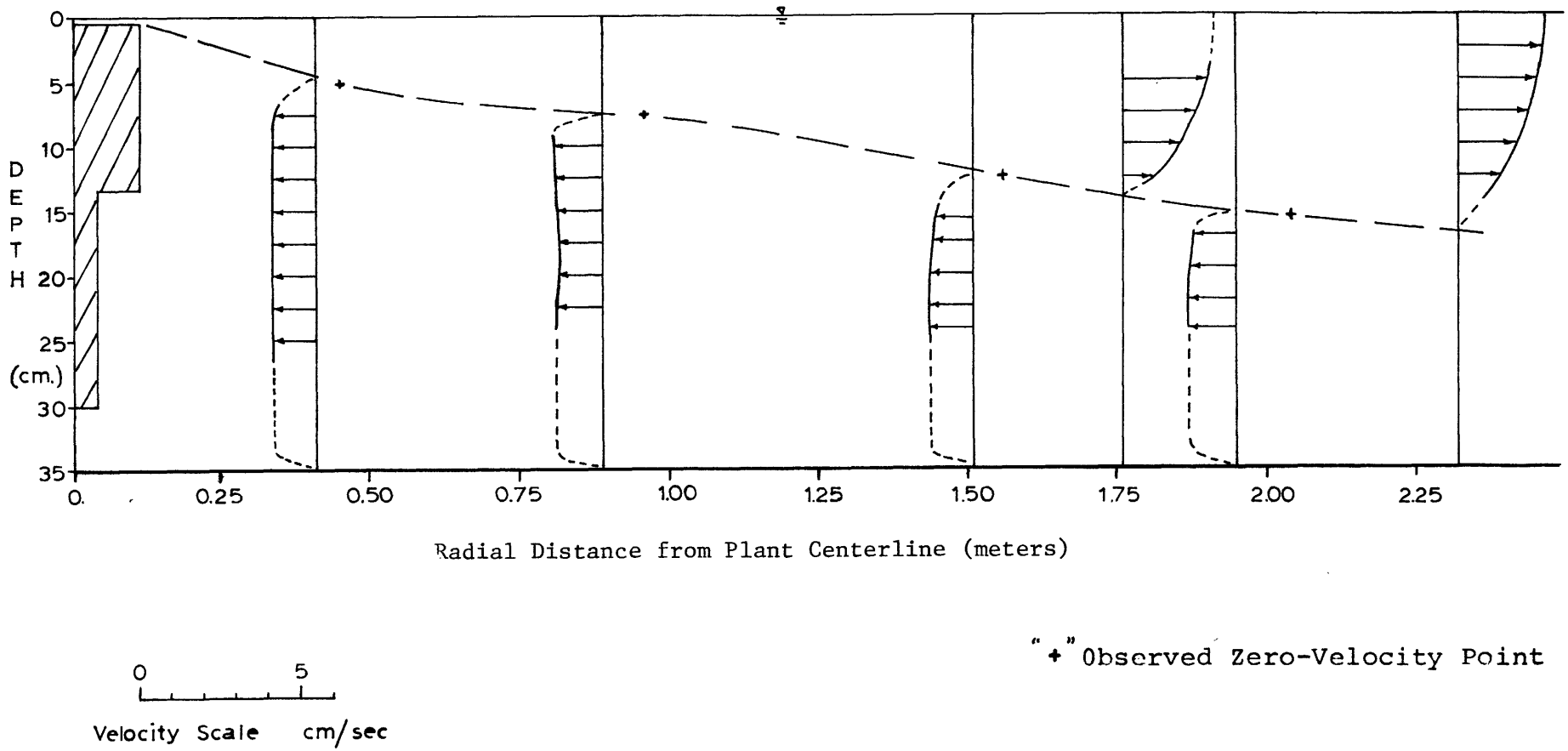

Figure B.3 Photographic Velocity Measurements, Exp #56

APPENDIX C

FAST PROBE TEMPERATURE MEASUREMENTS

$\mu_{\Delta T}$ = mean value of temperature record (above ambient)

σ = standard deviation of temperature

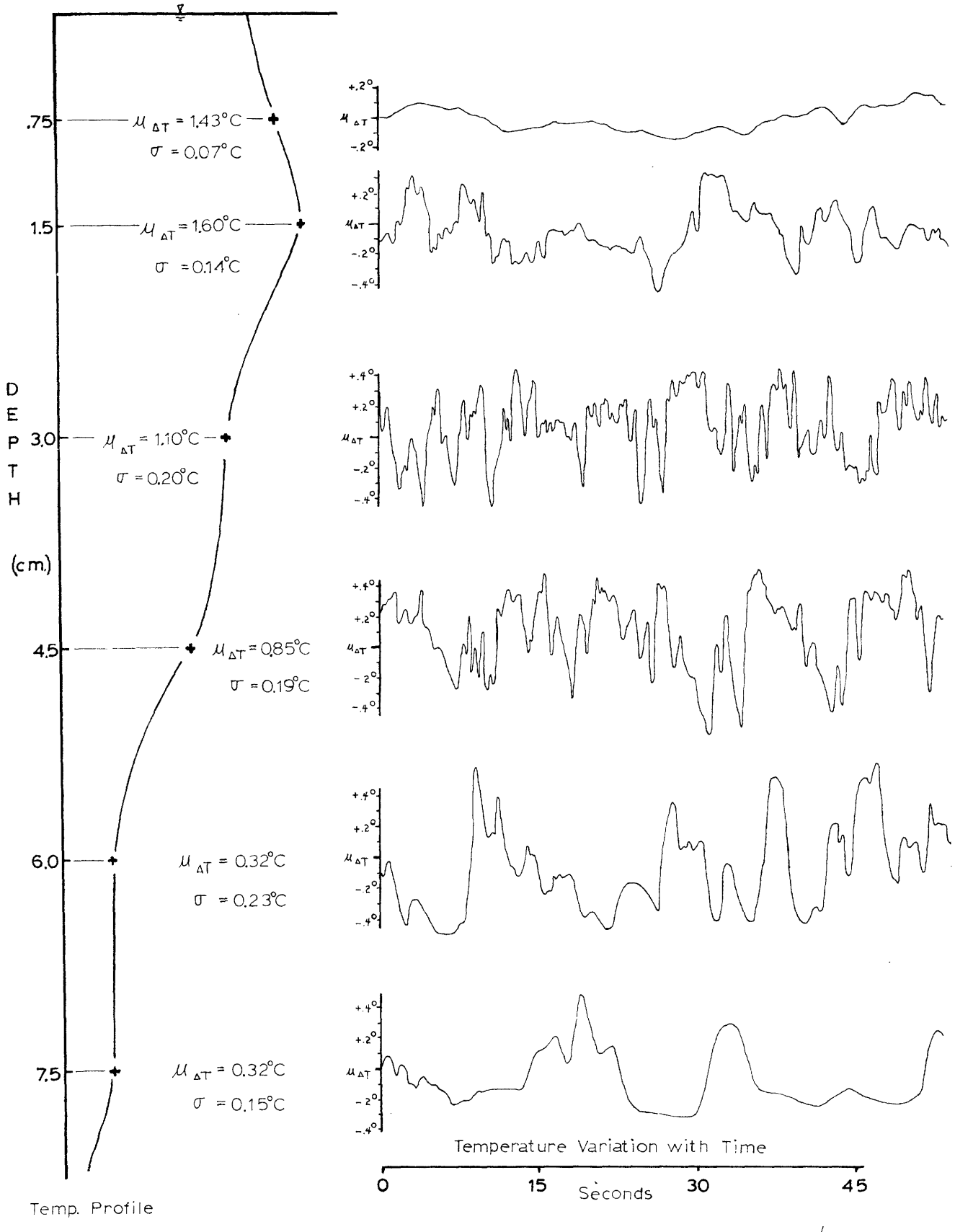

F_{r_o} = 14.3 r_o/h_o = 18.

H/h_o = 55.

Figure C.1 Experiment #60 @ r = 0.91m

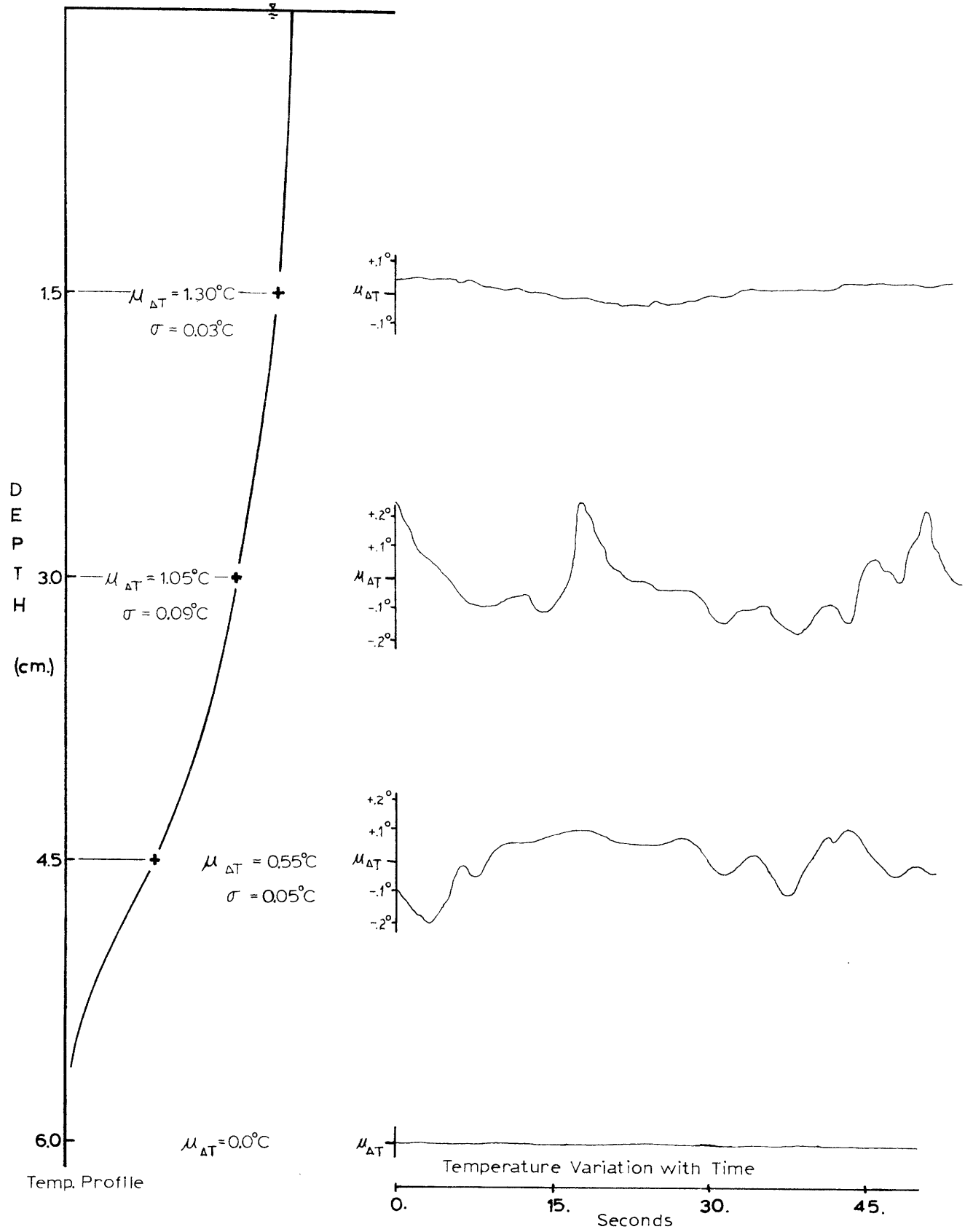

Figure C.2 **Experiment #61 @ r = 2.13m**

F_{r_o} = 14.4 r_o/h_o = 18.

H/h_o = 55.

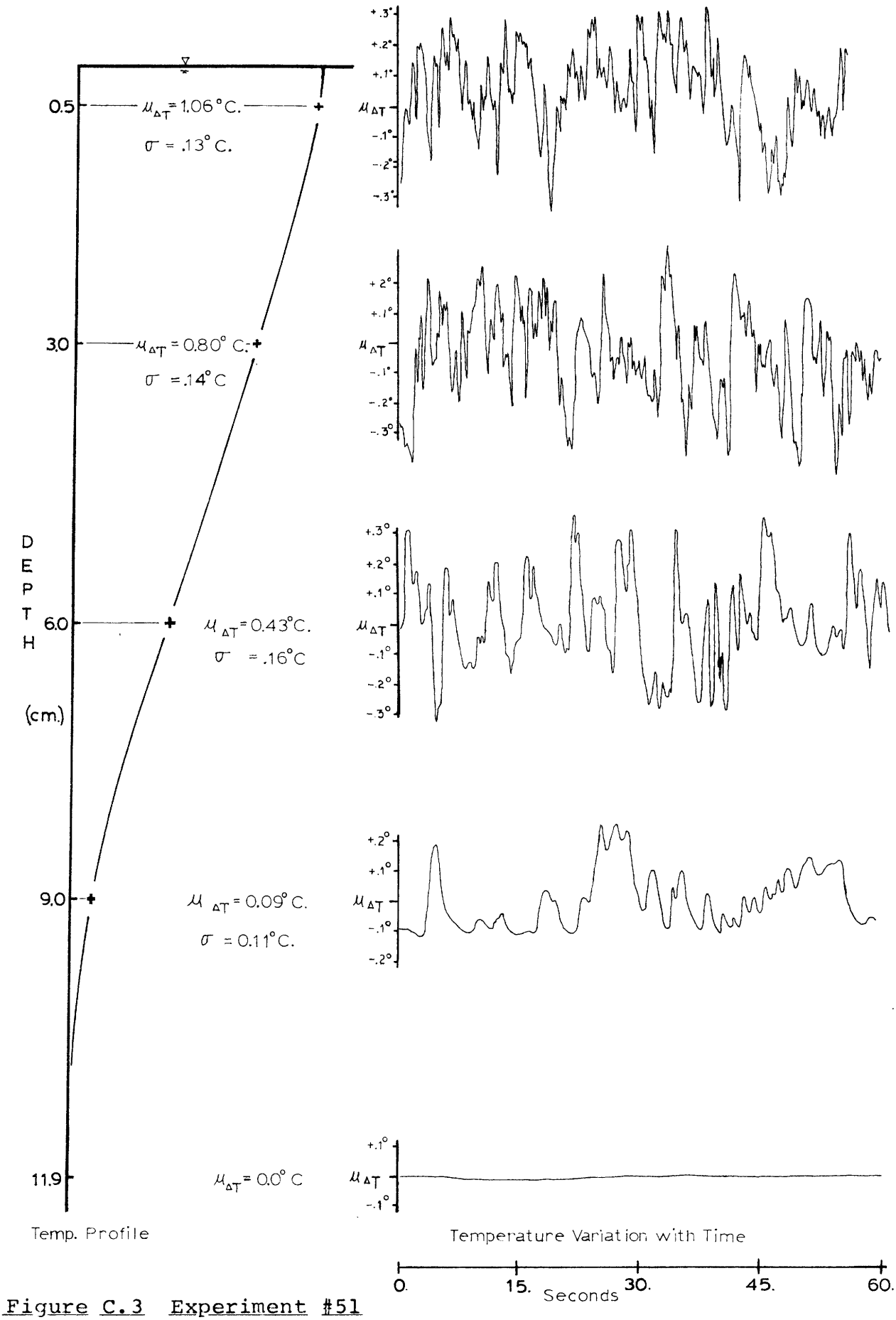

Figure C.3 Experiment #51 @ r = 0.91m

F_{r_o} = 79.5 r_o/h_o = 36.

H/h_o = 110.

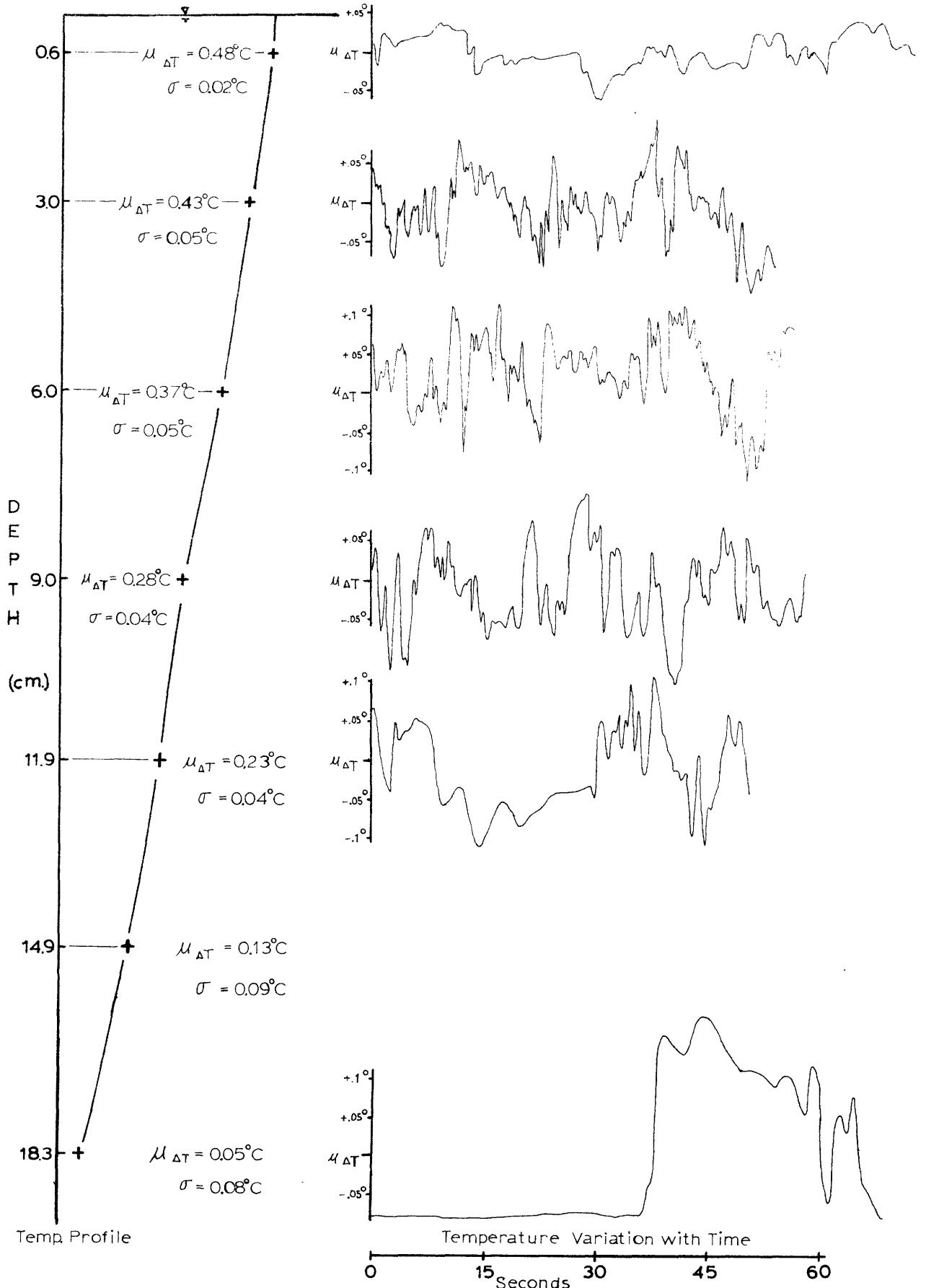

Figure C.4 Experiment #58 @ r = 2.13m

F_{r_o} = 80.7 r_o/h_o = 36.

H/h_o = 110.

APPENDIX D

DEVELOPMENT OF THE EQUATIONS FOR THE RADIAL JET DISCHARGE

The analysis of the steady-state external flow and temperature fields generated by a radially discharging OTEC power plant is best conducted in cylindrical coordinates as angular variations do not exist. By examining only the near field the discharge flow can be treated as a boundary layer (jet) using the turbulent fluid transport equations (Daily and Harleman, 1973). With these assumptions and using the hydrostatic approximation, the appropriate conservation equations for mass, momentum and heat are:

Continuity

$$\frac{1}{r}\frac{\partial ru}{\partial r} + \frac{\partial w}{\partial z} = 0 \qquad (D.1)$$

Momentum

$$r: \quad \rho\left\{\frac{1}{r}\frac{\partial ru^2}{\partial r} + \frac{\partial uw}{\partial z}\right. = -\frac{\partial p}{\partial r} - \rho\frac{\partial \tau_{rz}}{\partial z} \qquad (D.2)$$

$$z: \quad 0 = -\frac{\partial p}{\partial z} + \rho g \qquad (D.3)$$

Heat Transport

$$u\frac{\partial \rho c_p \Delta T}{\partial r} + w\frac{\partial \rho c_p \Delta T}{\partial z} = 0 \qquad (D.4)$$

r,z = coordinate directions; origin taken at the center of the plant; z is positive downward in the direction of gravity

u,w = velocities in r and z directions, respectively

p = pressure

τ_{rz} = turbulent shear stress

ρc_p = specific heat per unit volume

ΔT = temperature deviation from reference temperature

Integrating over the vertical extent of the jet; from the upper boundary, b_1, to the lower boundary, b_2; and applying Leibnitz rule the equations become:

Continuity

$$\frac{1}{r}\frac{d}{dr}\left[r\int_{b_1}^{b_2} u\,dz\right]-u\Big|_{b_2}\frac{db_2}{dz}+u\Big|_{b_1}\frac{db_1}{dr}+w\Big|_{b_1}^{b_2}=0 \qquad (D.5)$$

Momentum

$$r:\quad \rho\left\{\frac{1}{r}\frac{d}{dr}\left[r\int_{b_1}^{b_2} u^2\,dz\right]-u^2\Big|_{b_2}\frac{db_2}{dr}+u^2\Big|_{b_1}\frac{db_1}{dr}+(u,w)\Big|_{b_1}^{b_2}\right\} = -\int_{b_1}^{b_2}\left[\frac{dp}{dr}\,dz\right]+\tau_{rz}\Big|_{b_1}^{b_2} \qquad (D.6)$$

$$z:\quad p\Big|_{b_1}^{b_2} = \int_{b_1}^{b_2}\rho g\,dz \qquad (D.7)$$

Heat Transport

$$\frac{1}{r}\frac{d}{dr}\left[r\int_{b_1}^{b_2} u\Delta T\,dz\right]-(u\Delta T)\Big|_{b_2}\frac{db_2}{dr}+(u\Delta T)\Big|_{b_1}\frac{db_1}{dr}+(w\Delta T)\Big|_{b_1}^{b_2}=0 \tag{D.8}$$

The radial momentum equation simplifies further, since, by definition, there is no turbulent shear at the edge of the jet, $\tau_{rz}|_{b_1} = \tau_{rz}|_{b_2} = 0$.

These equations are general enough to apply to both the model and the prototype discharge fields. It is in considering the boundary conditions that the two situations vary.

D.1 Equations for the Jet at the Free Surface (Model)

Figure B.1 is a diagram of the vertical velocity and temperature distribution in the fully established (i.e. self-similar) jet region for the surface discharge situation in the model. The water surface is the jet centerline, $b_1 = 0$. The lower boundary of the jet is the depth, $b_2 = h_o$. The velocity in the region below the jet, u_b, constitutes the return flow velocity for the intake and entrained flow make-up water. Thus, the velocity within the jet is defined as:

$$u = u_r + u_b \tag{D.9}$$

where u_r is the relative velocity with respect to the return flow.

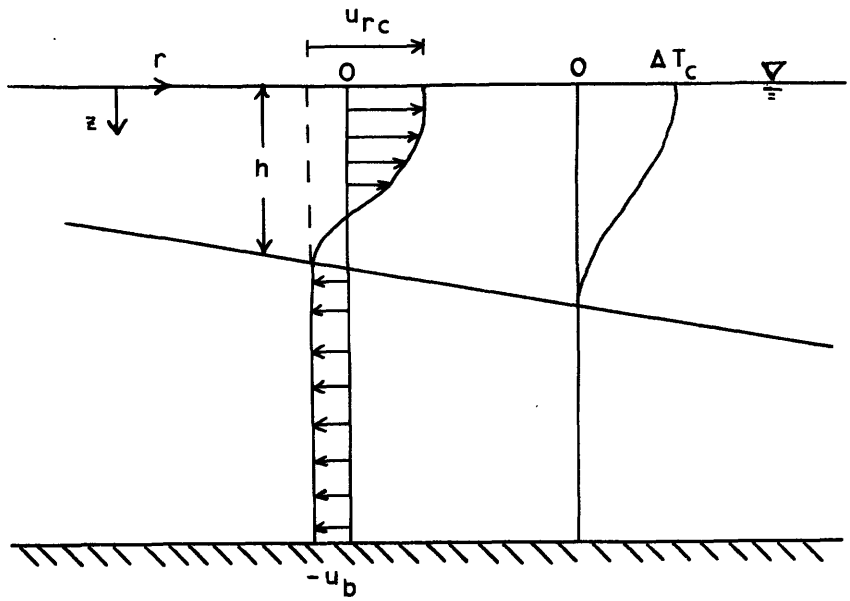

Figure D.1 Schematic Diagram of Surface Jet Vertical Velocity and Temperature Profiles.

(i) Substituting for u gives the general set of equations for an arbitrary return flow velocity u_b.

Continuity

$$\frac{1}{r}\ \frac{d}{dr}\ [r\int_0^h (u_r-u_b)dz]-u|_h\ \frac{dn}{dr} + w|_h\ =\ 0 \qquad (D.10)$$

Momentum

$$\frac{1}{r}\ \frac{d}{dr}\ [r\int_0^h (u_r+u_b)^2dz]-(u_r+u_b)^2|_h\ \frac{dh}{dr} + (u\ w)|_h \qquad (D.11)$$

$$= -\frac{1}{\rho}\int^h \frac{dp}{dr}\ dz$$

Heat Transport

$$\frac{1}{r}\ \frac{d}{dr}\ [r\int_o^h (u_r-u_b)\Delta T dz]\ =\ 0 \qquad (D.12)$$

(ii) For the case of the confined layer where the volumetric flow is equal in opposite directions, as found in the model situation, the return flow velocity is determined:

$$\int_o^h u_r dz\ =\ -u_b H \qquad (D.13)$$

The conservation equations become:

Continuity

$$(1 - \frac{h}{H}) \frac{1}{r} \frac{d}{dr} [r \int_0^h u_r dz] = -w|_h \qquad (D.14)$$

Momentum

$$\frac{1}{r} \frac{d}{dr} [r \int_0^h u_r^2 dz] - \frac{2}{Hr} \frac{d}{dr} [r (\int_0^h u_r dz)^2] + \frac{1}{H^2} \frac{d}{dr} [rh (\int_0^h u_r dz)^2]$$

$$- \frac{(\int_0^h u_r dz)^2}{H^2 r} \frac{dh}{dr} - \frac{(\int_0^h u_r dz)}{H} w|_h \qquad (D.15)$$

$$= -\frac{1}{\rho} \int_0^h \frac{dp}{dr} dz$$

Heat Transport

$$\frac{1}{r} \frac{d}{dr} [\int_0^h u_r \Delta T dz] - \frac{1}{Hr} \frac{d}{dr} [r (\int_0^h u_r dz)(\int_0^h \Delta T dz)] = 0 \qquad (D.16)$$

(iii) In the case of a semi-infinite region with no intake to cause a return flow the equations are simply:

Continuity

$$\frac{1}{r} \frac{d}{dr} [r \int_0^h u dz] = -w|_h \qquad (D.17)$$

Momentum

$$\frac{1}{r}\frac{d}{dr}\left[r\int_0^h u^2 dz\right] = -\frac{1}{\rho}\int_0^h \frac{dp}{dr}\, dz \qquad (D.18)$$

Heat Transport

$$\frac{1}{r}\frac{d}{dr}\left[r\int_0^h u\Delta T dz\right] = 0 \qquad (D.19)$$

For small return flows, u_b approaches zero, the equations for case (ii) approach those for case (iii).

D.2 Equations for the Jet at the Thermocline (Prototype)

The physical situation in the prototype discharge jet is different. Figure B.2 is a diagram of the velocity and temperature distributions. The receiving water upper layer is considerably smaller than the lower layer. Thus, the flow must be asymmetric with respect to the thermocline. However, as a first approximation, for small return flows in the upper layer, the velocity distribution in the upper half of the jet can be assumed symmetric with the velocity distribution in the lower half. The temperature distribution, though, is antisymmetric, providing a smooth transition between the upper layer temperature, T_1, and the lower layer temperature, T_2. The interface temperature is constant and equal to the plant discharge temperature, $T_o = (T_1+T_2)/2$.

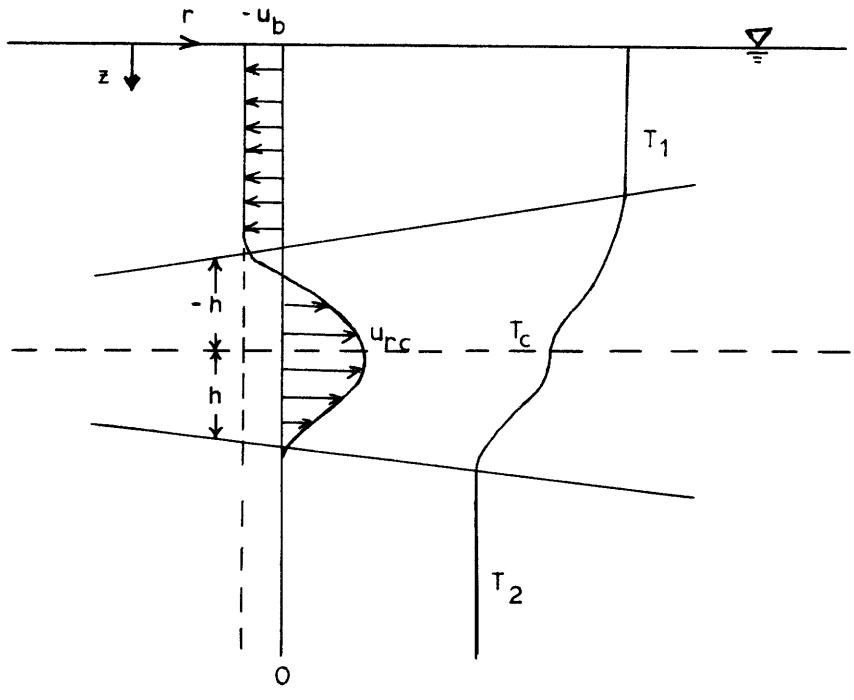

Figure D.2 Schematic Diagram of Interface Jet Vertical Velocity and Temperature Profiles.

The continuity and momentum equations are the same in form for the submerged jet as for the surface discharge case, equations (B.14) and (B.15). The heat transport equation differs from the surface jet because the heat flux in the jet is changing due to entrainment of water with different temperatures in the upper and lower layers.

The heat conservation equation is:

$$\frac{1}{r}\frac{d}{dr}\left[r\int_{-h}^{h} u\Delta T dz\right] = w\Big|_{-h}(T_1-T_2) \qquad (D.20)$$

where ΔT is the temperature difference from T_2.

Substituting for u, the equation becomes:

$$\frac{1}{r}\frac{d}{dr}\left[r\int_{o}^{h} u_r\Delta T dz\right] - \frac{1}{Hr}\frac{d}{dr}\left[\left(\int_{o}^{h} u_r dz\right)\left(\int_{o}^{h}\Delta T dz\right)\right] \qquad (D.21)$$

$$= w\Big|_{-h}(T_1-T_2)$$

APPENDIX E

DEVELOPMENT OF THE PRESSURE DERIVATIVE IN THE VERTICALLY INTEGRATED MOMENTUM EQUATION

The pressure derivative in the vertically integrated radial momentum equation can be reduced to a product of the unknown variables and known coefficients.

Pressure can be divided into two parts:

$$p = p_h + p_d \tag{E.1}$$

p_h = hydrostatic pressure

p_d = dynamic pressure

Density can also be divided into two parts:

$$\rho = \rho_a - \Delta\rho \tag{E.2}$$

$$\Delta\rho = \beta\Delta T \tag{E.3}$$

ρ_a = ambient (reference) density

β = thermal expansion coefficient

Using the hydrostatic pressure approximation in the treatment of the jet equations (Appendix D) the dynamic pressure component is neglected in the following, $p_d = 0$. The hydrostatic pressure is further defined as:

$$p_h = \int_0^z (\rho-\Delta\rho)gdz \quad (z \text{ positive down}) \tag{E.4}$$

The pressure derivative can be written:

$$\frac{dp}{dr} = \frac{d}{dr} \left[-\int_0^z \Delta\rho g dz\right] \tag{E.5}$$

Outside the jet region, $z = \infty$, no motion is assumed, so that

$$\frac{dp}{dr} = 0 \quad \text{at } z = \infty \tag{E.6}$$

$$0 = -\frac{d}{dr} \left[\int_0^\infty \Delta\rho g dz\right] \tag{E.7}$$

Subtracting Equation (C.7) from Equation (C.5) gives

$$\frac{dp}{dr} = \frac{d}{dr} \left[\int_z^\infty \Delta\rho g dz\right] \tag{E.8}$$

So

$$-\int_0^h \frac{dp}{dr} dz = -\frac{d}{dr} \int_0^h \int_z^h \Delta\rho g dz' dz \tag{E.9}$$

The limit 'h' is taken since the values outside the jet are zero.

E.1 Integrated Pressure Term for the Surface Jet

Knowing the temperature distribution function, g(z/h), where h is the jet depth, the pressure term for the surface discharge case becomes:

$$-\int_0^h \frac{dp}{dr}\,dz = -\frac{d}{dr}\,(\beta g \Delta T h^2 G_2) \qquad \text{(E.10)}$$

where G_2 is an integration constant

$$G_2 = \int_0^h \int_z^h g(z'/h)\,dz'\,dz \qquad \text{(E.11)}$$

$$\Delta T = \Delta T_c g(z/h) \qquad \text{(see Figure D.1)}$$

E.2 Integrated Pressure Term for the Submerged Jet at the Interface

Due to the antisymmetric temperature distribution the discharge jet at the thermocline is negatively buoyant with respect to the upper layer and positively buoyant with respect to the lower layer. Limiting the analysis to jets with width, h, smaller than the thermocline depth, H, $\frac{h}{H} << 1$, it is possible to approximate the integrated pressure term by:

$$-\int_{-h}^{+h} \frac{dp}{dr}\,dz = -\left\{ \frac{d}{dr}\left[\int_h^0 \int_z^{-\infty} \Delta\rho\,dz'\,dz\right] + \frac{d}{dr}\left[\int_0^{\infty} \int_z^{\infty} \Delta\rho\,dz'\,dz\right] = -2\,\frac{d}{dr}\,[\beta g \Delta T h^2 G_2]\right. \qquad \text{(E.12)}$$

where $\Delta T = \Delta T_c g(z/h)$. (see Figure D.2)

This result implies that the upper and lower layer buoyancy forces are equal and the same as for a surface jet with the same temperature distribution.